



Exciton and spin-valley properties in WSe₂ monolayers

Lei Ren

► To cite this version:

Lei Ren. Exciton and spin-valley properties in WSe₂ monolayers. Physics [physics]. INSA de Toulouse, 2023. English. NNT: 2023ISAT0002 . tel-04100552

HAL Id: tel-04100552

<https://theses.hal.science/tel-04100552>

Submitted on 17 May 2023

HAL is a multi-disciplinary open access archive for the deposit and dissemination of scientific research documents, whether they are published or not. The documents may come from teaching and research institutions in France or abroad, or from public or private research centers.

L'archive ouverte pluridisciplinaire **HAL**, est destinée au dépôt et à la diffusion de documents scientifiques de niveau recherche, publiés ou non, émanant des établissements d'enseignement et de recherche français ou étrangers, des laboratoires publics ou privés.



THÈSE

**En vue de l'obtention du
DOCTORAT DE L'UNIVERSITÉ DE TOULOUSE
Délivré par l'Institut National des Sciences Appliquées de
Toulouse**

Présentée et soutenue par

Lei REN

Le 16 février 2023

**Propriétés excitoniques et couplage spin-vallée dans les
monocouches de WSe₂**

Ecole doctorale : **SDM - SCIENCES DE LA MATIERE - Toulouse**

Spécialité : **Physique de la Matière**

Unité de recherche :

LPCNO - Laboratoire de Physique et Chimie des Nano-Objets

Thèse dirigée par

Xavier MARIE et Cédric ROBERT

Jury

Mme Maria VLADIMIROVA, Rapporteure

M. Clément FAUGERAS, Rapporteur

M. Lionel CALMELS, Examinateur

M. Christophe VOISIN, Examinateur

M. Xavier MARIE, Directeur de thèse

M. Cédric ROBERT, Co-directeur de thèse

“不以物喜，不以己悲”

---- 范仲淹，北宋

Contents

Abstract	I
Résumé en Français	III
Introduction	V
Chapter 1 Introduction to Transition Metal Dichalcogenides.....	1
1.1 2D Materials based on transition metal dichalcogenides.....	2
1.2 Crystal symmetry and energy band structure	5
1.3 Exciton states.....	11
1.4 Bright and dark excitons	17
1.5 Optical selection rules and spin-valley polarization	20
1.6 Conclusion	25
Chapter 2 Experimental Techniques.....	26
2.1 Sample fabrication	27
2.1.1 All-dry stamping deterministic transfer method and fabrication setups..	27
2.1.2 The drawbacks of all-dry stamping method and the solution	29
2.1.3 Identification of TMD monolayers and selection of hBN	31
2.2 Effects of hBN encapsulation on the optical and exciton properties.....	33
2.3 Optical spectroscopy experiments	35
2.3.1 Optical spectroscopy setups	35
2.3.2 Differential reflectivity measurement	38
2.3.2.1 Lorentzian model.....	39
2.3.2.2 Transfer matrix method	40
2.3.3 Photoluminescence spectroscopy.....	42
2.3.4 Polarization-resolved photoluminescence.....	43
2.3.5 Magneto-photoluminescence spectroscopy	44
2.4 Conclusion	45
Chapter 3 Control of the Splitting between Bright and Dark Excitons using Lamb Shift in WSe₂ Monolayers	46
3.1 Exciton fine structure in semiconductor nanostructures	47
3.2 Investigated samples and experimental methods.....	47

3.3	Experimental results	49
3.3.1	Luminescence linewidth study.....	50
3.3.2	The bright-dark exciton energy splitting	51
3.4	Theory and discussion.....	52
3.5	Conclusion	55
Chapter 4 Spin-valley Pumping of Resident Electrons in WSe₂ and WS₂ Monolayers		56
4.1	Spin-valley pumping in TMD monolayers	57
4.2	Investigated samples and experimental methods.....	57
4.3	X^{T^-} & X^{S^-} bright trions and X^{D^-} dark trion in WSe ₂ monolayers	59
4.4	Observations and results	60
4.5	Discussion.....	63
4.5.1	Possible mechanism of spin-valley pumping	64
4.5.2	Circular-polarization of X^{T^-} and X^{S^-} trions	65
4.5.3	Discussion on PL intensities for circular and linear excitations	69
4.6	Limitations of the bimolecular formation model.....	70
4.7	Similar results in WS ₂ monolayers	70
4.8	Conclusion	71
Chapter 5 Optical Detection of Long Electron Spin Transport Lengths in WSe₂ Monolayers		72
5.1	Spin-valley locking effect in TMD monolayers	73
5.2	Investigated sample and experimental method	73
5.3	Protocol of measurement and data processing	75
5.4	Trions: probe of electron spin	76
5.5	Dependence on pump and probe power	78
5.6	Dependence on doping density	78
5.7	Measurements of the electron spin diffusion length	79
5.8	Pump helicity-dependent circular polarization of trions	81
5.9	Temperature dependence.....	82
5.10	Conclusion	84
Chapter 6 Measurement of Conduction and Valence Bands <i>g</i>-factors in WSe₂ Monolayers		85

6.1	Exciton <i>g</i> -factor in TMD monolayers	86
6.2	Investigated samples and experimental method	87
6.3	Photoluminescence spectra of a WSe ₂ monolayer in the hole doping regime 87	
6.4	Method to measure the conduction and valence bands <i>g</i> -factor and results	90
6.5	Measurements for a second device	94
6.6	Discussion.....	95
6.7	Conclusion	97
 Chapter 7 Résumé en Français		98
Conclusion and Perspective		130
Appendix		132
List of Publications and Conferences.....		139
Bibliography		141

Acknowledgements

It was really magic that I came to Toulouse Three years ago. I had had been searching for PhD offers in renewable energy science but in the end I was “attracted” in two-dimensional semiconductor Physics and “trapped” in the beauty of the physics inside. This is like a free carrier captured by a defect in semiconductors and localized around it. During my PhD study at LPCNO, I have learned a lot not only knowledge on physics but also human relationship. I have met outstanding and considerate people; I would like to thank them all for their generous and wonderful help and support to this thesis.

I would like to first express my sincere gratitude to Maria VLADIMIROVA, Clément FAUGERAS, Lionel CALMELS, Christophe VOISIN to review my thesis, give me scientific and constructive advice, and join the jury members of my PhD defense.

Second, I am not able to express my highest gratitude in words to my thesis supervisors, Xavier MARIE and Cédric Robert for offering me this PhD thesis opportunity, for sharing their great passion in physics and for their guidance during the three-year study. Their strongest support plays a key and indispensable role for the development of this dissertation. Without them, I can not imagine how my PhD study would go on! Xavier is a big-league “enseignant-chercheur” in low-dimensional Physics and “quasi-professional” cyclist. He and I have shared the same office since two years; we sit back to back. This creates great opportunity for me to ask questions and discuss the experimental results. He can always use “simple” words to explain explicitly all kinds of effects in Physics. Moreover, Xavier is always willing to share time with me even though he has important responsibilities in lectures, project funding and administration. Besides, Xavier is a very nice and considerate supervisor. We discuss the latest word news, family and my professional carriers. He gives me a lot of constructive advice and precious help on job hunting. Cédric is an outstanding CNRS researcher and “future French cyclist” in 2024 Olympics. He knows every stuff in our Laboratory, from a tiny key’s position to the proper operation of the cryostats. He has teached me a lot of experimental skills and techniques on optical spectroscopy. He is extremely patient to explain the working principle of setups and to tech me the optical alignment skills hand by hand. Whenever I meet any technique problems, Cédric will help me to solve them.

Then, I highly appreciate Laurent LOMBEZ for his forwarded email that brought me to Toulouse. He was my teacher in my master study. Thanks to this email, I applied the PhD position at LPCNO and finally got this position. Laurent is a senior expert in transport experiments. I also worked with him for some time. I have learned skills on transport experiments from him.

Besides, I would like to thank Delphine LAGARDE, research engineer in our group, for her consistent technique support. Together with Cédric, Delphine is in charge of proper operation of all equipment in our group. Without their meticulous care in Lab, our group is not able to be so productive.

Thierry AMAND is an honored CNRS research director. He is extremely strong in mathematics. He will never stop once starts to talk about Physics. We worked together on several papers. I should have discussed Physics more with him during my PhD study instead of only focusing on experiments. Luckily, I have started to discuss exchange interactions in detail at the end of my PhD. I am very grateful for his private lecture.

Pierre RENUCCI, Andrea BALOCCHI, Hélène CARRERE, Thomas BOULIER are permanent teachers of INSA-Toulouse. Their research is more focused on classic semiconductors and magnetic materials. Pierre is a fan of “splitting banana”; Andrea is a swimming sportive; Hélène is a gluten-free gourmand. Thomas is a fan of music; Great thanks for their help and kindness.

I would like to thank Bernhard URBASZEK, Ioannis PARADEISANOS, Bo HAN and Shivangi SHREE, former group members in the group. I still remember the scientific discussions, daily conversations and jokes we had in the past three years. I wish you an excellent “settle down” in new place.

Vivekanand Tiwari is post-doc; Dorian BERET and Jules FRAUNIE are PhD students in the group. Very nice to meet them in Toulouse and wish them a promising future.

Special thanks for Prof. Brahim ELOUADI (University of La Rochelle) who gave me precious and constructive advice during all my study in France and for Prof. Wanqiang CAO (Hubei University) who encouraged me to pursue my study in France. Without you, I would never come to France.

My girlfriend, Xiaohui Liu (刘晓慧) who is always besides me, support me and encourage me. Though we have been together less than one year, we get used to each other and take good care of each other. We do a lot of things together, shopping, hiking, running, tourism, ...; Enormous photos have recorded our happiness. I really appreciate her company and I believe we can stay together all along.

I would like also to show my highest gratitude to my family members: grandfather, Lichen REN (任利成); grandmother, Guoqing LI (李国清); mother: Rong YUAN (袁蓉); Paternal uncle, ZhiLiang REN (任之良); Maternal uncle: Neng YUAN (袁能). Your efforts and encouragement make WHO I AM today.

I will never forget all friends I have met in Paris and in Toulouse. I feel like not far away from home since they are besides me.

Abstract

Triggered by the success of graphene, research on two-dimensional (2D) atomic crystals has grown extremely rapidly over the last decade. The family of 2D materials exhibits an exceptional variety of electronic properties related to their low-dimensional character, from insulators, to metals, semimetals, topological insulators, semiconductors, and superconductors. In addition, atomically-thin layers with different properties can be assembled in vertical stacks commonly referred as van der Waals heterostructures, allowing the design of artificial materials with tailored physical properties. These heterostructures open up new perspectives for controlling the optical and spin properties of materials. They can provide not only rich physics associated to novel phenomena but they are also promising for future applications in optoelectronics or spin(valley)tronics.

2D semiconductors based on Transition Metal Dichalcogenide (TMD) monolayers investigated in this thesis have very original properties: (1) 2H phase TMD have layer-dependent band structure: they become direct bandgap semiconductors when thinning down to monolayer while they remain indirect bandgap semiconductors in bulk form; (2) the light-matter interaction in TMD monolayers is very strong, for example, the absorbance of a single WS₂ layer can exceed 15%. This remarkable light-matter interaction is governed by excitons, tightly bound electron-hole pairs with typical binding energy of several hundreds of meV. (3) TMD monolayers have unique spin-valley properties which have been studied in detail in this manuscript.

In this work, we have used an all-dry stamping method to stack micron-size flakes onto each other and to fabricate high quality van der Waals heterostructures based on WSe₂ monolayers. Encapsulation of these WSe₂ monolayers by hexagonal boron nitride (hBN), an insulator with large band gap (~6 eV), enables us to reach spectral linewidths almost limited by the radiative rate of excitons. We performed photoluminescence experiments to demonstrate that the radiative rate and the resonance energy of the bright neutral exciton in WSe₂ monolayer can be tailored by the variation of the hBN encapsulation thickness. We show that the tuning of the radiative rate and resonance energy is the consequence of the Purcell effect and Lamb shift, respectively. Our results demonstrate that we can control the bright-dark exciton splitting as a result of Quantum Electrodynamical effects.

In a charge-tunable device, we also demonstrate a very efficient spin-valley optical pumping of resident electrons in *n*-doped WSe₂ and WS₂ monolayers. We observe that, using a continuous wave laser and appropriate doping and excitation densities, negatively charged exciton (trion) doublet lines exhibit circular polarization of opposite sign; using the same method, we also observe that the photoluminescence intensity of the triplet trion is more than four times larger with circular excitation than with linear excitation. We interpret our results as a consequence of a large dynamic polarization of resident electrons following circularly polarized excitation. Based on this efficient

spin-valley pumping method, we then measure the lateral transport of spin-valley polarized electrons over very long distances (tens of micrometers) in a single WSe₂ monolayer by using a spatially resolved optical pump-probe experiment. Finally, we present an original optical method that can quantify to the respective contribution of the conduction and valence band to the measured Zeeman splitting in longitudinal magnetic fields by exploiting the optical selection rules of exciton complexes. It yields a direct determination of single band g -factors of electron and hole in a WSe₂ monolayer.

Résumé en Français

Déclenchées par le succès du graphène, les recherches sur les cristaux atomiques bidimensionnels (2D) se sont développées extrêmement rapidement au cours de la dernière décennie. La famille des matériaux 2D présente une variété exceptionnelle de propriétés électroniques liées à leur faible dimensionnalité, des isolants aux métaux, semi-métaux, isolants topologiques, semiconducteurs et supraconducteurs. De plus, des couches atomiquement minces avec des propriétés différentes peuvent être assemblées en empilements verticaux communément appelés hétérostructures de van der Waals, permettant la conception de matériaux artificiels avec des propriétés physiques adaptées. Ces hétérostructures sont prometteuses pour de futures applications en optoélectronique ou en spin(vallée)-tronique.

Les semiconducteurs 2D à base de monocouches de dichalcogénure de métal de transition (TMD) étudiés dans cette thèse ont des propriétés très originales : (1) les TMD à phase 2H ont une structure de bande dépendante de l'épaisseur : ils deviennent des semiconducteurs à bande interdite directe lorsqu'ils sont amincis en monocouche alors qu'ils sont des semiconducteurs à bande interdite indirecte dans la forme massive ; (2) l'interaction lumière-matière dans les monocouches de TMD est très forte, par exemple, l'absorbance d'une monocouche de WS₂ peut dépasser 15%. Cette remarquable interaction lumière-matière est régie par les excitons, des paires électron-trou étroitement liées par l'interaction coulombienne avec une énergie de liaison typique de plusieurs centaines de meV. (3) les monocouches de TMD ont des propriétés uniques de spin-vallée qui ont été étudiées en détail dans ce manuscrit.

Dans ce travail, nous avons utilisé une méthode « all-dry stamping » pour empiler des flocons de taille micrométrique les uns sur les autres et pour fabriquer des hétérostructures van der Waals de haute qualité à base de monocouches de WSe₂. L'encapsulation de ces monocouches avec du nitrite de bore hexagonal (hBN), un isolant à large bande interdite ~6 eV, nous permet d'atteindre des largeurs de raies spectrales quasiment limitées par le taux de recombinaison radiative des excitons. Nous avons effectué des expériences de photoluminescence pour démontrer que le taux radiatif et l'énergie de résonance de l'exciton neutre brillant dans la monocouche de WSe₂ peuvent être modifiés par la variation de l'épaisseur d'encapsulation hBN. Nous montrons que le contrôle du taux de recombinaison radiatif et de l'énergie de résonance est la conséquence de l'effet Purcell et du décalage de Lamb, respectivement. Nos résultats démontrent que nous pouvons contrôler la séparation en énergie entre excitons brillants et noirs par des effets d'électrodynamique quantique.

Dans un dispositif à charge ajustable, nous avons également mis en évidence un pompage optique très efficace de spin-vallée des électrons résidents dans les monocouches de WSe₂ et de WS₂ dopées n. Nous observons qu'en utilisant un laser continu, des densités de dopage et d'excitation appropriées, les deux raies d'excitons chargés négativement (trion) présentent une polarisation circulaire de signe opposé et

l'intensité de photoluminescence du trion triplet est plus de quatre fois plus grande avec une excitation circulaire qu'avec une excitation linéaire. Nous interprétons nos résultats comme une conséquence d'une forte polarisation dynamique des électrons résidents. Sur la base de cette méthode de pompage efficace de spin-vallée, nous avons ensuite mesuré le transport latéral des électrons polarisés en spin-vallée sur de très longues distances (des dizaines de micromètres) dans une monocouche de WSe₂ en utilisant une expérience de pompe-sonde optique à résolution spatiale. Enfin, nous présentons une méthode optique originale qui permet de quantifier la contribution respective des bandes de conduction et de valence au dédoublement Zeeman mesuré dans des champs magnétiques longitudinaux ; cette méthode exploite les caractéristiques de recombinaison des complexes excitoniques. Elle conduit à une détermination directe des facteurs g de l'électron et du trou dans une monocouche de WSe₂.

Introduction

Human's civilization is strongly associated with the development of material science. Human history can be divided into different ages with a typical material or technique revolution: Stone Age, Bronze Age, Iron Age, Industrial Revolutions and Information Age. At each age, human improves life quality and creates social prosperity with the mastered new knowledge of material science. Looking back to our history, we used stone tools thousands of years ago to hunt animals but now we are able to send rockets in space and achieve secure quantum cryptography from a satellite to a ground station up to 1000 kilometers away [1]. All those remarkable progresses are largely owed to the development of material science.

We are now at Information Age where our individual life and society significantly depends on information technology (IT). It is hard to image our individual daily life without any electronic devices, like smartphone or personal computer. As a matter of fact, our collective society is also inseparable from IT since most of society functions are achieved with the help of IT, like public transport system and logistics. Our actual age is also called "Silicon Age" because silicon (Si) is the essential material for integrated electronic devices, which are at the heart of information technology. However, we have almost reached the limits of Si-based integrated circuits technique. In other words, we cannot further miniaturize the Si-based devices to gain higher performance and industrial production yields due to the intrinsic problems of this technology, for example quantum tunneling effect which can damage the on/off ratio when the channel of transistor narrows down to sub-nanometers.

Two-dimensional (2D) materials are regarded as promising materials for new generation of information processing and storage devices because we can design novel quantum structures by exploiting their advanced quantum phenomena, for instance, quantum state superposition and entanglement. The family of 2D materials exhibits an exceptionally large variety of electronic properties related to their low-dimensional character, from insulators, to metals, semimetals, topological insulators, semiconductors, and superconductors. These emerging 2D materials with original electronic, magnetic and optical properties provide an ideal research platform to investigate low-dimensional physics and to develop future revolutionary devices for different applications.

In this thesis, we have investigated transition metal dichalcogenides monolayers, one of the most promising family of 2D semiconductors.

We will present in Chapter 1 their general characteristics: crystal symmetry, energy band structure, exciton states, exciton fine structure, optical selection rules and spin-valley polarization properties.

In Chapter 2, we will present the main experimental techniques we used for the sample fabrication (exfoliation and all-dry stamping deterministic transfer methods)

and for their optical characterization (reflectivity measurement, polarization-resolved and magneto-photoluminescence spectroscopy).

In Chapter 3, we have investigated the exciton fine structure in atomically thin WSe₂. We encapsulate WSe₂ ML within a van der Waals heterostructure (top hBN/WSe₂ ML/bottom hBN); We demonstrate that the density of optical modes at the location of the semiconductor monolayer can be tuned by changing the Bottom hBN encapsulation layer thickness. The energy splitting between the bright and dark exciton has been measured by photoluminescence spectroscopy, which can be tuned by a few meV, as a result of a significant Lamb shift. We also measured in the same structures strong variations of the bright exciton radiative linewidth, as a result of the Purcell effect.

In Chapter 4, we have investigated the spin-valley properties in WSe₂ and WS₂ monolayers. We demonstrate a very efficient spin-valley optical pumping of resident electrons in *n*-doped WSe₂ and WS₂ monolayers by continuous wave circularly-polarized light. Spin-valley polarization up to 80% can be obtained in WSe₂ monolayer.

In Chapter 5, we have measured the lateral spin diffusion lengths of these resident electrons through an original spatially-resolved optical pump-probe experiment based on the results of Chapter 4. Up to 25% spin-valley polarization is observed for pump-probe separations up to 20 microns. Characteristic spin-valley diffusion lengths of $18 \pm 3 \mu\text{m}$ are revealed at low temperatures. We interpret this long spin-valley diffusion length as a result of the unique band structure and spin-valley locking effect in WSe₂ monolayer.

In Chapter 6, we will present an original method that can quantify the respective contribution of the conduction and valence band to the measured Zeeman splitting in WSe₂ monolayer in a longitudinal magnetic field. This method exploits the specific recombination features of exciton complexes in this monolayer. We show that the conduction band and valence band *g*-factors can be measured accurately with this optical method.

Chapter 1 Introduction to Transition Metal Dichalcogenides

In this Chapter, we will first introduce the general characteristics of two-dimensional (2D) materials and then focus on TMD monolayers. Group-VI TMD have interesting electrical and optical properties. They are indirect-bandgap semiconductors in bulk material while direct-bandgap when thinning down to monolayer. The optical properties of TMD monolayers are governed by excitons, *i.e.* Coulomb bound electron-hole pairs. The binding energy of exciton in TMD monolayers can reach up to several hundreds of meV, as a result of quantum confinement and reduced dielectric screening in 2D plane; This leads to strong light-matter interaction. Besides, TMD monolayers have chiral optical selection rules and spin-valley coupling due to the broken crystal inversion symmetry and strong spin-orbit coupling. Those unique properties make TMD monolayers promising in electronics, optoelectronics, spintronics and quantum technologies. Meanwhile, they are also a versatile platform for novel phenomena, for instance twistronics. Thanks to the weak van der Waals interactions between adjacent layers, we can easily build artificial 2D crystals by stacking different monolayers on top of each other, *i.e.* van der Waals heterostructures to obtain exotic effects for future applications.

We review in this Chapter the crystal symmetry and energy band structures of TMD monolayers. Then the exciton properties and the exciton fine structure are briefly introduced. Finally, the optical selection rules and spin-valley polarization are discussed.

This Chapter is organized with the following sections:

- 1.1 2D Materials based on transition metal dichalcogenides
- 1.2 Crystal symmetry and energy band structure
- 1.3 Exciton states
- 1.4 Bright and dark excitons
- 1.5 Optical selection rules and spin-valley polarization
- 1.6 Conclusion

1.1 2D Materials based on transition metal dichalcogenides

In the past decades, low dimensional materials, like quantum wells (2D), nanowires (1D) and quantum dots (0D) have attracted considerable attention and have been widely studied in multiple aspects: material growth, physical/chemical properties and potential applications. In this thesis, we will focus on transition metal dichalcogenides monolayers, semiconducting 2D material with original properties. In fact, 2D materials include a wide range of families: insulators, semiconductors, metals, superconductors..., as shown in **Figure 1.1**.

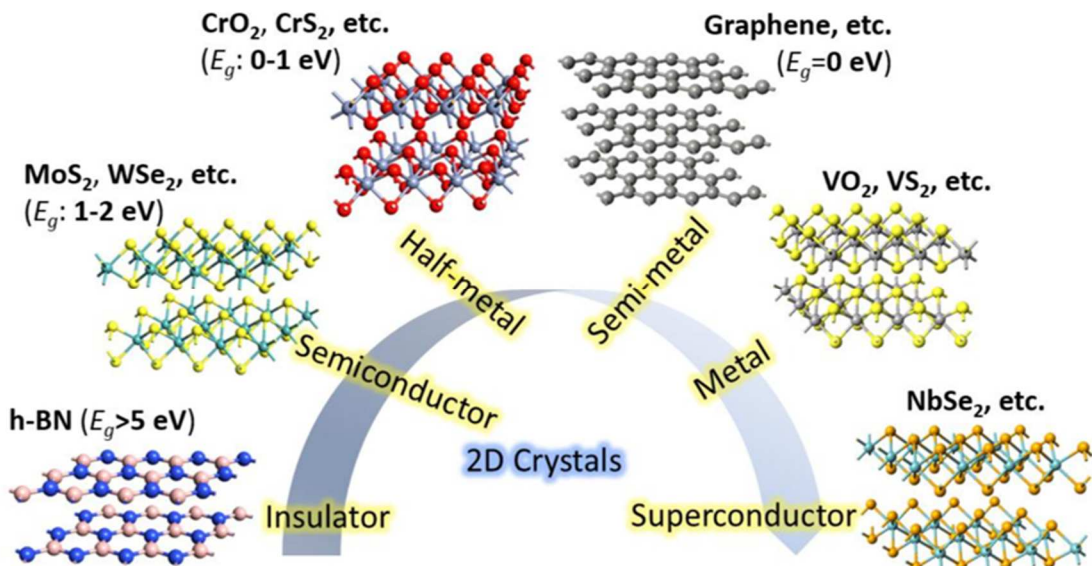


Figure 1.1 The main categories of 2D materials. E_g denotes bandgap. Extracted from Ref. [2].

The interest for 2D materials has been triggered by the discovery of graphene, a single layer of carbon atoms constituting an hexagonal structure as shown in **Figure 1.1**. It was first obtained by Konstantin Novoselov and Andre Geim through mechanical exfoliation method [3]. This outstanding breakthrough leads to the Nobel prize in Physics in 2010. Graphene exhibits spectacular properties: (1) carrier mobility exceeding $10^6 \text{ cm}^2 \cdot \text{V}^{-1} \cdot \text{s}^{-1}$ at 2 K [4] and exceeding $10^5 \text{ cm}^2 \cdot \text{V}^{-1} \cdot \text{s}^{-1}$ at room temperature when encapsulated in hexagonal Boron Nitride (hBN) layers [5]; (2) large thermal conductivity of around $5000 \text{ W} \cdot \text{mK}^{-1}$ at room temperature [6]; (3) the strongest material with breaking strength of $42 \text{ N} \cdot \text{m}^{-1}$ in a monolayer [7]. Its high carrier mobility has stimulated substantial research for transistor applications. However, graphene-made field-effect transistors (FETs) have relatively low on/off switching ratios due to the lack of bandgap [8], obstructing progress in high performance transistors. In contrast, TMD monolayers with 2H crystal structure possess bandgaps in the visible-near infrared range [9,10] thus promising for new FET and optoelectronic devices.

TMD have layered structure with the general form M-X-M, where M represents a transition metal atom (Mo, W) and X represents a chalcogen atom (S, Se or Te). In each single monolayer, the plane of transition metal atoms is sandwiched between the

two planes of chalcogen atoms, forming a trigonal prismatic structure as shown in **Figure 1.2**. The crystal structures of TMD are detailed in section 1.2. TMD have many unique electrical and optical properties, drawing significant attention in recent research. Here, we will quickly review them and they will be discussed in more detail in the following sections.

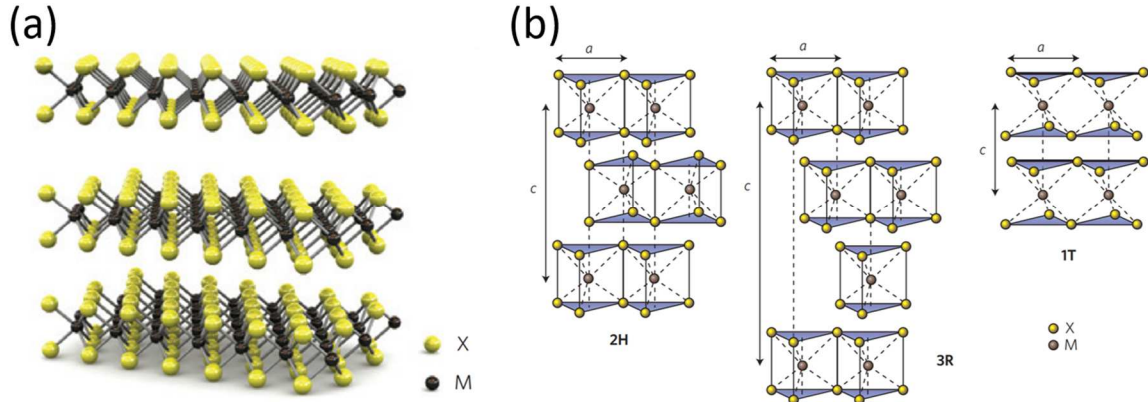


Figure 1.2 Crystal structures of TMD. (a) Schematic of layered structure of TMD. The plane of transition metal atoms (M , in grey) is sandwiched between the two adjacent planes of chalcogen atoms (X , in yellow). (b) Schematics of different polytypes of TMD: 1T, 2H and 3R. The stacking index c indicates the number of layers in each stacking order and the thickness of a single monolayer is $\sim 6.5 \text{ \AA}$. Extracted from Ref. [8].

(1) The bandgaps of TMD are layer-dependent: they become direct bandgap semiconductors when thinning down to monolayer while they remain indirect bandgap semiconductors for a number of layers ≥ 2 . More detail in section 1.2.

(2) Besides, the light-matter interaction in TMD monolayers is very strong; for example, the absorbance of a single-layer WS_2 can exceed 15% at the wavelength around 620 nm [11]. This remarkable light-matter interaction is governed by very robust excitons, *i.e.* Coulomb bounded electron-hole pairs with typical binding energy of several hundreds of meV [12–16]. This will be discussed in section 1.3.

(3) TMD monolayers have strong spin-orbit coupling and unique spin-valley degree of freedom, which will be discussed in more detail in section 1.2 and 1.5, respectively.

As a consequence, TMD monolayers have drawn important attention for various electronic and optoelectronic applications such as transistors [17–21], flexible/transparent devices [22–25], photovoltaics/light-emission devices [26–29] and sensors [30–32].

Van der Waals heterostructures

The properties of TMD monolayers are very rich as we will show in this thesis. We can now imagine making artificial crystals by stacking different 2D materials on top of each other, as shown in **Figure 1.3**. This assemblage is named van der Waals (vdW)

heterostructure, which can not only help to design devices with new functionalities but also provide a platform with rich physics. The great advantage of vdW heterostructures is to combine different materials which are usually very difficult to grow together because of lattice mismatching [33]. In those structures, the different 2D layers are coupled by relatively weak vdW forces while the strong covalent bonds keep in-plane stability of the structure. When two different materials are stacked together, the interaction at the interface can generate novel effects. The final result of this stacking is not simply equal to the sum of each individual component property. For example, when a TMD monolayer is deposited on a magnetic material, it can generate magnetic proximity effect. A large valley Zeeman splitting of 16 meV/T was reported in a vdW heterostructure composed of a WS₂ ML/ferromagnetic Europium(II) sulfide (EuS₂) [34]. This effect has also been reported in a vdW heterostructure WSe₂ ML and bi/trilayer Chromium(III) iodide (CrI₃) [35].

Furthermore, heterostructures made of two different TMD MLs can generate interlayer excitons (IXs), whose constituent carriers reside in different atomic layers. IXs retain valley and spin properties of their constituent layers, but have longer lifetimes and potentially enhanced tuneability with respect to excitons in a single TMD monolayer [36]. These unique properties offer possibilities to realize excitonic devices for information and signal processing, similar to electronic and spintronic devices but dependent on manipulation of excitons instead of electrons or spins.

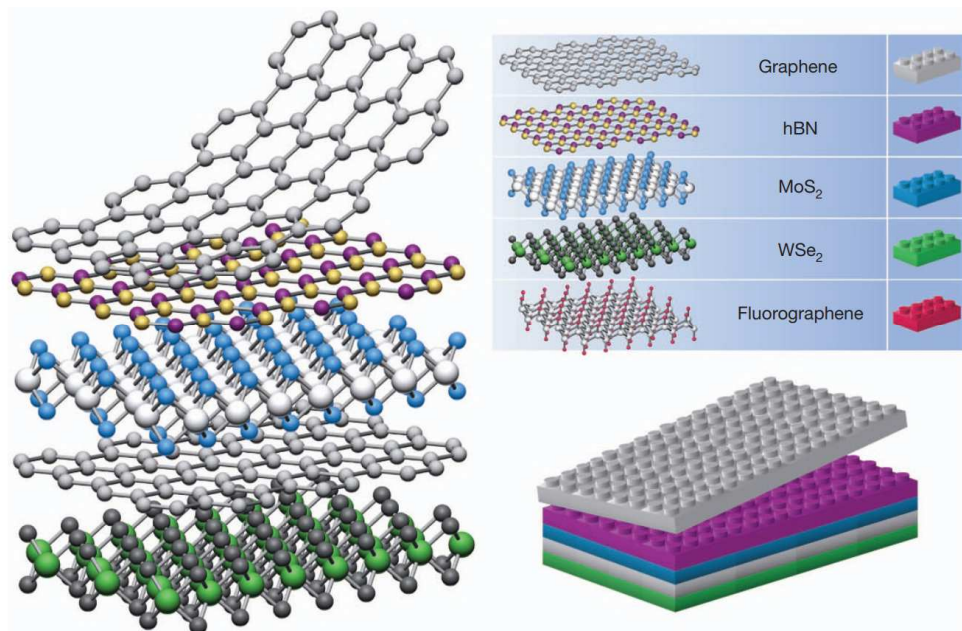


Figure 1.3 Van der Waals heterostructures. 2D layers can be considered as Lego blocks (right panel) and various vdW heterostructures with complex layer stacking can be built. This artificial crystal stacking is favorable thanks to the relatively weak vdW interaction between adjacent 2D layers. Extracted from Ref. [37].

Twistronics

Rich physics has been discovered in vdW heterostructures. What happens if one of the 2D layers is twisted by a certain angle with respect to the other and then stacked onto it? In fact, this can create moiré patterns, with a period which can be controlled by the twist angle and/or the lattice mismatch, as shown in **Figure 1.4**. Moiré patterns can greatly modify the electronic properties by locally changing the band structure. The study of correlation between the twisted angle of two-dimensional materials and their electronic properties is called twistronics. The first groundbreaking finding in twistronics was discovered in twisted bilayer graphene (TBG) in 2018. The “magic angle” of 1.1° in TBG gives rise to fascinating phenomena, for example, unconventional intrinsic superconductivity [38]. This triggered considerable attention on twistronics in 2D science community. Recent studies have shown for instance that the charge mobility in 30° twisted bilayer MoS₂ is almost 2 times higher than 0° structure, leading to larger on/off ratio of field-effect transistors [39].

To conclude, TMD can not only provide a polyvalent platform for fundamental physics but are also promising candidates for a new generation of devices in electronics or optoelectronics... In the following sections, we will detail the main properties of TMD.

Materials

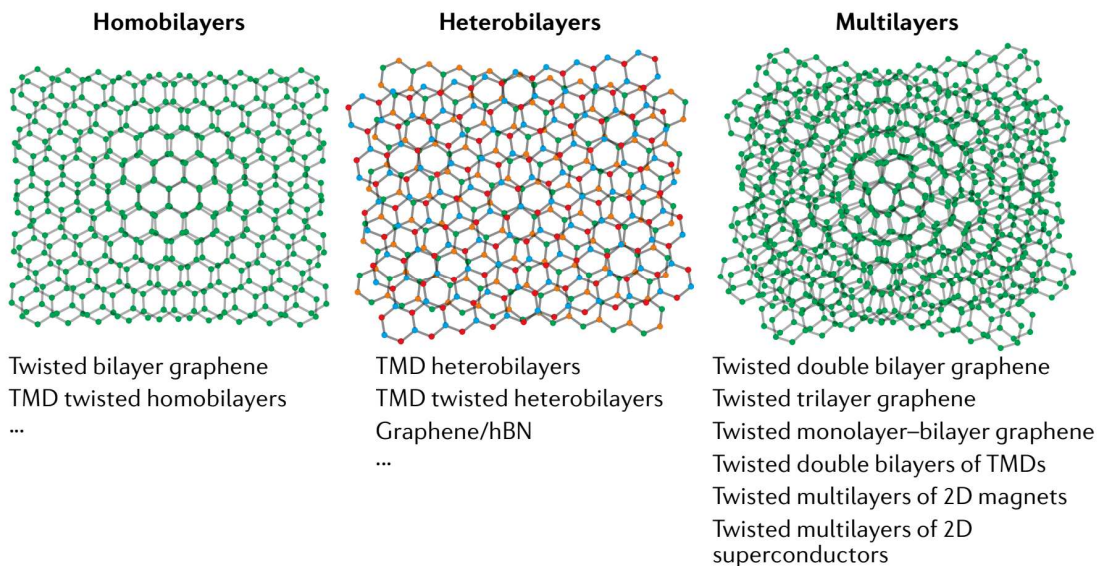


Figure 1.4 Various possibilities of moiré patterns in twisted homobilayers, heterobilayers and multilayers. The constituent 2D materials include graphene, transition metal chalcogenides, hexagonal boron nitride, 2D magnets and superconductors. Numerous fascinating phenomena have been observed in these moiré structures. Extracted from Ref. [40].

1.2 Crystal symmetry and energy band structure

The transition metal dichalcogenides are a family of about 60 materials and most of them are layered structures as a consequence of the weak interlayer van der Waals interactions [9]. In this thesis, we will focus on layered structure of the form M-X-M,

where M represents a transition metal atom (Mo, W) and X represents a chalcogen atom (S, Se or Te). In each single monolayer, the plane of transition metal atoms is sandwiched between the two adjacent planes of chalcogen atoms, as shown in **Figure 1.2(a)**. TMD can be categorized into different polytypes (1T, 2H, 3R) by considering stacking orders and transition metal atom coordination, as shown in **Figure 1.2(b)**. We mainly focus on 2H phase in this thesis because it is the most likely found form in grown bulk materials.

The band structures of TMD have been calculated by various theoretical tools [41–45]. **Figure 1.5(a)** show the calculated band structures of MoS₂, from bulk to monolayer. It is noted that the indirect bandgap between Γ point and the midpoint along $\Gamma - K$ in bulk form gradually shifts to direct bandgap at K point in monolayer form. The direct transitions energy at K point do not change much when thinning down to a monolayer while the bands at Γ point change significantly. As a consequence, TMD become direct bandgap semiconductor when thinning down to a single monolayer. This can be understood by the band hybridization. **Figure 1.5(b)** and **(c)** shows the calculated contributions of individual atomic orbitals for the band structures of different TMD monolayers. The conduction band (CB) and the valence band (VB) states at K point are mainly composed of d orbitals on the transition metal atoms, sandwiched by chalcogen atoms (X-M-X) and thus relatively less affected by the interlayer coupling effect. In contrast, the states near Γ point have non-negligible contributions from p orbitals of the chalcogen atoms, which have a strong interlayer coupling effect [46]. Therefore, the VB states near Γ point are more sensitive to the layer number than the states near K point. As the layer number reduces, the states near Γ point changes significantly, leading to a larger indirect bandgap but the direct states at K point are relatively unchanged.

There are two energy-degenerate but non-equivalent K valleys (K^+ and K^-) at the hexagonal Brillouin zone due to the broken inversion symmetry in TMD monolayers. We will give more details on those two valleys in the following sections.

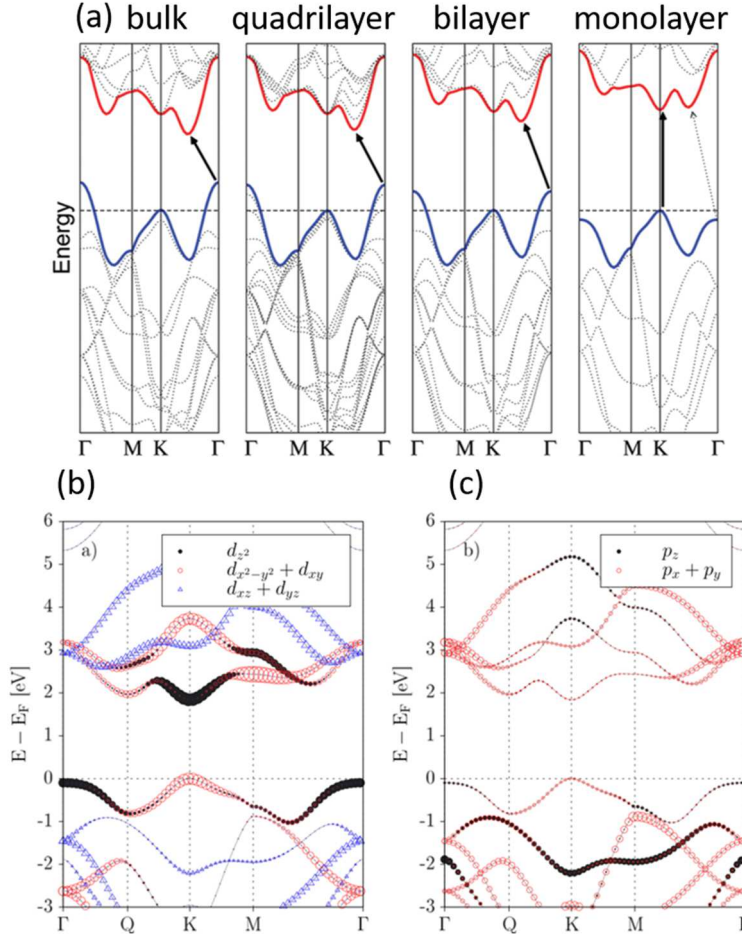


Figure 1.5 Characteristics of TMD band structures. (a) calculated band structures of MoS₂, from bulk to monolayer. The solid red curves (the solid blue curves) represent the conduction band (valence band). The solid black arrows indicate the lowest energy transitions. (b) and (c) hybridization of atomic orbitals in energy band of MX₂ ($M = Mo, W; X = S, Se$ or Te). (b): d orbitals of the metal atom; (c): p orbitals of the chalcogen atoms. The symbol size is proportional to the weight of the atomic orbital. The spin-orbit coupling effect was neglected. (a) extracted from Ref. [46]. (b) and (c) extracted from Ref. [47].

The band structures of TMD have also been investigated experimentally, for instance, using angle-resolved photoemission spectroscopy (ARPES) [48–52] and scanning tunneling spectroscopy (STS) [53].

ARPES is a powerful tool to investigate the dispersion curves between electron energy and momentum. Figure 1.6 shows ARPES data of doped/undoped monolayer and 8 MoSe₂ MLs. For the case of 8 MoSe₂ MLs, ARPES measurements show an indirect bandgap of 1.41 eV between the valence band at Γ point and the conduction band at K point. It is noted that ARPES can only measure the occupied states so that we need n -doped sample to measure the conduction band. For the case of monolayer, a direct bandgap of 1.58 eV is evidenced at K point [54]. This provides a direct visible proof that MoSe₂ shifts from indirect to direct bandgap semiconductor when thinning down to atomically thin layer.

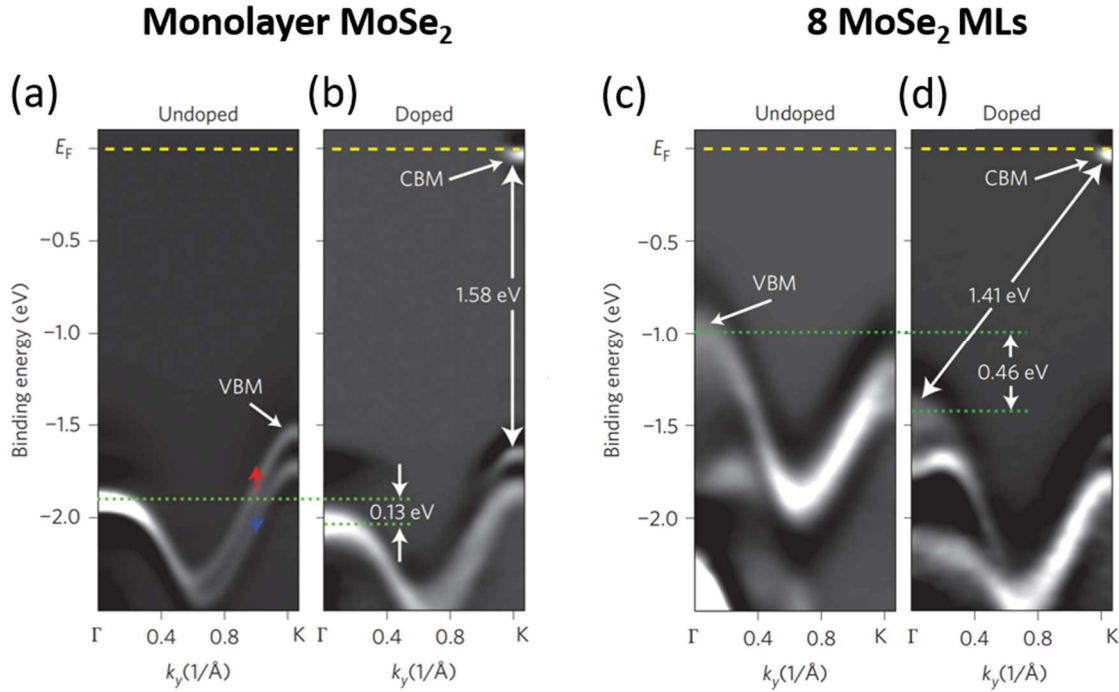
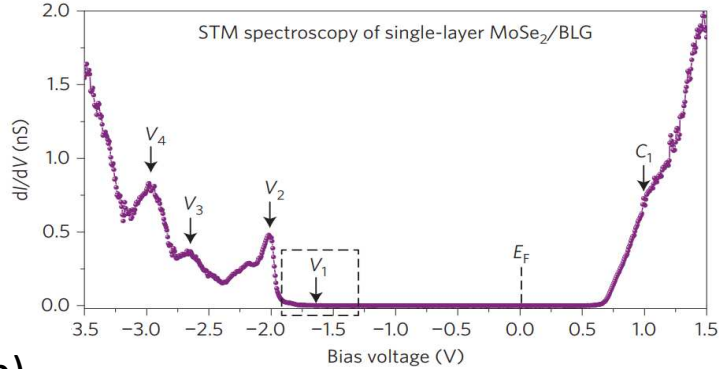


Figure 1.6 Band structures of MoSe₂ measured by ARPES. (a), (c), ARPES measurements of undoped monolayer (a) and 8 MoSe₂ MLs (c) along Γ -K direction. (b), (d), APERS measurements of doped monolayer (b) and 8 MoSe₂ MLs (d) along Γ -K direction. Yellow dashed lines: Fermi level. Green dotted lines: the valence band maximum. Blue and red arrows in (a): opposite spin directions near the K point in monolayer MoSe₂. Extracted from Ref. [48].

Scanning tunneling spectroscopy (STS) is a technique which measures the tunneling current between a metal tip and the material surface (non-contact) by varying the bias voltage applied on those two. It can thus provide the local electron density as function of their energy level. **Figure 1.7(a)** shows a STS dI/dV spectrum of a MoSe₂ monolayer grown by molecular beam epitaxy on epitaxy bilayer graphene (BLG). Four features (V_1 - V_4) are observed in the valence band regime and one feature (C_1) in the conduction band regime. The zero bias voltage represents the Fermi level (E_F) and the relative position of E_F with respect to the band edges reveals *n*-type doping of this sample. To better determine the band edges, **Figure 1.7(b)** plots the logarithm of dI/dV . It shows that the VB maximum (VBM) is located at -1.55 ± 0.03 V and the CB minimum (CBM) at 0.63 ± 0.02 V. The bandgap value for the structure MoSe₂/BLG is thus $E_g = E_{\text{CBM}} - E_{\text{VBM}} = 2.18 \pm 0.04$ eV. We note that the measured bandgap $E_g = 2.18$ eV differs from the optical bandgap $E_{\text{opt}} = 1.63$ eV measured by photoluminescence spectroscopy on a MoSe₂ ML on SiO₂. This difference is mainly due to the binding energy of the exciton, typically here ~ 0.55 eV. Let us note that the band structure of a TMD ML on graphene can be different from a monolayer on SiO₂ [55]. Thus, the modified band structure of MoSe₂ ML on bilayer graphene may also contribute to the difference 0.55 eV mentioned just above.

(a)



(b)

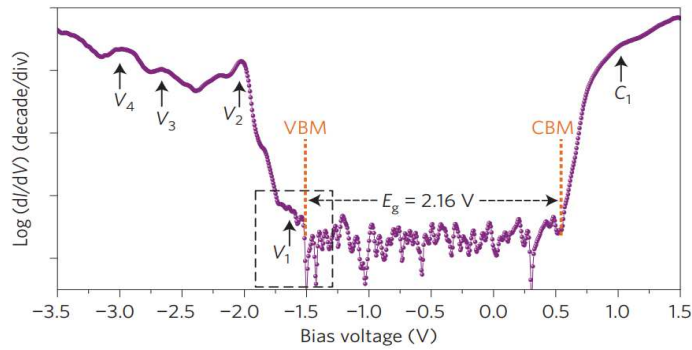


Figure 1.7 Electronic structure of monolayer MoSe₂/BLG. (a) Scanning tunneling spectroscopy dI/dV spectrum of the structure monolayer MoSe₂/BLG, showing the four features (V_1 - V_4) in valence band and one (C_1) in conduction band. The Fermi level corresponds to the zero bias position. (d) Logarithm of (a), clearly showing the band edges (VBM and CBM) and the bandgap E_g . Extracted from Ref. [53].

Besides, the conduction and valence bands in TMD monolayers are split into two subbands with opposite spin (see **Figure 1.8**) due to the spin-orbit coupling effect (SOC) [47]. The spin-orbit splitting Δ_{SOC}^{CB} in CB (Δ_{SOC}^{VB} in VB) is typically of the order of a few tens of meV [56–60] (a few hundreds of meV [12,48,58,61,62]). Thus, the spin degeneracy of both the conduction and valence bands are fully lifted at the K points. It is noted that spin-orbit splitting in the conduction band Δ_{SOC}^{CB} has opposite sign depending on the material; Δ_{SO}^{VB} in W-based monolayer is larger than Mo-based monolayer because the Tungsten atom is heavier [47].

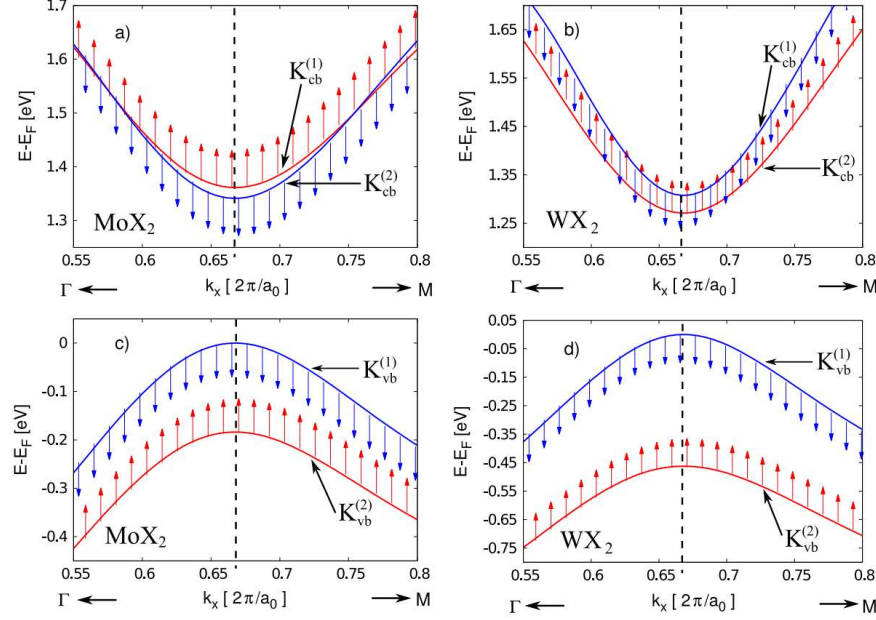


Figure 1.8 DFT calculated band structure with spin-orbit coupling in the vicinity of the K point for Mo- and W-based TMD monolayer. Blue (red) arrows indicated “spin up” (“spin down”). (a) and (c) results for MoX_2 ; (b) and (d) results for WX_2 . The vertical dashed line shows the position of K point. Extracted from Ref. [47]

Hence, we have two categories of excitons named A and B exciton series in TMD monolayers. **Figure 1.9** schematically shows A and B bright excitons in W-based monolayers. The optical transitions involving electrons and holes in the upper conduction and valence band are called A exciton; the counterpart transitions involving electrons and holes in the lower conduction and valence band are called B exciton. The transition energy difference between A and B exciton can reach several hundreds of meV [14,16] mainly due to the large SOC in valence bands.

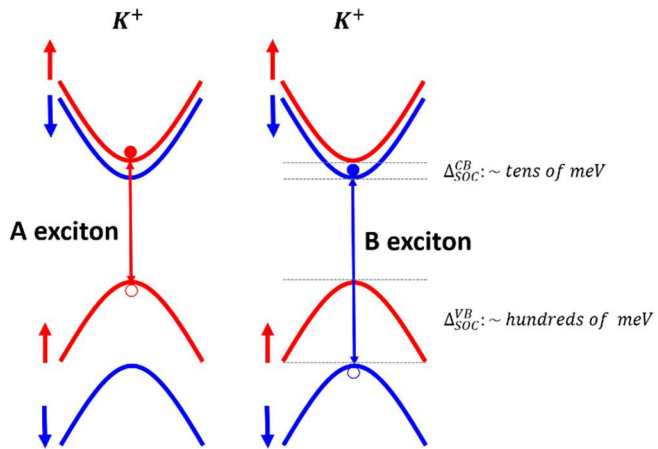


Figure 1.9 Schematic of A and B bright exciton transitions in monolayer WX_2 ($X=\text{S}, \text{Se}, \text{Te}$). The energy splitting due to SOC in conduction and valence subbands are denoted by Δ_{SOC}^{CB} and Δ_{SOC}^{VB} , respectively.

1.3 Exciton states

Before discussing exciton states in 2D environment, let us first review the concept of excitons in general. In semiconductors, an external photon excitation with suitable energy can promote an electron to the conduction band, leaving behind a hole in the valence band. The electron and the hole are hold together by the attractive Coulomb interaction. This neutral electron-hole pair is called exciton. There are two basic types of exciton: Wannier-Mott excitons and Frenkel excitons. **Figure 1.10** schematically illustrates these two types of excitons. The former ones have a radius much larger than the unit cell; they are usually delocalized states moving freely in the whole crystal. This is why they are also called “free exciton”. In contrast, the latter ones have a much smaller radius comparable to the size of the unit cell, which are thus localized states and tightly bound to certain atoms.

We will see later that the exciton Bohr radius in TMD monolayers is on the order of a few nanometers and the correlation between an electron and a hole extends over several lattice periods [63]. Thus, the excitons in TMD MLs are Wannier-Mott excitons. The Wannier description combined with effective mass approximation can explain the majority of the experimental observations.

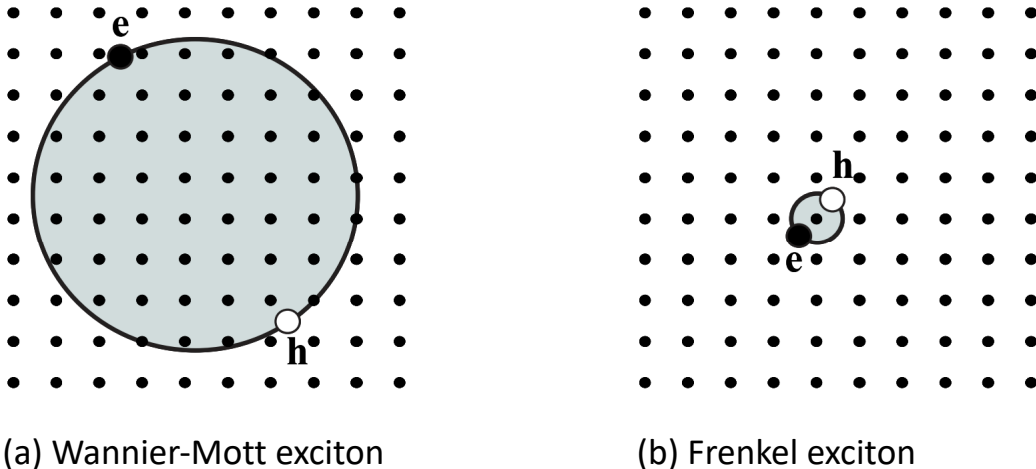


Figure 1.10 Schematic diagram of the two types of excitons. (a) A Wannier-Mott exciton and (b) A Frenkel exciton. Extracted from Ref. [64].

Let us recall that the exciton wave function ψ_{ex} in momentum space can be expressed as [65,66]:

$$\psi_{ex} = \sum_{e,h} C^X(k_e, k_h) |e;h\rangle$$

where $C^X(k_e, k_h)$ is the expansion coefficient of (k_e, k_h) electron-hole pairs; $|e\rangle$ and $|h\rangle$ are electron and hole Bloch wave functions. This expression shows that the exciton state in momentum space is a superposition of electron and hole states ($|e\rangle$ and $|h\rangle$) around the respective extrema of the bands. The relative contributions of these states are described by the coefficient $C^X(k_e, k_h)$. Small exciton radius in real space means

that the exciton state can extend significantly in momentum space. Hence, the states far away from the K point also have contributions for the exciton wave function in TMD monolayers [13,67]. **Figure 1.11** schematically presents the exciton state in momentum space. The widths of the shaded areas represent the contributions of the electron and hole states in the two bands (CB and VB).

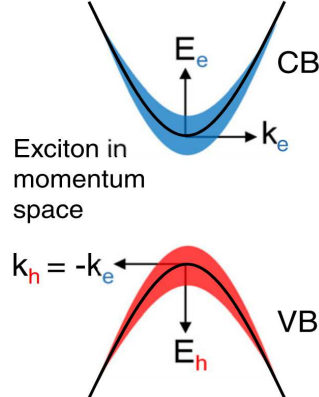


Figure 1.11 Sketch of exciton state in momentum space. The contributions of the electron and hole states in the conduction and valence bands are schematically shown by the widths of the shaded areas. Extracted from Ref. [63].

As we will explain in the following, the binding energy of excitons in TMD monolayers are 1 to 2 orders of magnitude larger than in conventional semiconductors such as Si or Ge [68,69] and quasi-2D systems such as GaAs or GaN quantum wells [70]. This unique property yields that the optical phenomena from cryogenic to room temperature are dominated by strong exciton resonances. **Figure 1.12** schematically illustrates the optical absorption of an ideal 2D semiconductor including both the energy series (denoted by n) of the bright exciton (see section 1.4) below the bandgap and the free particles absorption. The enhancement of the continuum absorption due to the Coulomb interaction is presented with the red solid line and no Coulomb enhancement presented with the red dashed line. The left inset shows the Rydberg-energy levels of the exciton states, denoted by their principal quantum number.

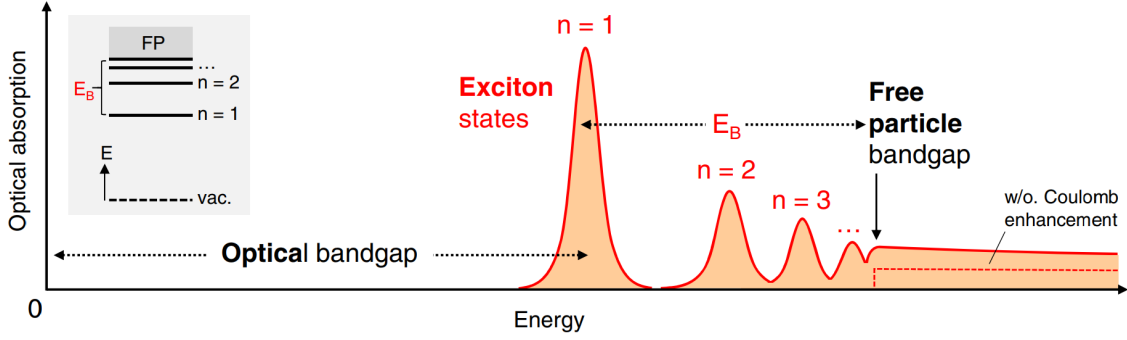


Figure 1.12 Schematic illustration of the optical absorption of an ideal 2D semiconductor. The exciton states ($n = 1, 2, 3 \dots$) are the ground state ($n = 1$) and the excited states ($n \geq 2$) of the bright exciton transitions. The absorption with (without) the Coulomb enhancement is represented by the red solid (dashed) line. The left inset shows the hydrogen atom like energy levels of the exciton states, denoted by their principal quantum number n . Extracted from Ref. [63]. E_B denotes the binding energy, i.e. the energy difference between the free particle bandgap and the optical transition energy.

3D exciton:

To better understand the exciton states in 2D regime, let us consider first an exciton in a 3-dimension homogeneous environment with relative dielectric constant ε_r . By analogy to hydrogen atom and using the effective mass approximations, the corresponding Schrödinger equation of the exciton can be written [71,72]:

$$\left[-\frac{\hbar^2}{2m_e^*} \nabla_e^2 - \frac{\hbar^2}{2m_h^*} \nabla_h^2 - \frac{e^2}{4\pi\varepsilon_0\varepsilon_r |r_e - r_h|} \right] \psi_{ex} = E \psi_{ex} \quad (1.1)$$

where m_e^* and m_h^* are the effective mass of the electron and the hole, respectively; ε_0 is the dielectric constant of the vacuum; ψ_{ex} is the wave function of the exciton; r_e and r_h are the position vector of the electron and the hole, respectively; E is the energy of the exciton. By introducing center of mass and relative variables:

$$R = \frac{m_e^* r_e + m_h^* r_h}{m_e^* + m_h^*} \quad r = r_e - r_h$$

$$K = k_e - k_h \quad k = \frac{m_e^* k_e + m_h^* k_h}{m_e^* + m_h^*}$$

where k_e and k_h are the wave vector of the electron and hole. The Hamiltonian then becomes:

$$\hat{H} = \frac{\hbar^2 K^2}{2(m_e^* + m_h^*)} + \left\{ \frac{\hbar^2 k^2}{2m_r^*} - \frac{e^2}{4\pi\varepsilon_0\varepsilon_r |r|} \right\}$$

where m_r^* is the reduced mass defined by $\frac{1}{m_r^*} = \frac{1}{m_e^*} + \frac{1}{m_h^*}$. The first term $\frac{\hbar^2 K^2}{2(m_e^* + m_h^*)}$ describes the motion of the center of the mass and the second term $\left\{ \frac{\hbar^2 k^2}{2m_r^*} - \frac{e^2}{4\pi\varepsilon_0\varepsilon_r |r|} \right\}$ represents the relative motion between the electron and the hole. By resolving Eq 1.1,

the excitonic energy of the n th level relative to the ionization limit is given by [72]:

$$E(n) = -\frac{m_r^* e^4}{2(4\pi\epsilon_0\epsilon_r)^2 \hbar^2} \frac{1}{n^2} = -\frac{R_{ex}}{n^2}$$

where R_{ex} is the Rydberg energy of the exciton:

$$R_{ex} = \frac{m_r^* e^4}{2(4\pi\epsilon_0\epsilon_r)^2 \hbar^2}$$

It is noted that $E(n)$ corresponds to the binding energy (E_B^{3D}) due to the Coulomb interaction. The total energy of exciton should be equal to the difference between the energy required to create electron-hole pair, namely, E_g (the bandgap energy) and the energy to hold the electron and hole together, *i.e.* the binding energy E_B^{3D} [64]:

$$E_n^{ex} = E_g - \frac{R_{ex}}{n^2}$$

If we take into account the kinetic energy of the center of the mass, the exciton states are then expressed as [72]:

$$E_{nK_{ex}}^{ex} = E_g - \frac{R_{ex}}{n^2} + \frac{\hbar^2 K_{ex}^2}{2(m_e^* + m_h^*)}$$

where $K_{ex} = k_e + k_h$, *i.e.* the momentum of the exciton. Thus, the exciton states can be named with the principal quantum number ($n = 1, 2, 3 \dots$) and the orbital labels ($s, p, d \dots$). **Figure 1.13** schematically presents the exciton energy series based on this hydrogen atom picture.

By analogy to hydrogen Bohr radius (a_B^H), we can also define the exciton Bohr radius (a_B^{ex}) which is correlated to the radius of the orbit for the ground state ($n = 1$) [72]:

$$a_B^{ex} = a_B^H \epsilon_r \frac{m_e}{m_r^*}$$

where m_e is the electron mass. Indeed, the exciton Bohr radius changes with the principal quantum number n . In a first approximation, the radius of the electron-hole orbit is given by [72]:

$$a_B^{ex}(n) \propto n a_B^{ex}$$

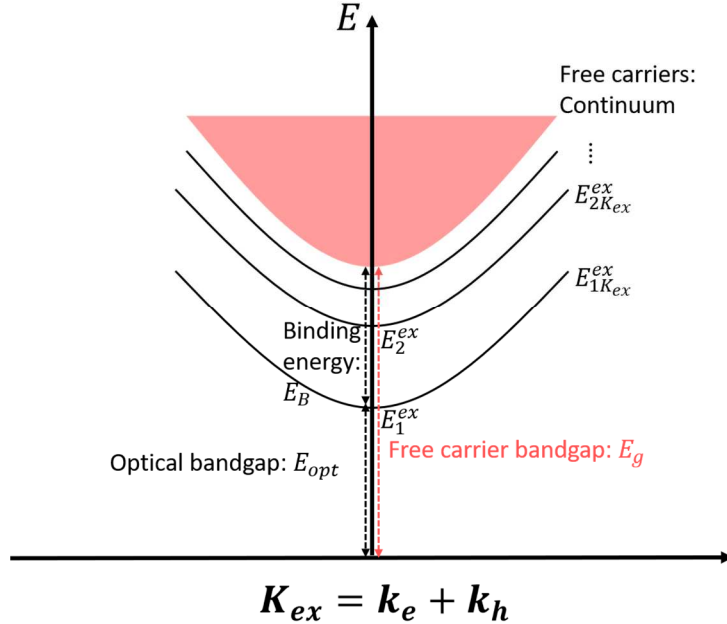


Figure 1.13 Sketch of exciton energy series. The discrete energy bands ($E_{1K_{ex}}^{ex}, E_{2K_{ex}}^{ex} \dots$) represent the exciton states and the continuum stands for free carrier states, i.e. unbounded electron and hole states. We highlight the free carrier bandgap E_g , the optical bandgap E_{opt} and the binding energy E_B .

2D excitons:

In the following, we will discuss the exciton states in two-dimension. As already explained, excitons in TMD monolayers are still considered to remain in the Wannier-Mott regime because the interaction within the electron-hole pair can extend over several lattice periods and they can freely move throughout the monolayer layer [63]. In an ideal 2D system, we have to include the quantum confinement and the momentum is restricted in 2D plane ($K_{ex} = K_x + K_y$). As a consequence, the exciton energy levels are given by [72]:

$$E_{nK_{ex}}^{2D} = E_g + E_Q - \frac{R_{ex}}{(n - \frac{1}{2})^2} + \frac{\hbar^2 K_{ex}^2}{2(m_e^* + m_h^*)}$$

where E_Q is the quantization energy of electron and hole confined in a 2D system. The binding energies of 2D excitons are [72]:

$$E_{Bn}^{2D} = \frac{R_{ex}}{(n - \frac{1}{2})^2}$$

Similarly, we can derive the Bohr radius of an excitonic state with principal quantum number [72]:

$$a_B^{ex}(n) \propto a_B^{ex} \left(n - \frac{1}{2} \right)$$

By comparing $E_{Bn}^{3D} = \frac{R_{ex}}{n^2}$ and $E_{Bn}^{2D} = \frac{R_{ex}}{(n-\frac{1}{2})^2}$, we see clearly that the exciton binding energies experience significant increase from 3D to 2D for a given excitonic state. In fact, the binding energy depends on several factors, as shown in **Figure 1.14**: (1) 2D confinement. When the dimensionality of exciton goes from 3D to 2D, the electron and the hole are confined in the 2D plane. As a result, they are much closer to each other, leading to stronger Coulomb interaction. (2) Reduced dielectric screening. The Coulomb interaction is inversely proportional to the dielectric constant of the electron-hole surroundings. The local environment (vacuum, SiO_2 , hBN etc) has a smaller dielectric constant compared to TMD bulk material. The exciton in TMD MLs experiences reduced dielectric screening of the Coulomb interaction compared with the exciton in 3D TMD bulk. (3) Larger effective mass. This factor is link to TMD itself instead of the reduced dimensionality. The exciton in TMD MLs has a larger reduced mass $m_r^* \approx 0.25 m_e$ compared with conventional semiconductors, for example, GaAs $m_r^* \approx 0.06 m_e$. Then binding energy increases with effective mass, as shown in the relation $E_{Bn}^{2D} = \frac{R_{ex}}{(n-\frac{1}{2})^2}$, where $R_{ex} \propto m_r^*$.

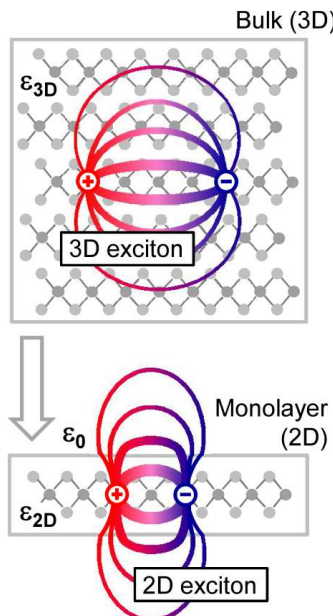


Figure 1.14 Schematic illustration of excitons for three-dimensional bulk and two-dimensional monolayer. The 2D confinement leads to closer distance between electron and hole. The changes in dielectric environment are indicated by different dielectric constants ϵ_{3D} , ϵ_{2D} and the vacuum one ϵ_0 . Extracted from Ref. [14].

2D exciton in an anisotropic environment:

As a matter of fact, the exciton binding energy in TMD monolayers does not follow the simple law $E_{Bn}^{2D} = \frac{R_{ex}}{(n-\frac{1}{2})^2}$ deduced from an ideal 2D system. The Coulomb interaction deviates strongly from the conventional law ($\frac{1}{r}$) due to the geometry of the system and the dielectric surroundings (vacuum, air, SiO_2 , hBN etc). The electric field between the

electron and hole is present both in the monolayer and the surroundings outside the monolayer, as shown schematically in **Figure 1.14**. As a result, the effective Coulomb interaction between the electron and hole is significantly modified by the dielectric properties of the environment. To describe this effect, we can use the Rytova-Keldysh potential [73,74] to model the effective Coulomb interaction between electron and hole in 2D exciton [14,75–77] :

$$V(r) = -\frac{e^2}{8\varepsilon_0 r_0} \left[H_0\left(\frac{\varepsilon_{ext} r}{r_0}\right) - N_0\left(\frac{\varepsilon_{ext} r}{r_0}\right) \right]$$

where r is the in-plane electron-hole separation; $r_0 = 2\pi\chi_{2D}$ is the screening radius; χ_{2D} is the 2D polarizability. H_0 and N_0 are the Struve and Neumann functions, respectively. ε_{ext} is the effective dielectric constant of the environment. The effective dielectric constant for a TMD ML can be estimated as an average value on the top and bottom sides of the 2D-plane, *i.e.* $\varepsilon_{ext} = \frac{1}{2}(\varepsilon_{top} + \varepsilon_{bottom})$. Ref. [78] gives an example to calculate the exciton states in TMD monolayers based on this Rytova-Keldysh potential.

1.4 Bright and dark excitons

In this section, we are going to discuss the main characteristics of the neutral exciton fine structure in TMD monolayers. We will recall the properties of the spin-allowed and spin-forbidden excitons (usually called bright and dark excitons). In Chapter 3 we will show that we can control the energy splitting between these excitons in a cavity-like structure.

Bright excitons are momentum and spin-allowed optically active excitonic species, as shown in **Figure 1.15**. In contrast, there are also optically dark excitons which are either spin-forbidden and/or momentum-forbidden transitions, as shown in **Figure 1.15**. If the correlated electron and hole are with opposite spin but in the same valley, *i.e.*, spin-forbidden but momentum-allowed, it is named dark intravalley exciton X_D (these are the dark excitons which will be discussed in this thesis). Alternatively, if the correlated electron and hole are with same spin but in different valleys, *i.e.*, spin-allowed but momentum forbidden, it is then called dark intervalley exciton, for example, indirect exciton (X_I), as shown in **Figure 1.15**. The bright excitons have larger oscillator strength than the dark excitons, leading to shorter radiative lifetime (several ps for bright neutral exciton X_0 [79–83]) than the dark ones (hundreds of ps for dark intravalley exciton X_D , see Chapter 3).

For simplicity, we name spin-forbidden intravalley exciton X_D as dark exciton in the following and we will specify the name of the other optically dark excitons if necessary. The bright excitons have in-monolayer-plane dipole moment [84,85], while the spin-forbidden dark excitons have out-of-monolayer-plane dipole moment (z mode) [86–88]. As a result, it is more efficient to detect this spin-forbidden dark excitons by in-plane detection, as shown in **Figure 1.16(d)**. This requires a tough alignment of the sample edge with respect to the microscope objective. However, we can also observe X_D in WSe₂ ML in our PL measurements by using a standard excitation and detection

perpendicular to the monolayer plane. The key reason is that we use an objective with large numerical aperture ($NA = 0.82$) [86]. Thus the electric field at the focal edge has a non-negligible out-of-plane component which enables detection of the spin-forbidden dark transitions at the normal incidence [86]. This technique gives a splitting between X_0 and X_D : $\Delta E \sim 40$ meV in WSe₂ ML (see **Figure 1.16(c)**) [86].

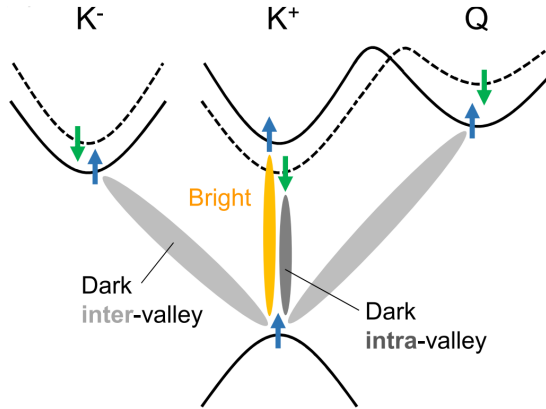


Figure 1.15 Schematic of optically allowed and forbidden transitions for bright and dark exciton states. The band structure is simplified for clarity. The order of the spin states in the conduction band corresponds to W-based monolayers. Extracted from Ref. [63].

To easily observe the spin-forbidden dark excitons, we can also apply an in-plane magnetic field [88–91] as shown in **Figure 1.16(b)** which leads to an admixture of bright and dark states. The oscillator strength of the “dark” transitions increases when the magnetic field increases, as shown in **Figure 1.16(a)**. Then we can easily measure the energy difference between X_0 and X_D ($\Delta E = E_{X_0} - E_{X_D}$) ($\Delta E \sim -1.4$ meV in MoSe₂ ML and ~ 14 meV in MoS₂ ML [88]). As we will discuss in more detail in Chapter 3, the bright-dark exciton splitting includes three well established contributions [88,92] $\Delta = \Delta_{\text{exch}} + \Delta_{\text{SO}} + \Delta_{\text{bind}}$, where Δ_{exch} is the short range exciton exchange energy, Δ_{SO} is the conduction band spin-orbit splitting, Δ_{bind} is the difference between the binding energies of bright and dark excitons due to the slightly different masses of spin \uparrow and spin \downarrow conduction bands. In Chapter 3 we will evidence a new additional contribution due to the coupling to the electromagnetic field (Lamb shift).

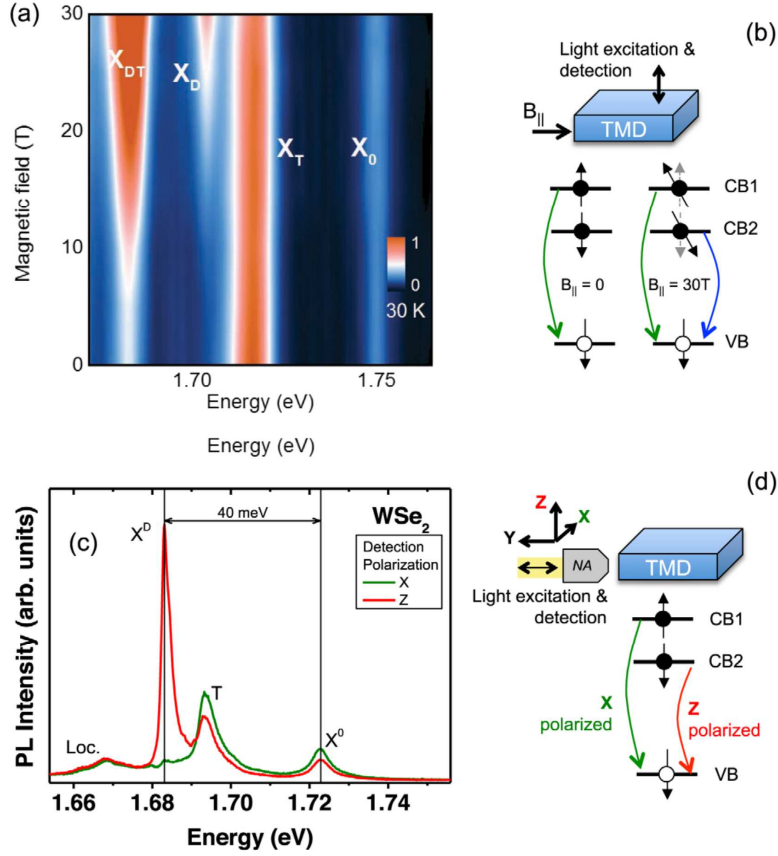


Figure 1.16 (a) Magneto PL of monolayer WSe_2 through application of an in-plane magnetic field, in which the dark exciton starts to appear at $\sim 5\text{ T}$ and gain intensity as the magnetic field increases. (b) Schematic of the brightening of the dark exciton transitions involving the spin states in the upper (CB1) and lower conduction band (CB2). (c) PL spectra of hBN-encapsulated monolayer WSe_2 , detected from out of the plane of the monolayer (Designated by the solid green line) and from the in plane of the monolayer (Designated by the solid red line). (d) Schematic of the excitation and detection from the edge of the sample to distinguish the optical mode of X_0 and X_D . Extracted from Ref. [63].

It turns out that dark excitons have fine structure in TMD monolayers. One is perfectly dark (“dark exciton”: spin-forbidden and electric dipole forbidden), at the lower energy state; the other one is partially optically active (“grey exciton”: spin-forbidden but electric dipole allowed, *i.e.* z-mode, out of ML plane), at the higher energy state. We can perform magneto-photoluminescence measurements with a magnetic field B_z applied perpendicular to the monolayer plane to measure the energy splitting δ of the two dark states, *i.e.* the “dark exciton” can gain oscillator strength from the grey one; it gives $\delta \lesssim 1\text{ meV}$ in TMD MLs. [88,89,93]. In this thesis, we only focus on the “grey exciton” and call it as “dark exciton” for simplicity.

So far, we have introduced bright and dark exciton (X_0 and X_D) and they are both neutral excitons without excess charge. As we will see in this thesis, there are also excitonic complexes with excess positive or negative charge, for instance negative trion (*i.e.* a combination of two electrons and one hole (three-particle picture), whose properties will be detailed in section 4.3). If we take many-body picture, we can treat

negative trion as Fermi-polaron, *i.e.* the interaction between an exciton and a Fermi sea of electrons. In this thesis (Chapter 4, Chapter 5 and Chapter 6), we restrict our study to moderate carrier (electron or hole) densities of a few 10^{11} cm^{-2} in TMD monolayers so that the simple three-particle picture (*i.e.* trion) is still valid [94–96].

1.5 Optical selection rules and spin-valley polarization

In this section, we will present the optical selection rules and the concept of spin-valley polarization in TMD monolayers. They are very essential to understand the main work of this thesis.

As already discussed, spin-orbit interaction in TMD monolayers is quite strong, leading to spin splitting Δ_{SOC}^{VB} in valence band and Δ_{SOC}^{CB} in conduction band at the K point (see **Figure 1.17**). Besides, TMD monolayers are characterized by the lower symmetry D_{3h} point group [63] in contrast to the bulk 2H phase TMD which belong to D_{6h} point symmetry group [9,97]. Due to this broken inversion symmetry in TMD monolayers, two nonequivalent valleys: K^+ and K^- emerge at the corners of the hexagonal Brillouin zone, as shown in **Figure 1.17(a)**. The difference between the two valleys is that the spin is opposite at the corresponding bands, as shown in **Figure 1.17****Figure 1.7(c)-(e)**. This unique band structure leads to the chiral optical selection rules for the interband transitions at K^\pm valley in TMD monolayers: K^+ (K^-) valleys are only coupled with σ^+ (σ^-) circularly polarized light [66,98,99]. This leads to optical generation and detection of the spin-valley polarization, *i.e.* spin and valley degrees of freedom. Note that, strictly speaking, this valley index is only relevant for carriers (electrons or holes). For excitons, we need to consider the exciton wavevector K_{ex} . Both excitons associated with σ^+ and σ^- light (composed of an electron in the K^+ or K^- valleys) have an exciton wavevector equal to 0. Thus, the two bright excitons are located at the Γ point (not K) in the exciton band structure (see **Figure 1.18**).

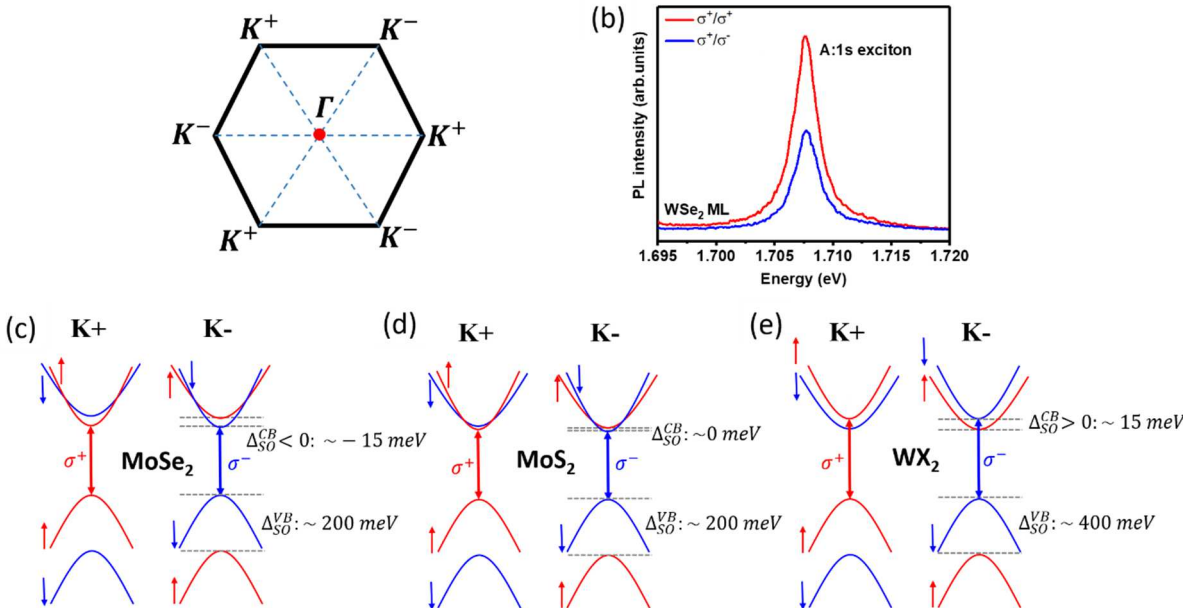


Figure 1.17 Schematic illustration of chiral optical selection rules in monolayer TMDs. (a) Sketch of the hexagonal 1st Brillouin Zone of the 2H phase. (b) Circular-polarization resolved PL measurements in hBN-encapsulated monolayer WSe₂ following σ⁺ circularly-polarized excitation laser (σ⁺ and σ⁻ detection). (c)-(d) Schematic illustrations of the chiral optical selection rules in Mo- and W-based TMD monolayers. The order of the conduction band is opposite between Mo- and W-based TMD monolayer. Note, here we include the effective mass effect in the conduction bands to emphasize the conduction band difference in TMD monolayers. In the following, we will simplify the band structure without considering the effective mass effect except the case we specify.

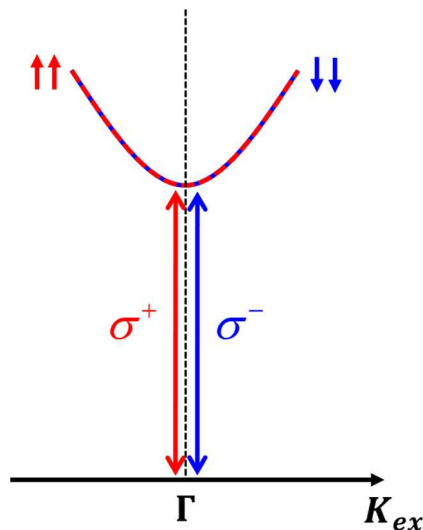


Figure 1.18 Schematic of the excitonic band structure in a TMD monolayer. The red and blue arrows represent the CB and VB with "spin up" and "spin down".

Following this chiral optical selection rules, we can selectively excite excitons composed of carriers in K^+ or K^- valley by carefully choosing the laser energy and

helicity (σ^+ or σ^-). These techniques are so called optical orientation techniques. Let us recall briefly the principle of these techniques which allow the investigation of the spin properties of carriers or excitons in semiconductors. We have used these powerful techniques in Chapter 4 and Chapter 5.

In a typical optical orientation experiment, the sample is excited by a circularly-polarized laser σ^+ and we collect the circularly-polarized luminescence components I_{σ^+} and I_{σ^-} . The circular polarization degree P_c of photoluminescence is defined as:

$$P_c = \frac{I_{\sigma^+} - I_{\sigma^-}}{I_{\sigma^+} + I_{\sigma^-}} \quad (1.2)$$

The circular polarization degree P_c in stationary measurements (see for instance **Figure 1.7(b)**) depends on the lifetime τ , the spin relaxation time τ_s and the initial polarization degree (P_0) generated by the laser. In a simple model, we can write [100]:

$$P_c = \frac{P_0}{1 + \frac{\tau}{\tau_s}} \quad (1.3)$$

It turns out that exploiting the polarization degree of freedom of excitons in TMD ML is challenging since both the radiative lifetime τ and depolarization time τ_s of excitons are quite short. For example, time-resolved photoluminescence and time-resolved Kerr rotation measurements reveal that both the radiative lifetime [80,83,100–102] and the depolarization time [100,103] of bright neutral exciton X_0 are in the ps range at low temperature. **Figure 1.19(a)** shows that the measured radiative lifetime of X_0 in a WSe₂ ML is around 2 ps. **Figure 1.9(b)** displays the Kerr rotation dynamics for right (σ^+) and left (σ^-) circularly-polarized pump (resonant with X_0) in a WSe₂ monolayer. A typical exciton spin relaxation time of 6 ps is measured. This very short depolarization time results from the long-range Coulomb exchange interaction [103].

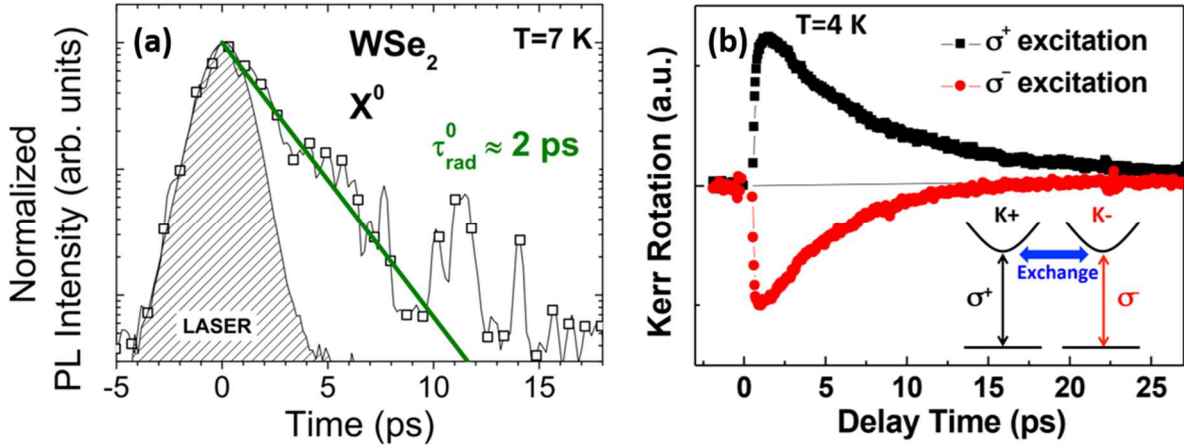


Figure 1.19 (a) Time-resolved photoluminescence measurement of the bright neutral exciton X_0 in WSe_2 monolayer. The monoexponential fit (the green curve) yields radiative lifetime of ~ 2 ps at $T = 7\text{ K}$. Extracted from Ref. [83]. (b) Kerr rotation dynamics for σ^+ and σ^- pump beam at $T = 4\text{ K}$. Inset: schematics of the optical selection rules of the excitons in K^+ and K^- valleys and their coupling by the long-range exchange interaction. Extracted from Ref. [103].

As for excitonic complexes, their radiative lifetime and depolarization time are relatively longer than the ones of bright neutral exciton but they are still limited. For example, **Figure 1.20** show radiative lifetime and depolarization time of the negative trion; we measure ~ 10 ps and 100 ps - 1 ns, respectively [104].

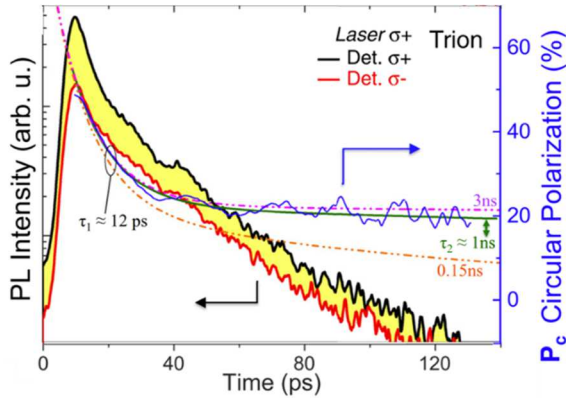


Figure 1.20 Time-resolved photoluminescence of trion in WSe_2 monolayer at $T = 4\text{ K}$. left axis: trion PL emission intensity (in log scale) co-polarized (black solid line) and cross-polarized (red solid line) with respect to the excitation laser as a function of time. Right axis: circular polarization degree of the PL emission. The polarization is fitted by a biexponential decay using an initial decay time $\tau_1 = 12$ ps and a long decay time $\tau_2 = 1$ ns (green solid line). The lower limit (dotted orange line for $\tau_2 = 150$ ps) and the upper limit (dotted purple line for $\tau_2 = 3$ ns) of the slow decay are shown. Extracted from Ref. [104].

The spin-valley relaxation of resident carriers is more promising as it is prevented by spin-valley locking and is not governed by efficient exchange interaction like for neutral excitons. This could be understood as following: for a resident carrier to change valley, as shown in **Figure 1.21**, it has either to flip its spin and change valley

(characteristic times τ_{sv}^e and τ_{sv}^h), or jump to higher energy band (characteristic times τ_v^e and τ_v^h), which is energetically unfavorable. Especially the hole has to overcome several hundreds of meV to do the spin-conserved intervalley scattering. In the same way, an intravalley spin flip (characteristic time τ_s^e and τ_s^h) has to accommodate the spin-orbit splitting energy. As a consequence, we expect very long spin-valley relaxation times for both electrons and holes.

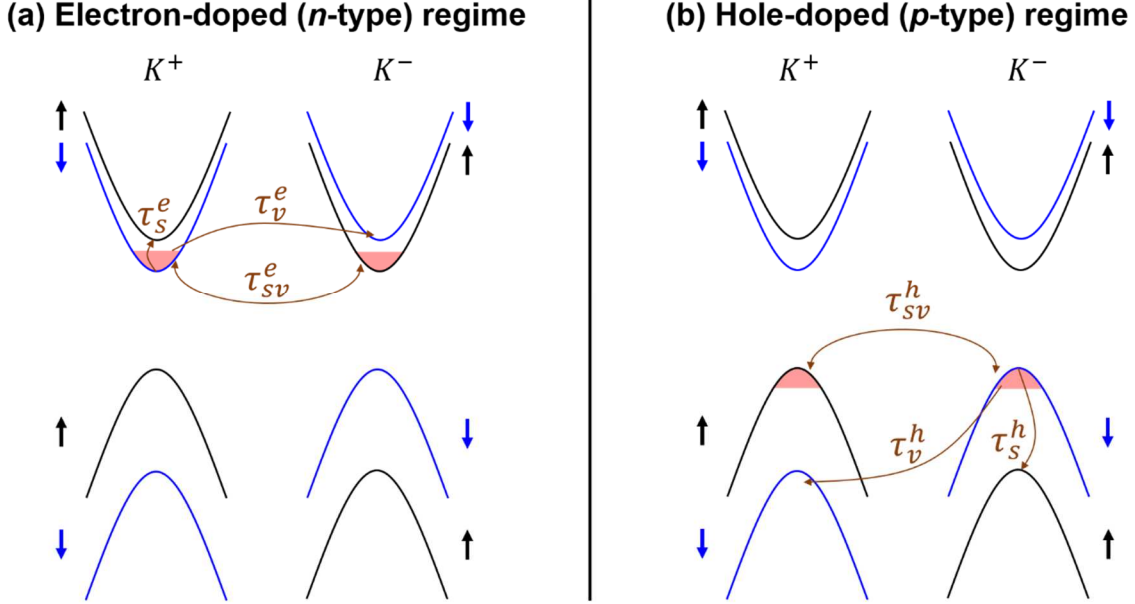


Figure 1.21 Schematics of spin/valley relaxation processes in W-based TMD monolayers in (a) n-doped regime for resident electrons and in (b) p-doped regime for resident holes. τ_v^e and τ_v^h designate electron and hole valley relaxation process, respectively. τ_{sv}^e and τ_{sv}^h designate electron and hole spin-valley relaxation process. The pink shaded parts represent the resident carriers (electrons or holes).

Spin-valley relaxation times as long as 100's ns to several μ s for electrons and holes have been measured in WSe₂ ML using time-resolved Kerr experiments and spin-valley noise spectroscopy [105–108]. **Figure 1.22** presents the Kerr rotation dynamics in a doped WSe₂ monolayer (p- or n-doped), where very long spin-valley relaxation times of both electrons and holes can be observed for moderate doping densities ($\sim 10^{11}$ cm⁻²). We will exploit this spin-valley locking effect to evidence effective spin-valley pumping in Chapter 4 and its consequences on spin transport in Chapter 5.

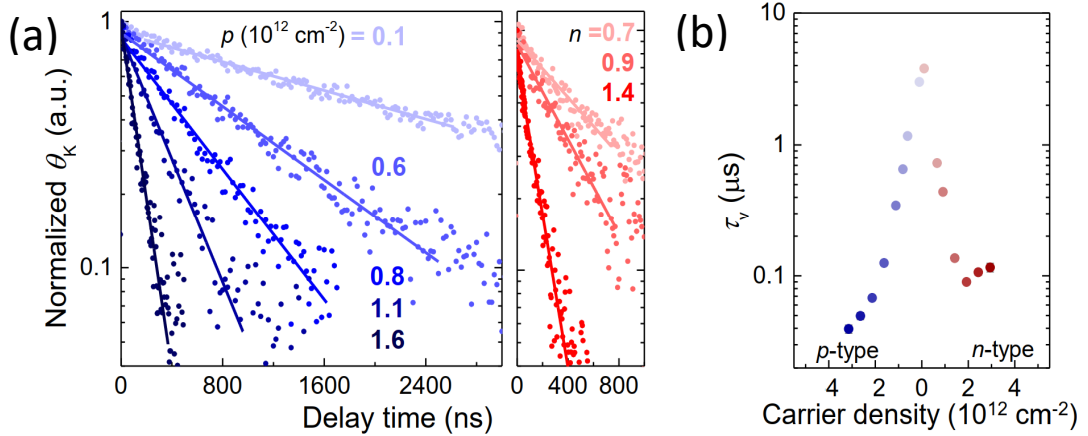


Figure 1.22 (a) Kerr rotation dynamics for WSe₂ ML for different carrier densities. The kinetics directly reflect the optically-induced spin-valley relaxation time of resident carriers. (b) Summary of the spin-valley relaxation time of resident carriers (electrons in the n-type region and holes in the p-type region) as function of carrier density. Extracted from Ref. [105].

1.6 Conclusion

In this Chapter, we have introduced TMD monolayers by highlighting their crystal structures, energy band structures and unique properties: (1) Direct bandgap semiconductors when thinning down to atomically thin layer. (2) Optical properties governed by exciton. (3) Spin-valley polarization. We have also introduced the exciton fine structure with bright and dark excitons.

Chapter 2 Experimental Techniques

In this Chapter, we will first present the vdW heterostructure samples fabrication process and the relevant fabrication setups. We have used an all-dry stamping method because it allows to transfer different layers onto a specific position with micrometer resolution. The side effects of this method and the corresponding solutions are also discussed in detail. Then we will explain how to identify TMD monolayer and how to select hBN layers with different thicknesses. Next we will see how hBN encapsulation plays a key role in the sample quality by protecting TMD monolayers from dielectric disorder. In the end, we will detail our microscopy setups and all the sample characterization techniques used in this thesis, including differential reflectivity, photoluminescence (PL) spectroscopy, magneto-PL and polarization-resolved PL. Lorentzian model and transfer matrix method are also introduced to better understand the reflectivity measurement.

This Chapter is organized with the following sections:

2.1 Sample fabrication

 2.1.1 All-dry stamping deterministic transfer method and fabrication setups

 2.1.2 The drawbacks of all-dry stamping method and

 2.1.3 Identification of TMD monolayers and selection of hBN

2.2 Effects of hBN encapsulation on the optical and exciton properties

2.3 Optical spectroscopy experiments

 2.3.1 Optical spectroscopy setups

 2.3.2 Differential reflectivity measurement

 2.3.2.1 Lorentzian model

 2.3.2.2 Transfer matrix method

 2.3.3 Photoluminescence spectroscopy

 2.3.4 Polarization-resolved photoluminescence

 2.3.5 Magneto-photoluminescence spectroscopy

2.4 Conclusion

2.1 Sample fabrication

2.1.1 All-dry stamping deterministic transfer method and fabrication setups

All our 2D van der Waals heterostructure samples are made by all-dry-viscoelastic stamping method [109]. A sketch of the fabrication setups and the detailed sample fabrication process are shown in **Figure 2.1**. First, TMD thin-layer flakes are mechanically exfoliated from commercial bulk materials (2D semiconductors TM or hq grapheneTM) by using a Nitto tape. Second, those flakes are transferred onto a piece of stamp, *i.e.* polydimethylsiloxane (PDMS, Gelpack®; retention level × 4), which is adhered to a glass slide to easily manipulate flakes. Third, the glass slide is placed under an optical microscope with a long working distance objective (Olympus® objective MPLFLN×10 with a working distance of 11 mm). Thanks to the transparency of the glass and the TMD flake contrast on PDMS, single layer TMD could be spotted by scanning the PDMS stamp and being monitored through an image display. Fourth, once a desired single layer is spotted, the PDMS stamp is placed right above a substrate (usually SiO₂/Si), and then the selected layer can be aligned to a specific position on the substrate, which is fixed on the sample stage (shown in **Figure 2.1**) by a vacuum pump. In the end, the PDMS stamp is lowered down until it is in contact with the substrate surface and then the stamp is slowly peeled off from the substrate. After each transfer process, the sample is annealed on a hot plate (detailed discussion shown in section 2.1.2). With the help of the 6 motorized actuators (Newport®, Models: TRB25CC and LTA-HL with 0.1 μm and 0.05 μm precision, respectively) integrated in both stamping and sample stage, the location of the transferred flakes can reach micrometer precision and the peeling-off rate can be lowered down to 1 μm/s. The temperature of the sample stage can be controlled from room temperature to 200 °C.

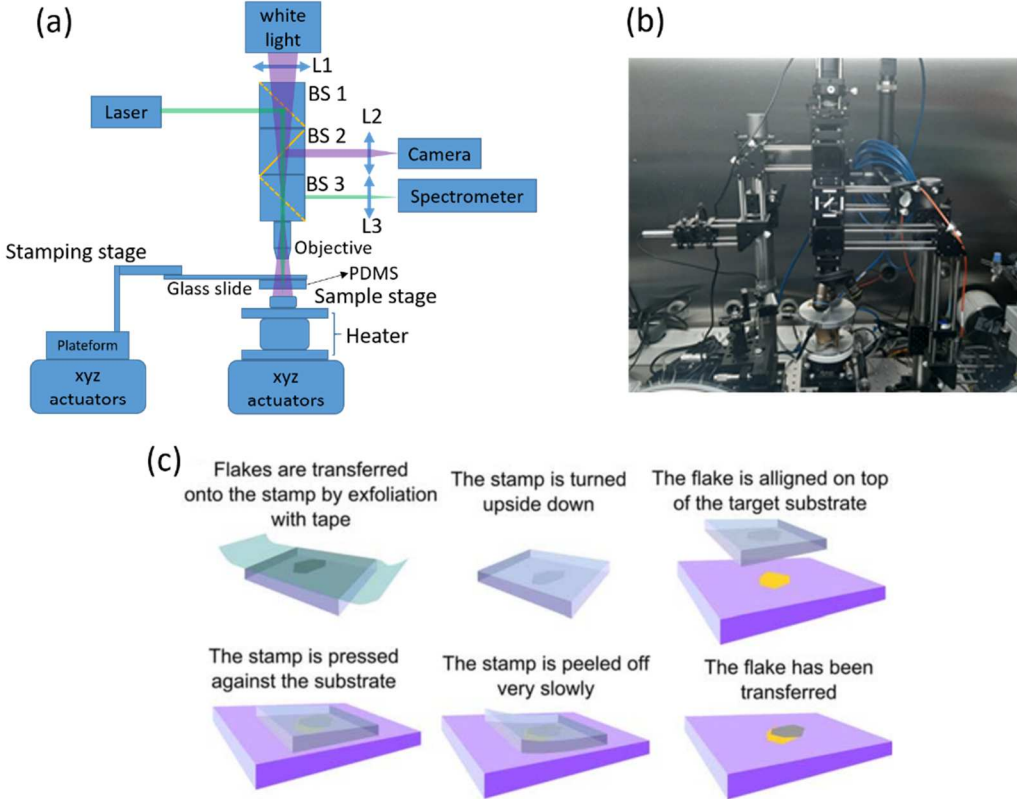


Figure 2.1 Fabrication setups and transfer process. (a) Sketch of the home-built fabrication setups. BS and L denote beam splitter and lens, respectively. The stamping stage controls the PDMS stamp on which lie the exfoliated TMD layers. The sample stage controls the position of the substrate. The image of the whole fabrication process can be monitored on live through the camera. In case of doubt, a 532 nm laser and a spectrometer are at disposition to do PL measurement at room temperature by inserting the two beam splitters: BS 1 and BS 2. (b) Photo of the home-built fabrication setups. The whole setups are installed inside a glovebox with controlled inert atmosphere. (c) Diagram of the steps from the exfoliation of TMD materials to deterministic transfer of a 2D single layer onto a selected location on the substrate, which is extracted from Ref. [109].

It is worth mentioning that the peeling-off rate plays an important role during the transfer process. Only with slow enough peeling-off rate, can the desired layer be transferred onto the substrate. This is because of the kinetically controlled switching between adhesion and release of solid objects to and from an elastomeric stamp [110]. In other word, the PDMS stamp becomes very adhesive when very quickly peeled off from a substrate but becomes less adhesive when the peeling-off rate is decreased.

A simple PL setup is also integrated in the fabrication setups, which can allow us to verify if the selected layer is a single layer of TMD by conducting room temperature PL measurement. Observable PL signal is expected when it is a single layer of TMD. In contrast, no PL signal or very weak intensity is expected for multilayers. This is due to the fact that TMD become direct-gap semiconductors when thinned down to a single layer as recalled in Chapter 1.

In order to create a homogeneous dielectric environment, we encapsulate TMD monolayers in between two hexagonal boron nitride (hBN) layers. This encapsulation can narrow PL linewidth and enable us to resolve more PL features at low temperature; this will be discussed in the section 2.2.

We can control the doping in our TMD monolayer through the charge-tunable device (shown in **Figure 2.2**), which can be seen as a simple capacitor. A TMD monolayer and few layers of graphene (FLG) act as the two opposite plates and a layered hBN bulk with hundreds of nanometer thickness is used as dielectric environment between the two plates. In order to isolate the entire device, the whole capacitor structure is embedded in two other hBN layers. Instead of doing lithography after layer transfer, we precisely transfer the exfoliated layers via dry-stamping method onto a SiO₂/Si substrate on which the Ti/Au electrodes has been patterned through lithography. The few layers of graphene exfoliated from a highly oriented pyrolytic graphite (HOPG) crystal are used for the back gate and to contact single layer of TMD. This method can produce high quality samples with no drift or hysteresis of the doping density with the applied bias. Typical PL linewidth at low temperature can reach ~2.5 meV (~1 meV) for neutral exciton in WSe₂ (MoSe₂) monolayer, reaching the state of the art [111].

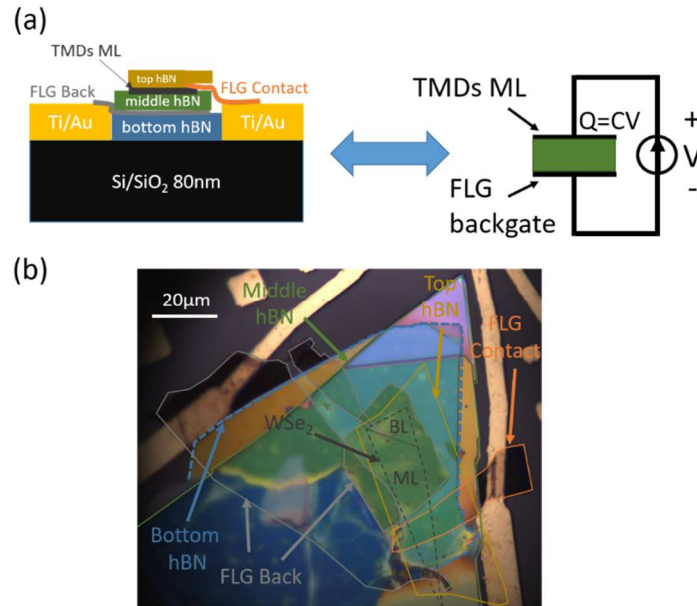


Figure 2.2 TMD monolayer charge-tunable device. (a) Sketch of a TMD monolayer charge-tunable device, equivalent to a capacitor structure, shown on the right. FLG denotes few layers of graphene, which serves as contact wire. (b) An optical microscopy image of a WSe₂ monolayer charge-tunable device.

2.1.2 The drawbacks of all-dry stamping method and the solution

The dry-stamping method with PDMS (Chemical formula: CH₃[Si(CH₃)₂O]_nSi(CH₃)₃) can produce substantial polymer residues, bubbles and wrinkles at the interface of layers [112,113]. **Figure 2.3(c)** shows a large area AFM topography map of a MoS₂ monolayer deposited on hBN extracted from Ref. [112]. Bubbles and wrinkles are

unambiguously observed. The red- and green- outlined region are examined with higher resolution in **Figure 2.3(d)** and **(e)**, in which a dense network of residue islands and a thick residue layer can be clearly identified from the MoS₂ flake. It is also reported that we can find large pressure inside the bubbles, for example, tens of MPa inside submicron bubbles and close to 1GPa inside sub-10 nm bubbles, and up to ~0.22 % compressive strain in a TMD monolayer transferred using PDMS [112,113].

The properties of 2D materials are quite sensitive to the surrounding environment. Surface protection and substrate flatness are key ingredients for obtaining stable, high-quality samples [114]. It is reported that a UV/ozone pre-cleaning of the PDMS surface before exfoliation significantly reduces organic residues on transferred TMD flakes [112]. It can be understood as following: UV/ozone treatment can not only break down the organic species at the stamp surface into CO₂, H₂O and simpler volatile organic products but also oxidize the silicon present at PDMS to form a thin layer (20-30 nm) of silicon oxide (SiO_x) on PDMS [115]. This SiO_x layer acts as a diffusion barrier to prevent the oligomers to pass on the exfoliated flakes. However, this UV/ozone treatment strongly modifies the adhesion properties of the PDMS, making the exfoliation on its surface difficult [116]. A simple alternative solution is to do annealing after the transfer of each layer. It can induce the aggregation of bubbles and residues present at interfaces. As a result, some sample area is cleaned, providing high-quality zone while others are covered by bubbles and residues. In practice, the annealing can provide a clean area without bubbles/residues at least over several μm which matches well the diameter of the laser excitation spot (about 1 μm in our experimental setups, discussed in the section optical spectroscopy setups).

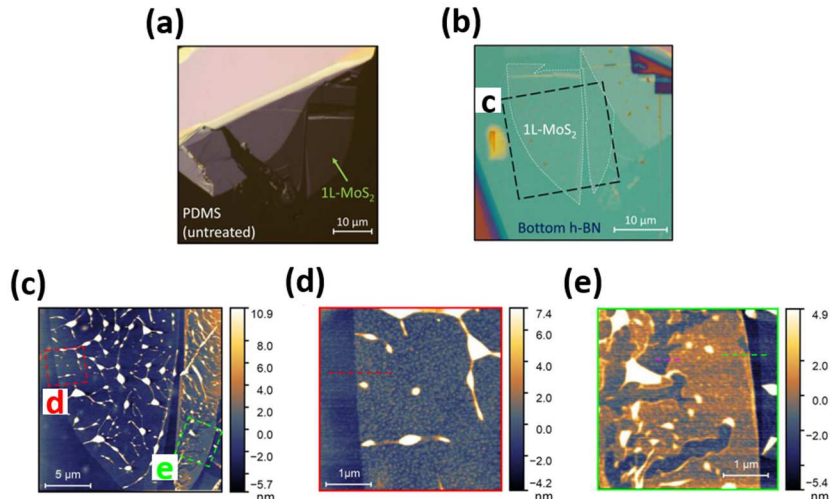


Figure 2.3 Characterization of PDMS residues. (a) Optical microscopy image of a MoS₂ monolayer flake exfoliated on PDMS. (b) Optical microscopy image of the same MoS₂ flake as in (a) deposited on hBN. (c) AFM image of the region outlined in (b). (d) Higher resolution AFM image of the red-outlined region in (c) with a dense network of residue islands. (e) Higher resolution AFM image of the green-outlined region in (c) with a thick layer of residue covering a majority of the area. Extracted from Ref. [112].

2.1.3 Identification of TMD monolayers and selection of hBN

In this thesis, TMD bulk crystals are purchased from 2D semiconductorsTM and hq+grapheneTM, which are either grown by chemical vapor transport (CVT) or flux-grown (FG) method. Hexagonal boron nitride (hBN) crystals are supplied by our collaborators Kenji Watanabe and Takashi Taniguchi of NIMS in Japan, grown by a high-pressure and high-temperature method [117]. Another hBN source is provided by Catherine Journet-Gautier and Bérangère Toury-Pierre from Claude Bernard University of Lyon France, synthetized by a preceramic polymer with a sintering step [118] and giving comparable quality as NIMS hBN [119]. The NIMS hBN is used throughout this thesis.

As mentioned previously, once the TMD bulk crystal is exfoliated on PDMS, we search for TMD monolayer with an optical microscope. **Figure 2.4(a)** shows an optical microscope image of a WSe₂ flake. The red dashed line shows a monolayer which is darkish and transparent. A grey layer (bilayer or trilayer) just lies down the monolayer and the other thicker parts give a huge contrast and are very shining. Even though the monolayer is just atomically thin, it surprisingly exhibits visible contrast on PDMS. This is due to the strong light-matter interaction in TMD monolayer explained in Chapter 1. This prominent optical property was first evidenced in monolayer MoS₂ [120]. **Figure 2.4(b)** shows near 10 % absorbance (black curve) of the neutral exciton in a MoS₂ monolayer and the corresponding photoluminescence signature (red curve) which is also quite significant. The strong oscillator strength of the neutral exciton yields large signals in reflectivity measurement, see for instance **Figure 2.4(c)** for WSe₂ ML.

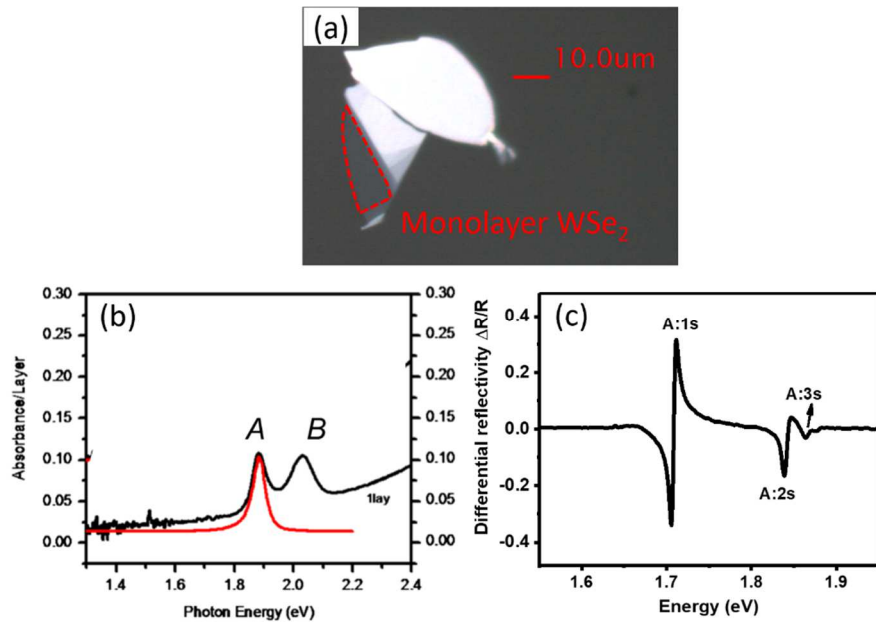


Figure 2.4 (a) Optical microscope image of a WSe₂ flake on PDMS. The PDMS side is face-up to enhance the contrast of the TMD monolayer. The red dashed line shows a monolayer. (b) Absorption spectra (left axis) and PL spectrum of a monolayer MoS₂ deposited on Si substrate. Extracted from Ref. [120]. (c) Differential reflectivity spectrum of a hBN-encapsulated WSe₂ monolayer.

The TMD ML is usually encapsulated by a bottom hBN layer of hundred nanometer and a top hBN layer with a typical thickness of ~ 10 nm. Effects of hBN encapsulation is discussed in the next section. It is important to select hBN with certain thicknesses for some studies. For example, the exciton radiative rate in these vdW heterostructures can be tailored by a simple change of the hBN encapsulation layer thickness as a consequence of the Purcell effect (see Chapter 3 and Ref. [101]) and the hBN encapsulation layer thickness can in principle influence spin-valley polarization time of neutral exciton in monolayer TMD through the tuning of the long-range exchange interaction between the electron and the hole in the exciton [121].

The hBN thickness can be obtained by at least two methods:

- (1) The color of hBN in reflectivity. hBN layers show different colors under white light as a result of interference effect. The color can be simulated by transfer matrix method (detailed in section 2.3.2.2) combined with the CIE XYZ color space [116]. **Figure 2.5(a)** shows a computed color map of hBN on SiO_2 (80 nm)/Si as function of thickness. It is actually a continuous color spectrum so it is still hard to precisely determine the thickness.
- (2) Atomic force microscope (AFM). It is used to measure the thickness of hBN with sub-nanometer resolution. **Figure 2.5(a)** gives an example of a hBN-encapsulated MoSe_2 monolayer sample in which the bottom hBN consists of 6 terraces with different thickness, labeled “A-F”. This kind of sample will be used in Chapter 3. **Figure 2.5(c)** shows the corresponding AFM image of **Figure 2.5(a)** and **(d)** displays the AFM cross-section of the linecut labeled in **Figure 2.5(a)**. The terrace thicknesses are A: 206 nm, B: 237 nm, C: 247 nm, D: 262 nm, E: 274nm and F: 358 nm. In this thesis, all the AFM measurements are conducted with the nano-Observer AFM (CSI instrument) in ambient environment.

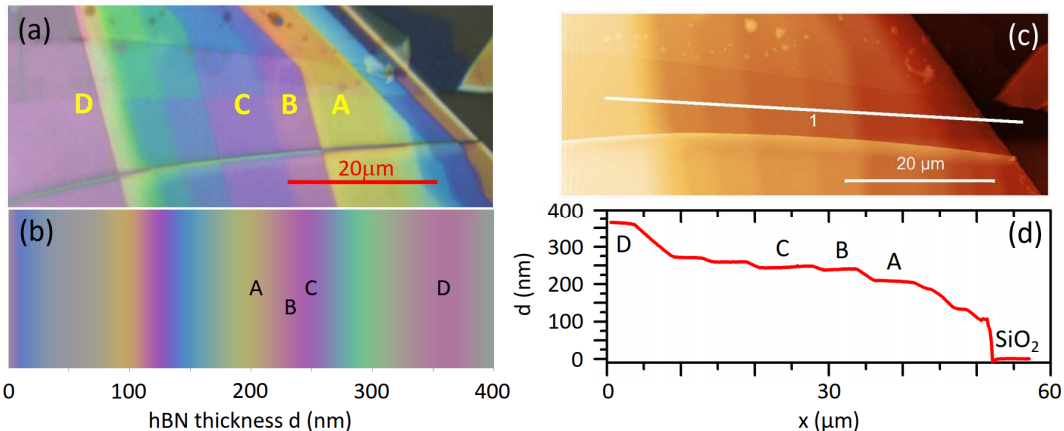


Figure 2.5 (a) Optical microscope image of a hBN-encapsulated MoSe_2 monolayer sample with different terraces. (b) White light reflectivity: simulation of hBN color on SiO_2 (80nm)/Si with the transfer matrix method, consistent with the colors showing in (a). (c) Corresponding AFM image of (a). (d) AFM cross-section of the linecut labeled “1” in (c). The thicknesses are A: 206 nm, B: 237 nm, C: 247 nm, D: 262 nm, E: 274nm and F: 358 nm. Extracted from Ref. [101].

2.2 Effects of hBN encapsulation on the optical and exciton properties

At the early stage of TMD ML research, the researchers just deposited monolayers directly onto a substrate, for example SiO_2/Si , without any top protective layers. As a matter of fact, TMD MLs are subject to the dielectric disorder from surroundings, *i.e.* local changes of the Coulomb interaction as a consequence of the fluctuation of the external dielectric environment [122]. A general illustration of the dielectric disorder is shown in **Figure 2.6(a)**. This local change of the external dielectric constant ϵ_{ext} has influences on the exciton states and free-particle bandgap [123–127]. Indeed, it is unreasonable to assume that the substrate is atomically flat, chemically pure and absolutely clean. There are always fluctuations of surface morphology and different adsorbates on the substrate or on the ML. It has been shown in Ref. [122] that these fluctuations result in dielectric disorder which is the main source of the inhomogeneous broadening in the optical spectra.

The influence due to the local Coulomb interaction variation can be calculated by an electrostatic theory of band-gap renormalization combined with an effective-mass theory of excitons [126]. An example of the calculation result on a WS_2 monolayer is summarized in **Figure 2.6(b)**. This figure presents the energy of the bandgap, the ground state ($n = 1$) and the first excited state ($n = 2$) of the exciton as function of the external dielectric screening constant (ϵ_{ext}). When the screening changes, the bandgap and the excitonic transition energies can vary strongly. The higher the principal quantum number of the excitonic state, the larger is the variation of the excitonic transition with the change of the external dielectric constant. Consequently, local dielectric disorder can strongly change the excitonic transition energies which results in inhomogeneous broadening. When the TMD monolayers are exfoliated and transferred onto Si/SiO_2 substrates [114–116], the full width half maximum (FWHM) of the neutral exciton is typically of the order of 10 meV (50 meV) at 4 K (300 K). Some studies even reported FWHM of ~ 50 meV at low temperature [102,128–130]. This broadening prevents in-depth studies on optical and spin-valley properties of TMD monolayers.

In order to create a favorable dielectric environment for TMD monolayers, hBN is introduced to encapsulate them. hBN is a wide bandgap (5.97 eV) insulator layered material, which is expected to be dangling bond- and surface charge-free. Furthermore, it is quite chemically inert because of the strong in-plane ionic bonds. Thanks to the weak vdW force between layers, hBN can be easily exfoliated into atomically flat layers, providing sub-nanometer planar surface and largely suppressing wrinkles on TMD monolayers. Once they are encapsulated by hBN layers, a significant improvement of the FWHM is observed as shown in **Figure 2.7**. The FWHM of the transition linewidth measured in PL and reflectivity can be down to several meV, for instance ,2-3 meV in hBN-encapsulated WSe_2 monolayer and less than 2 meV in MoS_2 and MoSe_2 monolayer [114]. The linewidth and the intensity of the optical response under hBN encapsulation are unchanged after several cool-down cycles to low temperatures, which is in stark contrast to the uncapped MoS_2 [131] and WS_2 [132,133] monolayers directly exfoliated onto SiO_2/Si substrates.

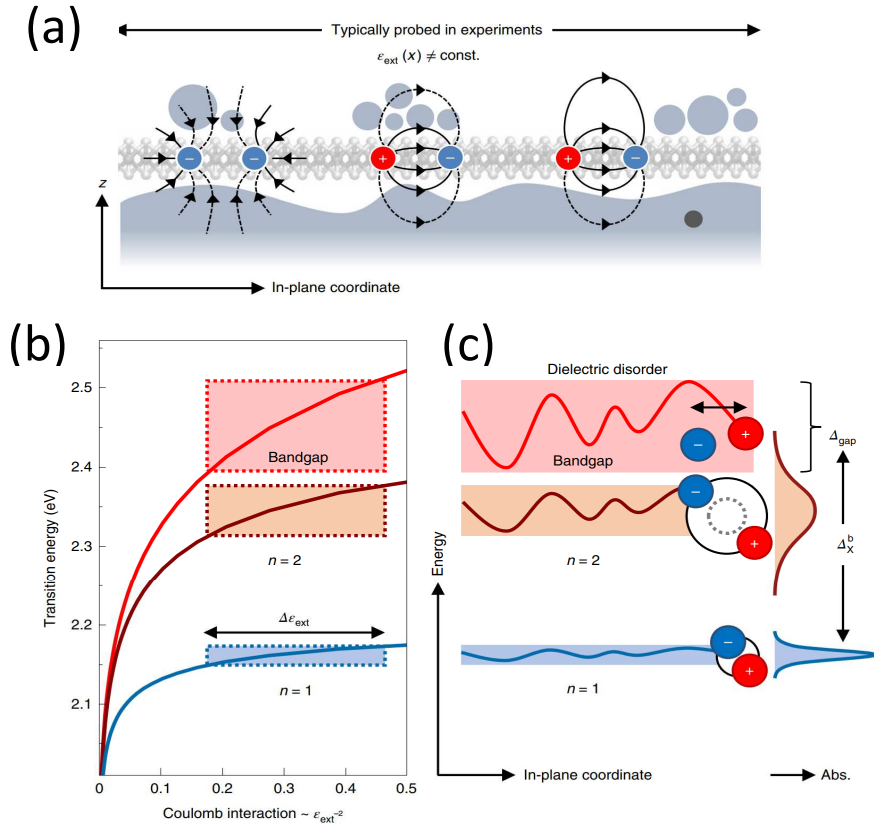


Figure 2.6 Dielectric disorder due to spatial fluctuations of the external environment. (a) Schematic illustration of the electron-electron and electron-hole interaction in different local dielectric screening situation due to the variations of substrate morphology, impurities and adsorbates. (b) Theoretical simulation of the energies of the bandgap and the exciton states. (c) Illustration of the fluctuations of the bandgap and exciton energy due to the dielectric disorder and the expected inhomogeneous broadening in optical spectroscopy. Extracted from Ref. [122].

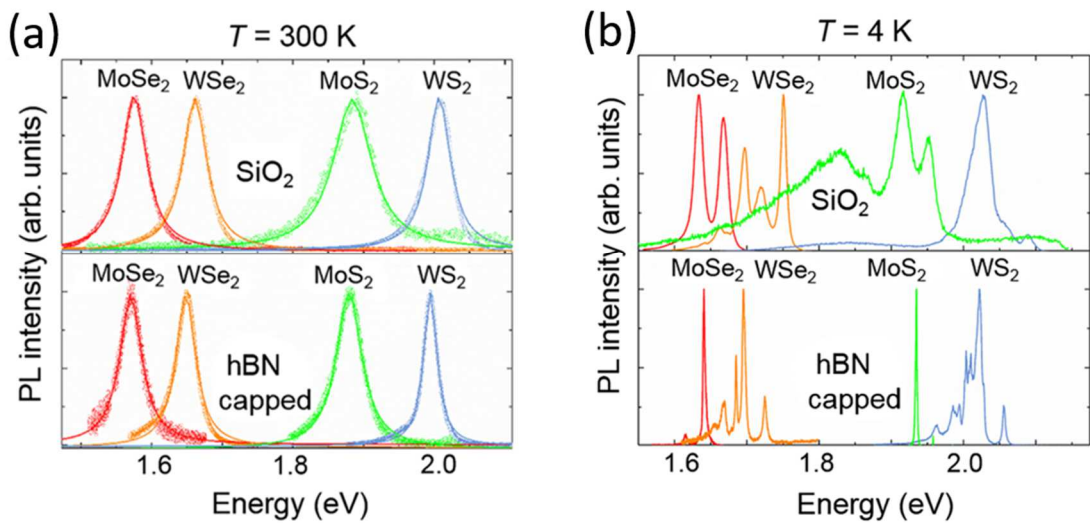


Figure 2.7 PL spectra of monolayer TMD at 300 K (a) and 4 K (b) when exfoliated onto SiO_2/Si substrate (top) and when encapsulated by hBN (bottom). Extracted from Ref. [114].

In conclusion, top and bottom hBN layers isolate the TMD monolayer from the fluctuations of the local Coulomb interaction due to the variations of substrate morphology and prevent physio-and chemisorption. This hBN encapsulation leads to a significant narrowing of the photoluminescence or reflectivity linewidths, which are almost controlled by homogeneous contributions. This allows to access new information concerning the optoelectronic and spin-valley properties.

2.3 Optical spectroscopy experiments

2.3.1 Optical spectroscopy setups

Figure 2.8 shows a sketch of our optical spectroscopy setups, which can be divided into the following main parts: excitation light source, optical path, cryostats, spectrometer and detector. We can integrate different optical elements such as waveplate and polarizer to perform various optical spectroscopy measurements, photoluminescence and reflectivity measurements, for instance. In the following, we are going to detail all the experimental techniques used in this thesis.

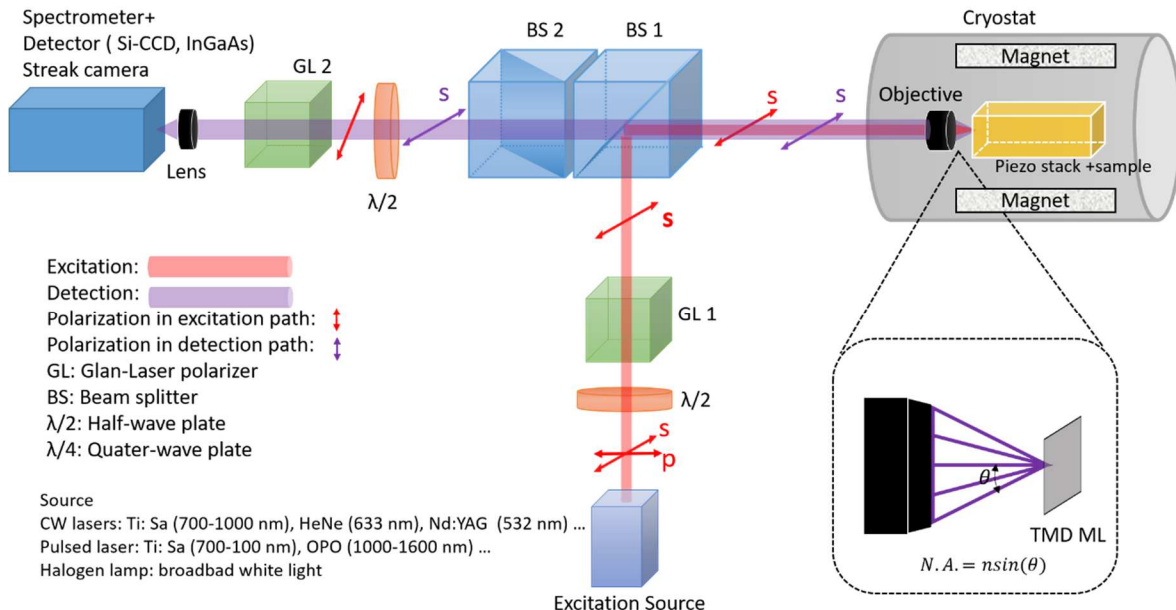


Figure 2.8 Optical spectroscopy setups. Here we give an example of linear excitation and linear detection. Depending on cryostats, a superconducting coil can be integrated inside.

Excitation light sources:

The excitonic transitions of TMD monolayers vary from the visible to near-infrared wavelength [134]. Depending on experiment, the light source can be a continuous-wavelength (cw) laser or a pulsed laser. For cw-experiments, we have used for instance a frequency doubled Nd:YAG laser (532 nm) and an Helium-Neon gas laser (He-Ne laser, 632.8 nm).

We have also used tunable titanium sapphire (Ti:Sa) lasers, which are quite versatile because they are not only tunable in wavelength from 700 nm to 1000 nm but can also operate either in cw or pulsed mode (picosecond or femtosecond). Our cw Ti:Sa laser is a M-squared® (Model: SolsTiS). Our pulsed Ti: Sa laser is a Tsunami from Spectra Physics® (typical pulse width ~1.5 ps, repetition rate: 80 MHz). Besides, coupling a Ti:Sa laser with an optical parametric oscillator (OPO) and/or a frequency doubling crystal can cover the full visible range and part of the NIR. As for the reflectivity measurement, a broadband white light source is required to cover the full visible wavelength range. A tungsten-halogen lamp is then commonly used in this case.

The setup of reflectivity measurement is quite similar to the microscopy setup shown in **Figure 2.8**. but without all the polarization elements and the configuration of the light source part is shown in **Figure 2.9**. The dispersed light from halogen lamp is converged onto the translating pinhole by the “Lens 1”. The translating pinhole allows to select a proper light source area without the shadow of the filament. In the end, the light is collimated by the “Lens 2”.

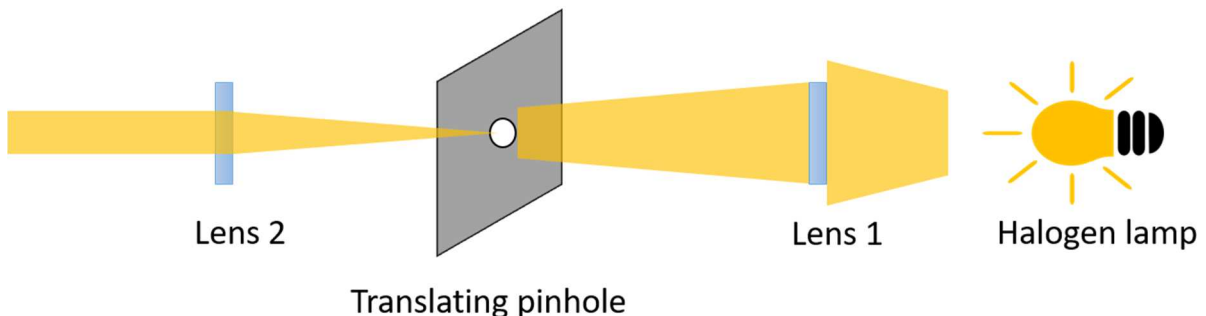


Figure 2.9 Configuration of the light source for reflectivity measurement.

Optical path:

For the excitation part, a half-wave plate ($\lambda/2$) and a Glan-Laser polarizer (GL 1) are mounted just before the beam splitter (BS 1) (see **Figure 2.8**). The reflection of BS1 is polarization-dependent and it has only a maximum reflection of ~ 4 % for the s-polarized light (*i.e.* the component normal to the incident plane). The GL 1 is aligned with respect to BS 1 to ensure that only s-polarized light can go through BS 1. The half-wave plate can tune the polarization of the excitation laser. Then, the total excitation power can be easily tuned by rotating the half-wave plate. Finally, the excitation light is focused by the objective onto the sample.

Since the sample size is in micrometer scale, an objective with high numerical aperture is required to achieve high spatial resolution. The diameter (D) of the excitation laser beam spot on the focal plane of the objective can be estimated through Rayleigh criterion as following:

$$D = 1.22 \times \frac{\lambda}{N.A.} \quad (2.1)$$

λ : the wavelength of the laser.

N.A.: the value of the numerical aperture of the objective.

where $N.A.$ is determined by $N.A. = n \sin(\theta)$ and n is the refractive index of the medium between the objective and the sample (in our case of vacuum environment, $n = 1$). θ is the half-angle of the light cone of the objective, as shown in **Figure 2.8**.

Depending on the experimental requirement, different objectives can be integrated inside the cryostats. For instance, an achromatic objective (Partec®) with a numerical aperture 0.82 is typically used. By bringing this $N.A.=0.82$ and $\lambda=632.8$ nm (He:Ne laser) into the equation above, we can then evaluate the diameter of the laser beam in the focal plane of the objective, which is around 1 μm .

Beside the micrometer size of exfoliated TMD MLs, high spatial resolution is also required by the spatial inhomogeneity of TMD MLs. Indeed, optical properties can vary from point to point on the sample due to different reasons: local dielectric environment, localized states and local strains. A proper area can be then carefully selected on the sample thanks to the high spatial resolution of the objective.

For the detection part, the objective also collects the signal (the purple double arrow line, shown in **Figure 2.8**) coming from the focal plane in confocal geometry. It goes through the two beam splitters, BS 1 and BS 2. The beam splitter has different transmission coefficient for s- and p-polarized light. When the signal goes through the BS 1, the polarization will change. In order to preserve the original polarization of the signal, the BS 2 is mounted to an angle of 45° with respect to the x-y plane so that a s-polarized (p-polarized) signal for BS 1 is a p-polarized (s-polarized) component for BS 2. Consequently, the BS 2 can compensate the polarization change and restore the polarization. The detection efficiency of the diffraction gratings in the spectrometer is also polarization-dependent. Thus, another Glan-Laser polarizer (GL 2) is fixed in a particular direction to optimize the efficiency and to simultaneously act as an analyzer. Another half-wave plate is mounted right after the combination of beam splitters to select either co- or counter-linear component part which is distinguished by an angle of 45° in rotation of the $\lambda/2$. This half-wave plate can be replaced by a Liquid Crystal Retarder (LCR) which can retard the phase between the two light components by application of an external voltage (detailed discussion in 2.3.4). In such a way, the measurement errors caused by a mechanical rotation and the manufacture imperfection can be minimized.

For linear polarization resolved photoluminescence experiments (shown in **Figure 2.8**), the linear polarization degree (P_l) is defined as

$$P_l = \frac{I_{co} - I_{counter}}{I_{co} + I_{counter}} \quad (2.2)$$

where I_{co} ($I_{counter}$) represents the co-polarized (counter-polarized) PL intensity. For the case of circular polarization resolved measurements, please refer the section 2.3.4.

Cryostat:

Samples are loaded inside a cryostat (For example, AttoDry 700), which possesses the following main characteristics: (1) Cryogen-free. Thanks to the closed-cycle cooling system with liquid helium (He), it avoids expensive He supply. (2) Low-mechanical vibration. The mechanical vibrations due to coldhead are minimized in order to maintain the stability of the platform. This is very important because the size of exfoliated TMD monolayers is usually around several micrometers in width and tens of micrometers in length. (3) Temperature stability. The heating system inside the cryostats enables precise temperature control over 5-300 K. A sensor is embedded between the sample stage and the piezo stack to monitor the sample temperature,

The sample is glued on the sample stage (non-magnetic) with silver paste (Electrolube SCP03B) which guarantees good thermal conduction between the sample and the coldhead. The nanopositioners inside the cryostats are designed based on piezoelectric mechanism. Depending on drive technology, the travel range of a nanopositioner working in cryogenic environment varies from few microns to centimenters. For instance, the z-nanopositioner of Attocube® ANP z101 has a step precision of 10 nm and a travel range of 5 μm . Two in-plane nanopositioners and one out-of-plane are combined together to fully control the nanopositions in three dimensions (xyz). Special non-magnetic materials like titanium are used in order to avoid problems when magnetic fields are applied.

Spectrometer and detector:

The collected signal from the sample is analyzed through a spectrometer (for example, Acton SP2500i, Princeton Instruments®) coupled with a charged-coupled device camera (CCD camera). According to experiment requirement, different grating can be chosen to obtain appropriate spectral coverage. The CCD should be also carefully chosen to adapt the wavelength of the signal. Si-CCD can usually cover a spectral range of 400-1000 nm but it has a poor spectral response beyond 1000 nm. In this thesis, a Si-CCD (Spec-10:100BR, Princeton Instruments®) with 1340×100 pixels ($20 \mu\text{m} \times 20 \mu\text{m}$ each) has been used for the detection of the optical transitions of TMD monolayers (WSe₂, WS₂, MoSe₂ and MoS₂). Otherwise, Indium Gallium Arsenide (InGaAs) photodiode arrays can be used for wavelengths in the range 1000 nm-1600 nm.

2.3.2 Differential reflectivity measurement

In this thesis, we perform differential reflectivity measurement to probe the excitonic resonances in TMD monolayers. The differential reflectivity is defined as:

$$\frac{DR}{R} = \frac{R_{ML} - R_{ref}}{R_{ref} - R_{back}} \quad (2.3)$$

where R_{ML} is the reflectivity raw data of the full vdW heterostructure comprising the monolayer TMD (Top hBN/ML TMD/bottom hBN/SiO₂/Si), R_{ref} is the reflectivity raw data of this structure without monolayer TMD and R_{back} is the acquisition by blocking

the excitation light. Compared to reflectivity raw data, differential reflectivity can strongly enhance the signature of the excitonic transitions and make them more visible. In the following, we start to model the reflectivity spectrum by introducing Lorentzian model and transfer matrix method.

2.3.2.1 Lorentzian model

The classic model of light-matter interaction can be described by the concept of the Lorentzian dipole oscillator. It is well-known that Maxwell's equations predict tha oscillating electric dipole could emit electromagnetic waves. Henrick Antoon Lorentz first proposed that there were oscillating dipoles in solids without knowing the existence of electron and nuclei at that age. This model assumes that when the light passes through a medium, the electromagnetic force will drive oscillations of the dipole at its own frequency ω . If ω coincidentally equals one of the natural resonant frequencies of the dipole, ω_0 , the dipole then will absorb the energy from the light and oscillates with large amplitude. This is the so-called resonance phenomenon. If ω does not equal to any natural frequencies of the dipole, the dipole will not absorb the energy and oscillates with a phase lag.

There are many optical resonances in TMD MLs. Those optical responses can be modeled by Lorentzian model. The j_{th} resonance at the frequency ω_0 is characterized by the complex refractive index $\tilde{n} = n(\omega) + i\kappa(\omega) = \sqrt{\varepsilon(\omega)}$, where ω is the angular frequency of the incident light and $\varepsilon(\omega) = \varepsilon_1(\omega) + i\varepsilon_2(\omega)$ is the material's complex dielectric constant. Lorentzian model writes dielectric constants as following [72]:

$$\begin{aligned}\varepsilon(\omega) &= \varepsilon_b + \frac{f_j}{\omega_0^2 - \omega^2 - i\omega\Gamma_j} \\ \varepsilon_1(\omega) &= \varepsilon_b + \frac{f_j(\omega_0^2 - \omega^2)}{\omega_0^2 - \omega^2 - i\omega\Gamma_j} \\ \varepsilon_2(\omega) &= \frac{\omega\Gamma_j f_j}{(\omega_0^2 - \omega^2)^2 + \omega^2\Gamma_j^2}\end{aligned}$$

where ε_b is the background dielectric constant from all the other oscillators than the j_{th} one; Γ_j is the damping rate of the j_{th} resonance; f_j is the oscillator strength, which characterizes the coupling strength between the external optical field and the j_{th} oscillator. f_j can be determined by Fermi's golden rule through quantum mechanics:

$$f_j \propto \left| H_{im}^{(1)} \right|^2$$

where $\left| H_{im}^{(1)} \right|^2 = |\langle m | H^{(1)} | i \rangle|^2$ is the transition probability between the initial system state i and the final state m ; $H^{(1)}$ is the dipole operator.

2.3.2.2 Transfer matrix method

For stacked structures with different refractive index of each layer (shown in **Figure 2.10**), we can use transfer matrix method to model the reflectivity. This method is developed by our collaborators: Mikhail Glazov and Marina Semina from Ioffe Institute (St Petersburg). Let us consider a multilayer system with a refractive index series: n_1, n_2, \dots, n_N . To simplify our discussion, we assume that the incident light propagates along z-axis and is normally pitched into the layered stack. Accordingly, the solution of wave propagation equation in the layer j can be written as:

$$\varepsilon_j = \varepsilon_j^+ \exp(ik_j z) + \varepsilon_j^- \exp(-ik_j z), k_j = \frac{\omega}{c} n_j \quad (2.14)$$

where ε_j^+ and ε_j^- represent the amplitude of the light propagating forward and the light propagating backward, respectively.

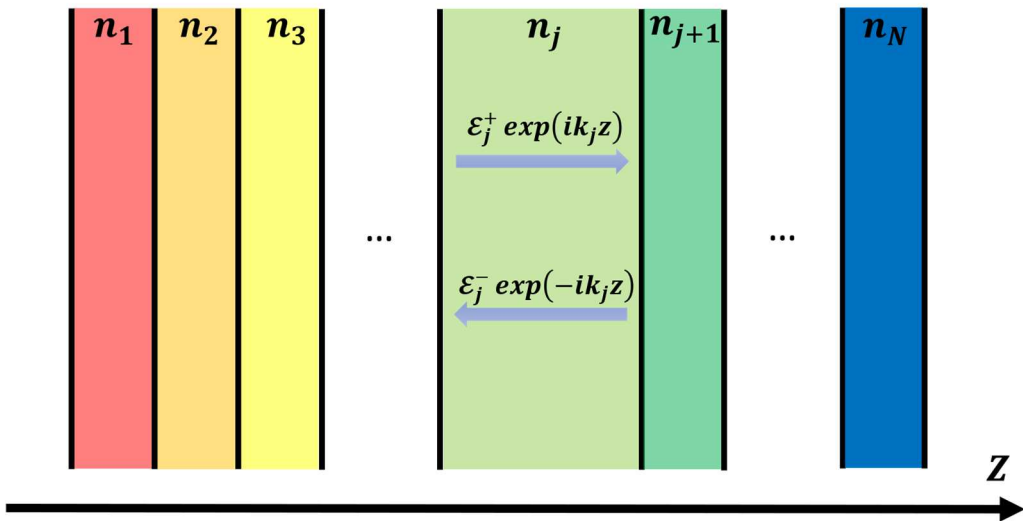


Figure 2.10 Light propagation within a multilayer system.

At the interface of the layer j and the layer $j + 1$, we can build wave equations according to the Maxwell's boundary conditions and write them into matrix form as:

$$\begin{pmatrix} \varepsilon_{j+1}^+ \\ \varepsilon_{j+1}^- \end{pmatrix} = \frac{1}{2n_j} \begin{pmatrix} n_j + n_{j+1} & n_{j+1} - n_j \\ n_{j+1} - n_j & n_j + n_{j+1} \end{pmatrix} \begin{pmatrix} \varepsilon_j^+ \\ \varepsilon_j^- \end{pmatrix} = \hat{T}_{n_j \rightarrow n_{j+1}} \begin{pmatrix} \varepsilon_j^+ \\ \varepsilon_j^- \end{pmatrix}$$

where $\hat{T}_{n_j \rightarrow n_{j+1}}$ is called interface matrix.

As for the propagation within a homogeneous layer with refractive index n_j and thickness d_j , transfer matrix accounts for the phase shifts and this effect is captured by the matrix below:

$$\hat{T}_j = \begin{pmatrix} \exp(ik_j d) & 0 \\ 0 & \exp(-ik_j d) \end{pmatrix}, k_j = \frac{\omega}{c} n_j$$

The effect of the excitonic resonance within a TMD monolayer is modeled by:

$$\hat{T}_{ML} = \frac{1}{t} \begin{pmatrix} t^2 - r^2 & r \\ -r & 0 \end{pmatrix}$$

$$r = \frac{i\Gamma_{rad}^{hBN}}{\omega_0 - \omega - i(\Gamma_{rad}^{hBN} + \Gamma_{nrad})}, t = 1 + r$$

where r and t are the reflection and transmission coefficients of the monolayer TMD within infinite homogeneous hBN, Γ_{rad}^{hBN} is the TMD excitonic radiative damping rate within hBN ($\Gamma_{rad}^{hBN} = \Gamma_{rad}^{vacuum}/n_{hBN}$), ω_0 is the excitonic resonance frequency and Γ_{nrad} is the excitonic non-radiative damping rate.

Now we are capable to model the light propagation within the classic van der Waals heterostructure where a TMD monolayer is embedded within the top and bottom hBN and which is deposited on SiO₂/Si substrate by the transfer matrices below:

$$\hat{T}_{tot} = \hat{T}_{SiO_2 \rightarrow Si} \hat{T}_{SiO_2} \hat{T}_{hBN \rightarrow SiO_2} \hat{T}'_{hBN} \hat{T}_{ML} \hat{T}_{hBN} \hat{T}_{air \rightarrow hBN}$$

where the prime denotes the bottom hBN layer. The Si layer is assumed to be thicker than the absorption length, thus the reflection between the air and the Si layer is disregarded.

Then we can build the relationship between the amplitude of the reflection (r_{tot}) and the transmission (t_{tot}) of the whole structure through:

$$\hat{T}_{tot} \begin{pmatrix} 1 \\ r_{tot} \end{pmatrix} = \begin{pmatrix} t_{tot} \\ 0 \end{pmatrix}$$

Hence, r_{tot} and t_{tot} can be resolved through the transfer matrix method. Note that the absorbance of the monolayer TMD can be calculated by $\mathcal{A} = 1 - |r_{tot}|^2 - |t_{tot}|^2/n_{Si}$.

Here, we give an example of reflectivity modeling of a vdW heterostructure with a MoS₂ ML through transfer matrix method. **Figure 2.11(a)** shows a schematic of this sample. **Figure 2.11(b)** shows the measured and the modeled differential reflectivity. The strong transition at lower energy is due to the A-exciton ground state absorption. At higher energies, three more transitions are clearly visible; the broader one is due to the B-exciton ground state while the other two are tentatively ascribed to be the first two excited states of the A exciton: A:2s and A:3s [75]. The simulations are obtained by keeping the top hBN layer at 10 nm but varying the thicknesses of SiO₂ layer and the bottom hBN layer. The red curve simulation is obtained by using the hBN thicknesses determined by atomic force microscopy, which perfectly fits the experiment data. This demonstrates the transfer matrix method is a powerful tool to model the reflectivity measurement.

On the other hand, we can also see in **Figure 2.11** that the peak intensity and shape of the excitonic transitions (fine magenta, green, and blue curves) in the modeled differential reflectivity spectrum strongly depend on the thicknesses of the bottom hBN and the SiO₂ layer. This results from the interferences within a cavity-like structure between the MoSe₂ ML and the interface of SiO₂/Si. This will be investigated in more detail in Chapter 3.

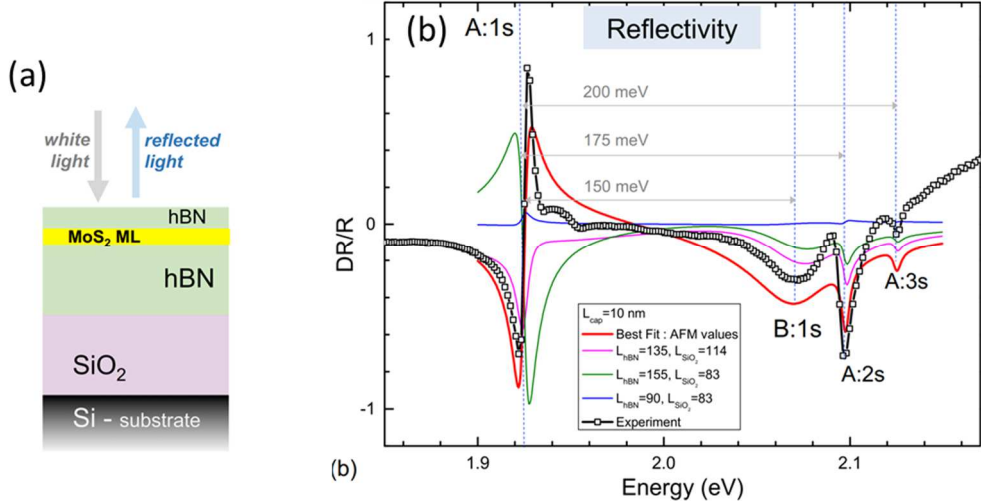


Figure 2.11 (a) Schematic of a vdW heterostructure with MoS₂ ML. (b) Differential reflectivity measurement and reflectivity simulations using transfer matrix method. Extracted from Ref. [75].

2.3.3 Photoluminescence spectroscopy

Photoluminescence spectroscopy is a well-known non-contact, nondestructive method to study optical and electronic properties of materials [135]. Figure 2.12 shows a simplified schematics of the exciton photoluminescence process: external light source excites carriers from ground states to excited states. Then the excited hot exciton relaxes down to the bottom of the band by interacting with phonons. This relaxation process is indicated by the cascade within the band. Each step corresponds to a scattering with phonon, which must satisfy the energy and momentum conservation laws. In the end, the relaxed excitons are accumulated in the form of thermal distribution on the bottom of the band. Then, these excitons can recombine radiatively by emitting light. The PL emission is represented by a downward vertical arrow in Figure 2.12. The emission therefore occurs near $K_{ex} = 0$ and corresponds to the energy of the optical bandgap, $E_{g,optical}$. If this photoluminescence process is simplified by a two-level system, ground state and excited state, then the number of the emitted photons per unit time can be determined by:

$$\frac{dN}{dt} = -AN$$

where N is the population of excitons and A is the Einstein coefficient, which also could be viewed as radiative emission rate. The evolution of the radiative emission is characterized by the solution of the equation above:

$$N(t) = N(0) \exp(-At) = N(0) \exp\left(-\frac{t}{\tau_r}\right)$$

where $N(0)$ represents the population of the excitons at $t = 0$ and $\tau_r = A^{-1}$ is called the exciton radiative lifetime.

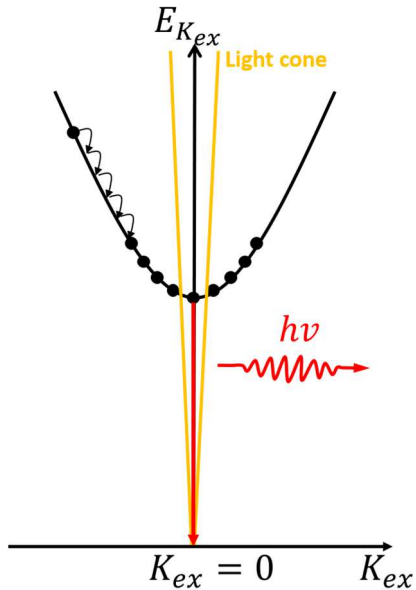


Figure 2.12 Schematic diagram of the photoluminescence process in a TMD ML. Excitons (black solid circle) are generated by the external light excitation. Then they relax to the minimum energy state and recombine radiatively (indicated by the red solid arrow) by emitting light (red wave arrow) once reaching within the light cone (yellow solid line). $K_{ex} = 0$ corresponds to the center of exciton Brillouin zone.

2.3.4 Polarization-resolved photoluminescence

In Chapter 1, we have introduced the spin-valley properties of TMD MLs. Due to the broken symmetry and strong spin-orbit coupling in TMD MLs, K^+ (K^-) valleys can be selectively excited with $\sigma^+(\sigma^-)$ circularly polarized light. In order to investigate this new degree of freedom, we need to perform circular polarization-resolved photoluminescence measurements. In addition, we can perform linear polarization-resolved photoluminescence measurements to study the valley coherence [136,137]. In this case, the experimental setup has been detailed in section 2.3.1. Here, we will focus on the circular one.

For circular excitation, a quarter-wave plate ($\lambda/4$) is mounted between BS 1 and the cryostats, shown in **Figure 2.13**, which can convert linearly-polarized light into circularly-polarized light if the neutral axis of the $\lambda/4$ is rotated to an angle of $+/-45^\circ$ with respect to the linear polarization. In **Figure 2.13**, the $\lambda/4$ converts the s-polarized excitation light into σ^+ polarized light ($\lambda/4$ for $+45^\circ$, σ^- can be obtained for -45°). In the detection path, the circularly polarized light (σ^+/σ^-) coming from the sample can be converted into two orthogonal linearly polarized components after passing through the $\lambda/4$ ($\sigma^- \rightarrow p$, shown in **Figure 2.13**). Then, it goes through the two beam splitters, BS 1 and BS 2 without any polarization change since the BS 2 acts as a compensator to preserve the original polarization of the signal. The half-wave plate ($\lambda/2$) is mounted right after the combination of beam splitters to select either co- and counter-circular component which are distinguished by an angle of 45° in rotation of the $\lambda/2$. This half-wave plate can be replaced by a LCR, as mentioned previously.

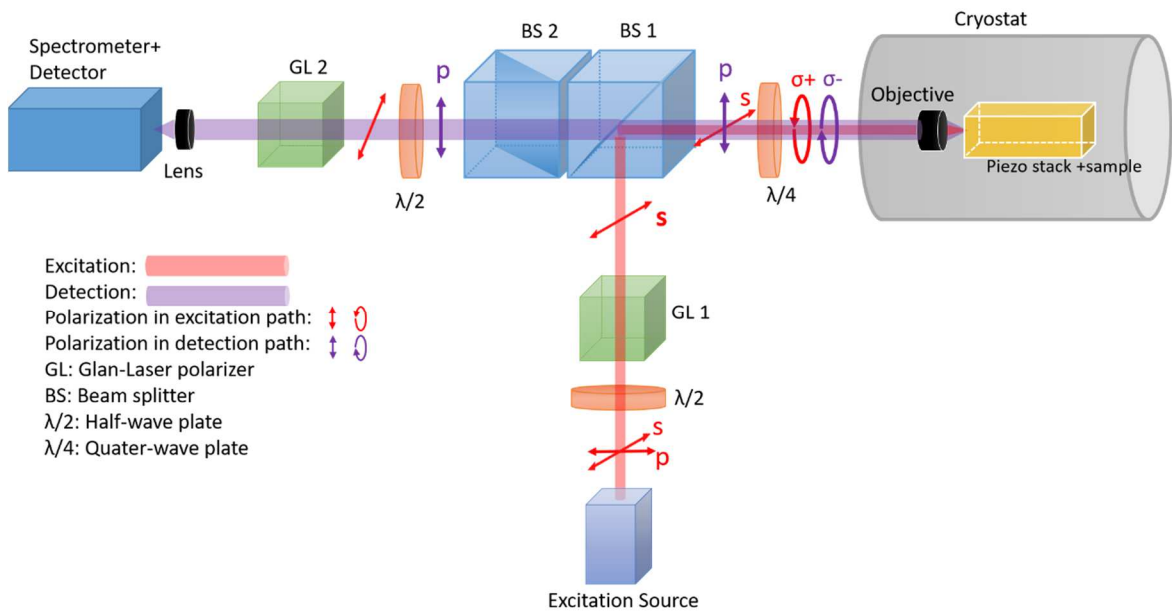


Figure 2.13 Experimental setups for circular polarization-resolved PL measurements. Compared with the linear polarization-resolved PL measurements, a quarter-wave plate ($\lambda/4$) is mounted between the BS 1 and the cryostats. This quarter-wave plate can convert linearly-polarized light into circularly-polarized one if the neutral axis of the $\lambda/4$ is rotated to an angle of 45° with respect to the linear polarization.

For circular polarization resolved photoluminescence experiments, the circular polarization degree (P_c) is defined as

$$P_c = \frac{I_{co} - I_{counter}}{I_{co} + I_{counter}}$$

where I_{co} ($I_{counter}$) represents the co-polarized (counter-polarized) PL intensity components.

2.3.5 Magneto-photoluminescence spectroscopy

In this thesis, we have performed magneto-photoluminescence measurements. **Figure 2.14** shows a photo of our magneto-optical setups which allow us to perform PL and reflectivity measurements. The optical design is almost like the setup shown in **Figure 2.8**, except that the detected signal is connected to the spectrometer with a single mode fiber. This setup can be qualified as a “Confocal setup” as the excitation and the detection light paths are the same and share the same objective and the core of the single mode fiber plays the role of a spatial filter that blocks the out-of-focus signal and increases the spatial resolution. In our setups, the fiber has a diameter $\sim 2\text{-}3 \mu\text{m}$

A He-Ne laser is also fibered with this setup to serve as the excitation source. The cryostat (AttoDRY 1000) is a closed-cycle liquid He cooling system equipped with a superconducting magnet up to 9 T (out-of-plane). There are two features in this setup:

(1) A liquid crystal retarder (Meadowlark Optics) is mounted on the detection path to select desired polarized signal. This retarder can provide tunable polarization by tuning the effective birefringence of the crystal with applied voltage, thus converting the input polarized light to any desired elliptical, linear or circular polarization. This key feature of the electrically-control retarder can avoid artifacts comparing with mechanical retarder which may deviate the optical path of the collected signals. This is very useful especially here since our detection is fibered with the spectrometer and the fiber core is of around 2-3 μm . This retarder is usable from 450 nm to 1800 nm and compatible with computer control. (2) An achromatic cryogenic magnetic field-compatible objective (Attocube: LT-APO/VISIR) is installed to avoid measurement artefacts due to cryogenic temperature and high magnetic field.

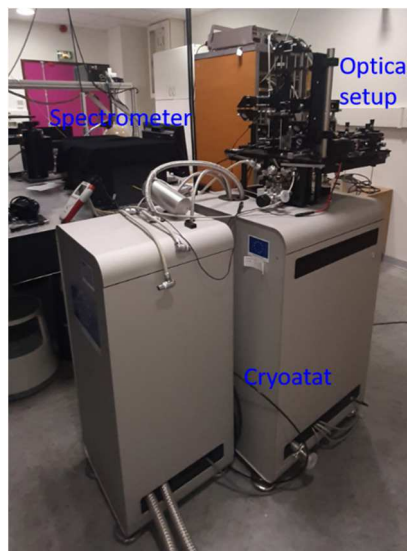


Figure 2.14 Photo of the Magneto-optical spectroscopy setup. The optical setup is installed just above the cryostat. The excitation source and the detection pathway are connected to the setup with an optical fiber. A superconducting magnet up to 9 T is integrated inside this cryostat.

2.4 Conclusion

In this Chapter, we have presented the sample fabrication process we have used for all the van der Waals heterostructures investigated in this thesis. We have also detailed the procedures to identify the TMD monolayers and to select the hBN layers with the desired thickness. The role of the hBN encapsulation has been emphasized: to provide a homogeneous dielectric environment for monolayers and to narrow the photoluminescence/reflectivity linewidths. We have also summarized all the optical spectroscopy techniques used in this thesis, such as photoluminescence and differential reflectivity.

Chapter 3 Control of the Splitting between Bright and Dark Excitons using Lamb Shift in WSe₂ Monolayers

In this Chapter, we are going to investigate the exciton fine structure in atomically thin WSe₂-based van der Waals heterostructures. We have tuned the density of optical modes at the location of the WSe₂ monolayer by changing the hBN encapsulation layer thickness in the heterostructure. The energy splitting Δ between the bright and dark exciton has been measured by photoluminescence spectroscopy. We demonstrate that Δ can be tuned by a few meV, as a result of a significant Lamb shift of the optically active exciton which arises from emission and absorption of virtual photons triggered by the vacuum fluctuations of the electromagnetic field. We also measured in the same structures strong variations of the bright exciton radiative linewidth, as a result of the Purcell effect. All these experimental results illustrate the strong sensitivity of the excitons to local vacuum field. We found that they are in very good agreement with a model developed by M. Glazov and M. Semina (Ioffe Institute) that demonstrates the equivalence, for our system, between a classical electrodynamical transfer matrix formalism and a quantum-electrodynamical approach.

This Chapter is organized with the following sections:

- 3.1 Exciton fine structure in semiconductor nanostructures
- 3.2 Investigated samples and experimental methods
- 3.3 Experimental results
 - 3.3.1 Luminescence linewidth study
 - 3.3.2 The bright-dark exciton energy splitting
- 3.4 Theory and discussion
- 3.5 Conclusion

3.1 Exciton fine structure in semiconductor nanostructures

The exciton fine structure plays a crucial role for the light-matter coupling in semiconductor nanostructures [138]. The short range part of the electron-hole exchange interaction yields a splitting of the exciton states corresponding to different relative orientations of electron and hole spins [139–141]. As a result, the lowest energy exciton state is usually a dark state. In (In)GaAs quantum wells or quantum dots this splitting between bright and dark exciton states is rather small, of the order of hundreds of μeV [142–145]. As already mentioned in Chapter 1, the energy splitting Δ between bright and dark exciton in TMD MLs depends on exciton exchange interaction and the band structure parameters; the dark exciton states can lie tens of meV below the bright ones [86,88,89,146–150]. In that cases the exciton fine structure can have a dramatic impact on the emission yield of these new semiconductor nanostructures, even at room temperature [148,149].

One usually considers that the splitting between bright and dark exciton in semiconductors is solely governed by the band structure and the amplitude of the exchange interaction between the electron and the hole. In the following, we demonstrate that the coupling to light has also to be taken into account [151,152]. We evidence in our van der Waals heterostructure structure a clear tuning of the bright-dark exciton splitting as a result of a significant Lamb shift of the optically active exciton. This shift results from the emission and re-absorption of virtual photons, similarly to atomic systems [153–155]. In contrast, the dark exciton has an oscillator strength orders of magnitude smaller than the bright exciton one yielding a negligible energy shift due to the optical environment. As a consequence, the energy difference between the bright and the dark exciton varies with characteristics of the electromagnetic field at the position of the semiconductor nanostructure. This can be achieved in an heterostructure (top hBN/WSe₂ ML/bottom hBN) in the weak coupling regime as we demonstrate in this Chapter or by tuning the distance between the semiconductor layer and an external mirror. As already discussed in Chapter 2, the key advantage of the hBN encapsulation technique is that it yields narrow optical transitions approaching the homogenous exciton linewidth governed by radiative recombination.

3.2 Investigated samples and experimental methods

We have fabricated WSe₂ ML based van der Waals heterostructures (top hBN/WSe₂/bottom hBN) with the method detailed in Chapter 2. The whole structure is deposited on to a 83 nm SiO₂/Si substrate. The top hBN thickness does not play an important role here considering its small value, typically \sim 5-10 nm. The bottom hBN thicknesses d are measured by AFM. The four samples used in this Chapter are characterized by different bottom hBN layer thickness; they are listed below in **Table 3.1**, including two “rainbow samples” where the same WSe₂ ML is deposited on a hBN flake exhibiting different terraces and steps. **Figure 3.1(a)** shows a schematics of a “rainbow sample”; **Figure 3.1(b)** shows an optical microscope image of Sample IV.

Table 3.1 Samples characterized with different bottom hBN thickness.

Sample	Bottom hBN thickness d (nm)
Sample I	101
	113
Sample II (rainbow)	115
	119
	132
	135
Sample III	186
Sample IV (rainbow)	214
	224
	239
	269

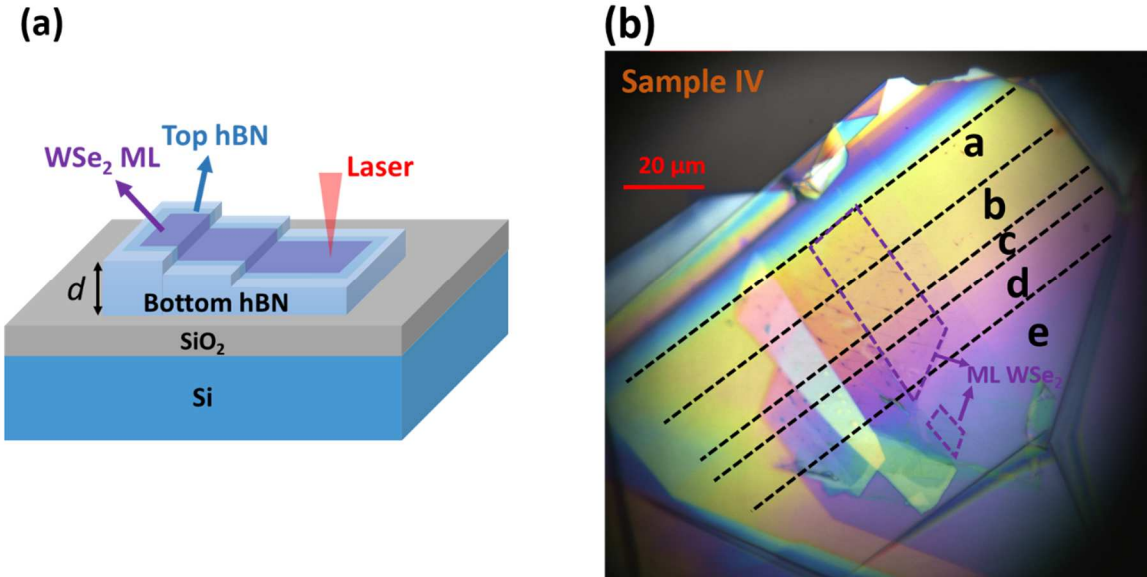


Figure 3.1 (a) Schematics of the investigated hBN-encapsulated WSe₂ monolayer, where the same monolayer is embedded in a staircase heterostructure characterized by different bottom hBN layer thickness d . (b) Optical microscope image of Sample IV showing different bottom hBN thicknesses: a ($d=210$ nm), b ($d=214$ nm), c ($d=224$ nm), d ($d=239$ nm) and e ($d=269$ nm). The black dashed lines separate different terraces and the WSe₂ monolayer is indicated by the purple dashed line.

We have performed simple cw photoluminescence experiments at $T=5$ K using a He-Ne laser. The typical excitation power is $5\text{ }\mu\text{W}$, *i.e.* in the linear regime of excitation. This setup has been discussed in Chapter 2. Time-resolved photoluminescence experiments have been performed on a charge-tunable WSe₂ ML sample, which is also used in Chapter 6 (see sample details in section 6.2). In this case, the sample is excited with a Ti:Sa mode-locked laser (695 nm, ~ 1.5 ps pulse width, 80 MHz repetition rate). The PL kinetics are recorded by a synchro-scan Hamamatsu streak camera with

a typical time-resolution of 2 ps [101]. We will not focus on the time-resolved photoluminescence experiments in this thesis, please see the details on the experimental set-ups in Ref. [83,101].

3.3 Experimental results

Figure 3.2 displays the cw PL spectrum for $d=214$ nm. In agreement with previous reports, the luminescence of the WSe₂ ML is dominated by the recombination of the neutral bright exciton (X_0) and the spin-forbidden dark exciton (X_D) with an energy splitting of $\Delta=41$ meV [86,88,89,148–150]. As already explained in section 1.4, we are able to detect the dark exciton with a microscope objective with high numerical aperture, even though the light propagates mainly along z (perpendicular to the ML plane). This explains the clear dark exciton X_D PL line in **Figure 3.2**. We also observe much smaller PL components, associated to the recombination of singlet (X^{S^-}) and triplet (X^{T^-}) negatively charged excitons and indirect exciton X_I as already identified in many reports [156–158]. The properties of the trion doublet (X^{S^-} and X^{T^-}) will be presented in Chapter 4. Note that the observation of the indirect exciton and a large spin-forbidden dark exciton guarantees that the sample is close to charge-neutrality even without gate control.

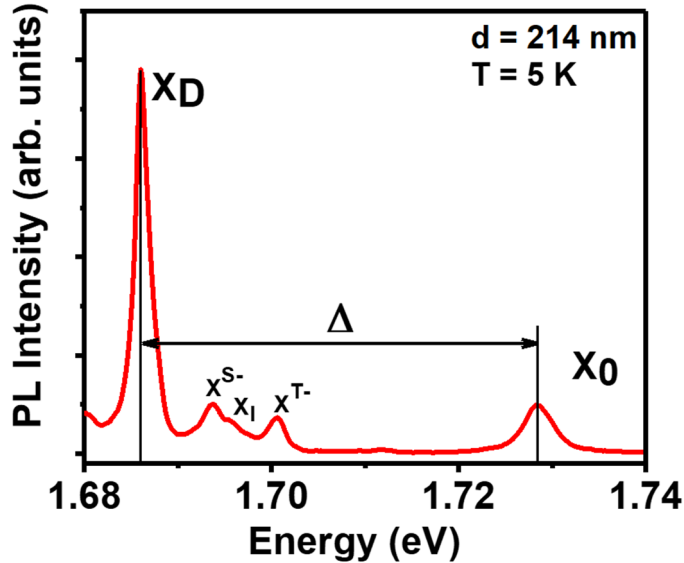


Figure 3.2 cw photoluminescence spectrum of the WSe₂ monolayer ($d=214$ nm) showing the emission of the neutral bright (X_0) and dark exciton (X_D), the two negative triions (X^{S^-} and X^{T^-}) and the indirect exciton (X_I) at $T = 5$ K. The energy difference between the neutral bright (X_0) and dark exciton (X_D) is denoted as Δ .

Figure 3.3 presents the time evolution of both bright (X_0) and dark (X_D) exciton luminescence following a picosecond excitation laser pulse in a WSe₂ monolayer with $d= 290$ nm. In agreement with previous reports mentioned in Chapter 1, we measure the X_0 lifetime in \sim ps range. In contrast, we measure a much longer PL decay time, \sim

800 ps, for the dark exciton X_D . This result tells us that the dark exciton oscillator strength is at least 3 orders of magnitude weaker than the bright exciton one. Though a non-radiative contribution cannot be excluded here for the dark exciton, this oscillator strength ratio is in agreement with results obtained by density functional theory calculations [159]. As a consequence, we can expect that the Lamb shift of the dark exciton will be negligible compared to the possible energy shift of the bright exciton linked to absorption/emission of virtual photons.

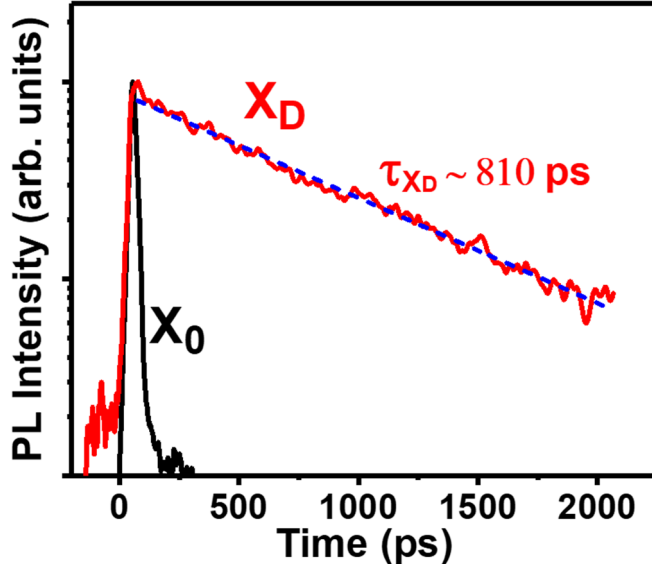


Figure 3.3 Normalized photoluminescence intensity as a function of time for the neutral bright exciton (X_0 , black solid line) and dark exciton (X_D , red solid line), $d=290 \text{ nm}$. The blue dashed line corresponds to a mono-exponential fit of the decay time τ_{X_D} .

3.3.1 Luminescence linewidth study

First, we investigate the dependence of the X_0 luminescence linewidth as a function of d . **Figure 3.4(a)** displays the normalized PL spectra for $d=101$ and 186 nm . We observe a clear increase by more than a factor 2 (4.3 meV compared to 2 meV) in the luminescence linewidth (FWHM). As shown in **Figure 3.4(b)**, $d=101 \text{ nm}$ and $d=186 \text{ nm}$ correspond to position of the ML at the node and the anti-node of the optical field intensity respectively in the cavity-like structure (calculations based on the transfer matrix method, detailed in Chapter 2). Thus the larger PL linewidth in **Figure 3.4(a)** for $d=186 \text{ nm}$ reflects the decrease of the radiative recombination time due to Purcell effect already observed in MoSe₂ MLs [101,160–162]. **Figure 3.4(b)** presents the variation of X_0 FWHM for eleven values of d , confirming the clear control of the linewidth due to the cavity effect. In order to reduce uncertainties, each value displayed in **Figure 3.4(b)** is the average of about twenty measurements obtained at different points of the ML flake for a fixed d . The novelty here is the demonstration of the effect in WSe₂ monolayer. In contrast to MoSe₂, the bright exciton in WSe₂ monolayer lies *above* the dark exciton X_D , as shown in the inset of **Figure 3.5(a)**. The clear dependence of the bright exciton linewidth evidenced in **Figure 3.4(a)** demonstrates

that it is dominated by the radiative recombination and that the relaxation channel from cold bright exciton to the lower lying dark exciton plays a minor role.

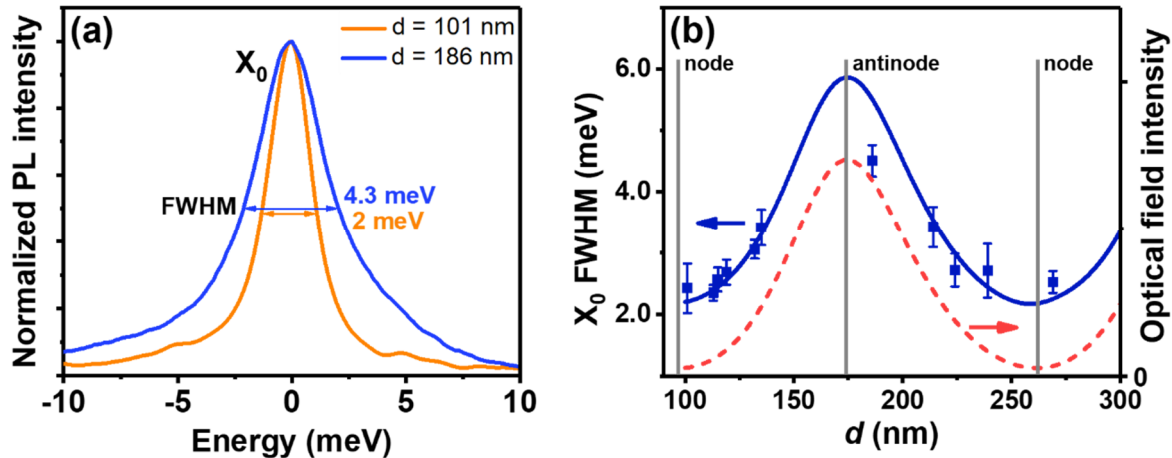


Figure 3.4 (a) Normalized cw PL intensity of the neutral exciton for $d = 101 \text{ nm}$ and $d = 186 \text{ nm}$ showing different linewidths. In order to compare the linewidths, the origin of the energy axis is taken at the PL peak. The double arrow lines indicate the FWHM linewidths, which are vertically shifted in purpose for better visibility. (b) Measured (blue symbols) and calculated (blue solid line) bright neutral exciton linewidth as function of the bottom hBN thickness d . The red dashed curve is the calculated optical field intensity at the monolayer plane. The thickness where the ML is located at the nodes and antinodes are indicated by the vertical grey bars.

3.3.2 The bright-dark exciton energy splitting

Figure 3.5(a) and **(b)** present the key result of this Chapter. We have measured the bright-dark exciton energy splitting Δ for the same samples and hBN thicknesses d as the ones used for the investigation of the Purcell effect. **Figure 3.5(a)** displays for instance the PL spectra for $d=132$ and $d=214 \text{ nm}$ (the energy origin has been chosen at the dark exciton X_D energy). We observe very clearly a variation $\delta E \approx 1.7 \text{ meV}$ of the splitting. The variation δE of the bright-dark splitting as a function of d is displayed in **Figure 3.5(b)**. Note that the splitting between X_0 and X_D is $\Delta + \delta E$, choosing $\delta E = 0$ for $d=100 \text{ nm}$, i.e. when the WSe₂ ML is at the node of the electric field in the cavity-like structure. We evidence a significant and oscillatory modulation of δE as a function of the electromagnetic field amplitude. These results demonstrate that the energy difference between bright and dark excitons is not only controlled by electron-hole exchange interaction and the semiconductor band structure parameters but the coupling to the electro-magnetic field has also to be taken into account.

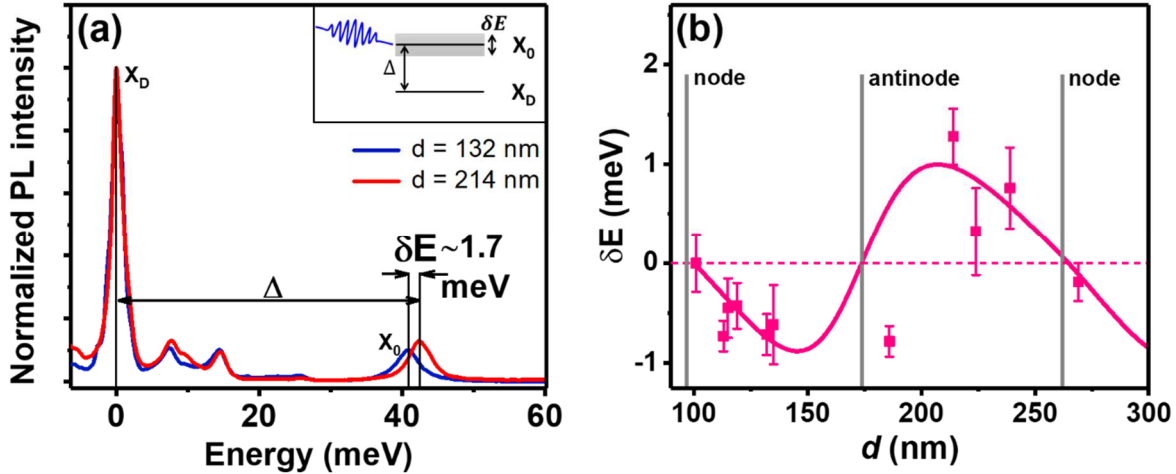


Figure 3.5 (a) Normalized PL spectra for $d=132 \text{ nm}$ and $d=214 \text{ nm}$. The energy axis is taken at the X_D PL peak to show the transition energy shift δE of X_0 . Inset: schematics of the transition energy shift of X_0 (grey shadow) due to Lamb shift. (b) Measured (pink symbols) and calculated (pink solid line) variation δE of the bright-dark exciton splitting as a function of the hBN bottom thickness d .

3.4 Theory and discussion

Both the exciton linewidth variation and the tuning of the bright-dark exciton energy splitting presented in **Figure 3.4(b)** and **Figure 3.5(b)** can be well understood on the basis of a model based on transfer matrix formalism and quantum-electrodynamical approaches (see Appendix). This model was developed by M. Glazov and M. Semina (Ioffe Institute, St Petersburg). In order to compare the experiments and the theoretical predictions, we have calculated the linear response functions (reflectivity, transmission and absorbance) of our stacking “top hBN layer/WSe₂ ML/bottom hBN layer/SiO₂/Si” with the measured 10 nm top hBN thickness, 83 nm SiO₂ thickness and crucially the variable bottom hBN thickness d . In the calculations, we used the following refractive indices: $n_{\text{hBN}} = 2.2$, $n_{\text{SiO}_2} = 1.46$, $n_{\text{Si}} = 3.5$ [75].

The full line in **Figure 3.4(b)** is the calculated dependence of the bright exciton linewidth $\Gamma = \Gamma_0 + \Gamma_{\text{nr}}$, where Γ_0 and Γ_{nr} are the radiative and non-radiative contributions respectively extracted from the calculated absorption coefficient. We notice a very good agreement between the measured and calculated dependence using the exciton radiative rate in vacuum $\Gamma_0^{\text{vac}} = 2 \text{ meV}$ and $\Gamma_{\text{nr}} = 0.6 \text{ meV}$. Note that the radiative decay rate is consistent with previous experimental and theoretical estimations of the recombination rate in WSe₂ monolayer where the cavity effect was not considered [80,83,163]. Remarkably the same parameters in the model also yield a very good description of the dependence of the exciton bright-dark splitting as a consequence of the Lamb shift, see the full line in **Figure 3.5(b)**. The discrepancy observed for $d=186 \text{ nm}$ could be due to an anomalously large value of the doping density for this point attested by a larger trion PL intensity.

In quantum electrodynamics, both the variation of the radiative decay rate and energy of the exciton stem from its coupling with vacuum fluctuations of

electromagnetic field. Change in the bottom hBN thickness d changes the local structure of electromagnetic modes in the system and, consequently, Γ_0 and δE . The analysis in Appendix shows that these quantities can be also evaluated semiclassically, using the transfer matrix method and expressed via the electrodynamic Green's function. Compact analytical expressions can be derived neglecting the cap layer effect, in that case (see Appendix and Ref. [101]):

$$\Gamma_0 + i \delta E = \Gamma_0^{\text{vac}} (1 + r_{bg}), \quad (3.1)$$

where r_{bg} is the complex reflection coefficient of a three-layer structure “hBN/SiO₂/Si”, thus the Purcell factor and Lamb shift are proportional to the real and imaginary parts of the substrate's reflection coefficient. It is instructive to consider an illustrative case of a simplified open cavity structure based on a WSe₂ ML lying at a distance d' from a non-absorbing mirror characterized by a real reflection coefficient r (inset in **Figure 3.6**) [164]. In that case $r_{bg} = r \exp(2iqd')$, $q = \omega/c$, c is the speed of light and $\hbar\omega$ the exciton energy, and the exciton radiative linewidth and the bright-dark splitting variation write simply (see Appendix):

$$\Gamma_0 = \Gamma_0^{\text{vac}} [1 + r \cos(2qd')], \quad (3.2a)$$

$$\delta E = r \Gamma_0^{\text{vac}} \sin(2qd'). \quad (3.2b)$$

These simple expressions directly show why the two measurements are in quadrature in **Figure 3.4(b)** and **Figure 3.5(b)**. In contrast to the linewidth which exhibits as expected minima and maxima at the nodes and anti-nodes respectively, the bright-dark splitting variation δE is strictly zero for these two positions, in perfect agreement with Eq. (3.2b). Such a behavior is general and follows from the dispersion relations for the reflectivity in Eq. (3.1), see Appendix for details.

Figure 3.6 presents the calculated dependence of the bright-dark splitting energy variation for a WSe₂ monolayer in this simple open cavity composed of a mirror with a 100% reflection coefficient; we used here the same exciton radiative rate in vacuum $\Gamma_0^{\text{vac}} = 2$ meV as the one used in the calculated curves in **Figure 3.4(b)** and **Figure 3.5(b)**. A variation of the bright-dark splitting as large as 4 meV due to the Lamb shift can be obtained. These huge variations result from Lamb shift orders of magnitude larger than the ones evidence in atomic systems [151–155,165], a straightforward consequence of the very large oscillator strengths (and hence Γ_0^{vac}) of excitons in TMD monolayers, Eq. (3.2b).

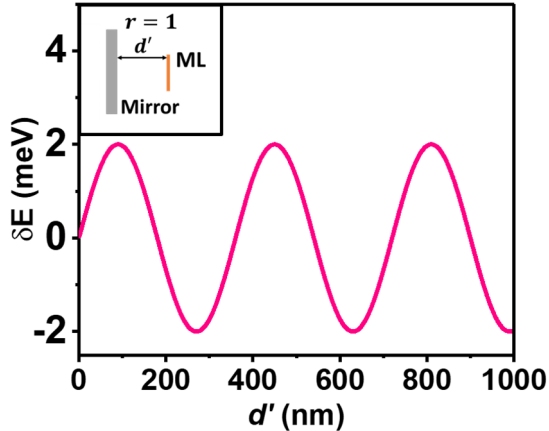


Figure 3.6 Calculated variation δE of the bright-dark exciton splitting as a function of the distance between the mirror (with reflection coefficient $r = 1$) and the monolayer. Inset: schematics of the simple configuration where the monolayer is at a distance d' from the mirror.

As mentioned previously, the bright-dark exciton splitting Δ in TMD semiconductor monolayers includes three contributions: $\Delta_3 = \Delta_{\text{exch}} + \Delta_{\text{so}} + \Delta_{\text{bind}}$, where Δ_{exch} is the short range exciton exchange energy, Δ_{so} is the conduction band spin–orbit splitting and Δ_{bind} is the difference between the binding energies of bright and dark excitons. The exchange term is $\Delta_{\text{exch}} \sim 10$ meV [158,166]. In **Figure 3.6**, we show that the new contribution due to Quantum Electrodynamical (QED) effect, δE , could be as large as 4 meV, *i.e.* $\sim 40\%$ of the exchange term resulting in $\Delta = \Delta_3 + \delta E$. We can anticipate that similar effects should occur in other TMD monolayers, including WSe₂ and MoS₂ as they are characterized by rather similar exciton binding energies and as a consequence very large oscillator strengths [14–16,78] compared to WSe₂. For MoSe₂ monolayers, the impact of the optical environment could be even more interesting since the dark exciton lies slightly above the bright one with reported values of $\Delta = -1.5$ meV [88,167], *i.e.* of the order of the energy shifts we have evidenced in WSe₂ MLs (see **Figure 3.5(b)**). This means that a proper engineering of the quantum fluctuations should reverse the bright-dark exciton ordering in van der Waals heterostructures based on MoSe₂ MLs. We emphasize that this should occur in *the weak coupling regime*, in contrast to the change of bright-dark ordering evidenced for exciton-polaritons *in the strong coupling regime* for a WSe₂ monolayer placed inside a high finesse optical cavity [168]. In GaAs quantum wells, the free exciton oscillator strength of the exciton is typically ~ 10 times weaker than the one in TMD monolayers [167]; thus Eq. (3.2b) predicts a typical variation of the bright-dark splitting in a cavity-like structure of the order of ~ 100 μeV (using $r=1$). Remarkably this value is similar to the bright-dark splitting due to the exchange interaction measured in GaAs/AlGaAs quantum wells [142,143]. For 2D perovskites significant variations of the exciton bright-dark splitting are also expected [146].

Finally we can note that the electromagnetic quantum fluctuations could also impact long-range exchange interaction between the electron and the hole in the exciton, as theoretically predicted both in bulk and 2D semiconductors [121,138,169].

3.5 Conclusion

In conclusion, we have shown in this Chapter that not only the exciton radiative lifetime is controlled by the optical environment in a 2D semiconductor but the bright-dark exciton splitting can also be modified by the potential induced by quantum fluctuations of the electromagnetic field. All these results show that the excitons in semiconductor nanostructures are very sensitive probes of the local vacuum field. The control of the bright-dark splitting demonstrated here should apply to any semiconductor nanostructures.

Chapter 4 Spin-valley Pumping of Resident Electrons in WSe₂ and WS₂ Monolayers

In the previous Chapter, we have shown that the bright exciton radiative linewidth and the bright/dark exciton splitting can be tailored using quantum electrodynamics effects. In this Chapter, we will present now results on the spin-valley properties in WSe₂ and WS₂ monolayers.

Monolayers of transition metal dichalcogenides are ideal materials to control both spin and valley degrees of freedom either electrically or optically. Nevertheless, optical excitation mostly generates excitons species with inherently short lifetime and spin-valley relaxation time (see **Figure 1.19**). In this Chapter, we demonstrate a very efficient spin-valley optical pumping of resident electrons in *n*-doped WSe₂ and WS₂ monolayers. We observe that, using a continuous wave laser and appropriate doping and excitation densities, negative trion doublet lines exhibit circular polarization of opposite sign and the photoluminescence intensity of the triplet trion is more than four times larger with circular excitation than with linear excitation. We interpret our results as a consequence of a large dynamic polarization of resident electron spin using circularly-polarized excitation light. Spin-valley polarization up to 80% can be obtained.

This Chapter is organized with the following sections:

- 4.1 Spin-valley pumping in TMD monolayers
- 4.2 Investigated samples and experimental methods
- 4.3 X^{T-} & X^{S-} -bright trions and X_D^- dark trion in WSe₂ monolayers
- 4.4 Observations and results
 - 4.5 Discussion
 - 4.5.1 Possible mechanism of spin-valley pumping
 - 4.5.2 Circular-polarization of X^{T-} and X^{S-} trions
 - 4.5.3 Discussion on PL intensities for circular and linear excitations
 - 4.6 Limitations of the bimolecular formation model
 - 4.7 Similar results in WS₂ monolayers
 - 4.8 Conclusion

4.1 Spin-valley pumping in TMD monolayers

As we already mentioned in the section 1.5, thanks to chiral optical selection rules, circularly polarized light can photo-generate carriers in either K^+ or K^- valleys with either spin up or spin down. Thus, TMD MLs were quickly considered as an ideal platform to control both spin and valley degrees of freedom with potential applications in quantum information processing. Nevertheless, light excitation usually yields neutral excitons and using these photo-generated species to encode spin or valley information is inherently limited by both their short recombination time (~ps) [80,83,170] (see Chapter 3) and their very fast spin relaxation time induced by electron-hole exchange interaction (~ps), as shown in **Figure 1.19** and **Figure 1.20**.

Recently other strategies have been proposed using longer lived excitonic species such as dark excitons, dark trions or interlayer excitons in heterostructures [171–173]. Another promising route consists in using resident electrons or holes in doped monolayers. Beyond its obvious advantage for future devices as compared to the manipulation of excitons, the spin-valley relaxation of resident carriers is prevented by spin-valley locking and is not governed by efficient exchange interaction like for excitons. Spin-valley relaxation times as long as 100's ns to several μ s for electrons and holes have been measured in WSe₂ using time-resolved Kerr experiments (see **Figure 1.22**) and spin-valley noise spectroscopy, as discussed in the section 1.5.

Nevertheless, very little is known about the polarization mechanism and the maximum degree of polarization one can reach for resident carriers (electrons or holes). Back *et al.* [174] showed that a near complete valley polarization of electrons can be reached in a *n*-doped MoSe₂ ML but it requires an out-of-plane magnetic field of 7 T that is incompatible with the development of future devices.

4.2 Investigated samples and experimental methods

We have fabricated a WSe₂ ML charge-tunable device with hBN encapsulation in the inert atmosphere of a glove box. Fabrication process, sample sketch and microscope image of the WSe₂ sample are detailed in section 2.1. The WS₂ ML sample is fabricated with hBN encapsulation using the same technique but without electrodes. The investigation on WS₂ sample have been done in collaboration with the group of Fabian Cadiz in Laboratoire PMC (Ecole Polytechnique).

By tuning the voltage bias between a back gate and the ML we can electrostatically dope the ML. The carrier density in the monolayer can be estimated using a simple plate capacitance model knowing the applied voltage (V), the hBN thickness t (210 nm in our device) and using a hBN dielectric constant of $\epsilon_{hBN} \sim 3$ [174,175]. The change of electron (hole) density Δn (Δp) is related to a change of bias voltage ΔV by Δn (Δp) = $\frac{\epsilon_0 \epsilon_{hBN}}{e * t} \Delta V$. Note that by convention, we choose that a positive (negative) bias leads to hole (electron) doping.

Alternatively, we can use the oscillations in the reflectivity spectrum of the bright exciton as a function of gate voltage observed at +9 T in the *p*-doped regime (see **Figure 4.1(b)**). As demonstrated in Ref. [176], these oscillations are due to the

interaction of the exciton with the quantized Landau levels of the hole Fermi sea (see the sketch of **Figure 4.1(a)**). The period of the oscillations ΔV_{LL} is related to the filling of one Landau level $P_{LL} = \frac{eB}{2\pi\hbar} = 2.18 \times 10^{11} \text{ cm}^{-2}$. We can thus calculate the hole density as a function of the gate voltage by: $\Delta p = \Delta V \frac{P_{LL}}{\Delta V_{LL}}$. This yields the same estimation of the carrier density as the one deduced from the capacitance model. The advantage of this method is that it does not require knowledge of material parameters (hBN thickness and dielectric constant).

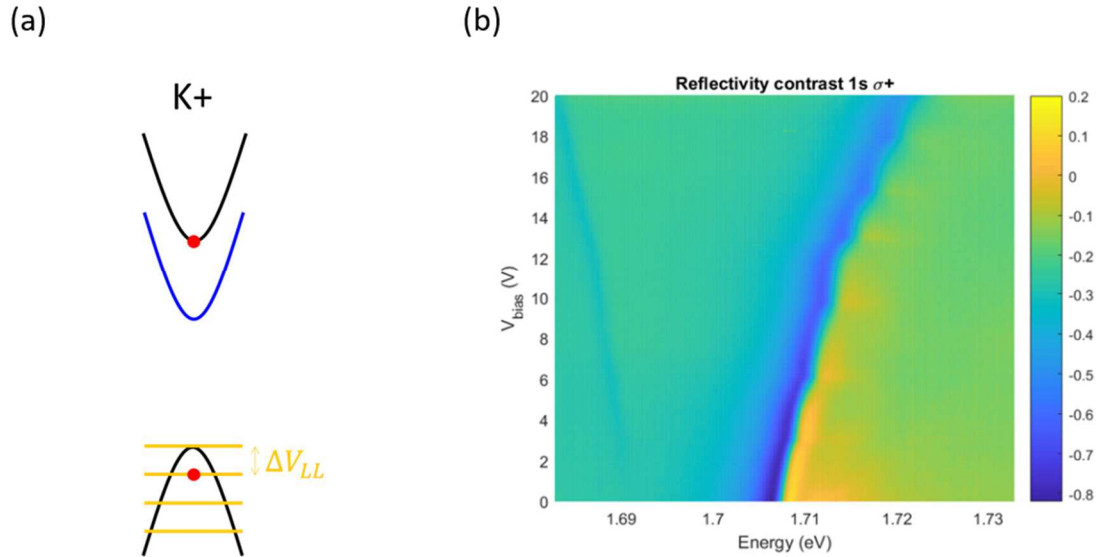


Figure 4.1 (a) Sketch of the band structure of the K^+ valley (in p -doped regime) at positive magnetic field showing the Landau levels. (b) First derivative of the reflectivity contrast with σ^+ detection as a function of the gate voltage at +9 T.

Polarization measurements are performed in the optical spectroscopy set-ups presented in section 2.3.4. For WSe₂, we use the cw 632.8 nm line of a He-Ne laser at $T= 4$ K. Unless otherwise stated, the excitation power is 5 μW . As already explained in Chapter 1, we restrict our study to moderate electron densities of a few 10^{11} cm^{-2} in the WSe₂ ML so that the simple three particles picture (*i.e.* trions) is equivalent to the many-body picture (*i.e.* Fermi polarons). For naturally n -doped WS₂ ML without charge tuning, a cw dye laser at a wavelength of 570 nm with an excitation power of 18 μW at $T= 20$ K has been used. Polarization measurements are performed in the optical spectroscopy set-ups presented in the section 2.3.4. The time-resolved photoluminescence (TRPL) measurements presented hereafter are performed in similar conditions: we used a ps-pulsed laser (Ti:Sa) at a wavelength of 695 nm for WSe₂, and an OPO at 570 nm for WS₂. The signal is detected by a Hamamatsu streak camera with a time resolution of ~2-3 ps.

4.3 X^{T-} & X^{S-} bright trions and X_D^- dark trion in WSe₂ monolayers

We first present in **Figure 4.2** the PL color plot as a function of bias in the charge tunable WSe₂ device in the *n*-doped regime. We recognize several exciton species including the bright neutral exciton (X_0), the dark neutral exciton (X_D), the bright trions (intervalley triplet X^{T-} and intravalley singlet X^{S-}) and the dark trion (X_D^-), in agreement with previous studies [86,87,91,156,157,177–180]. The spectral linewidth of X_0 at the neutrality point is as low as 2.5 meV (FWHM) vouching for the state-of-the-art quality of the sample [178].

In the following, we will first detail the three excitonic species: X^{T-} , X^{S-} and X_D^- , then focus on the electron doping density of $4 \times 10^{11} \text{ cm}^{-2}$ (see white dashed line in **Figure 4.2**) where X^{T-} and X^{S-} dominate the PL spectrum.

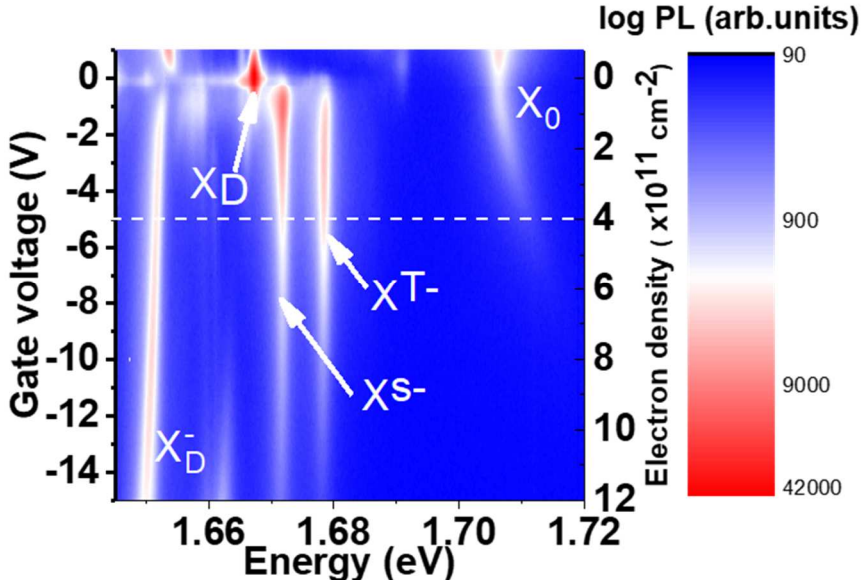


Figure 4.2 Excitonic states in *n*-doped WSe₂. PL intensity as a function of electron density. The excitation energy is 1.96 eV.

In the *n*-doped regime considered here, the Fermi level crosses the lowest conduction band. The two negative trions, intervalley trion X^{T-} and intravalley trion X^{S-} , appear at ~28 meV and ~35 meV lower than X_0 . For intervalley trion, it can be viewed in a simplified picture as a combination of a bright neutral exciton in one valley and an electron in the other valley, as shown in **Figure 4.3(a)**. In this case, the two constituent electrons have the same spin index, locating in the top and lower conduction bands in different valley. As a result, it is also called triplet. For intravalley trion, in contrast the two electrons reside in the same valley with opposite spin, as shown in **Figure 4.3(b)**. The four possible configurations of the negative trion and the respective associated polarized light are shown in **Figure 4.3**. The energy splitting between the two negative trion is around 7 meV, which was first discussed in Ref. [181] and also observed later in Ref. [156,157].

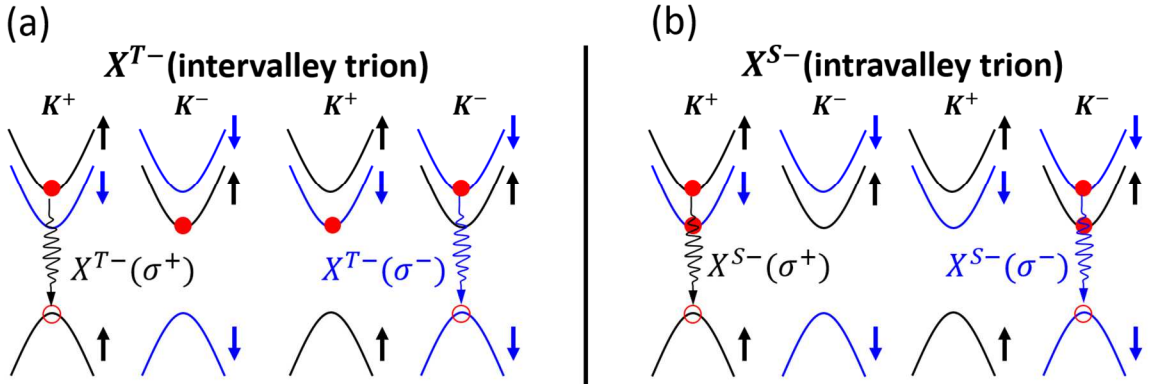


Figure 4.3 Configurations of the negative bright trions and their associated polarized light in monolayer WSe₂. (a) Two possible configurations for X^{T-} : $X^{T-}(\sigma^+)$ and $X^{T-}(\sigma^-)$. (b) Two possible configurations for X^{S-} : $X^{S-}(\sigma^+)$ and $X^{S-}(\sigma^-)$. Red filled (unfilled) circle represents electron (hole); The blue and black arrows represent the spin orientation: up and down.

In addition to the negative bright trions, the negative dark trion (X_D^-) is also a prominent feature, located at ~ 55 meV lower than X_0 and it is characterized by a g -factor of $|9.5|$ [158]. Figure 4.4 shows the two configurations of X_D^- in both valleys K^+ and K^- . In a simple three-particle picture, it consists of a dark exciton (X_D) in one valley and an electron in the other valley. Like spin-forbidden dark neutral exciton (X_D , presented in Chapter 1), it is also polarized out-of-plane dipole, *i.e.*, z-mode [182].

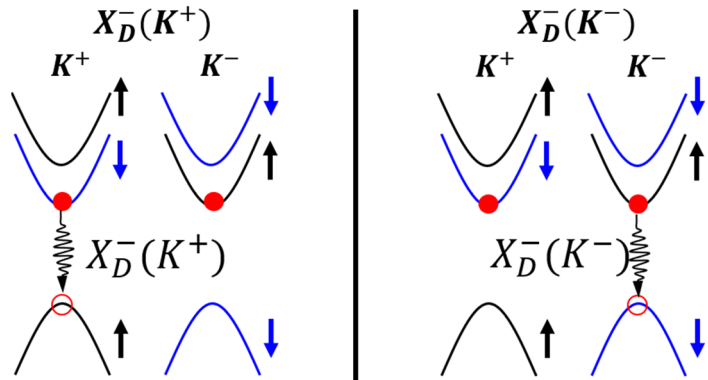


Figure 4.4 Schematic of the two configurations of the dark intravalley $X_D^-(K^+)$ and $X_D^-(K^-)$ Red filled (unfilled) circle represents electron (hole); The blue and black arrows represent the spin orientation: up and down.

4.4 Observations and results

Circular excitation and detection. Figure 4.5 presents the key results of this Chapter. In Figure 4.5(a), we show the photoluminescence spectra for both σ^+ and σ^- detections following σ^+ excitation. While the bright exciton X_0 exhibits a positive circular polarization below +20% as a consequence of the efficient long-range exchange interaction, the lines of the bright trion doublet show strong circular

polarization of opposite sign: +91% for X^{T-} and -40% for X^{S-} at the peak. Note that this negative polarization on the singlet has been observed elsewhere recently in state-of-the-art samples [178]. The dark trion X_D^- shows no circular polarization in agreement with its out of plane polarization [86,177,180].

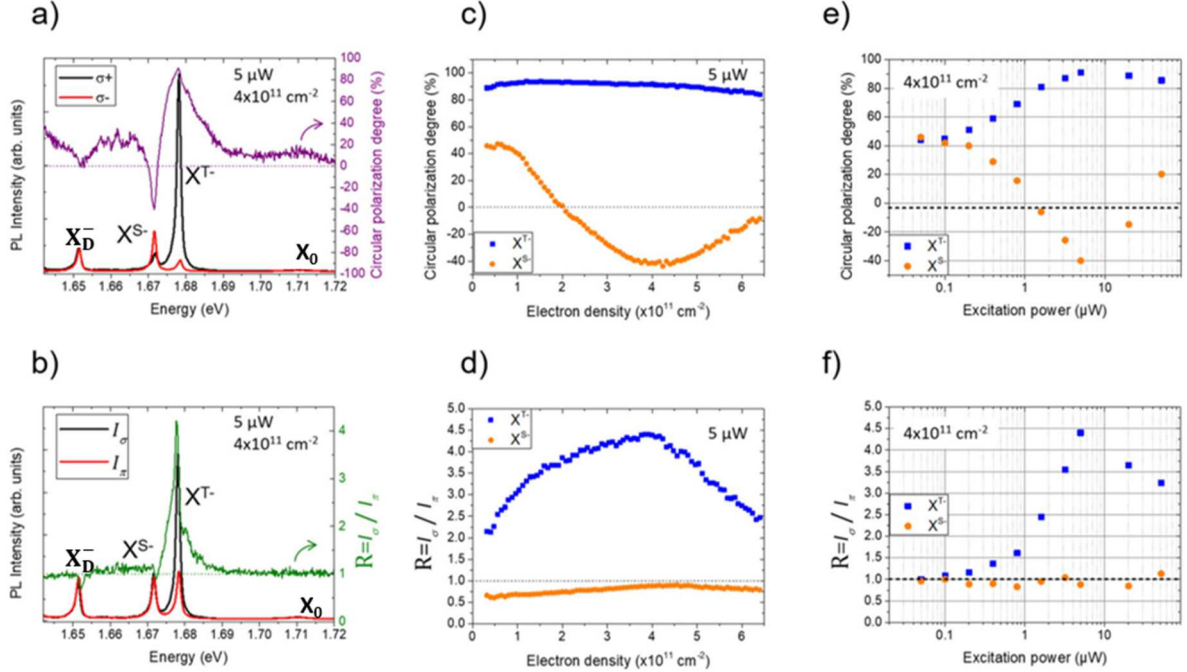


Figure 4.5 Experimental observations in n -doped WSe_2 . (a) Photoluminescence and circular polarization spectra for σ^+ and σ^- detections with σ^+ excitation. (b) Total photoluminescence spectra with circular excitation and linear excitation. (c) Circular polarization degree at the peak of triplet and singlet negative trions as a function of electron density. (d) Ratio of PL intensities between circular and linear excitations at the peak for both triplet and singlet as a function of electron density. (e) Circular polarization degree at the peak of triplet and singlet as a function of excitation power. (f) Ratio of PL intensities between circular and linear excitations at the peak for both triplet and singlet as a function of excitation power.

Circular and linear excitation. Then we switch to linear excitation π_X and measure both co-linear I_X and cross-linear I_Y intensities. We define the total PL intensity following linear excitation as $I_\pi = I_X + I_Y$ and the total intensity following circular excitation as $I_\sigma = I_{\sigma^+} + I_{\sigma^-}$. We show in **Figure 4.5(b)** both I_π and I_σ and the ratio $R = I_\sigma / I_\pi$. There is no difference in intensity for X_0 between linear and circular excitation (i.e. $R=1$). On the other hand, R reaches a very large value of 4.4 at the peak of X^{T-} and slightly below 1 for X^{S-} and X_D^- . In other words and surprisingly, the PL intensity of X^{T-} is more than 4 times larger when we excite with circularly polarized light. We present in **Figure 4.6** the same measurements performed on different spots of the sample and showing the same results. Moreover, we show in **Figure 4.7** that this result is independent from the direction of the linearly polarized excitation.

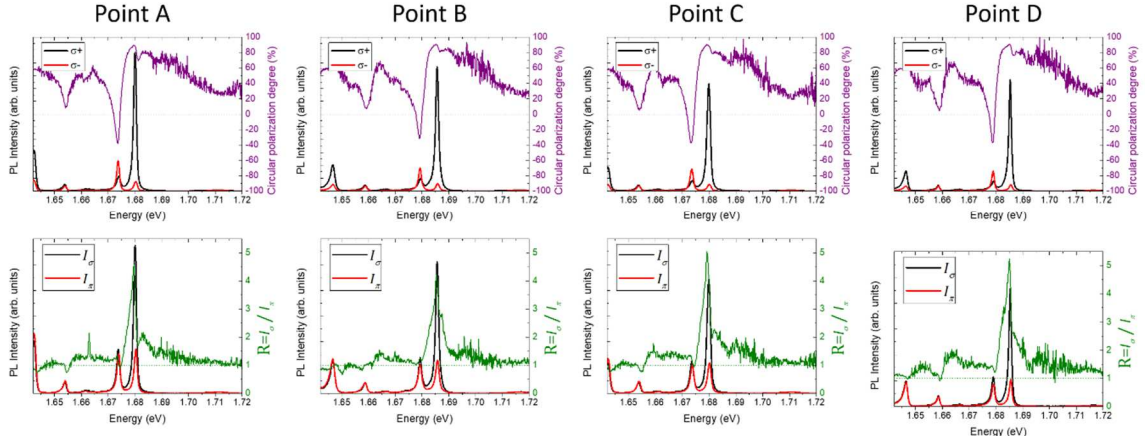


Figure 4.6 PL measurements on different sample spots. Photoluminescence and circular polarization spectra for σ^+ and σ^- detections with σ^+ excitation and total photoluminescence spectra with circular excitation and linear excitation on 4 different spots of the sample. The ratio is also displayed in green curves. The excitation power is 5 μW and the doping density is $4 \times 10^{11} \text{ cm}^{-2}$.

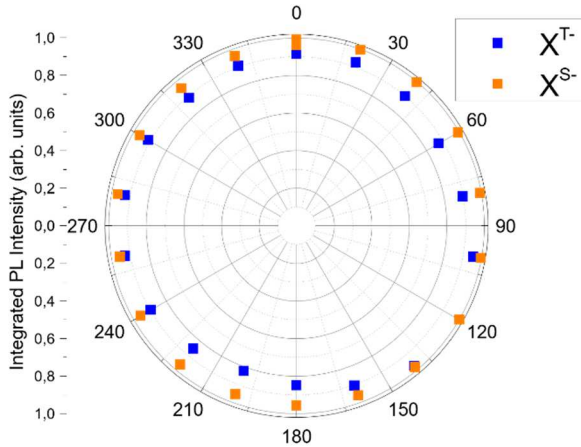


Figure 4.7 Integrated intensities of the triplet and singlet trions as a function of the angle of the linear excitation. Excitation power is 5 μW and the doping density is $4 \times 10^{11} \text{ cm}^{-2}$.

Electron density and excitation power dependences. In **Figure 4.5(c)** and **(d)**, we show P_c and R measured at the emission peaks of the bright trion doublet as a function of electron density for a fixed excitation power of 5 μW . The very large positive polarization of X^{T-} is nearly constant while for X^{S-} it varies from positive at small doping to negative for densities above $2 \times 10^{11} \text{ cm}^{-2}$ and reaches the minimum value of -40% for $4 \times 10^{11} \text{ cm}^{-2}$. Concerning the ratio of PL intensities between circular and linear excitations (see **Figure 4.5 (d)**), it remains above $R=2$ in the whole investigated electron density range for X^{T-} and slightly below 1 for X^{S-} . Finally, we present in **Figure 4.5 (e)** and **(f)** the excitation power dependence at an electron doping density of $4 \times 10^{11} \text{ cm}^{-2}$. We clearly see that when we reduce the excitation power, P_c converges to a value around 50 % for both X^{T-} and X^{S-} and that R decreases and gets closer to 1 for X^{T-} , while it stays constant and close to 1 for X^{S-} .

4.5 Discussion

In the following, we will tentatively explain these results focusing on three clear observations:

- (i) the circular polarization of the triplet trion can reach very high positive values up to 90%.
- (ii) the circular polarization of the triplet and singlet trions are of opposite sign at sufficiently large doping level.
- (iii) the intensity of the triplet trion is more than 4 times larger with circular excitation than with linear excitation.

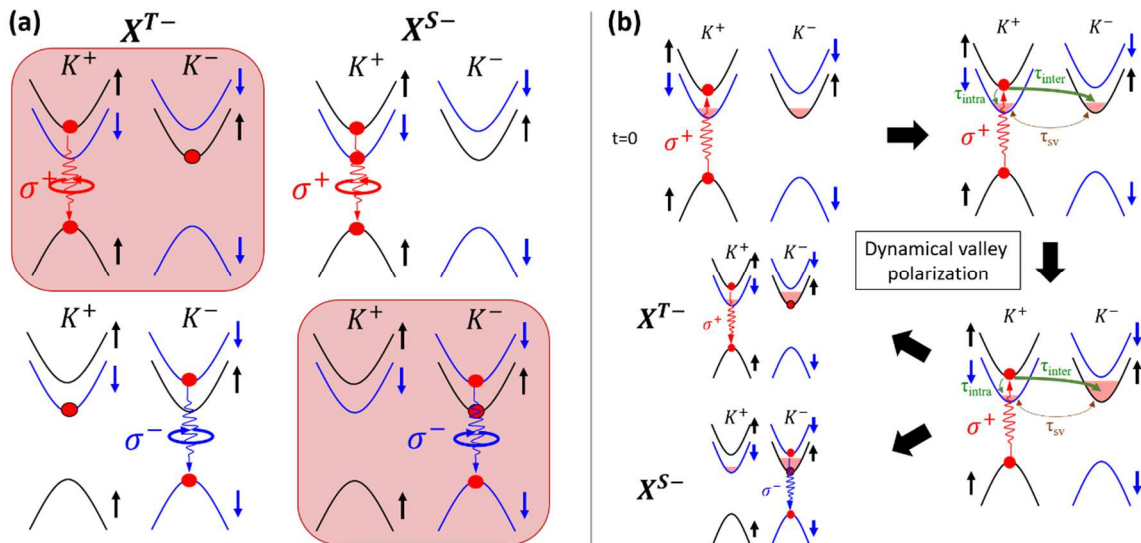


Figure 4.8 Spin-valley pumping mechanism. (a) Sketches of the three particle pictures of bright triplet X^{T-} and singlet X^{S-} negative trions with σ^+ and σ^- emission. The two majority trions following a σ^+ cw-excitation are highlighted in red. (b) Sketch of the dynamic polarization of resident electrons with σ^+ excitation. τ_{inter} (τ_{intra}) represents the intervalley spin-conserving (intravalley spin-flip) relaxation times of topmost electrons while τ_{sv} corresponds to the spin/valley relaxation time of resident electrons.

We show in **Figure 4.8(a)** the three-particle configurations of σ^+ and σ^- triplet and singlet trions. As already explained previously, a triplet trion consists of a photo-generated electron-hole pair (exciton made of an electron in the topmost conduction band and a missing electron in the same valley) bound to a resident electron in the bottom conduction band lying in the other valley. On the other hand, a singlet trion is composed of a photo-generated electron-hole pair bound to a resident electron in the same valley. Experimentally, we observe that when exciting with a σ^+ polarized laser the two strongest PL peaks are the σ^+ triplet trion and the σ^- singlet trion (see **Figure 4.5(a)**). These two configurations are highlighted in red in **Figure 4.8(a)**. In both cases the resident electron in the three-particle complex lies in the K^- valley. Thus, if we assume that the formation mechanisms of triplet and singlet trions are the same, the

opposite sign of polarization of triplet and singlet trions can only be explained by a larger population of resident electrons in the K^- valley as compared to the K^+ valley; *i.e.* by spin-valley pumping of resident electrons with spin up in K^- valley using σ^+ -polarized light.

4.5.1 Possible mechanism of spin-valley pumping

We propose in **Figure 4.8(b)** a mechanism that dynamically polarizes the resident electrons, in a manner analogous to dynamic spin polarization in conventional semiconductors [183–185].

Without light excitation and magnetic field, the densities of resident electrons are similar in the K^+ and K^- valleys. By continuously exciting with σ^+ polarized light, electrons are photo-generated in the conduction-band top valley of K^+ . These electrons are either free or bound to photo-generated holes and can relax to the bottom conduction bands both in K^+ and K^- valleys through different mechanisms. Intravalley relaxation (time constant τ_{intra} in **Figure 4.8(b)**) requires an electron spin-flip whereas intervalley relaxation (time constant τ_{inter} in **Figure 4.8(b)**) conserves the electron's spin. When energy relaxation is governed by electron-phonon interactions, spin-conserving relaxation is associated to the gradient of the spin-independent component of the crystal potential, while spin-flip interactions are associated to the spin-orbit interaction component. As long as the electronic states are not strongly spin-mixed, the spin conserving processes are typically stronger, resulting in faster momentum relaxation compared with spin relaxation (*i.e.* $\tau_{inter} < \tau_{intra}$). Recently, He *et al.* analyzed the dark trions' polarization in a WSe₂ ML and showed that spin-conserving intervalley relaxation, mediated by zone-edge phonons, is indeed stronger than spin-flip intravalley relaxation that is mediated by zone-center phonons [178]. Consequently, the electron population in the bottommost K^- conduction band becomes larger than the electron population in the bottommost K^+ conduction band upon excitation by a circularly polarized light σ^+ (*i.e.*, valley polarization).

Under cw-excitation, the mechanism of **Figure 4.8(b)** is repeated multiple times resulting in a dynamical buildup of valley polarization. This dynamical valley polarization is sustainable if the generation rate of photo-excited electron-hole pairs is faster than the rate at which electrons reestablish thermal equilibrium between the bottommost conduction-band valleys of K^+ and K^- through intervalley spin-relaxation (the spin-valley relaxation time τ_{sv} in **Figure 4.8(b)**). The latter is a relatively slow process at low temperatures, measured to be as long as 100's ns to several μ s in a WSe₂ ML [105–108] (as shown in **Figure 1.22**), because it is mediated by spin-flip intervalley transitions, which are forbidden to leading order by time-reversal symmetry [186,187]. Thus, even if the buildup of dynamical valley polarization is slow because the intervalley spin-conserving relaxation (τ_{inter}) is not much faster than the intravalley spin-flip one (τ_{intra}), the attainable valley polarization can still be very large (we will give an estimate of ~80% in the following). We mention that other mechanisms of polarization transfer from photo-generated carriers to resident electrons have been proposed by Ersfeld *et al.* [188] and Fu *et al.* [189] considering differences in the recombination rates of indirect excitons and spin-forbidden dark

excitons or differences in the relaxation rates of singlet and triplet to the dark trions. In each scenario, the two ingredients are the same: creation of an asymmetry in the population of resident electrons and long spin-flip intervalley relaxation times.

4.5.2 Circular-polarization of X^{T^-} and X^{S^-} trions

Once we consider that resident electrons mainly populate the K^- valley, we can explain the very large polarization of the triplet trion and the negative polarization of the singlet trion. Before detailed discussion on the polarization of the two trions, we first assume that the bright trions are formed through the binding of photo-generated bright excitons with a resident electron (*i.e.* a bimolecular formation [190]).

Before entering the detail of this model, we make two other assumptions:

(1) Electron density is much larger than the photo-generated exciton density. This assumption can exclude that the trion can importantly affect the population of resident electrons, justifying the circular polarization of the two trions is a “probe” of the polarization of the resident electrons. This assumption can be justified as following:

We can estimate the density of photo-generated bright electron-hole pairs (or excitons) from the excitation power density, the absorption coefficient and the lifetime of photo-generated electron-hole pairs. We have:

$$N_X = \frac{P_S \times \tau \times \alpha}{E_{photon}}$$

where P_S is the excitation power density (500 W.cm⁻² for a power of 5 μ W and a spot size of 1 μ m²), $E_{photon}=1.96$ eV for an excitation wavelength of 633 nm. A significant uncertainty comes from the absorption coefficient. For this non resonant wavelength, α was measured for free standing WSe₂ ML in the range 2-3% [11]. Assuming a lifetime τ of ~1 ps, this gives $N_X \sim 4 \times 10^7$ cm⁻², thus much smaller than the doping density.

(2) The spin relaxation of trions is much slower than their recombination lifetimes (*i.e.* the observed polarization in cw experiments correspond to the polarization at the trion formation). We give some experimental justifications below.

As already discussed in Chapter 1, the degree of circular polarization of a state in a cw experiment is usually given by:

$$P = \frac{P_G}{1 + \frac{\tau}{\tau_s}}$$

where P_G is the degree of circular polarization at the generation, τ is the lifetime of the state and τ_s is the spin (or valley) relaxation time (assuming here a single relaxation mechanism). In the simple model we will present below, we consider that the measured degrees of circular polarization for the triplet and the singlet directly reflect P_G . In other words we disregard the role of τ and τ_s . We give some experimental justifications below. We performed time-resolved photoluminescence in a second WSe₂ charge

tunable device and in the same WS_2 monolayer that will be presented in section 4.7. In WSe_2 we measured the lifetime of both triplet and singlet as function of the doping density and in WS_2 we measured the decay of the circular polarization. Results are presented in **Figure 4.9**. At very low doping regime ($\sim 1 \times 10^{11} \text{ cm}^{-2}$), the triplet and the singlet luminescence decay with a lifetime τ of the order of 10-20 ps. When the doping increases to a few 10^{11} cm^{-2} , the decay is strongly reduced to ~ 1 ps. We can have an idea of the spin relaxation time of trions τ_s by looking at the decay of the circular polarization of the triplet in WS_2 (**Figure 4.9(c)**). Our results suggest that this time is very slow (longer than 200 ps), thus much longer than the lifetime. In conclusion, it is reasonable to assume that $P \approx P_G$.

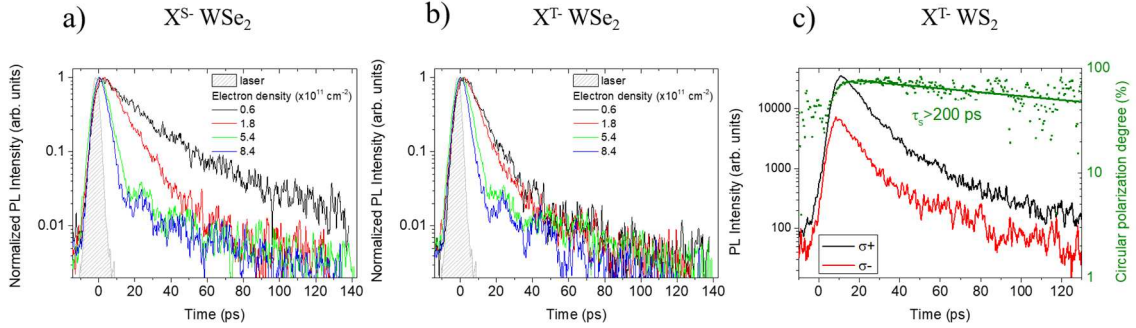


Figure 4.9 Time-resolved photoluminescence measurements of trions in WSe_2 and WS_2 monolayers. Time-resolved photoluminescence measurements of the (a) singlet and (b) triplet in a second WSe_2 charge tunable device showing the shortening of the lifetime when the electron doping increases. (c) Time-resolved photoluminescence measurements of the triplet in the WS_2 monolayer sample investigated in the section 4.7. In this measurement, we excite with σ^+ polarized light and detect both σ^+ and σ^- decays. In green we plot the circular polarization degree as a function of time. It shows that the spin/valley relaxation time of trions is much longer than the lifetime.

Now, we can estimate the circular polarization of the two trions based on the simple bimolecular formation model. The population of a given trion configuration $N_{X^{S,T-}}^{\sigma^{+,-}}$ is proportional to the population of the photogenerated bright exciton $N_0^{K^+,K^-}$ times the population of resident electrons $n_e^{K^+,K^-}$. Thus, we can write the degree of circular polarization for X^{T-} and X^{S-} as:

$$P_c(X^{T-}) = \frac{N_{X^{T-}}^{\sigma^+} - N_{X^{T-}}^{\sigma^-}}{N_{X^{T-}}^{\sigma^+} + N_{X^{T-}}^{\sigma^-}} \propto \frac{N_0^{K^+} n_e^{K^-} - N_0^{K^+} n_e^{K^-}}{N_0^{K^+} n_e^{K^-} + N_0^{K^-} n_e^{K^+}} \quad (4.1)$$

$$P_c(X^{S-}) = \frac{N_{X^{S-}}^{\sigma^+} - N_{X^{S-}}^{\sigma^-}}{N_{X^{S-}}^{\sigma^+} + N_{X^{S-}}^{\sigma^-}} \propto \frac{N_0^{K^+} n_e^{K^+} - N_0^{K^-} n_e^{K^-}}{N_0^{K^+} n_e^{K^+} + N_0^{K^-} n_e^{K^-}} \quad (4.2)$$

we can also define the degree of polarization of the photo-generated bright exciton (hot photo-generated excitons; or unbound electron-hole pairs that eventually bind to resident electrons to form trions) as:

$$P_0 = \frac{N_0^{K^+} - N_0^{K^-}}{N_0^{K^+} + N_0^{K^-}} \quad (4.3)$$

and the degree of polarization of resident electrons as:

$$P_e = \frac{n_e^{K^+} - n_e^{K^-}}{n_e^{K^+} + n_e^{K^-}} \quad (4.4)$$

Combining the four equations we can show that:

$$P_c(X^{T-}) = \frac{\mathbf{P}_0 - \mathbf{P}_e}{\mathbf{1} - \mathbf{P}_0 \mathbf{P}_e} \quad (4.5)$$

$$P_c(X^{S-}) = \frac{\mathbf{P}_0 + \mathbf{P}_e}{\mathbf{1} + \mathbf{P}_0 \mathbf{P}_e} \quad (4.6)$$

Using the same model we can write the total PL intensities of triplet and singlet following circularly polarized excitation as:

$$I_{circ}(X^{T-}) \propto N_{X^{T-}}^{\sigma^+} + N_{X^{T-}}^{\sigma^-} \propto N_0^{K^+} n_e^{K^-} + N_0^{K^-} n_e^{K^+} \quad (4.7)$$

$$I_{circ}(X^{S-}) \propto N_{X^{S-}}^{\sigma^+} + N_{X^{S-}}^{\sigma^-} \propto N_0^{K^+} n_e^{K^+} + N_0^{K^-} n_e^{K^-} \quad (4.8)$$

For linear excitation, the total intensity is:

$$I_{lin}(X^{T-}) = I_{lin}(X^{S-}) \propto \frac{1}{2} (N_0^{K^+} + N_0^{K^-})(n_e^{K^+} + n_e^{K^-}) \quad (4.9)$$

Thus the ratio of intensities between circular and linear excitation simply write:

$$R(X^{T-}) = \frac{I_{circ}(X^{T-})}{I_{lin}(X^{T-})} = \mathbf{1} - \mathbf{P}_0 \mathbf{P}_e \quad (4.10)$$

$$R(X^{S-}) = \frac{I_{circ}(X^{S-})}{I_{lin}(X^{S-})} = \mathbf{1} + \mathbf{P}_0 \mathbf{P}_e \quad (4.11)$$

In **Figure 4.10**, we plot $P_c(X^{T-})$, $P_c(X^{S-})$, $R(X^{T-})$ and $R(X^{S-})$ as a function of P_0 and P_e .

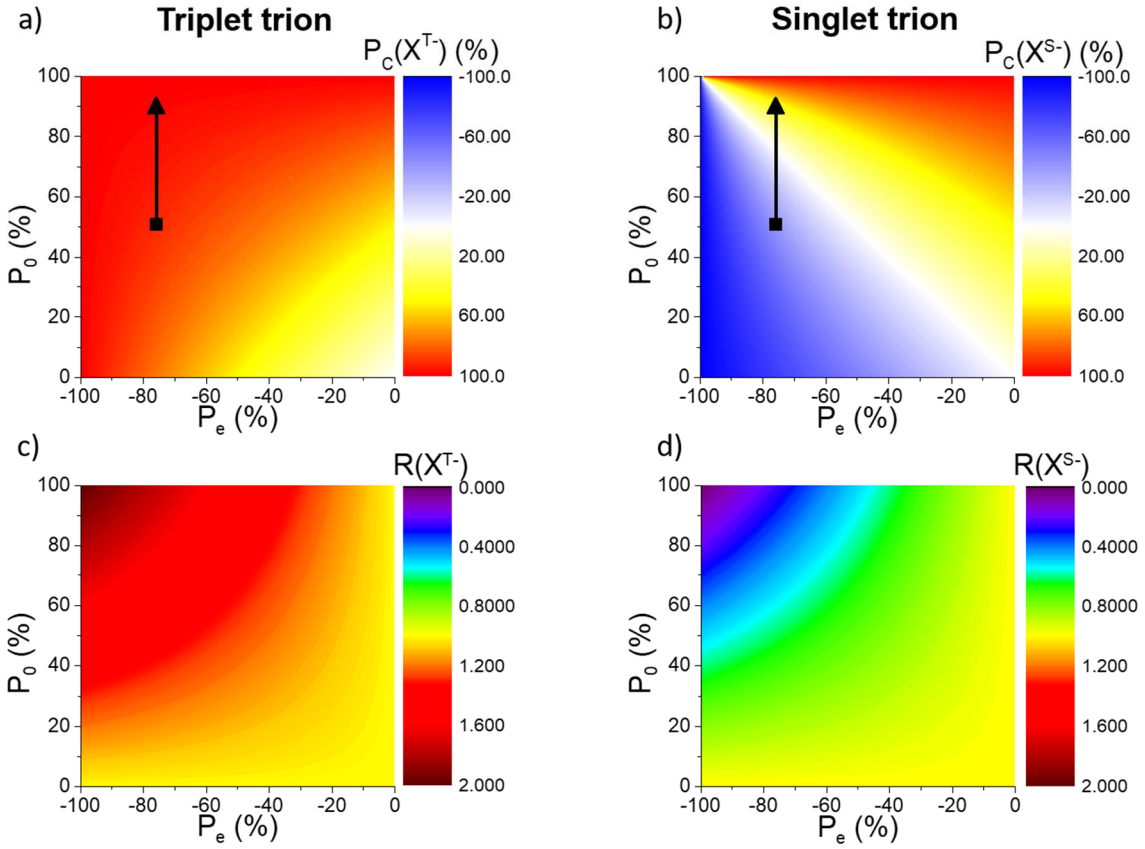


Figure 4.10 Bimolecular model. Calculated degrees of PL circular polarization P_c for (a) triplet and (b) singlet trions as function of the polarization of resident electrons (P_e) and the polarization of photogenerated excitons (P_0). (c) and (d) show the calculated ratio R for both triplet and singlet using the same model. The black data point corresponds to the regime of **Figure 4.5(a)** of the main text where $P_c(X^{T-})=91\%$ and $P_c(X^{S-})=-40\%$. The vertical arrow corresponds to the possible increase of P_0 when the doping decreases that may explain the results of **Figure 4.5(c)** where $P_c(X^{S-})$ turns positive and $P_c(X^{T-})$ remains very large.

The results of **Figure 4.5(a)** ($P_c(X^{T-})=91\%$ and $P_c(X^{S-})=-40\%$) match well with $P_0=51\%$ and $P_e=-76\%$; i.e. the resident electrons are strongly polarized in the K^- valley.

This simple scenario of dynamic polarization of electrons is consistent with the power dependence of **Figure 4.5(e)**. Indeed, when the excitation power decreases, the polarization of both X^{T-} and X^{S-} converge to the same value of around +50%. In this case, the photo-generation rate of electrons is not sufficient to create a significant polarization of resident electrons. Thus the polarizations of X^{T-} and X^{S-} mainly reflect the polarization of the exciton reservoir just before the formation of trions (i.e. the polarization of the hot excitons P_0). Furthermore, the doping density dependence of trions circular polarization of **Figure 4.5(c)** can be qualitatively explained. For doping densities above $4 \times 10^{11} \text{ cm}^{-2}$, the polarization in absolute value of both X^{T-} and X^{S-} drops because the density of photo-generated electrons is not large enough to fully

polarize the resident electrons. In **Figure 4.11**, we show that increasing the excitation power ($20 \mu\text{W}$) results in larger polarizations for larger doping densities. As compared to the measurements of **Figure 4.5(c)** and **(d)** (taken at $5 \mu\text{W}$), the minimum of $P_c(X^{S-})$ is shifted above $4 \times 10^{11} \text{ cm}^{-2}$, and the maximum of $R(X^{T-})$ is found around $5 \times 10^{11} \text{ cm}^{-2}$ as compared to $3-4 \times 10^{11} \text{ cm}^{-2}$ at $5 \mu\text{W}$. The overall shifts toward higher electron density is consistent with our scenario of dynamical polarization of resident electrons.

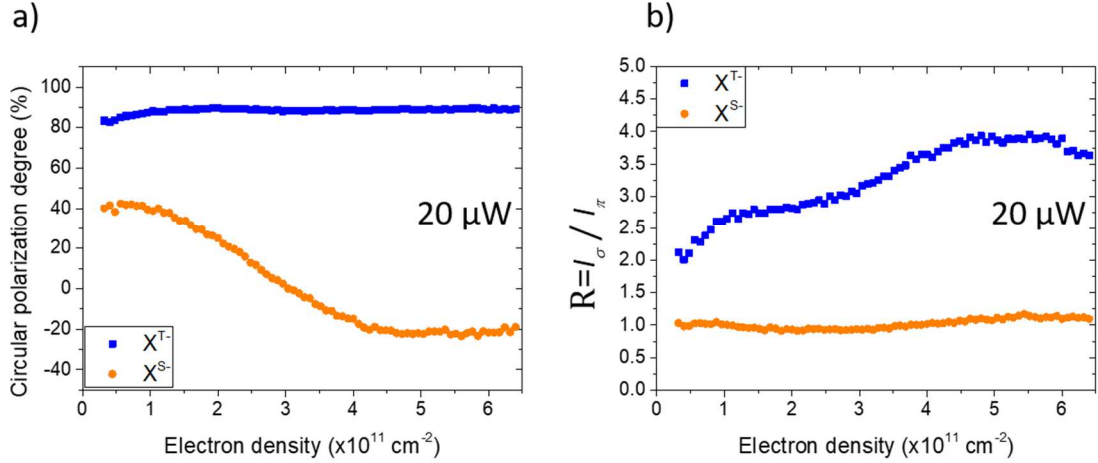


Figure 4.11 (a) Circular polarization degree at the peak of triplet and singlet negative trions as a function of electron density for an excitation power of $20 \mu\text{W}$. (b) Ratio of PL intensities between circular and linear excitations at the peak for both triplet and singlet as a function of electron density for an excitation power of $20 \mu\text{W}$.

4.5.3 Discussion on PL intensities for circular and linear excitations

We now discuss the third main result of our observations which is another consequence of the efficient spin-valley pumping of resident electrons: the PL intensity of the triplet trion is stronger with circular excitation than with linear excitation (**Figure 4.5(b)**). Note that this characteristic has been observed in GaAs-based alloys (GaAsN, GaAlAs) where it was attributed to spin dependent recombination via paramagnetic centers [191–193]. Here we attribute it to the efficient spin-valley pumping of resident electrons. Considering the same simple model based on the bimolecular formation of trions that we used to calculate the degrees of circular polarization, we can show that the ratio of PL intensities between circular and linear excitation are (detailed in section 4.5.2):

$$\text{Triplet} \quad R(X^{T-}) = 1 - P_0 P_e \quad (4.10)$$

$$\text{Singlet} \quad R(X^{S-}) = 1 + P_0 P_e \quad (4.11)$$

Using the values $P_0=51\%$ and $P_e=-76\%$ as determined previously we get qualitative agreement with our experimental results: the PL intensity of the triplet trion is larger with circular excitation (i.e. $R(X^{T-}) = 1.39 > 1$) and the PL intensity of the singlet trion is larger with linear excitation $R(X^{S-}) = 0.61 < 1$.

4.6 Limitations of the bimolecular formation model

Nevertheless, our simple model does not describe three quantitative aspects:

- (1) The ratio of the total intensities (triplet + singlet: $R(X^{T-} + X^{S-})$) using this model is equal to 1 while it is clearly larger than 1 in **Figure 4.5(b)**.
- (2) $R(X^{T-})$ cannot be larger than 2 in equation (4.10) while it is experimentally larger than 4.
- (3) The circular polarization of the singlet trion turns positive at low doping in **Figure 4.5(c)**.

The first limitation suggests that considering the subspace triplet+singlet is insufficient to fully explain our results (*i.e.* we have a deficit of luminescence for linear excitation). As shown in **Figure 4.5(b)**, we clearly see that the ratio $R(X_D^-)$ for the dark trion transition is also below 1; *i.e.* more intensity with linear excitation than with circular excitation. The dark trion formation path should thus be included.

The two other limitations (2) and (3) suggest alternative mechanisms for the formation of the trion species (bright and dark). Theoretical and experimental studies on the trion formation processes in TMD MLs are very scarce. Singh *et al.* measured the bright trion formation time in MoSe₂ ML using resonant excitation at the bright exciton transition energy [194] and linked it to the exciton-electron interaction. Here we use non-resonant excitation above the free carrier band gap of WSe₂. We can thus propose different formation mechanisms. The bright trions can be formed through the binding of bright excitons with resident electrons (*i.e.* the bimolecular process already considered above) but also through the binding of two electrons and a hole (*i.e.* a trimolecular process). In addition, singlet and triplet trions can be formed through the binding of a topmost conduction band electron with respectively a spin-forbidden dark exciton and a momentum-indirect exciton. Similar mechanisms should also be considered for the formation of dark trions in addition to the possible relaxation from bright trions. The dominant formation processes certainly depend on the doping density. For instance, the trimolecular process has been demonstrated as dominant in GaAs quantum wells at sufficiently high doping while the bimolecular one is dominant at lower doping densities [190]. The exact determination of the trion formation processes is beyond the scope of this thesis and will require additional theoretical work.

4.7 Similar results in WS₂ monolayers

Finally, we show that the manifestations of efficient spin valley-pumping of resident electrons in WSe₂ are also observed in WS₂. In **Figure 4.12**, we show the PL spectra, the circular polarization degree and the ratio $R = \frac{I_\sigma}{I_\pi}$ for a hBN-encapsulated WS₂ ML.

In this case, the ML is not gated but it is intrinsically slightly *n*-doped as proved by the presence of both triplet and singlet negative trions (X^{T-} and X^{S-}) in the luminescence spectra [195–197]. The results are very similar to slightly *n*-doped WSe₂: X^{T-} is strongly positively polarized (76% at the peak) and more intense with circular excitation than with linear excitation $R(X^{T-})=1.85$. We do not observe the negative polarization

for the singlet as in **Figure 4.5(a)** but $P_c(X^{S-})$ is slightly positive as observed for WSe₂ at smaller doping (**Figure 4.5(c)**). Similar power dependence is also observed and presented in **Figure 4.13**. The results are very similar to WSe₂ (**Figure 4.5(e)**): when the excitation power decreases, $P_c(X^{T-})$ and $P_c(X^{S-})$ converge to the same value (around 30% for WS₂) and $R(X^{T-})$ and $R(X^{S-})$ converge to 1.

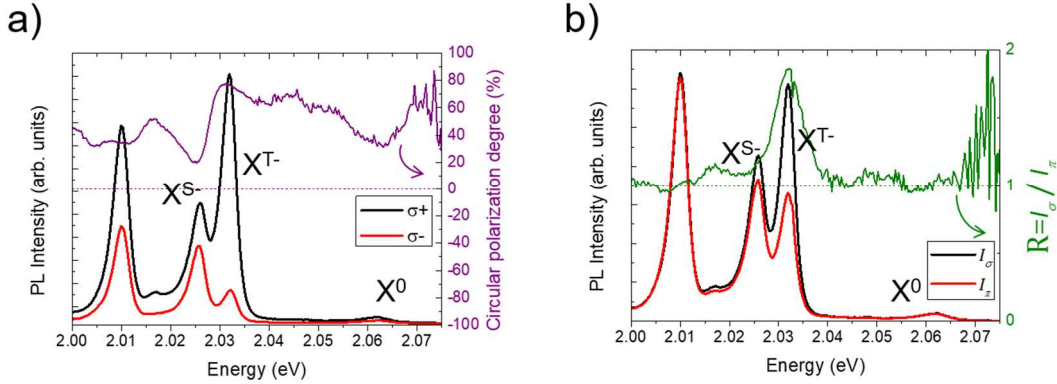


Figure 4.12 Experimental observations in *n*-doped WS₂. (a) Photoluminescence spectra of a WS₂ ML for σ^+ and σ^- detection with σ^+ excitation. (b) Photoluminescence spectra of a WS₂ ML with circular excitation and linear excitation. Excitation power is 18 μW .

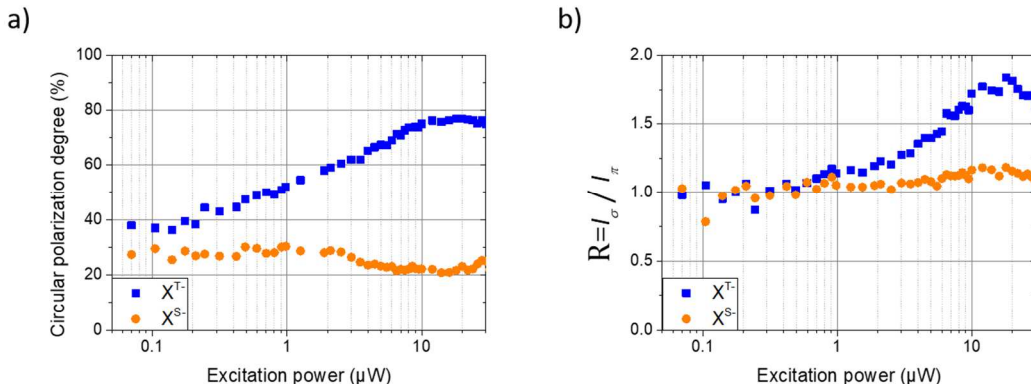


Figure 4.13 (a) Circular polarization degree at the peak of triplet and singlet as a function of excitation power. (b) Ratio of PL intensities between circular and linear excitations at the peak for both triplet and singlet as a function of excitation power.

4.8 Conclusion

In summary, we demonstrated very efficient spin-valley pumping of resident electrons in both WSe₂ and WS₂ monolayers using circularly polarized light. This process manifests as a large positive circular polarization of the triplet trion, a negative polarization of the singlet trion and a large increase of the triplet trion PL intensity with circular excitation as compared to linear excitation. Interestingly, these results demonstrate that circularly polarized excitation photo-generates electron-hole pairs in one valley and dynamically polarizes resident electrons in the opposite valley. This work could thus be an important step towards the development of valleytronic devices based on TMD MLs.

Chapter 5 Optical Detection of Long Electron Spin Transport Lengths in WSe₂ Monolayers

In the previous Chapter, we have demonstrated very efficient spin-valley pumping of resident electrons in both WSe₂ and WS₂ monolayers using cw circularly polarized light. In other words, we can create spin-valley polarized resident electrons in monolayers. In this Chapter, we are going to measure the lateral spin diffusion lengths of these resident electrons through a spatially-resolved optical pump-probe experiment. The lateral transport of spin-valley polarized electrons is measured over very long distances (tens of micrometers) in a single WSe₂ monolayer. By locally pumping the Fermi sea of 2D electrons to a high degree of spin-valley polarization (up to 75%) using circularly-polarized light, the lateral diffusion of the electron polarization can be mapped out via the photoluminescence induced by a spatially-separated and linearly-polarized probe laser. Up to 25% spin-valley polarization is observed at pump-probe separations up to 20 microns. Characteristic spin-valley diffusion lengths of $18 \pm 3 \mu\text{m}$ are revealed at low temperatures. The dependence on temperature, pump helicity, pump intensity, and electron density highlight the key roles played by spin relaxation time and pumping efficiency on polarized electron transport in this monolayer semiconductor possessing spin-valley locking.

This Chapter is organized with the following sections:

- 5.1 Spin-valley locking effect in TMD monolayers
- 5.2 Investigated sample and experimental method
- 5.3 Protocol of measurement and data processing
- 5.4 Trions: probe of electron spin
- 5.5 Dependence on pump and probe power
- 5.6 Dependence on doping density
- 5.7 Measurements of the electron spin diffusion length
- 5.8 Pump helicity-dependent circular polarization of trions
- 5.9 Temperature dependence
- 5.10 Conclusion

5.1 Spin-valley locking effect in TMD monolayers

TMD ML such as MoS₂ have sparked a renewed interest in exploiting both spin and valley degrees of freedom, owing to the remarkable spin-valley locking effects that originate from their lack of inversion symmetry and strong spin-orbit coupling [198–201]. As explained in Chapter 1, this dictates that the spin and valley degrees of freedom for carriers in the band extrema (electron in the bottom conduction band or holes in the top valence band) are mutually protected; *i.e.* relaxation requires both a change of valley (for instance with a momentum-conserving phonon), and also a spin-flip¹. An important consequence is that electron or hole spin relaxation times can reach very large values – in the microsecond range [105,106,202]. One can expect that this spin-valley locking will also have a strong impact on the lateral transport of electron spin polarization [203]. However, very little is known about the spatial dependence of free carrier spin polarization in these TMD monolayers despite its crucial relevance for spin(valley)tronics applications using 2D materials [204–206]. Spatial mapping of lateral spin transport in these 2D layers is also important from the point of view of fundamental physics, as it should reveal critical information about possible magnetic phase transitions and valley-polarized collective states that have been theoretically predicted in electron- or hole-doped TMD MLs [207–209].

Spatial mapping studies of spin polarization are scarce since (1) in transport experiments, the fabrication of four-terminal nonlocal geometry devices is very challenging with a single TMD ML [210,211] and (2) in optical measurements, the properties are usually dominated by robust exciton complexes that are characterized by picosecond lifetimes and very limited diffusion lengths, *i.e.* typically $\sim 1 \mu\text{m}$ at low temperature [212–220]. Small spin diffusion lengths of holes L_s less than $0.1 \mu\text{m}$ were estimated from valley Hall effect measurements in a WSe₂ ML [221] whereas electron spin transport investigations in few-layer MoS₂ using a two-terminal spin-valve configuration geometry yielded $L_s \sim 0.4 \mu\text{m}$ [222]. The spin-valley diffusion properties have also been investigated in WS₂-WSe₂ bilayer heterostructure where the diffusion length is controlled by both inter-layer excitons and resident holes [223].

5.2 Investigated sample and experimental method

We use the same WSe₂ ML charge-tunable device mentioned in Chapter 4 to perform spatially-resolved pump-probe experiment. **Figure 5.1** presents a schematic of the pump-probe PL experiment performed on the device. We still restrict our study to moderate electron densities of a few 10^{11} cm^2 in WSe₂ ML as in the last Chapter. Continuous wave HeNe laser beams ($\lambda=632.8 \text{ nm}$) are used for both pump and probe. Using the same high numerical aperture objective, the two beams are focused on the sample at two different positions separated by a distance d . The pump beam is right circularly polarized (σ^+) whereas the probe beam is linearly polarized (σ_x). We detect both right (σ^+) and left (σ^-) circularly polarized luminescence triggered by the probe beam, as a function of the pump-probe separation d . The σ^+ circularly polarized light

¹ In the following of the text and for a sake of simplicity we will mainly use the term spin instead of spin-valley knowing that the two degrees of freedom are coupled.

can locally create spin polarized resident electrons under the pump spot as detailed in Chapter 4. The σ_x linearly polarized (much weaker excitation power compared to the pump) light serves as a probe to detect the circular polarization of the two trions under the probe spot, which is an indicator of the spin polarization of the resident electron. In the end, we can map out the spin polarization of the resident electron by varying the pump-probe distance d .

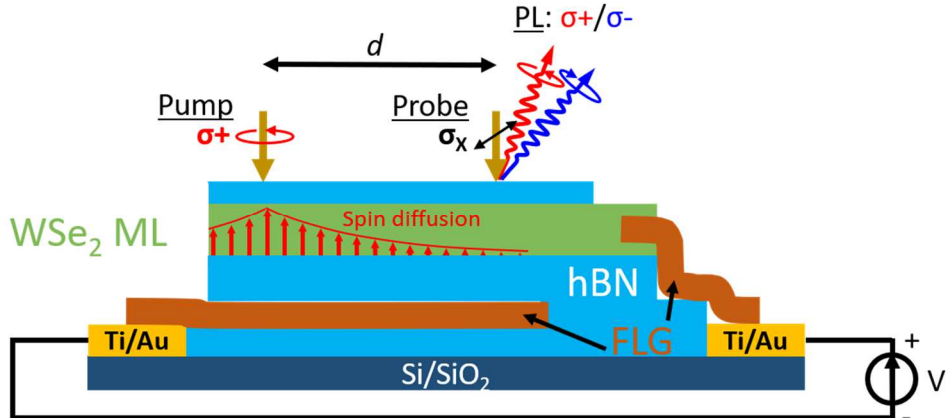


Figure 5.1 Sketch of the charge-tunable WSe₂ ML. Two laser spots (pump and probe) separated by a distance d , are focused on the sample. The pump is circularly polarized (σ^+) and dynamically polarizes the resident electrons in the K^- valley with spin up. This spin/valley polarization diffuses over long distances (sketched by the vertical red arrows representing the average electron spin along the direction perpendicular to the ML) and is detected by a linearly polarized (σ_x) probe. The circular polarization of the probe-induced X^{S-} -and X^T- PL provides a quantitative measurement of the polarization of the 2D electron sea at the location of the probe spot.

The experimental setup is sketched in **Figure 5.2**. Two He-Ne laser beams (pump and probe) are directed towards the sample through mirrors (M) and beam splitters (BS and BS1). Mirrors (M) and beam splitters (BS) are placed on kinematic mirror mounts to allow adjusting the distance between pump and probe spots on the sample. We chose to fix the probe spot and vary the separation by moving the pump spot on the sample without keeping a fixed angle between the two spots. The distance between the two spots is determined through an imaging system (not sketched). The polarizations of the pump and probe lasers were adjusted with a combination of linear polarizer, half wave plate ($\lambda/2$) and quarter wave plate ($\lambda/4$). We rotated the $\lambda/2$ and $\lambda/4$ plates to pre-compensate the polarization before the mirrors and beam splitters, to ensure that the pump and probe beams were circularly (σ^+) polarized and linearly polarized, respectively, before entering the cryostat. Unless stated otherwise, we fixed the pump and probe excitation powers to 5 μW and 200 nW, respectively. The photoluminescence signal was collected by the same microscope objective and was directed to a spectrometer equipped with a Si-CCD camera. In the detection path we placed a quarter wave plate ($\lambda/4$) and a linear polarizer. By rotating the $\lambda/4$ plate we selected either σ^+ or σ^- PL signal. Note that we used a second beam splitter (BS2) identical to BS1 as a polarization compensator. We adjusted the alignment to optimize the detection of the PL induced by the probe. Nevertheless, we could still detect a

significant part of the PL induced by the pump, especially for small pump-probe separations. To mitigate this issue, we used a subtraction protocol that is presented in the next section.

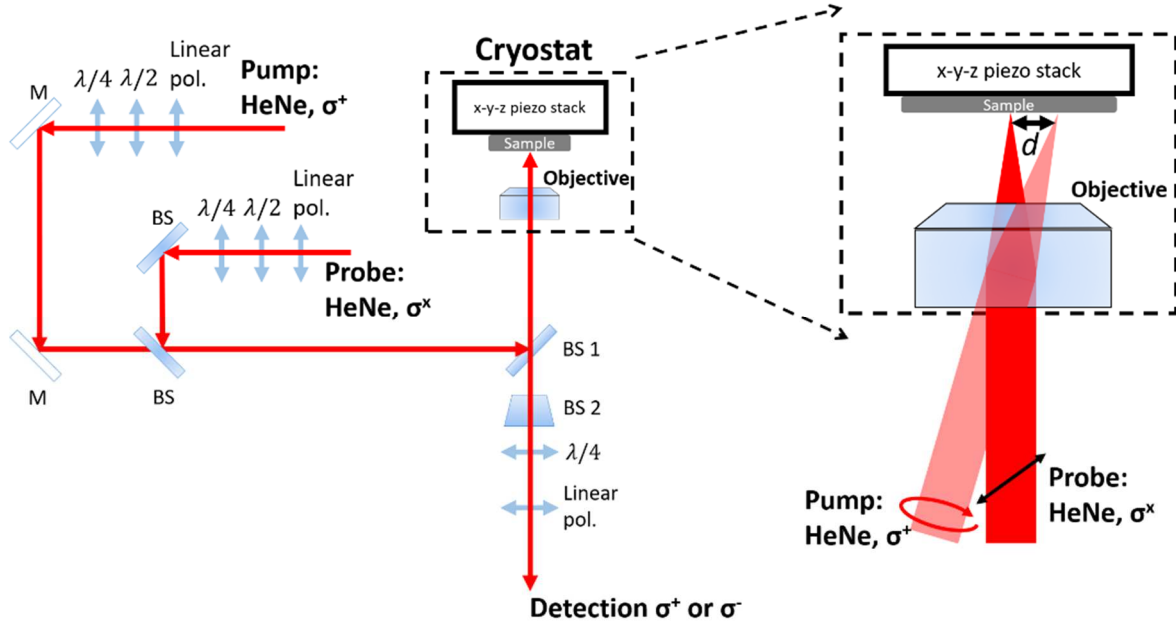


Figure 5.2 Sketch of the experimental setup.

5.3 Protocol of measurement and data processing

In order to eliminate the PL signal coming from the pump, we first measured the PL signal (σ^+ and σ^- detections) in the presence of both pump and probe, named $I_{\text{pump-probe}}^{\sigma^+}$ and $I_{\text{pump-probe}}^{\sigma^-}$. Then we performed the measurement only with the pump and recorded again σ^+ and σ^- at the detection. We name these signals $I_{\text{pump}}^{\sigma^+}$ and $I_{\text{pump}}^{\sigma^-}$. We obtained the net σ^+ and σ^- PL signals just under the probe position (shown in **Figure 5.3(c)**) by $(I_{\text{pump-probe}}^{\sigma^+} - I_{\text{pump}}^{\sigma^+})$ and $(I_{\text{pump-probe}}^{\sigma^-} - I_{\text{pump}}^{\sigma^-})$. The circular polarization is defined as:

$$P_c = \frac{(I_{\text{pump-probe}}^{\sigma^+} - I_{\text{pump}}^{\sigma^+}) - (I_{\text{pump-probe}}^{\sigma^-} - I_{\text{pump}}^{\sigma^-})}{(I_{\text{pump-probe}}^{\sigma^+} - I_{\text{pump}}^{\sigma^+}) + (I_{\text{pump-probe}}^{\sigma^-} - I_{\text{pump}}^{\sigma^-})}$$

Note that despite this protocol it is difficult to obtain reliable results for pump-probe separations less than $\sim 8 \mu\text{m}$ because the PL signal due to the pump laser is much larger than the signal due to the probe. Also, our scan range is limited to $\sim 25 \mu\text{m}$ because of the limited aperture of the objective.

5.4 Trions: probe of electron spin

Importantly the degree of circular polarization of the trion X^{T-} and X^{S-} PL can serve as a quantitative probe of the spin-valley polarization of the resident electrons, as demonstrated in the previous Chapter and as summarized below. Assuming that the trions are formed through the binding of photo-generated bright excitons with a resident electron (*i.e.* a bimolecular formation process [190]), the circular polarization of the triplet $P_c(X^{T-})$ and singlet $P_c(X^{S-})$ are simply related to the spin polarization of the resident electrons $P_e = \frac{n_e^{\uparrow K^-} - n_e^{\downarrow K^+}}{n_e^{\uparrow K^-} + n_e^{\downarrow K^+}}$ (where $n_e^{\uparrow K^-}$ and $n_e^{\downarrow K^+}$ are the populations of resident electrons with spin up (K^- valley) and spin down (K^+ valley) and the polarization of the photo-generated excitons $P_0 = \frac{N_0^{K^+} - N_0^{K^-}}{N_0^{K^+} + N_0^{K^-}}$ (where $N_0^{K^+}$ and $N_0^{K^-}$ are the populations of photo-generated bright excitons with carriers in the K^+ and K^- valleys). Note that in the previous Chapter we defined $P_e = \frac{n_e^{\downarrow K^+} - n_e^{\uparrow K^-}}{n_e^{\downarrow K^+} + n_e^{\uparrow K^-}}$ and here we redefine P_e to avoid negative spin polarization degree. Following this new convention, the spin polarization degree is now positive because there are more resident electrons in the K^- valley than in the K^+ valley following σ^+ excitation.). One obtains:

$$\text{Triplet} \quad P_c(X^{T-}) = \frac{P_0 + P_e}{1 + P_0 P_e} \quad (5.1)$$

$$\text{Singlet} \quad P_c(X^{S-}) = \frac{P_0 - P_e}{1 - P_0 P_e} \quad (5.2)$$

By measuring both $P_c(X^{T-})$ and $P_c(X^{S-})$ we can thus easily quantify the polarization of the resident electrons P_e .

We first characterize in **Figure 5.3(a)** the PL spectra emitted following a circularly polarized (σ^+) laser excitation (power=5 μW and electron doping density=4x10¹¹ cm⁻²). The circular polarization of the triplet trion X^{T-} PL reaches very large positive values, while it is negative for the singlet trion X^{S-} PL. As detailed in the previous Chapter, It is a direct consequence of a spin-valley pumping mechanism that dynamically polarizes the resident electrons in the K^- valley with spin up. Note that the efficiency of the spin-valley pumping mechanism depends on both excitation power and doping density. The electron density chosen here maximizes the electron spin polarization while keeping a sufficiently intense trion PL. Using the values of $P_c(X^{T-})$ and $P_c(X^{S-})$, we find that the polarization of resident electrons induced by the laser attains values as large as $P_e=76\%$ (*i.e.* the resident electrons mainly populate the lower spin-up conduction band in the K^- valley) while the polarization of the photogenerated excitons P_0 is 51%.

We then show, in **Figure 5.3(b)** the PL spectra emitted following a weak linearly polarized (σ_X) laser excitation (power=200 nW). As expected, there is no circular polarization of X^{T-} or X^{S-} PL because $P_0 = 0$ (linear excitation) and $P_e = 0$ (no spin/valley pumping mechanism for linear excitation).

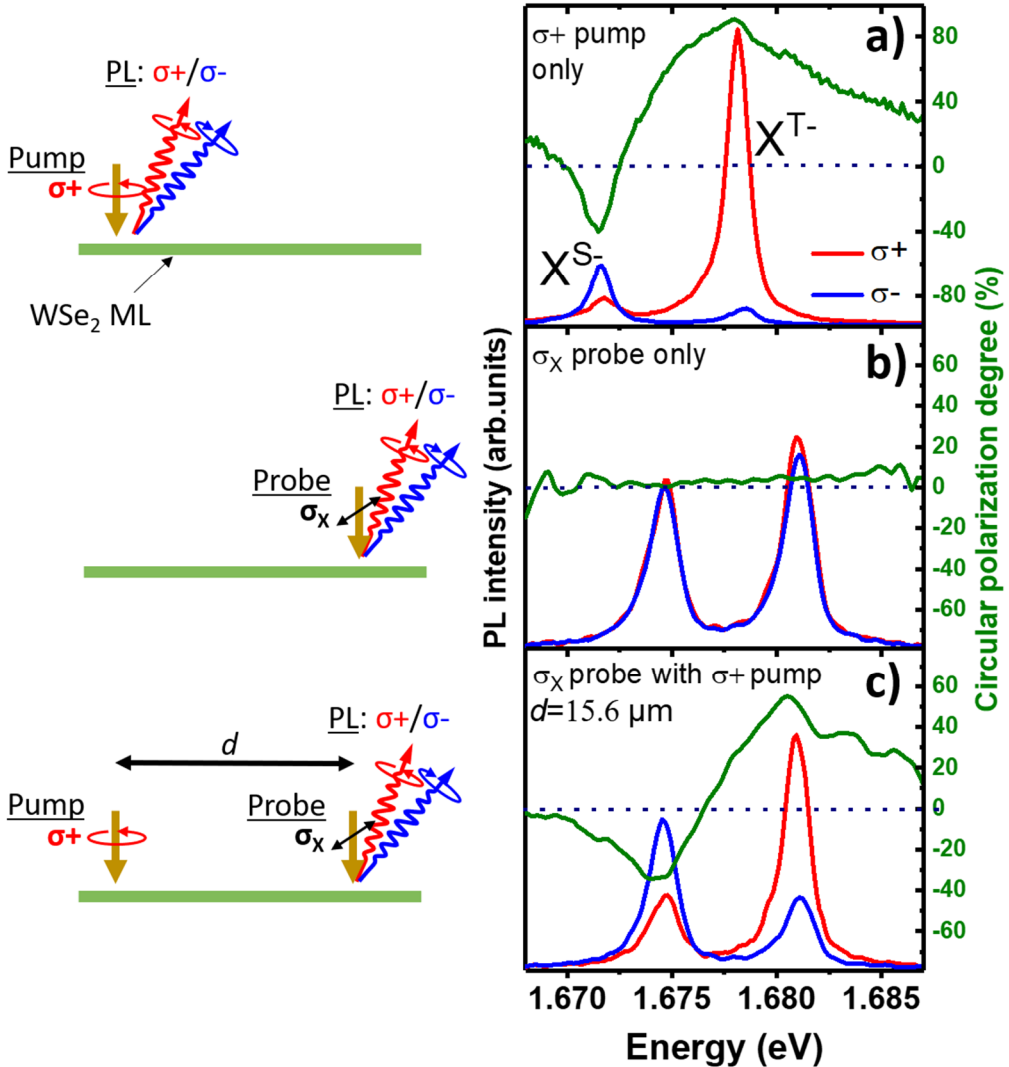


Figure 5.3 Right (σ^+) and left (σ^-) circularly-polarized PL spectra and corresponding circular polarization degree, in response to (a) the σ^+ pump only, (b) the linear σ_x probe only and (c) the σ_x probe in the presence of a σ^+ pump separated by distance $d=15.6 \mu\text{m}$. The strong circular polarization of the trion PL demonstrates that the resident electrons are strongly spin-valley polarized at the position of the probe laser. $T=5 \text{ K}$.

Figure 5.3(c) shows the first key result of this Chapter. It presents the PL spectrum induced by the weak σ_x laser (probe), but now in the presence of the σ^+ laser (pump) that is separated by a distance $d=15.6 \mu\text{m}$ (schematically shown in **Figure 5.1**). Remarkably, now we observe a very large circular polarization for both trions (~+50% for X^{T-} and ~-40% for X^{S-}). Because $P_0 = 0$ for the probe (linear excitation), this result directly reveals the polarization of the resident electrons at the location of the probe (i.e. $P_c(X^{T-}) = P_e$ and $P_c(X^{S-}) = -P_e$; see equations (6.1) and (6.2)). Because the linearly-polarized probe itself does not polarize the resident electrons (as shown above), this demonstrates that the spin polarization of the resident electrons induced by the pump propagates in the 2D layer plane and can be detected by measuring the circular polarization of trion PL below the probe. A key

advantage of this PL-based pump-probe experiment in comparison to well-known and powerful Kerr/Faraday rotation spin imaging methods [224,225] is that it allows to quantify, in absolute terms, the spin polarization of the electron Fermi sea. We show in the next two sections the dependence of the signal on both pump and probe power as well as the dependence with the doping density.

5.5 Dependence on pump and probe power

We present in **Figure 5.4** the circular polarization of X^{T-} - and X^{S-} - PL in the pump-probe experiment as a function of both pump and probe power, for a fixed pump-probe separation d and at $T=5$ K. As expected, the circular polarization drops smoothly when the pump power decreases. This is due to the decrease of the spin-valley pumping efficiency (*i.e.* there are not enough photogenerated carriers to spin-valley polarize the resident electrons). Opposite behavior is observed for the probe power dependence. When the probe power is too large, the photoexcited carriers generated by the probe tend to depolarize the resident electrons. At the beginning of this Chapter we present the results using a very small probe power of 200 nW, a value that minimizes the effect of depolarization by the probe while keeping measurable PL signal.

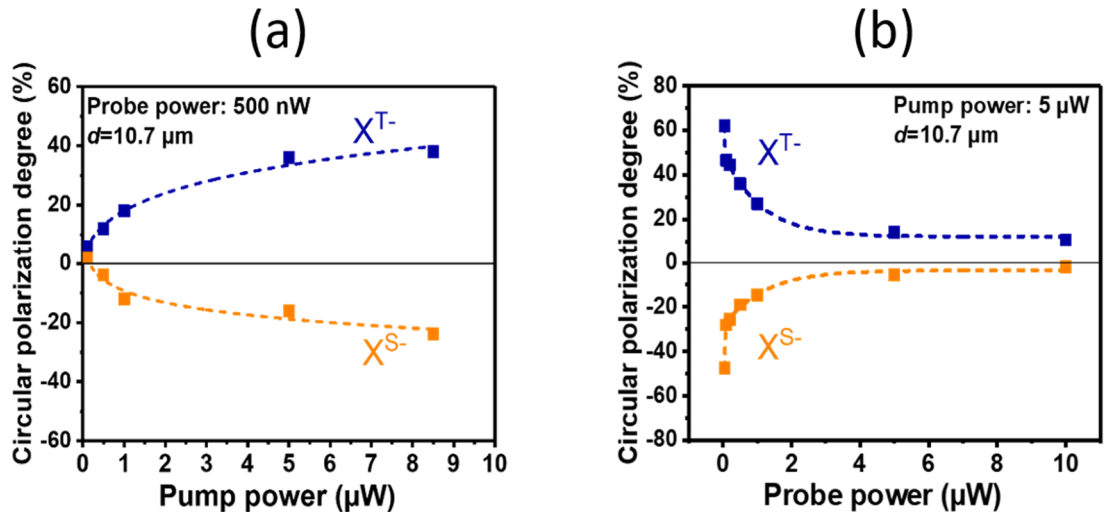


Figure 5.4 PL circular polarization of X^{T-} - and X^{S-} -induced by the probe for a fixed pump-probe separation as a function of (a) the pump power and (b) the probe power. Dashed lines are guides for the eye. $T=5$ K.

5.6 Dependence on doping density

We present in **Figure 5.5(a)**, the PL circular polarization induced by the probe as a function of the electron doping density for a fixed pump-probe separation. We observe that the measured spin-valley polarization drops when we decrease the doping density below $3 \times 10^{11} \text{ cm}^{-2}$ and also slightly decreases above $5 \times 10^{11} \text{ cm}^{-2}$. This variation is partially linked to the variation of the spin-valley pumping efficiency as shown below.

The spin-valley pumping efficiency can be traced back by measuring the polarization of both trions below the pump spot. The results are shown in **Figure 5.5(b)**, and are

very similar to our result in the previous Chapter. Using the two relations $P_c(X^{T-}) = \frac{P_0+P_e}{1+P_0P_e}$ and $P_c(X^{S-}) = \frac{P_0-P_e}{1-P_0P_e}$, we can extract the values of P_0 and P_e below the pump at each doping density (**Figure 5.5(c)**). We clearly see that the polarization of the resident electrons below the pump (noted P_e^0 in **Figure 5.5(c)**) drops at low doping density and also slightly decreases above $5 \times 10^{11} \text{ cm}^{-2}$ in agreement with the variation of the electron polarization measured below the probe (**Figure 5.5(a)**).

Despite this qualitative agreement, we would like to highlight that the drop of the electron polarization at low doping density is more drastic below the probe (it reaches 0% in **Figure 5.5(a)**) than below the pump (where it only decreases down to 40% in **Figure 5.5(c)**). This suggests that the drop of electron polarization below the probe may also be due to a decrease of the spin diffusion length at low doping densities. Further investigations are required to study this low doping regime.

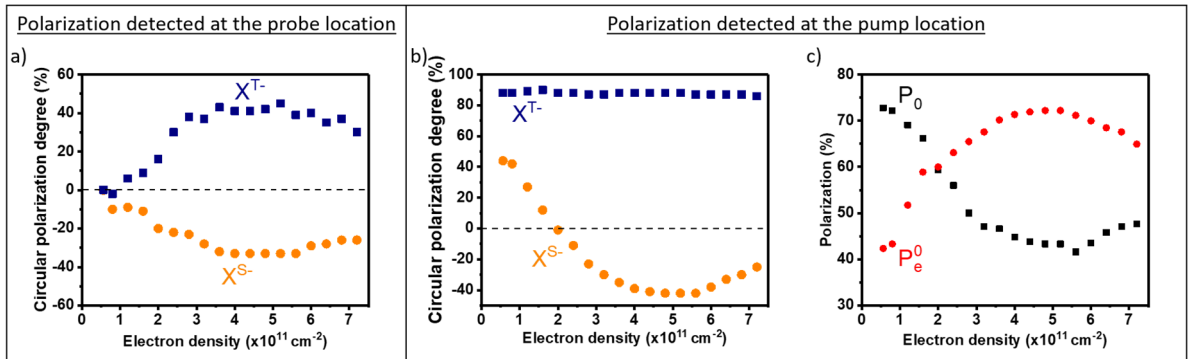


Figure 5.5 (a) PL circular polarization of X^{T-} and X^{S-} induced by the probe for a fixed pump-probe separation of $12.8 \mu\text{m}$ as a function of the doping density. Pump power: $12.5 \mu\text{W}$, probe power: 500 nW , $T=5 \text{ K}$. (b) PL circular polarization of X^{T-} and X^{S-} -generated below the pump spot as a function of the doping density. (c) Polarization of the photogenerated excitons P_0 and of the resident electrons P_e^0 generated below the pump spot calculated using the measurements shown in (b) and the two relations $P_c(X^{T-}) = \frac{P_0+P_e}{1+P_0P_e}$ and $P_c(X^{S-}) = \frac{P_0-P_e}{1-P_0P_e}$.

5.7 Measurements of the electron spin diffusion length

Figure 5.6 presents the main result of this work. It displays the dependence of the probe PL circular polarization of both trions as a function of the pump-probe separation d . A spatial decay of the spin polarization of resident electrons is clearly evidenced, but the resident electron polarization induced by the pump can propagate on length scales larger than $20 \mu\text{m}$. We find that the spin polarization decays approximately exponentially with a spin diffusion length of $L_s=18 \pm 3 \mu\text{m}$. This is among the longest spin diffusion lengths reported in semiconductors, despite a modest carrier mobility [226–228]. It is ten times larger than L_s measured in Silicon or p -type GaAs at low temperature, and is similar to the spin diffusion length measured in n -doped GaAs bulk [225,229–231] or quantum wells [232–234]. Remarkably, the spin diffusion length we measure here for a WSe₂ ML is very similar to the one determined in graphene

monolayers, which are usually characterized by a much larger electron mobility and lower spin-orbit coupling. Using ‘non-local’ spin valve geometries in graphene, spin diffusion lengths of 2 μm were measured and record values of $L_s=30 \mu\text{m}$ were more recently reported [235,236]. This underlines the key role played by the spin-valley locking effect in TMD MLs on carrier spin propagation.

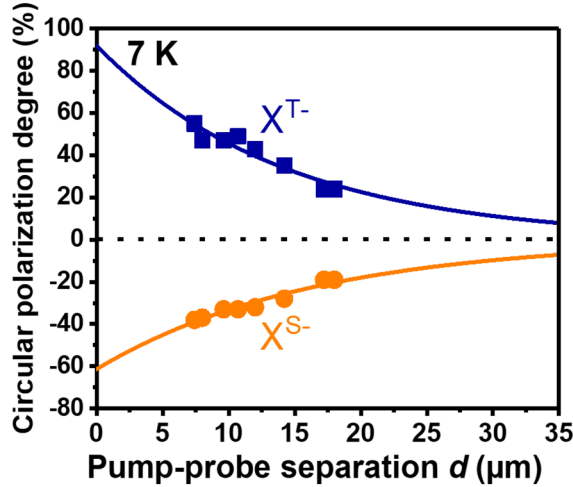


Figure 5.6 Circular polarization degree of the X^{T-} - and X^{S-} - trion PL, as a function of the pump-probe separation d . The solid lines are exponential fits.

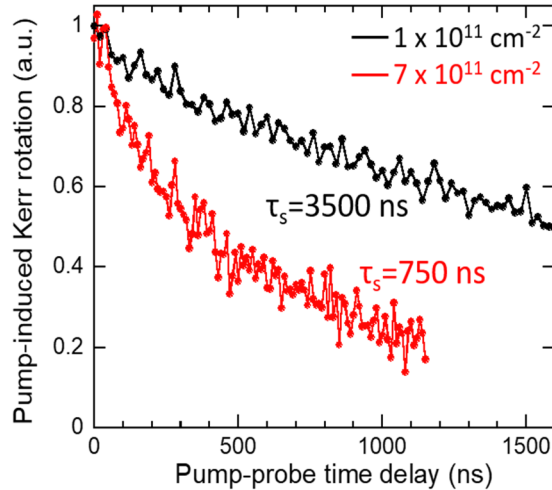


Figure 5.7 TRKR measurement of resident electron spin lifetimes, in an electrostatically-gated hBN/WSe₂ ML/hBN sample. The black and red curves were acquired for electron densities of approximately $1\times 10^{11}/\text{cm}^2$ and $7\times 10^{11}/\text{cm}^2$, and reveal electron spin-valley lifetimes of ~ 3 and $\sim 0.750 \mu\text{s}$, respectively, at a temperature of 5.8 K.

Note that the measured spin diffusion length of 18 μm is consistent with electron spin-valley relaxation time and electron mobilities recently measured in very comparable n -doped WSe₂ ML devices. In a simplified picture based on Einstein relations, we can infer a calculated spin diffusion length of $L_s = \sqrt{D_s \tau_s} \sim 10 \mu\text{m}$, using:

(1) the electron mobility μ_e recently measured in hBN encapsulated TMD MLs - typically $3000 \text{ cm}^2/(\text{V}\cdot\text{s})$ [226–228] and assuming that the spin diffusion coefficient is equal to the charge diffusion coefficient ($D_s = D_c \approx \mu_e kT/e \sim 1 \text{ cm}^2/\text{s}$) [234,236];

(2) the spin-valley relaxation time obtained from time-resolved Kerr rotation (TRKR): $\tau_s \sim 1 \mu\text{s}$ for a doping density of about $4 \times 10^{11} \text{ cm}^{-2}\text{m}$, measured by Scott Crooker group in Los Alamos), shown in **Figure 5.7** [105]. This measurement is conducted in an electrostatically-gated hBN/WSe₂ ML/hBN sample with very similar layer structure and optical quality in comparison to the gated hBN/WSe₂ ML/hBN sample studied in the spin diffusion measurements described above. The spatially-resolved studies of spin diffusion described above were performed at a background electron density of $4 \times 10^{11} \text{ cm}^{-2}$ (*i.e.*, midway between the two densities at which the TRKR studies shown in **Figure 5.7** new were explicitly performed), and at similar low temperatures. We therefore estimate that the spin-valley lifetime of the resident electrons in the spin diffusion studies is long, on the order of $1 \mu\text{s}$.

5.8 Pump helicity-dependent circular polarization of trions

Next, we demonstrate that the electron spin polarization detected at the probe location smoothly tracks the helicity of the pump beam as expected for spin diffusion process. **Figure 5.8** presents the circular polarization degree of X^{T-} and X^{S-} at the probe spot when the pump spot is continuously tuned from purely circular σ^+ to purely circular σ^- through elliptical and linear polarizations. As expected we observe a change of sign of PL circular polarization when the helicity of the pump is reversed, and a near-linear dependence of the electron spin polarization on the circular polarization degree of the pump excitation.

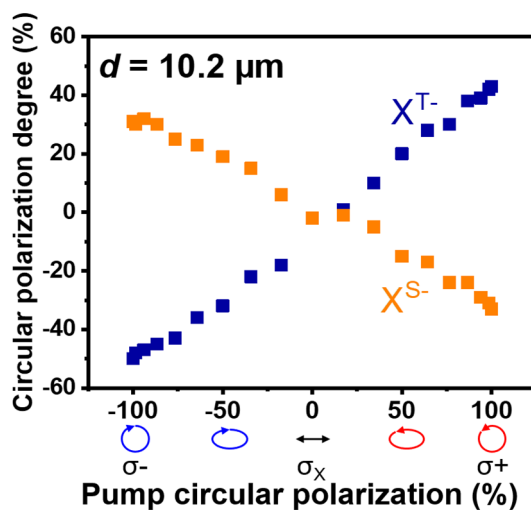


Figure 5.8 Circular polarization degree of X^{T-} and X^{S-} trion PL, at a fixed pump-probe separation, versus the pump helicity. $T=7 \text{ K}$.

5.9 Temperature dependence

Finally, we investigate the temperature dependence of the lateral transport of electron spin in the WSe₂ ML. **Figure 5.9(a)** shows the spin polarization of the resident electrons P_e as a function of the pump-probe separation, and at various temperatures. Because slightly different values of P_e can be inferred from the polarization of X^{T-} and X^{S-} (see **Figure 5.6**), we plot here an average between the two values ($P_e = \frac{P_c(X^{T-}) - P_c(X^{S-})}{2}$).

While electron spin transport can be clearly observed up to a temperature of 25 K, the amplitude of the spin polarization decreases compared to the measurements at T=5 K. For temperatures larger than 25 K, no spin polarization can be observed at a distance larger than 10 μm . It turns out that the main origin of this drop of the non-local spin polarization is the decrease of the efficiency of the spin pumping itself, *i.e.* the generation of spin polarized resident electrons by the pump. **Figure 5.9(b)** displays the temperature dependence of the resident electron spin polarization obtained from the measured X^{T-} and X^{S-} trions PL circular polarization induced by the pump and detected at the pump location [237] (same experiment as in **Figure 5.3(a)**, measurements shown in **Figure 5.10** and the raw data are plotted in **Figure 5.11**). We observe that the dynamical polarization of the resident electron decreases drastically between 5 and 30 K. This is a consequence of the decrease of the spin-valley pumping efficiency due itself to the decrease of the spin-valley relaxation time which drops by a factor ~ 10 in this temperature range, as measured recently by time-resolved Kerr rotation experiments on a similar gated and hBN-encapsulated WSe₂ ML [105].

We note that our spatially-resolved studies are consistent with lateral diffusion of spin polarized electrons in the WSe₂ monolayer, and do not show evidence of a spontaneous magnetic ordering in the spin-polarized electron gas, as was theoretically predicted to occur in TMD MLs as a consequence of strong exchange interactions [207–209,238]

Specifically, the measured non-local electron polarization varies smoothly with changes in pump intensity, pump helicity, and temperature, and does not show any abrupt discontinuities or saturation or hysteresis that would indicate a transition to an ordered ferromagnetic phase. Moreover, the approximately exponential spatial decay of the polarization signal is in line with expectations of a spin diffusion process, and does not show any sudden variations that might be expected from the formation of ferromagnetically-ordered domains.

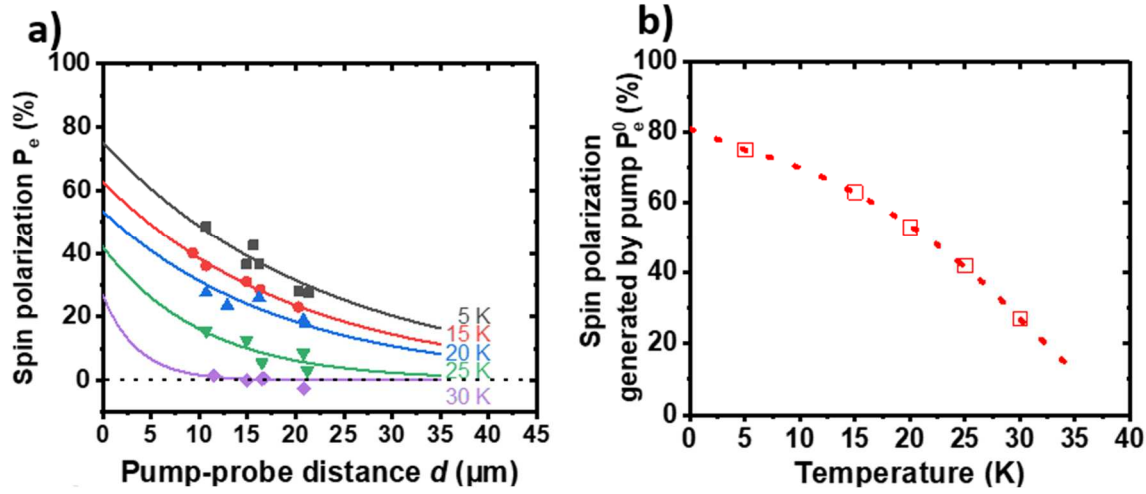


Figure 5.9 (a) Temperature dependence of the spin polarization of the resident electrons (P_e) at the probe location, versus pump-probe separation d . (b) Spin polarization generated below the pump spot (P_e^0) as a function of temperature, as extracted from the measurement of the circular polarization of X^{T-} and X^{S-} shown in **Figure 5.10** and **Figure 5.11**. The red dotted line is a guide for the eye. These values of P_e^0 are used to fit the results of panel a with monoexponential decays $P_e(d) = P_e^0 \exp(-d/L_S)$ that are shown by the solid lines in (a).

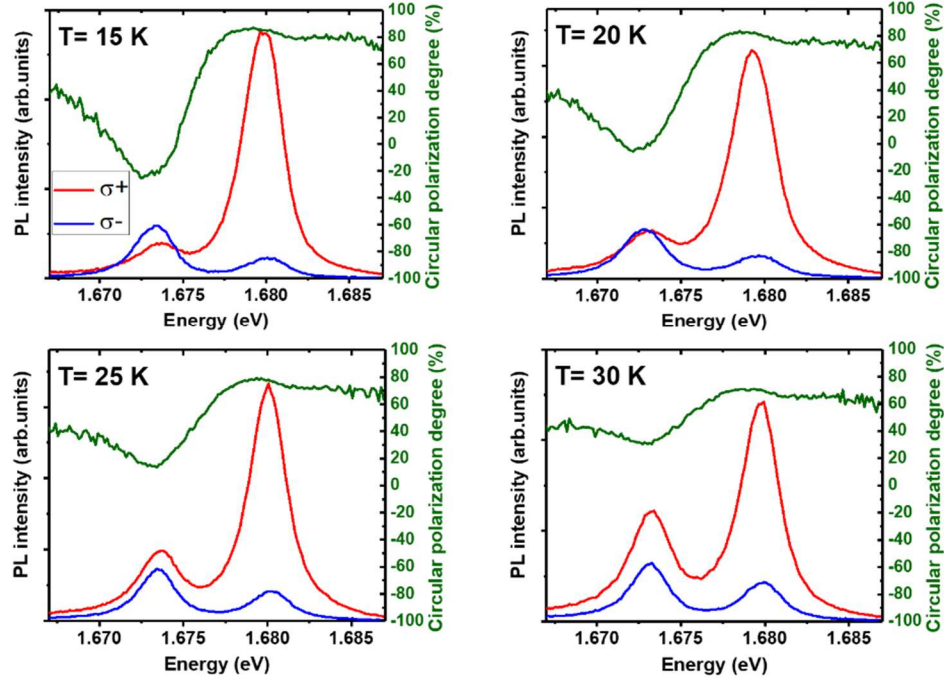


Figure 5.10 PL and circular polarization degree induced by the pump only (power $5 \mu\text{W}$) as a function of temperature. Measuring both circular polarization of the triplet $P_c(X^{T-})$ and singlet $P_c(X^{S-})$ triions and using their relation to the spin polarization of the resident electrons P_e and the polarization of the photo-generated excitons P_0 (namely $P_c(X^{T-}) = \frac{P_0 + P_e}{1 + P_0 P_e}$ and $P_c(X^{S-}) = \frac{P_0 - P_e}{1 - P_0 P_e}$), we extract P_e and P_0 as a function of temperature; results are summarized in **Figure 5.11**.

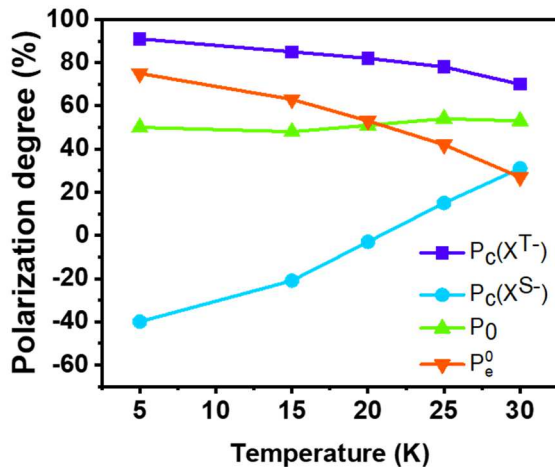


Figure 5.11 Polarization degrees induced by the pump only (power 5 μW) as a function of temperature.

5.10 Conclusion

In conclusion we have investigated the spin-valley diffusion of free electrons in a WSe₂ ML. In contrast to previous investigations in TMD MLs where the diffusion properties were dominated by short-lived exciton complexes, the efficient spin-valley pumping of resident electrons allow us to evidence transport of spin-valley information over very long distances, with a typical diffusion length of 18 μm . This is a consequence of the long spin-valley relaxation time induced by the unique spin-valley locking effect in this atomically-thin crystal.

Chapter 6 Measurement of Conduction and Valence Bands g -factors in WSe₂ Monolayers

In this Chapter, we are going to use the recombination features of different excitonic complexes to measure the conduction and valence bands g -factors in a WSe₂ ML.

The electron valley and spin degree of freedom in monolayer transition-metal dichalcogenides can be manipulated in optical and transport measurements performed in magnetic fields. In an optical spectroscopy experiment, the Zeeman splitting of the neutral exciton can be easily measured through a magnetic field with orientation perpendicular to the monolayer plane [239–247]. However, the separate contribution of the electron and hole g -factor, is inaccessible in this kind of measurements. Here we will present an original method that gives access to the respective contribution of the conduction and valence band to the measured Zeeman splitting. It exploits the optical selection rules of exciton complexes, in particular the ones involving inter-valley phonons. g -factors of electrons or holes can also be determined in transport measurements [248]. However, those experiments are performed in larger carrier density regime (usually larger than a few 10^{12} cm⁻²), where strong renormalization effects occur and induce strong modifications of the g -factors. The advantage of our technique is that it can yield a direct determination of single band g -factors (electron or hole) at low densities, *i.e.* without the collective effect corrections. We measure $g_{c1} = 0.86 \pm 0.1$, $g_{c2} = 3.84 \pm 0.1$ for the bottom (top) conduction bands and $g_v = 6.1 \pm 0.1$ for the valence band of monolayer WSe₂. These measurements are helpful for quantitative interpretation of optical and transport measurements performed in magnetic fields. In addition, the measured g -factors are valuable input parameters for optimizing band structure calculations of these 2D materials.

This Chapter is organized with the following sections:

- 6.1 Exciton g -factor in TMD monolayers
- 6.2 Investigated samples and experimental method
- 6.3 Photoluminescence spectra of a WSe₂ monolayer in the hole doping regime
- 6.4 Method to measure the conduction and valence bands g -factor and results
- 6.5 Measurements for a second device
- 6.6 Discussion
- 6.7 Conclusion

6.1 Exciton g -factor in TMD monolayers

The effective Landé g -factor of electrons, holes, and excitons in low-dimensional semiconductor systems has received considerable attention in the past 40 years since it provides precious information on the band structure [183,249–251]. The determination of the g -factor relies on measurement of the Zeeman energy splitting $\Delta E = g\mu_B B$, where μ_B is the electron's Bohr magneton and B is an external magnetic field which lifts the time inversion symmetry. Common techniques to measure the g -factor are electron spin resonance [252,253], Hanle effect [254], magneto-photoluminescence/absorption [144], spin quantum beats [255,256] or spin flip Raman scattering [257] experiments. It was first shown by Roth *et al.* that electrons in semiconductors can have an effective g -factor that differs substantially from the free-electron value $g_0 = 2$ as a consequence of the spin-orbit interaction (SOI), which couples the orbital motion with the spin degree of freedom [258].

Magneto-photoluminescence (Magneto-PL) or reflectivity measurements with out-of-plane magnetic fields were performed on ML-MoS₂, MoSe₂, MoTe₂, WS₂ and WSe₂ [239–247]. These experimental investigations yield the exciton g -factors, but do not give the respective contribution linked to the conduction band and valence band g -factors. **Figure 6.1** shows the valley Zeeman splittings of bright neutral exciton X_0 and trion X^- as function of out-of-plane magnetic field, which give a g -factor around 4 [241].

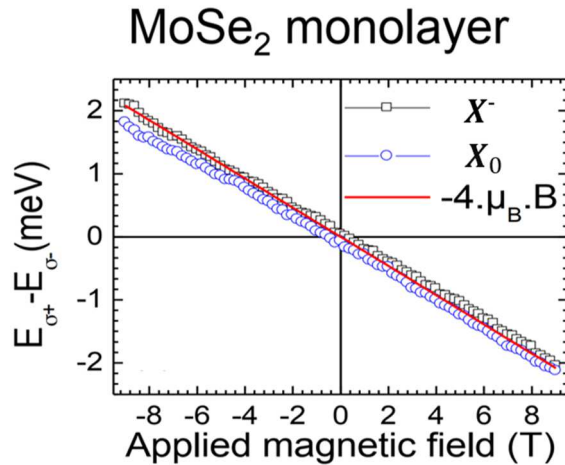


Figure 6.1 Energy difference of σ^+/σ^- component of neutral exciton and X_0 (blue circles) and trion X^- (black squares) in MoSe₂ ML as function of out-of-plane magnetic field. The function $-4\mu_B B$ is shown for comparison. Adapted from Ref. [241].

The Zeeman splitting between right and left circularly-polarized light components σ^+/σ^- (defined as $E_{\sigma^+} - E_{\sigma^-} = g\mu_B B$) yields a bright exciton g -factor close to $g \approx -4$ for most TMD MLs (except for MoS₂ ML). Surprisingly, this measured value is in agreement with a simple “atomic physics” model where the CB and VB g -factors result simply from the addition of three contributions, labelled by spin, valley and orbital terms [242,247,259]. However, the exciton g -factor with this approach just reflects the contribution of the VB orbital terms. As a consequence, no decisive information can be obtained on the CB or VB g -factor values. Moreover, this simple model usually fails to predict the carrier g -factors in other semiconductor structures (for instance the well-

known g -factor of holes in GaAs [241]). It has indeed been shown that accurate determination of the g -factor requires precise description of the band-structure electronic states and in particular the mixing induced by the SOI [260,261]. In addition, the measurement of both CB and VB g -factors (g_c and g_v) should provide valuable information on the electronic structure in TMD MLs, for which many unknowns persist. For example, the value of the effective mass in the CB is still under debate [262–265]. The knowledge of the single particle g -factor is also essential to interpret the magneto-transport experiments in which the large carrier density induces strong renormalization effects due to many-body interactions [248,263].

6.2 Investigated samples and experimental method

In this work, we use a charge-tunable sample similar to the one used in Chapters 4 and 5. The only difference is that the metallic contacts were done by e-beam lithography after the fabrication of the heterostructure. Same results have been obtained in the sample used in Chapter 4. **Figure 6.2** shows a small sketch and an optical image of the sample.

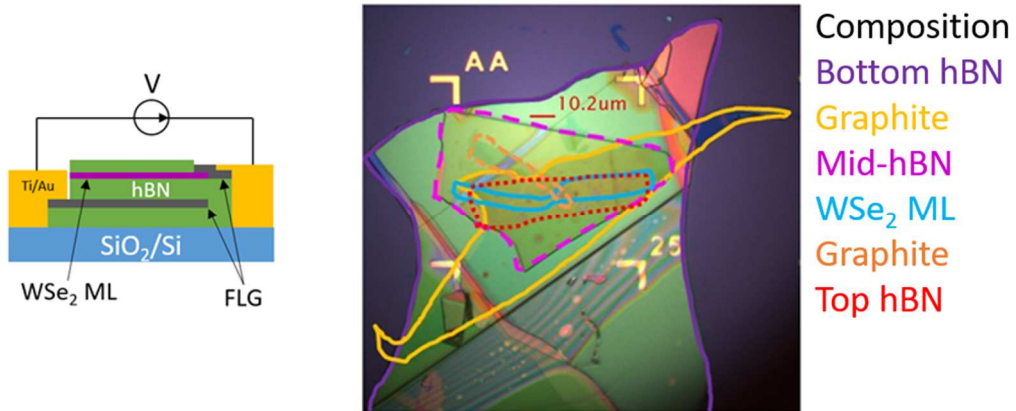


Figure 6.2 Sketch and an optical image of the sample.

Magneto-PL experiments at $T = 5$ K and in magnetic fields up to 9 T have been carried out in the confocal microscope setup mentioned in the section 2.3.5. The sample is excited by a HeNe laser (1.96 eV) with linear polarization and both circular σ^+ and σ^- polarized PL signals are detected using a liquid crystal retarder and an analyzer in the detection path. The average laser power is around 10 μW , which is still in the linear absorption regime.

6.3 Photoluminescence spectra of a WSe₂ monolayer in the hole doping regime

We first present low temperature ($T=5$ K) reflectivity contrast and PL intensity (shown in **Figure 6.3(a)** and **(b)**, respectively) as a function of the hole doping density (tuned by the applied voltage V). The estimation of the carrier density is presented in the

section 4.2. The neutrality region is easily identified in reflectivity when only the signature of the neutral exciton X_0 is seen (**Figure 6.3(a)**). When we increase the hole density, a clear signature of positively charged exciton X^+ (located ~ 20 meV below X_0 and formed by one electron in the upper conduction band and two holes of opposite spins, **Figure 6.4(a)**) is observed in agreement with previous reports [177,266–269]. Depending on where the electron is, X^+ is associated with circularly-polarized light (σ^+/σ^-). Another attractive peak in *p* type regime is the positively charged dark trion (X_D^+) (located ~ 52 meV below X_0 and formed with one electron in the lower conduction band and two holes of opposite spins, shown in **Figure 6.4(b)**). Similar to the dark exciton X_D in the neutrality regime (presented in the section 1.5), this dark trion has an out-of-plane dipole and recombine by emitting a z-polarized photon. Dark trions can also radiatively recombine through alternative pathways: phonon replicas.

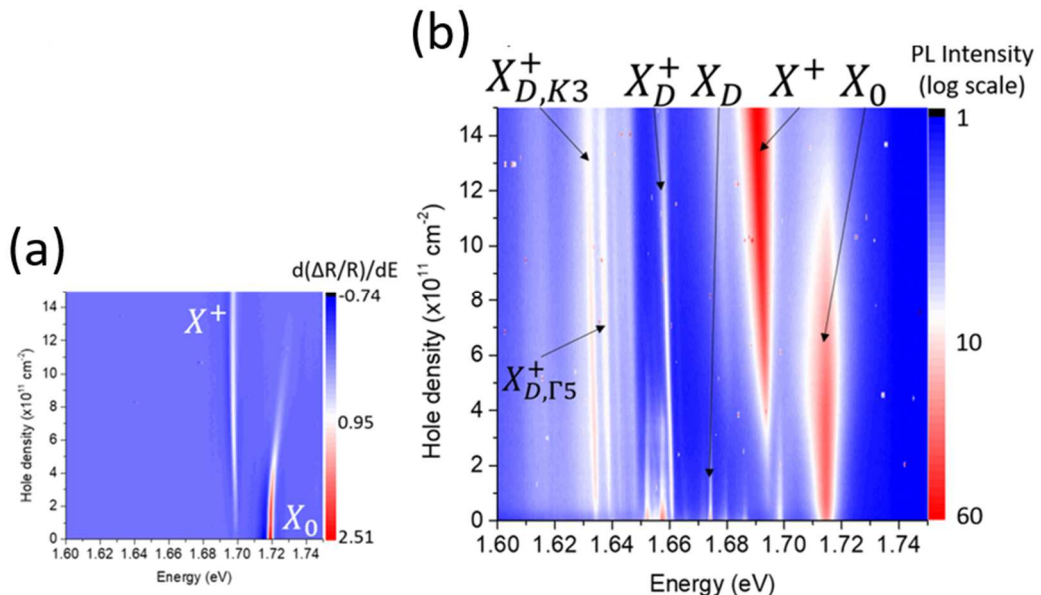


Figure 6.3 (a) First derivative of the reflectivity contrast and (b) photoluminescence intensity as a function of hole doping for a magnetic field $B=0$ T.

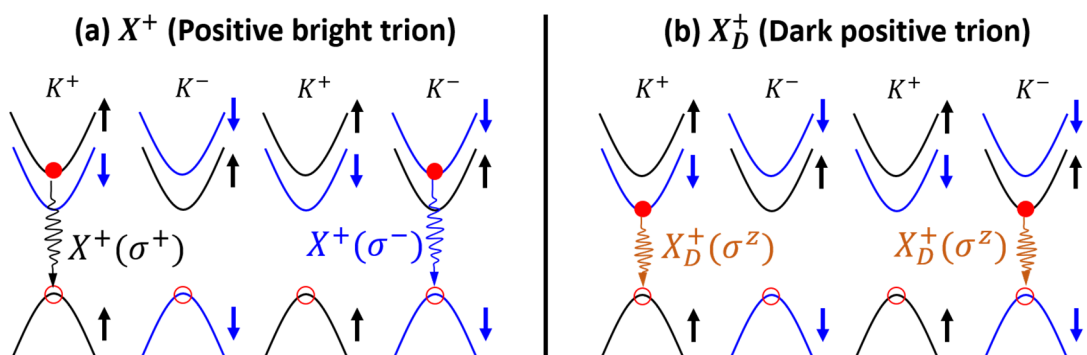


Figure 6.4 Configurations of the positive triions and their associated polarized light in monolayer WSe₂. (a) Two possible configurations for X^+ : $X^+(\sigma^+)$ and $X^+(\sigma^-)$. (b) Two possible configurations for X_D^+ . Red filled (unfilled) circle represents electron (hole); The blue and black arrows represent the spin orientation: up and down.

The notation of phonons $K3$ and $\Gamma5$ has its origin in the Koster notation of the K -point irreducible representations of the C_{3h} point double-group [187,270]. “Phonon replicas” involve phonon-assistant recombination. For example, **Figure 6.5** shows the recombination process of $X_{D,\Gamma5}^+(\sigma^\pm)$ and $X_{D,K3}^-(\sigma^\pm)$: at initial time, we have $X_D^+(K^\pm)$ which consists of one electron in the lower conduction band of K^\pm valley and two holes with opposite spins. Then the electron is scattered into a virtual energy level by emitting $\Gamma5$ (**Figure 6.5(a)**) or $K3$ (**Figure 6.5(b)**) phonon and finally recombine with the hole and emit σ^+ or σ^- . Phonon replicas $X_{D,K3}^+$ and $X_{D,\Gamma5}^+$ lie 26 and 21 meV below X_D^+ , respectively, shown in **Figure 6.3(b)**. This energy differences correspond to the $K3$ and $\Gamma5$ phonon in WSe₂ ML. **Figure 6.6** shows the phonon energy dispersion diagram of ML WSe₂, where we can easily find $K3$ and $\Gamma5$ are zone-edge and zone-center phonon modes, respectively.

Now, we discuss the polarization of those phonon replicas. It is noted that $X_{D,K3}^+$ are co-circularly polarized and $X_{D,\Gamma5}^+$ are cross-circularly polarized. This can be understood by the spin-valley pumping process (detailed in Chapter 4) and the formation process of X_D^+ (just detailed above). Briefly, cw σ^+ excitation can spin polarize the resident electrons, leading to larger population of electrons in K^- valley than K^+ valley. This favors the formation of $X_D^+(K^-)$ than $X_D^+(K^+)$. Besides, $X_D^+(K^-)$ can also emit σ^- light following a $\Gamma5$ phonon-assisted electron scattering within the K^- valley ($X_{D,\Gamma5}^-(\sigma^-)$), on the left of **Figure 6.5 (a)**, or emit σ^+ light through a $K3$ phonon-assisted intervalley scattering ($X_{D,K3}^+(\sigma^+)$), on the right of **Figure 6.5(b)**). For more characteristic of the two phonon replicas, please see Ref. [178].

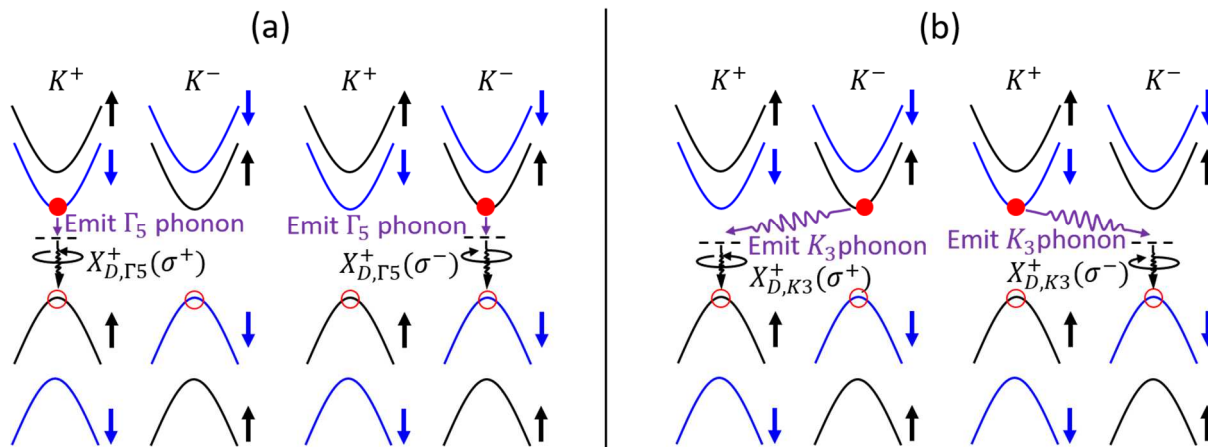


Figure 6.5 Phonon replicas of positive dark trion X_D^+ . (a) Schematic of the formation process of $X_{D,\Gamma5}^-(\sigma^\pm)$ and (b) of $X_{D,K3}^-(\sigma^\pm)$. The dark and blue represent the bands with electron with spin up and down, respectively. Filled and unfilled circles represent the electron and hole, respectively. The dashed lines stand for virtual states.

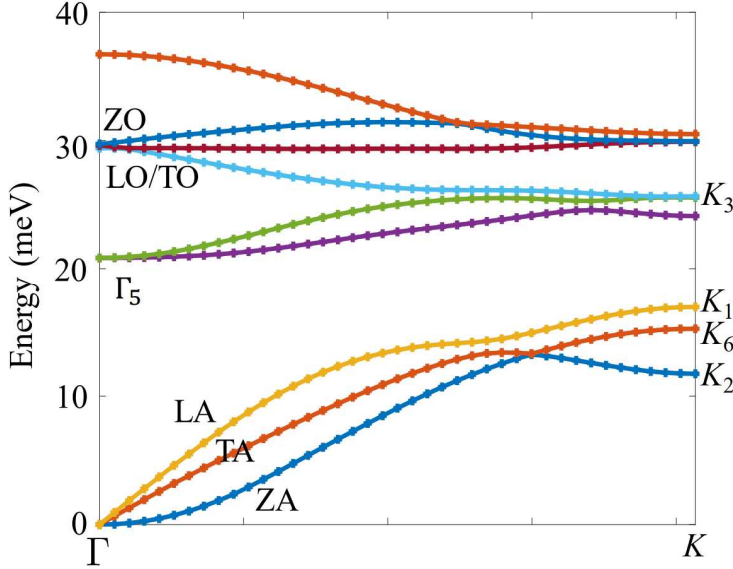


Figure 6.6 The phonon energy dispersion of monolayer WSe₂ along the axis between the first Brillouin zone Γ and K points. Zone-center and pertinent zone-edge phonon modes are indicated. Extracted from Ref. [178].

6.4 Method to measure the conduction and valence bands g -factor and results

The method presented below to determine the CB and VB g -factors will be applied first in the very low doping density regime, typically $p \sim 10^{11} \text{ cm}^{-2}$, in order to avoid band-gap renormalization effects [271]. Note that this doping density is two orders of magnitude weaker than the critical Mott density in ML WSe₂ [272,273].

Figure 6.7(b) presents schematically the single-particle band structure of ML WSe₂ at the vicinity of its CB and VB edges, along with optical selection rules associated to the radiative recombination of the dark trion X_D^+ and its phonon replicas $X_{D,K3}^+$ in an out-of-plane positive magnetic field ($B > 0$). It will allow us to present the method which yields the determination of CB and VB g -factors.

As explained in Chapter 1, the absorption/emission of right and left circularly-polarized light occurs in the inequivalent valleys K^+ and K^- of the 2D hexagonal Brillouin zone [58,274–277]. Here we will focus on the lowest energy transitions involving only the top VB, characterized by a g -factor g_v . The bottom and top CB g -factors are labelled g_{c1} and g_{c2} , respectively. The g -factor of a given transition with in-plane dipole ($X_0, X_{D,K3}^+$) writes simply: $E_{\sigma^+} - E_{\sigma^-} = g\mu_B B$. For transitions with an out-of-plane dipole (X_D, X_D^+), the light polarization is perpendicular to the ML plane and we define the g -factor by $E_{K^+} - E_{K^-} = g\mu_B B$ (see **Figure 6.7(b)** and **(c)**). **Figure 6.7(a)** shows the change of band structure of ML WSe₂ under the application of a magnetic field ($B > 0$). For bright neutral exciton transition in K^+ valley ($X_0(\sigma^+)$), the transition energy is $E_{X_0(\sigma^+),B>0} = E_{X_0(\sigma^\pm),B=0} + (g_{c2}\mu_B B - g_v\mu_B B)$ and likewise, we have $E_{X_0(\sigma^-),B>0} = E_{X_0(\sigma^\pm),B=0} + (-g_{c2}\mu_B B + g_v\mu_B B)$ for $X_0(\sigma^-)$, where $E_{X_0(\sigma^\pm),B=0}$ is the transition energy without magnetic field. Then we can easily get $g_{X_0}\mu_B B =$

$E_{X_0(\sigma^+),B>0} - E_{X_0(\sigma^-),B>0} = -2(g_v - g_{c2})\mu_B B$. As a result, we can determine the the g -factor of bright neutral exciton transition (X_0):

$$g_{X_0} = -2(g_v - g_{c2}). \quad (6.1a)$$

Likewise, we can get the g -factor of dark neutral exciton transition (X_D):

$$g_{X_D} = -2(g_v - g_{c1}). \quad (6.1b)$$

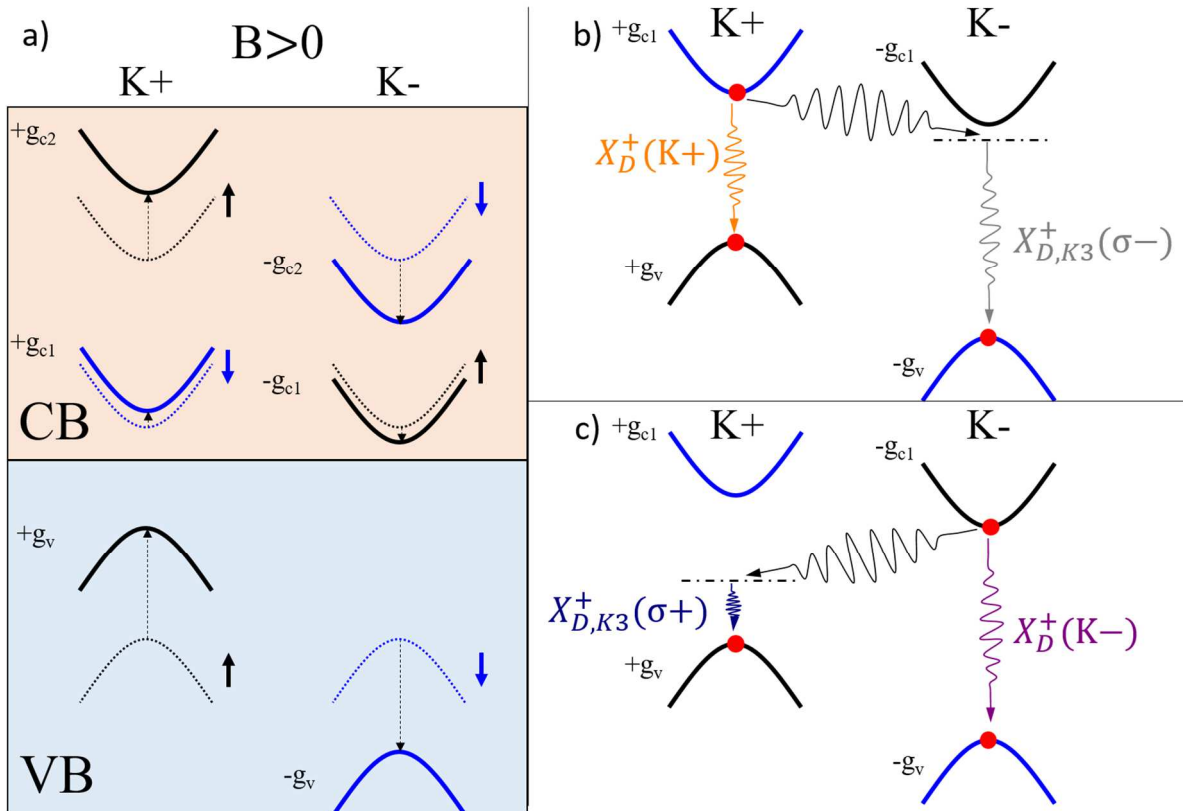


Figure 6.7 (a) Schematics of the band structure in valleys K^+ and K^- of ML WSe₂ at the neutrality point; the dotted and full lines correspond to bands with $B=0$ and $B>0$, respectively. The vertical dotted lines indicate the magnetic field induced shift of the bands. Only the top valence band is considered here (type-A optical transitions). Schematics of the band structure for $B>0$ and hole doping displaying the optical transition corresponding to the K_3 phonon replica of positive dark trion, $X_D^{+}(K_3)$, in (b) valley K^- and (c) valley K^+ . The optical transition of X_D^+ is also indicated. The top CBs are not displayed.

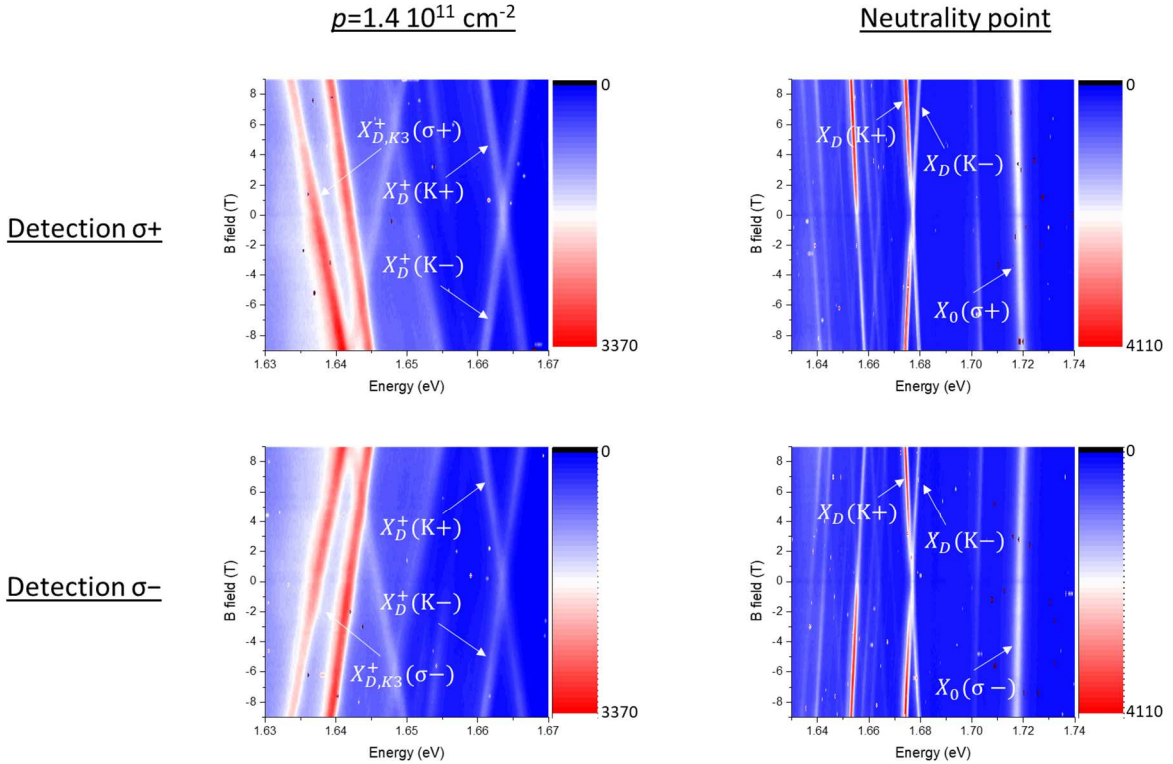


Figure 6.8 PL intensity as a function of magnetic field for $p=1.4 \times 10^{11} \text{ cm}^{-2}$ and neutrality point after linearly polarized excitation. The energy of the peaks reported in this thesis are extracted from these plots.

Figure 6.8 shows PL intensity as a function of magnetic field, in which the Zeeman splitting of different optical transitions is clearly observed. Then the transition energies of different peaks are extracted from these measurements. **Figure 6.9** shows the extracted transition energies for a magnetic field varying between $B=-9$ and $B=+9$ Tesla. X_0 and X_D are measured at charge neutrality, while X_D^+ and $X_{D,K3}^+$ are measured in a low p doping regime ($p=1.4 \times 10^{11} \text{ cm}^{-2}$). In agreement with previous reports [178,241], we find $g_{X_0} = -4.5 \pm 0.1$ and $g_{X_D} = -10.2 \pm 0.1$. As these two transitions imply two different CBs, these measurements cannot yield a determination of the CB and VB g -factors (see Eq. (6.1)). On the other hand, the selection rules associated with the positive dark trion optical transitions X_D^+ and $X_{D,K3}^+$ allow us to solve this problem. As illustrated in **Figure 6.7(b)** and **(c)**, the positive dark trion optical transitions $X_D^+(K+)$ or $X_D^+(K-)$ denote recombination of the neutral dark exciton component and they occur between opposite VB and CB spins of the same valley (the second hole in the time-reversed valley can be considered as a “spectator”). As expected, the extracted g -factor of this transition is very close to the one of the neutral dark exciton since $g_{X_D^+} = -2(g_v - g_{c1})$; we measure $g_{X_D^+} = -10.5 \pm 0.1$ [178,278].

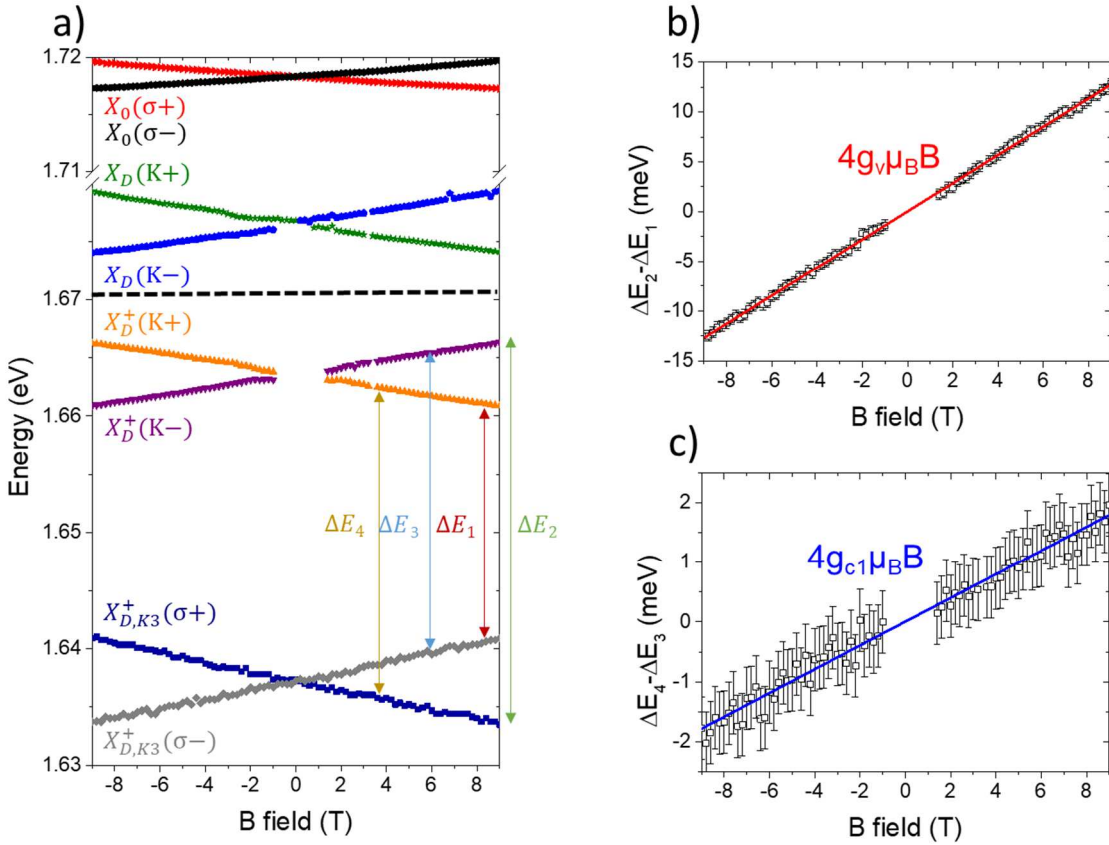


Figure 6.9 (a) Magnetic field dependence of bright and dark excitons at the neutrality point of the device and positive dark trion, X_D^+ , and its phonon replica involving the inter-valley phonon K_3 , $X_{D,K3}^+$, measured for $p=1.4\times 10^{11} \text{ cm}^{-2}$. Magnetic field dependence of the energy difference of the optical transitions (b) $\Delta E_2 - \Delta E_1$ and (c) $\Delta E_3 - \Delta E_4$ yielding the determination of g_v and g_{c1} (see arrows in (a)).

In contrast, optical transitions that are associated with the K_3 phonon replica, $X_{D,K3}^+$, involve the second hole of the trion, which is no more a “spectator” for the optical transition (**Figure 6.7(b)** and (**c**)) [279]. As a consequence, the energy difference between the optical transitions X_D^+ and $X_{D,K3}^+$ will depend only on single band g -factors g_{c1} and g_v and the energy of the phonon E_{K3} :

$$\begin{aligned}\Delta E_1 &= E(X_D^+(K+)) - E(X_{D,K3}^+(\sigma^-)) = E_{K3} - 2g_v\mu_B B, \\ \Delta E_2 &= E(X_D^+(K-)) - E(X_{D,K3}^+(\sigma^+)) = E_{K3} + 2g_v\mu_B B, \\ \Delta E_3 &= E(X_D^+(K-)) - E(X_{D,K3}^+(\sigma^-)) = E_{K3} - 2g_{c1}\mu_B B, \\ \Delta E_4 &= E(X_D^+(K+)) - E(X_{D,K3}^+(\sigma^+)) = E_{K3} + 2g_{c1}\mu_B B.\end{aligned}\quad (6.2)$$

Figure 6.9(b) presents the variation of $\Delta E_2 - \Delta E_1$ as a function of the applied magnetic field. The slope of the curve ($4g_v\mu_B B$) in **Figure 6.9(b)** yields a direct determination of the valence band g -factor. We find $g_v = 6.1 \pm 0.1$. **Figure 6.9(c)** presents the magnetic field variation of the difference $\Delta E_4 - \Delta E_3$ following the same procedure. The slope gives a direct determination of the bottom CB g -factor; we measure $g_{c1} = 0.86 \pm 0.1$. Then, using the measured g -factor of the neutral exciton transition (**Figure 6.9(a)** and Eq. (6.1)), we can deduce the top CB g -factor: $g_{c2} =$

3.84 ± 0.1 . Finally, we extract the bottom VB g -factor, g_{v2} , using the relation $g_{X_0,B} = -2(g_{v2} - g_{c1})$, where $g_{X_0,B}$ corresponds to the type-B neutral exciton (optical transition with in-plane dipole between bottom VB and CB). From the previously measured value of $g_{X_0,B} = -3.9 \pm 0.5$ [247], and our result for $g_{c1} = 0.86 \pm 0.1$, we get that $g_{v2} = 2.81 \pm 0.5$.

6.5 Measurements for a second device

We confirmed the values of the single band g -factors in the device used in Chapter 4 and 5. The magneto-PL measurements for $p=1.4 \times 10^{11} \text{ cm}^{-2}$ and neutrality point are shown in **Figure 6.10**. The magnetic field dependence of the different excitonic species shown in **Figure 6.10** are very similar to the ones presented above. The extracted g -factors in this second device are $g_v = 6.09$ and $g_{c1} = 0.87$, *i.e.* very close to the ones measured in the first device $g_v = 6.1$ and $g_{c1} = 0.86$.

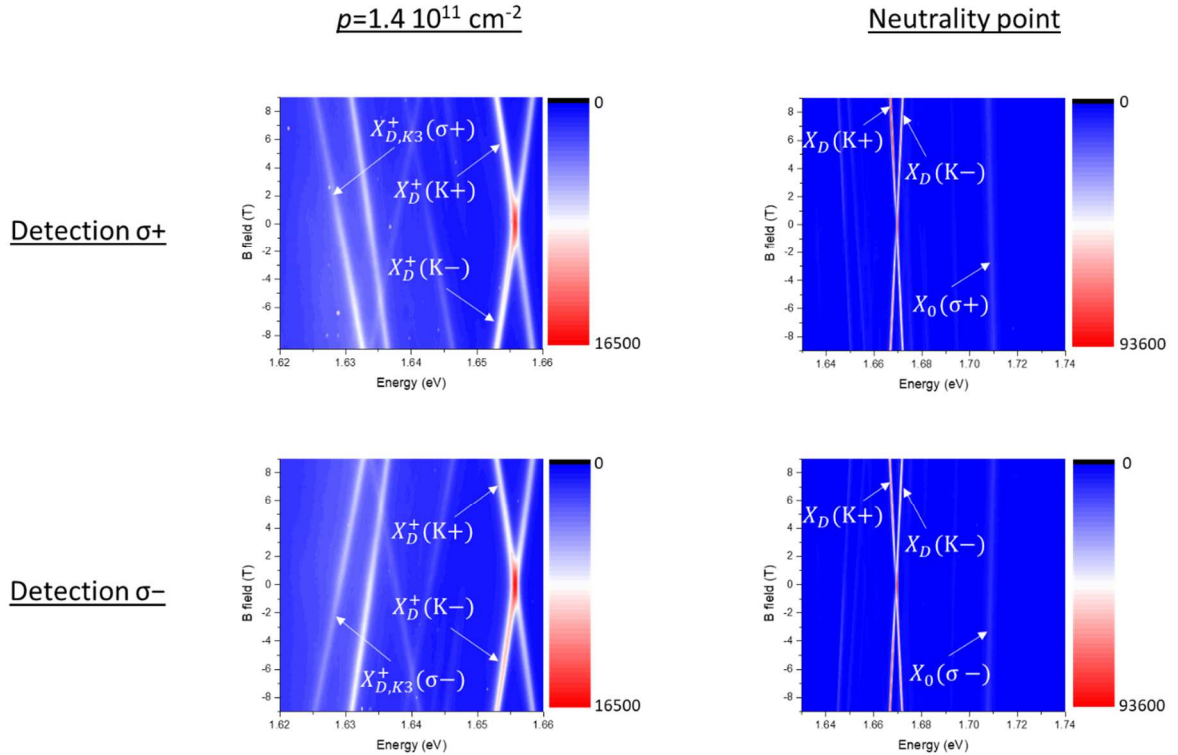


Figure 6.10 PL intensity as a function of magnetic field for $p=1.4 \times 10^{11} \text{ cm}^{-2}$ and neutrality point after linearly polarized excitation for the second device.

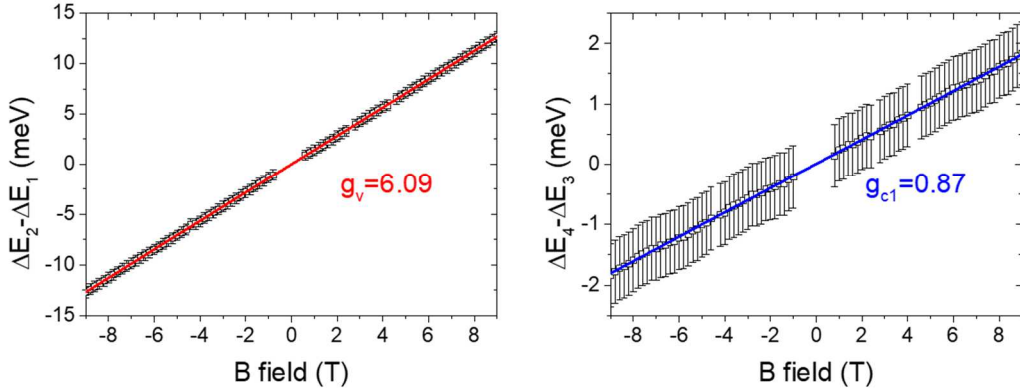


Figure 6.11 Extraction of g_v and g_{c1} in the second device.

6.6 Discussion

Zeeman splitting and corresponding g -factors were calculated in TMD MLs using DFT, tight-binding or k.p approaches [280–284]. As shown in **Table 6.1**, our measurements are in excellent agreement with the single-band g -factors calculated recently by DFT. Despite the largest uncertainty associated to the measurement of the type-B exciton Zeeman energy that we took from Ref. [247], we note that the extracted value of the bottom VB g -factor ($g_{v2} = 2.81 \pm 0.5$) is also close to the DFT calculated one (3.15) [280].

Moreover, our measurements clearly demonstrate that the simple model for calculating the g -factor based on the additive contribution of the magnetic coupling to the electron spin, valley and orbital angular momenta from the transition-metal atoms is oversimplified (see the last column in **Table 6.1** and Ref. [242,259,285] for more details on this model). Though it gives a top valence band g_v value close to the measured one (5.5), it fails to predict the g -factor of the CB as the simple calculation gives $g_{c2} = 3.5$ and $g_{c1} = 1.5$, assuming identical CB and VB mass ($0.4m_0$). This shows that in a similar way to other semiconductors, the calculation of the g -factor in TMD MLs requires a rather detailed description of the band structure that takes into account subtle effects of the SOI [258,260,261,286,287].

Table 6.1 Comparison of measured and calculated g -factors

Beyond the importance of the presented technique to extract the single particle g -factor in the CB and VB of TMD MLs, the results of this work merit discussion of three important points. The first one deals with the relation between the free electron (or hole)

g -factor and that of excitons/trions. Our interpretation of the experiment assumes that the exciton Zeeman splitting is the sum of the Zeeman splitting energies in the CB and VB. Similar to the case of various semiconductors, we have neglected effects linked to the exciton wavefunction [249,286,287]. As the exciton binding energy in TMD MLs is of the order of few hundreds meV (*i.e.* large extension in reciprocal space), one can question if the single-particle approach is accurate enough. Several calculations based on DFT coupled to Bethe-Salpeter Equation predicted a reduction of the exciton g -factor up to 30% compared to the single-particle approach [280,283], resulting from a decrease of the magnetic moment away from the band extrema. However, we believe that the excitonic correction is negligible in ML-WSe₂ for two reasons: (i) The measured values of g -factors match very well the predicted single band g -factors (**Table 6.1**) rather than the ones calculated with the exciton corrections. (ii) Previous measurements of the neutral exciton g -factor showed that $g_n = -4.3 \pm 0.2$ for the ground and excited exciton states from $n=1$ to $n=4$ [288]. While these states are characterized by distinct extension in k -space, their g -factors are essentially the same within the experimental uncertainty.

The second point deals with the carrier-density dependence of the g -factors. It is well known that exchange interactions in quantum wells of III-V semiconductors lead to enhancement of the effective g -factors [289]. This enhancement has been recently evidenced in magneto-transport experiments of heavily doped TMD MLs [248,290,291], and in Landau-quantized excitonic absorption spectroscopy of bright trions [266,292,293]. Wang *et al.* reported $g_v \sim 8.5$ and $g_{c1} \sim 4.4$ for a carrier density of $\sim 6 \cdot 10^{12} \text{ cm}^{-2}$ in ML-WSe₂ [266], whereas Liu *et al.* found $g_v \sim 15$ and $g_{c1} \sim 2.5$ for densities larger than 10^{12} cm^{-2} [292]. In contrast, our measured values, $g_v = 6.1$ and $g_{c1} = 0.86$, show relatively little change when the gate-induced hole density changes from $\sim 10^{11} \text{ cm}^{-2}$ (**Figure 6.9**) to $1.1 \times 10^{12} \text{ cm}^{-2}$ (**Figure 6.12**), during which the corresponding Landau level filling factor at $B=9\text{T}$ increases from $\nu < 1$ to $\nu > 6$. The reason for the disparity in the reported g -factor values remains an open question, and the relation between the energy-shift of various optical transitions and exchange interactions at large doping densities is yet to be quantified. Additional work is required.

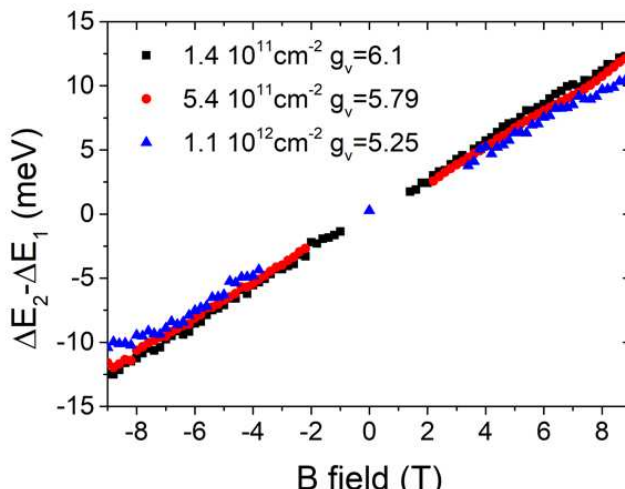


Figure 6.12 $\Delta E_2 - \Delta E_1$ as a function of the magnetic field yielding the determination of g_v for three values of hole density.

6.7 Conclusion

In summary, we have performed magneto-photoluminescence spectroscopy in gated WSe₂ ML device. Based on the knowledge of the optical selection rules of different exciton complexes, we have proposed a new method to measure the single particle *g*-factor. Recently this technique has been used in a joint work performed by universities of Warsaw and LNCMI Grenoble to measure *g*-factors of the conduction and valence bands in WS₂ monolayers [90]. Instead of using positive dark trion X_D⁺ and its phonon replicas X_{D,K3}⁺, they use their counterparts: negative dark trion X_D⁻ and its phonon replicas X_{D,K3}⁻ (configurations shown in **Figure 6.13(a)** and **(b)**). Then they determined $g_{c1} = \frac{\Delta E_4 - \Delta E_3}{4\mu_B B} = 1.1$ and $g_v = \frac{\Delta E_2 - \Delta E_1}{4\mu_B B} = 5.5$, shown in **Figure 6.13(c)** and **(d)**, and $g_{c2} = 3.7$ with the aid of $g_{X_0} = -2(g_v - g_{c2})$.

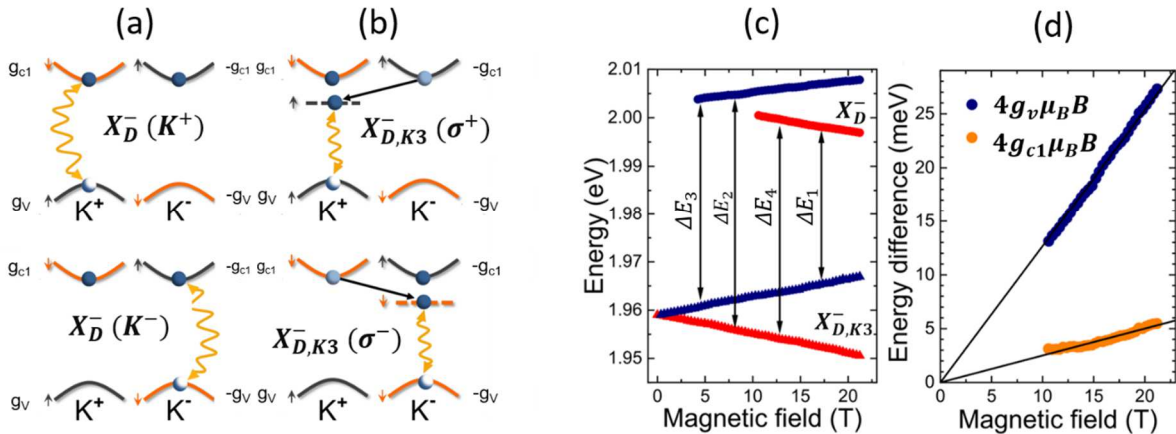


Figure 6.13 Schematic illustration of configurations for (a) negative dark trion (X_D⁻) and for (b) its K3 phonon replicas (X_{D,K3}⁻). (c) transition energies of the σ⁺/σ⁻ (red/blue points) components of the X_D⁻ and X_{D,K3}⁻ as function of the out-of-plane magnetic field. Black arrows show energy difference between different optical transitions, denoted as ΔE₁, ΔE₂, ΔE₃ and ΔE₄, similar definition as Eq.(6.2). (d) Magnetic field dependence of 4g_vμ_BB = ΔE₂ − ΔE₁ and 4g_{c1}μ_BB = ΔE₄ − ΔE₃, from which g_v and g_{c1} are extracted by linear fitting (the black solid lines). Adapted from Ref. [90].

These measurements should make it possible to improve the band structure calculations in monolayer transition-metal dichalcogenides, in particular the dispersion curves of the conduction bands which are still little known. Knowledge of the single band *g*-factors should be valuable for understanding the properties of van der Waals heterostructures in which interlayer or Moiré exciton transitions could be identified thanks to their Zeeman splitting.

Chapter 7 Résumé en Français

Matériaux 2D à base de dichalcogénures de métaux de transition

Au cours des dernières décennies, les matériaux de faible dimension, comme les puces quantiques (2D), les nanofils (1D) et les boîtes quantiques (0D) ont attiré une attention considérable et ont été largement étudiés sous de multiples aspects : croissance des matériaux, propriétés physiques/chimiques et applications potentielles. Dans cette thèse, nous nous intéresserons aux monocouches de dichalcogénures de métaux de transition, matériau semi-conducteur 2D aux propriétés originales. En effet, les matériaux 2D regroupent un large éventail de familles: isolants, semi-conducteurs, métaux, supraconducteurs..., comme le montre la **Figure 7.1**.

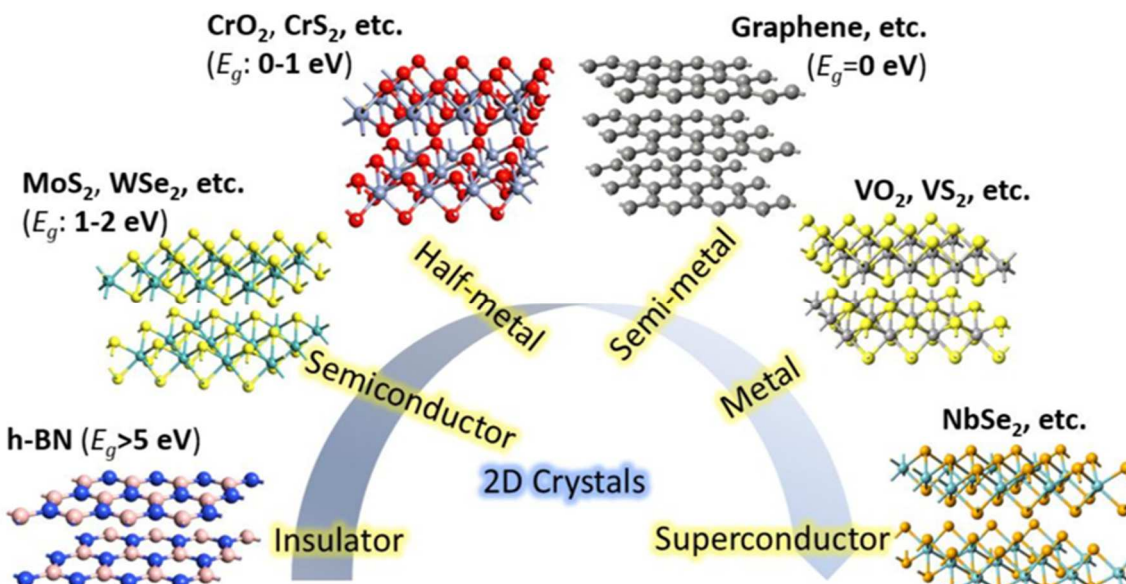


Figure 7.1 Les principales catégories de matériaux 2D. E_g désigne la bande interdite.
Extrait de Réf. [2].

L'intérêt pour les matériaux 2D a été suscité par la découverte du graphène, une seule couche d'atomes de carbone constituant une structure hexagonale comme le montre la **Figure 7.1**. Il a été obtenu pour la première fois par Konstantin Novoselov et Andre Geim par la méthode d'exfoliation mécanique [3]. Cette percée exceptionnelle conduit au prix Nobel de physique en 2010. Le graphène présente des propriétés spectaculaires: (1) une mobilité des porteurs supérieure à $10^6 \text{ cm}^2.\text{V}^{-1}.\text{s}^{-1}$ à 2 K [4] et supérieure à $10^5 \text{ cm}^2.\text{V}^{-1}.\text{s}^{-1}$ à température ambiante lorsqu'il est encapsulé dans des couches hexagonales de nitrite de bore (hBN) [5] ; (2) grande conductivité thermique de l'ordre de 5000 W.mK^{-1} à température ambiante [6] ; (3) le matériau le plus résistant avec une résistance à la rupture de 42 N.m^{-1} en monocouche [7]. Sa mobilité élevée des porteurs a stimulé des recherches substantielles pour les applications des

transistors. Cependant, les transistors à effet de champ (FET) fabriqués au graphène ont des rapports de « on/off » relativement faibles en raison du manque de bande interdite [8], ce qui entrave les progrès des transistors de hautes performances. En revanche, les monocouches TMD à structure cristalline 2H possèdent des bandes interdites dans le domaine visible-proche infrarouge [9,10], ce qui est prometteur pour les nouveaux dispositifs FET et optoélectroniques.

Les TMD ont une structure en couches avec la forme générale M-X-M, où M représente un atome de métal de transition (Mo, W) et X représente un atome de chalcogène (S, Se ou Te). Dans chaque monocouche, le plan des atomes de métal de transition est pris en sandwich entre les deux plans d'atomes de chalcogène, formant une structure prismatique trigonale comme le montre la **Figure 7.2**. Les TMD ont de nombreuses propriétés électriques et optiques uniques, attirant une attention particulière dans les recherches récentes. Ici, nous les passerons rapidement en revue et ils seront discutés plus en détail dans les sections suivantes.

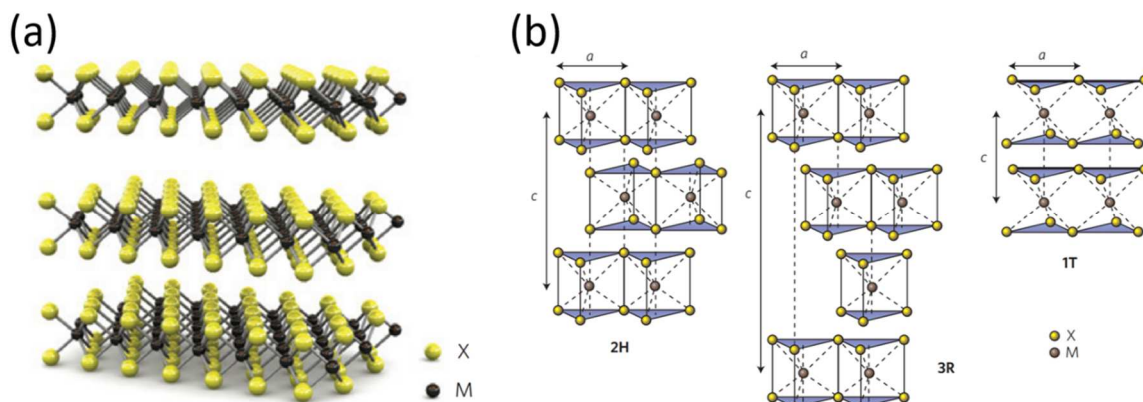


Figure 7.2 Structures cristallines de TMD. (a) Schéma de la structure en couches du TMD. Le plan des atomes de métaux de transition (M, en gris) est pris en sandwich entre les deux plans adjacents des atomes de chalcogène (X, en jaune). (b) Schémas de différents polytypes de TMD : 1T, 2H et 3R. L'indice d'empilement c indique le nombre de couches dans chaque ordre d'empilement et l'épaisseur d'une seule monocouche est d'environ 6,5 Å. Extrait de Réf. [8].

(1) Les bandes interdites de TMD dépendent de la couche : elles deviennent des semi-conducteurs à bande interdite directe lorsqu'elles s'amincent en monocouche alors qu'elles restent des semi-conducteurs à bande interdite indirecte pour un nombre de couches ≥ 2 .

(2) Par ailleurs, l'interaction lumière-matière dans les monocouches TMD est très forte; par exemple, l'absorbance d'un WS₂ monocouche peut dépasser 15 % à la longueur d'onde autour de 620 nm [11]. Cette remarquable interaction lumière-matière est régie par des excitons très robustes, c'est-à-dire des paires électron-trou liées par l'interaction Coulomb avec une énergie de liaison typique de plusieurs centaines de meV [12-16].

(3) Les monocouches TMD ont un fort couplage spin-orbite et un degré de liberté spin-vallée unique.

En conséquence, les monocouches TMD ont attiré une attention importante pour diverses applications électroniques et optoélectroniques telles que les transistors [17–21], les dispositifs flexibles/transparents [22–25], les dispositifs photovoltaïques/lumineux [26–29] et les capteurs [30 –32].

Hétérostructures de Van der Waals

Les propriétés des monocouches TMD sont très riches comme nous allons le montrer dans cette thèse. Nous pouvons maintenant imaginer fabriquer des cristaux artificiels en empilant différents matériaux 2D les uns sur les autres, comme le montre la **Figure 7.3**. Cet assemblage est nommé hétérostructure de van der Waals (vdW), qui peut non seulement aider à concevoir des dispositifs avec de nouvelles fonctionnalités, mais également fournir une plate-forme avec une physique riche. Le grand avantage des hétérostructures vdW est de combiner différents matériaux qui sont généralement très difficiles à faire croître ensemble en raison de la désadaptation des réseaux [33]. Dans ces structures, les différentes couches 2D sont couplées par des forces vdW relativement faibles tandis que les fortes liaisons covalentes maintiennent la stabilité dans le plan de la structure. Lorsque deux matériaux différents sont empilés, l'interaction à l'interface peut générer de nouveaux effets. Le résultat final de cet empilement n'est pas simplement égal à la somme de chaque propriété de composant individuel. Par exemple, lorsqu'une monocouche TMD est déposée sur un matériau magnétique, elle peut générer un effet de proximité magnétique. Un dédoublement Zeeman de grande vallée de 16 meV/T a été rapporté dans une hétérostructure vdW composée d'un sulfure WS₂ ML/Europium (II) ferromagnétique (EuS₂) [34]. Cet effet a également été rapporté dans une hétérostructure vdW WSe₂ ML et bi/tricouche d'iodure de chrome (III) (CrI₃) [35].

De plus, les hétérostructures constituées de deux ML TMD différents peuvent générer des excitons intercouche (IX), dont les porteurs constitutifs résident dans différentes couches atomiques. Les IX conservent les propriétés de vallée et de spin de leurs couches constitutives, mais ont des durées de vie plus longues et une accordabilité potentiellement améliorée par rapport aux excitons dans une seule monocouche TMD [36]. Ces propriétés uniques offrent des possibilités de réaliser des dispositifs excitoniques pour le traitement de l'information et du signal, similaires aux dispositifs électroniques et spintroniques mais dépendant de la manipulation d'excitons au lieu d'électrons ou de spins.

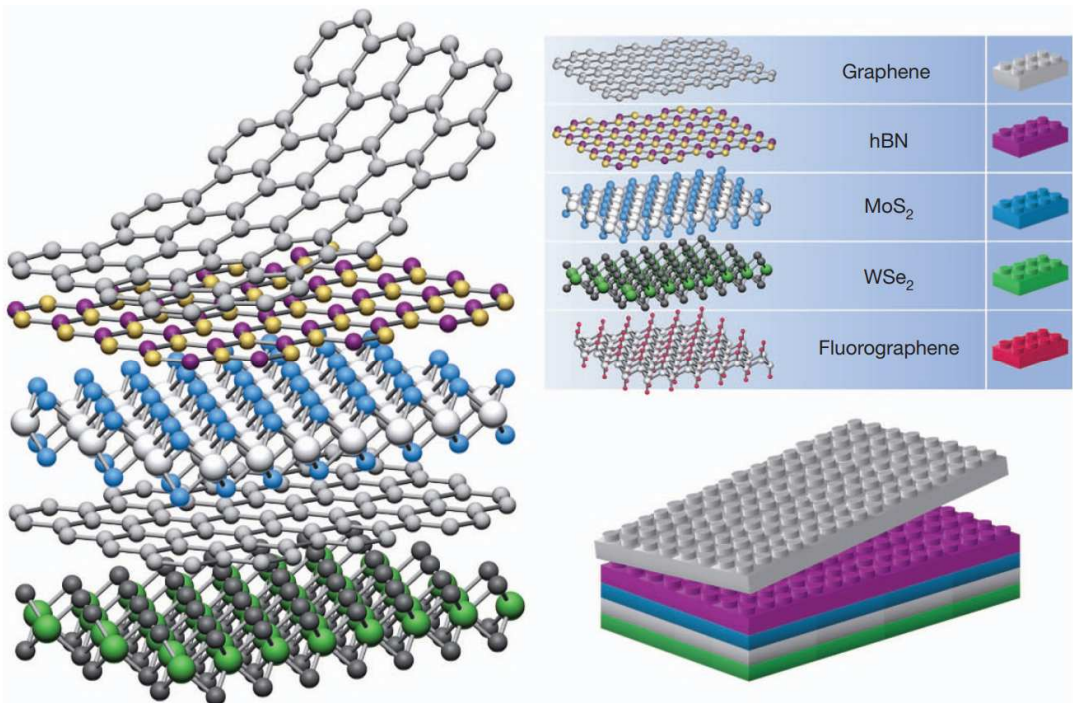


Figure 7.3 Hétérostructures de Van der Waals. Les couches 2D peuvent être considérées comme des blocs Lego (panneau de droite) et diverses hétérostructures vdW avec un empilement complexe de couches peuvent être construites. Cet empilement de cristaux artificiels est favorable grâce à l'interaction vdW relativement faible entre les couches 2D adjacentes. Extrait de Réf. [37].

Symétrie cristalline et structure des bandes d'énergie

Les dichalcogénures de métaux de transition sont une famille d'environ 60 matériaux et la plupart d'entre eux sont des structures en couches résultant des faibles interactions intercouche de van der Waals [9]. Dans cette thèse, nous nous concentrerons sur la structure en couches de la forme M-X-M, où M représente un atome de métal de transition (Mo, W) et X représente un atome de chalcogène (S, Se ou Te). Dans chaque monocouche, le plan des atomes de métal de transition est pris en sandwich entre les deux plans adjacents d'atomes de chalcogène, comme le montre la **Figure 7.2(a)**. Le TMD peut être classé en différents polytypes (1T, 2H, 3R) en tenant compte des ordres d'empilement et de la coordination des atomes de métal de transition, comme le montre la **Figure 7.2(b)**. Nous nous concentrerons principalement sur la phase 2H dans cette thèse car il s'agit de la forme la plus stable dans la nature.

Les structures de bande de TMD ont été calculées par divers outils théoriques [41–45]. La **Figure 7.4(a)** montre les structures de bande calculées de MoS₂, du volume à la monocouche. Il est à noter que la bande interdite indirecte entre le point Γ et le point médian le long de $\Gamma - K$ sous forme massive se déplace progressivement vers la bande interdite directe au point K sous forme monocouche. L'énergie des transitions directes au point K ne change pas beaucoup lors de l'amincissement en une monocouche tandis que les bandes au point Γ changent de manière significative. En conséquence, le TMD devient un semi-conducteur à bande interdite directe lors de l'amincissement en une seule monocouche. Ceci peut être compris par l'hybridation des bandes. Les

Figure 7.4(b) et (c) montrent les contributions calculées des orbitales atomiques individuelles pour les structures de bande de différentes monocouches TMD. Les états de la bande de conduction (CB) et de la bande de valence (VB) au point K sont principalement composés d'orbitales d sur les atomes de métal de transition, pris en sandwich par des atomes de chalcogène ($X-M-X$) et donc relativement moins affectés par l'effet de couplage intercouche. En revanche, les états proches du point Γ ont des contributions non négligeables des orbitales p des atomes de chalcogène, qui ont un fort effet de couplage intercouche [46]. Par conséquent, les états VB proches du point Γ sont plus sensibles au nombre de couches que les états proches du point K . Au fur et à mesure que le nombre de couches diminue, les états proches du point Γ changent de manière significative, conduisant à une bande interdite indirecte plus grande, mais les états directs au point K sont relativement inchangés.

Il existe deux vallées K dégénérées en énergie mais non équivalentes (K^+ et K^-) dans la zone hexagonale de Brillouin en raison de la symétrie d'inversion brisée dans les monocouches TMD.

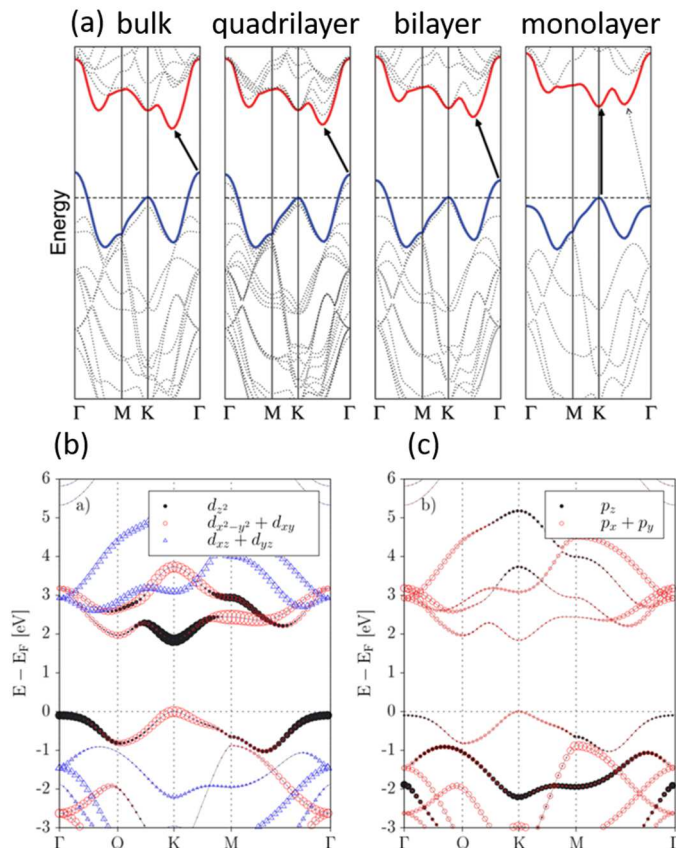
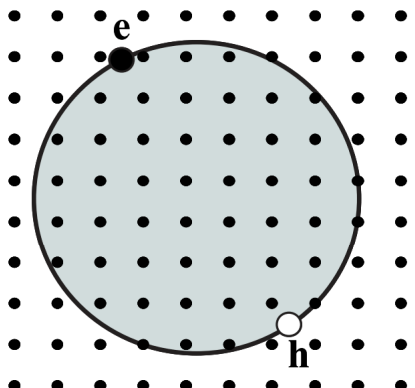


Figure 7.4 Caractéristiques des structures de bande TMD. (a) structures de bande calculées de MoS_2 , de la masse à la monocouche. Les courbes rouges pleines (les courbes bleues pleines) représentent la bande de conduction (bande de valence). Les flèches noires pleines indiquent les transitions d'énergie les plus basses. (b) et (c) hybridation d'orbitales atomiques dans la bande d'énergie de MX_2 ($M=\text{Mo}, \text{W} ; X=\text{S}, \text{Se ou Te}$). (b) : orbitales d de l'atome de métal ; (c) : orbitales p des atomes de chalcogène. La taille du symbole est proportionnelle au poids de l'orbitale atomique. L'effet de couplage spin-orbite a été négligé. (a) extrait de Réf. [46]. (b) et (c) extraits de Réf. [47].

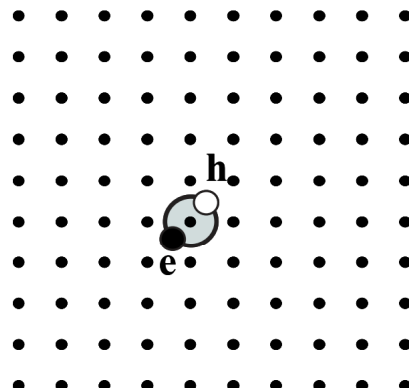
États excitoniques

Avant de discuter des états d'excitons dans un environnement 2D, passons d'abord en revue le concept d'excitons en général. Dans les semi-conducteurs, une excitation photonique externe avec une énergie appropriée peut promouvoir un électron dans la bande de conduction, laissant un trou dans la bande de valence. L'électron et le trou sont maintenus ensemble par l'interaction coulombienne attractive. Cette paire électron-trou neutre est appelée exciton. Il existe deux types d'excitons : les excitons de Wannier-Mott et les excitons de Frenkel. La **Figure 7.5** illustre schématiquement ces deux types d'excitons. Les premiers ont un rayon beaucoup plus grand que la cellule unitaire ; ce sont généralement des états délocalisés se déplaçant librement dans tout le cristal. C'est pourquoi on les appelle aussi « exciton libre ». En revanche, ces derniers ont un rayon beaucoup plus petit comparable à la taille de la cellule unitaire, qui sont donc des états localisés et étroitement liés à certains atomes.

Nous verrons plus loin que le rayon de Bohr de l'exciton dans les monocouches TMD est de l'ordre de quelques nanomètres et que la corrélation entre un électron et un trou s'étend sur plusieurs périodes de réseau [63]. Ainsi, les excitons dans les ML TMD sont des excitons de Wannier-Mott. La description de Wannier combinée à l'approximation de la masse effective peut expliquer la majorité des observations expérimentales.



(a) Wannier-Mott exciton



(b) Frenkel exciton

Figure 7.5 Schéma de principe des deux types d'excitons. (a) Un exciton de Wannier-Mott et (b) Un exciton de Frenkel. Extrait de Réf. [64].

Exciton 2D au milieu anisotrope:

En effet, l'énergie de liaison des excitons dans les monocouches TMD ne suit pas la loi simple $E_{Bn}^{2D} = \frac{R_{ex}}{(n-\frac{1}{2})^2}$ déduite d'un système 2D idéal. L'interaction de Coulomb s'écarte fortement de la loi conventionnelle (¹) en raison de la géométrie du système et de l'environnement diélectrique (vide, air, SiO₂, hBN etc). Le champ électrique entre l'électron et le trou est présent à la fois dans la monocouche et dans l'environnement

extérieur à la monocouche. En conséquence, l'interaction coulombienne effective entre l'électron et le trou est considérablement modifiée par les propriétés diélectriques de l'environnement. Pour décrire cet effet, nous pouvons utiliser le potentiel de Rytova-Keldysh [73,74] pour modéliser l'interaction coulombienne effective entre l'électron et le trou dans l'exciton 2D [14,75–77] :

$$V(r) = -\frac{e^2}{8\varepsilon_0 r_0} \left[H_0 \left(\frac{\varepsilon_{ext} r}{r_0} \right) - N_0 \left(\frac{\varepsilon_{ext} r}{r_0} \right) \right]$$

où r est la séparation électron-trou dans le plan ; $r_0 = 2\pi\chi_{2D}$ est le rayon d'écran ; χ_{2D} est la polarisabilité 2D. H_0 and N_0 sont respectivement les fonctions Struve et Neumann. ε_{ext} est la constante diélectrique effective de l'environnement. La constante diélectrique effective pour un TMD ML peut être estimée comme une valeur moyenne sur les côtés supérieur et inférieur du plan 2D, c'est-à-dire $\varepsilon_{ext} = \frac{1}{2}(\varepsilon_{top} + \varepsilon_{bottom})$. Réf. [78] donne un exemple pour calculer les états d'excitons dans les monocouches TMD à partir de ce potentiel de Rytova-Keldysh.

Excitons brillants et noirs

Les excitons brillants sont des espèces excitoniques optiquement actives autorisées par le moment et le spin, comme le montre la **Figure 7.6**. En revanche, il existe également des excitons optiquement désactive qui sont des transitions à spin interdit et/ou à moment interdit, comme le montre la **Figure 7.6**. Si l'électron et le trou corrélés sont de spin opposé mais dans la même vallée, c'est-à-dire avec spin interdit mais moment autorisé, il est nommé exciton noir intravallée X_D (ce sont les excitons noirs qui seront discutés dans cette thèse). Alternativement, si l'électron et le trou corrélés ont le même spin mais dans des vallées différentes, c'est-à-dire que le spin est autorisé mais le moment interdit, il est alors appelé exciton noir intervallée, par exemple exciton indirect (X_I), comme le montre la **Figure 7.6**. Les excitons brillants ont une plus grande force d'oscillateur que les excitons noirs, ce qui conduit à une durée de vie radiative plus courte (plusieurs ps pour l'exciton neutre brillant X_0 [79–83]) que les excitons noirs (des centaines de ps pour l'exciton noir intravallée X_D , voir chapitre 3).

Pour simplifier, nous nommons l'exciton intravallée à spin interdit X_D comme exciton noir dans ce qui suit et nous préciserons le nom des autres excitons optiquement désactive si nécessaire. Les excitons brillants ont un moment dipolaire dans le plan de monocouche [84, 85], tandis que les excitons noirs à spin interdit ont un moment dipolaire perpendiculaire du plan monocouche (mode z) [86–88]. En conséquence, il est plus efficace de détecter ces excitons noirs à spin interdit par détection dans le plan, comme le montre la **Figure 7.7(d)**. Cela nécessite un alignement rigoureux du bord de l'échantillon par rapport à l'objectif du microscope. Cependant, nous pouvons également observer X_D dans WSe₂ ML dans nos mesures PL en utilisant une excitation et une détection standard perpendiculaires au plan monocouche. La principale raison est que nous utilisons un objectif à grande ouverture numérique (NA = 0,82) [86]. Ainsi le champ électrique au bord focal a une composante perpendiculaire du plan non négligeable qui permet de détecter les transitions noirs à l'incidence

normale [86]. Cette technique donne un découpage entre X_0 et X_D : $\Delta E \sim 40$ meV dans WSe₂ ML (voir **Figure 7.7(c)**) [86].

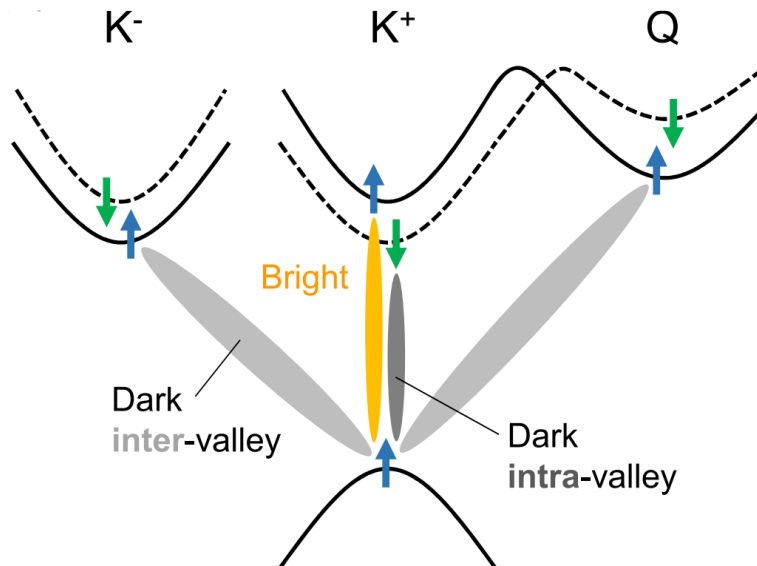


Figure 7.6 Schéma des transitions optiquement autorisées et interdites pour les exciton brillants et noirs. La structure des bandes est simplifiée pour plus de clarté. L'ordre des états de spin dans la bande de conduction correspond aux monocouches à base de W. Extrait de Réf. [63].

Pour observer facilement les excitons noirs à spin interdit, nous pouvons également appliquer un champ magnétique dans le plan [88–91] comme le montre la **Figure 7.7(b)** qui conduit à un mélange d'états brillants et noirs. La force de l'oscillateur des transitions "noirs" augmente lorsque le champ magnétique augmente, comme le montre la **Figure 7.7(a)**. Ensuite, nous pouvons facilement mesurer la différence d'énergie entre X_0 et X_D ($\Delta E = E_{X_0} - E_{X_D}$) ($\Delta E \sim -1,4$ meV dans MoSe₂ ML et ~ 14 meV dans MoS₂ ML [88]). Comme nous le verrons plus en détail au chapitre 3, la séparation des excitons brillants-noirs comprend trois contributions bien établies [88, 92] $\Delta = \Delta_{\text{exch}} + \Delta_{\text{so}} + \Delta_{\text{bind}}$, où Δ_{exch} est l'énergie d'échange d'excitons à courte portée, Δ_{so} est la bande de conduction séparation spin-orbite, Δ_{bind} est la différence entre les énergies de liaison des excitons brillants et noirs en raison des masses effectives légèrement différentes des bandes de conduction spin \uparrow et spin \downarrow . Dans le chapitre 3 nous mettrons en évidence une nouvelle contribution supplémentaire due au couplage au champ électromagnétique (décalage de Lamb).

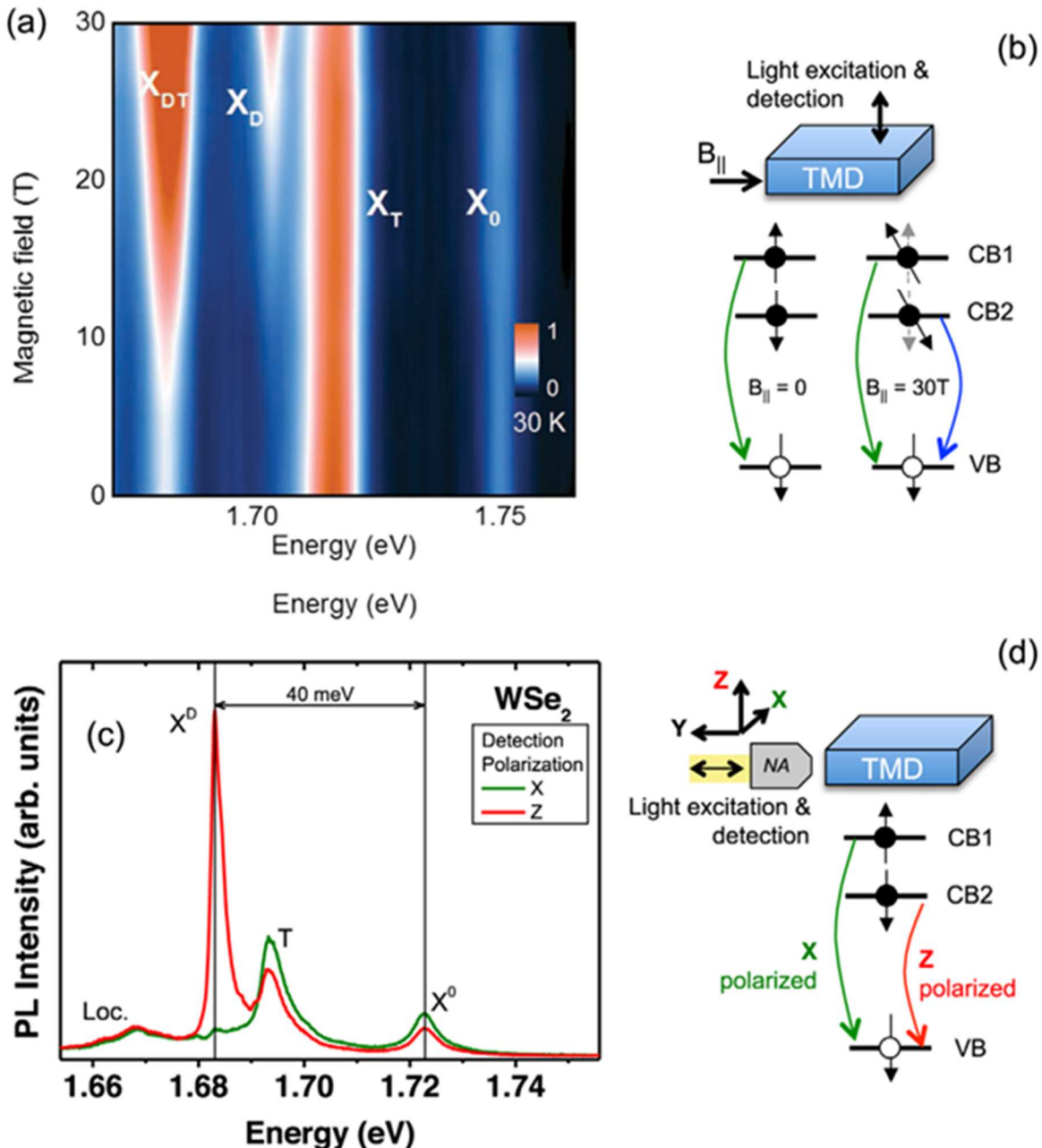


Figure 7.7 (a) Magneto PL de la monocouche WSe_2 sous champ magnétique dans le plan, dans lequel l'exciton noir commence à apparaître à ~ 5 T et gagne en intensité à mesure que le champ magnétique augmente. (b) Schéma de l'éclaircissement des transitions d'excitons noirs impliquant les états de spin dans les bandes de conduction supérieure (CB1) et inférieure (CB2). (c) Spectres PL de la monocouche WSe_2 encapsulée dans hBN, détectés hors du plan de la monocouche (désignés par la ligne verte continue) et dans le plan de la monocouche (désignés par la ligne rouge continue). (d) Schéma de l'excitation et de la détection depuis le bord de l'échantillon pour distinguer le mode optique de X_0 et X_D . Extrait de Réf. [63].

Il s'avère que les excitons noirs ont une structure fine dans les monocouches TMD. L'un est parfaitement noir (« exciton noir » : spin interdit et dipôle électrique interdit), à l'état d'énergie le plus bas ; l'autre est partiellement optiquement actif ("exciton gris": spin interdit mais dipôle électrique autorisé, c'est-à-dire mode z, perpendiculaire du

plan ML), à l'état d'énergie le plus élevé. On peut effectuer des mesures de magnéto-photoluminescence avec un champ magnétique B_z appliqué perpendiculairement au plan de la monocouche pour mesurer la séparation d'énergie δ des deux excitons noirs. Cette technique peut mélanger les deux états noirs, c'est-à-dire que "l'exciton noir" peut gagner en force d'oscillateur venue du gris ; il donne $\delta \lesssim 1$ meV dans les ML TMD. [88,89,93]. Dans cette thèse, nous nous concentrerons uniquement sur "l'exciton gris" et l'appelons "exciton noir" pour plus de simplicité.

Jusqu'à présent, nous avons introduit des excitons brillants et noirs (X_0 et X_D) et ce sont les deux excitons neutres sans excès de charge. Comme nous le verrons dans cette thèse, il existe également des complexes excitoniques avec un excès de charge positive ou négative, par exemple le trion négatif (c'est-à-dire une combinaison de deux électrons et d'un trou (image à trois particules), dont les propriétés seront détaillées dans la section 4.3). Si nous prenons une image à plusieurs corps, nous pouvons traiter le trion négatif comme un polaron de Fermi, c'est-à-dire l'interaction entre un exciton et une mer de Fermi d'électrons. Dans cette thèse (chapitre 4, chapitre 5 et chapitre 6), nous restreignons notre étude à des densités modérées de porteurs (électrons ou trous) de quelques 10^{11}cm^2 dans des monocouches TMD de sorte que l'image simple à trois particules (i.e. trion) est toujours valide [94–96].

Règles de sélection optique et polarisation spin-vallée

Comme déjà discuté, l'interaction spin-orbite dans les monocouches TMD est assez forte, conduisant à une séparation du spin Δ_{SOC}^{VB} dans la bande de valence et Δ_{SOC}^{CB} dans la bande de conduction au point K (voir **Figure 7.8**). En outre, les monocouches de TMD sont caractérisées par le groupe de points de symétrie D_{3h} inférieur [63] contrairement au TMD de phase 2H massif qui appartient au groupe de symétrie de points D_{6h} [9,97]. En raison de cette symétrie d'inversion brisée dans les monocouches TMD, deux vallées non équivalentes : K^+ and K^- émergent aux coins de la zone hexagonale de Brillouin, comme le montre la **Figure 7.8(a)**. La différence entre les deux vallées est que le spin est opposé au niveau des bandes correspondantes, comme le montre la **Figure 7.8(c)-(e)**. Cette structure de bande unique conduit aux règles de sélection optique chirale pour les transitions interbandes au niveau de la vallée K^\pm dans les monocouches TMD : les vallées K^+ (K^-) ne sont couplées qu'avec de la lumière polarisée circulairement $\sigma^+(\sigma^-)$ [66,98,99]. Cela conduit à la génération et à la détection optiques de la polarisation de vallée de spin, c'est-à-dire des degrés de liberté spin-vallée.

En suivant ces règles de sélection optique chirale, nous pouvons exciter sélectivement des excitons composés de porteurs dans la vallée K^+ or K^- en choisissant soigneusement l'énergie laser et l'hélicité (σ^+ or σ^-). Ces techniques sont dites techniques d'orientation optique. Rappelons brièvement le principe de ces techniques qui permettent d'étudier les propriétés de spin des porteurs ou excitons dans les semi-conducteurs. Nous avons utilisé ces techniques puissantes dans les chapitres 4 et 5.

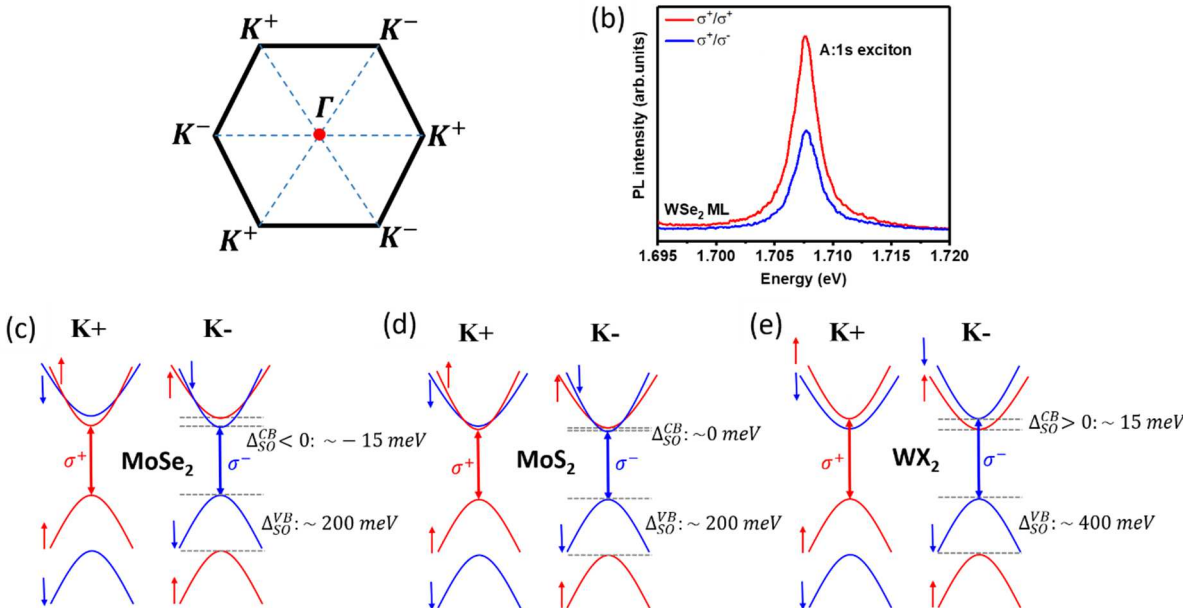


Figure 7.8 Illustration schématique des règles de sélection optique chirale dans les TMD monocouches. (a) Croquis de la 1ère zone de Brillouin hexagonale de la phase 2H. (b) Mesures de PL résolues en polarisation circulaire dans une monocouche WSe₂ encapsulée dans hBN après σ^+ laser d'excitation à polarisation circulaire (detection σ^+ et σ^-). (c) - (d) Illustrations schématiques des règles de sélection optique chirale dans les monocouches TMD à base de Mo et de W. L'ordre de la bande de conduction est opposé entre la monocouche TMD à base de Mo et de W. Notez que nous incluons ici l'effet de masse effectif dans les bandes de conduction pour souligner la différence de bande de conduction dans les monocouches TMD. Dans ce qui suit, nous allons simplifier la structure des bandes sans tenir compte de l'effet de masse effectif sauf dans le cas que nous spécifions.

Fabrication d'échantillons et techniques expérimentales

Tous nos échantillons d'hétérostructure de van der Waals 2D sont fabriqués par la méthode « all-dry-viscoelastic stamping » [109]. Un croquis des configurations de fabrication et le processus de fabrication de l'échantillon détaillé sont illustrés à la **Figure 7.9**. Tout d'abord, les flocons en couche mince de TMD sont exfoliés mécaniquement à partir de matériaux en vrac commerciaux (2D semiconductorsTM ou hq grapheneTM) à l'aide d'un ruban Nitto. Deuxièmement, ces flocons sont transférés sur un morceau de tampon, c'est-à-dire le polydiméthylsiloxane (PDMS, Gelpack®; niveau de rétention $\times 4$), qui est collé sur une lame de verre pour manipuler facilement les flocons. Troisièmement, la lame de verre est placée sous un microscope optique avec un objectif à longue distance de travail (objectif Olympus® MPLFLN x 10 avec une distance de travail de 11 mm). Grâce à la transparence du verre et au contraste des flocons de TMD sur le PDMS, le TMD à une seule couche a pu être repéré en scannant le tampon PDMS et en étant surveillé via un microscope optique. Quatrièmement, une fois qu'une couche souhaitée est repérée, le tampon PDMS est placé juste au-dessus d'un substrat (généralement SiO₂/Si), puis la couche sélectionnée peut être alignée sur une position spécifique sur le substrat, qui est fixée sur la scène de l'échantillon illustré à la **Figure 7.9**) par une pompe à vide. À la fin, le

tampon PDMS est abaissé jusqu'à ce qu'il soit en contact avec la surface du substrat, puis le tampon est lentement décollé du substrat. Après chaque processus de transfert, l'échantillon est recuit sur une plaque chauffante (discussion détaillée présentée dans la section 2.1.2). Avec l'aide des 6 actionneurs motorisés (Newport®, modèles : TRB25CC et LTA-HL avec une précision de 0,1 µm et 0,05 µm, respectivement) intégrés à la fois dans le support d'emboutissage et d'échantillonnage, la localisation des flocons transférés peut atteindre une précision micrométrique et le pelage-off taux peut être abaissé jusqu'à 1 µm/s. La température de la platine échantillon peut être contrôlée de la température ambiante à 200 °C.

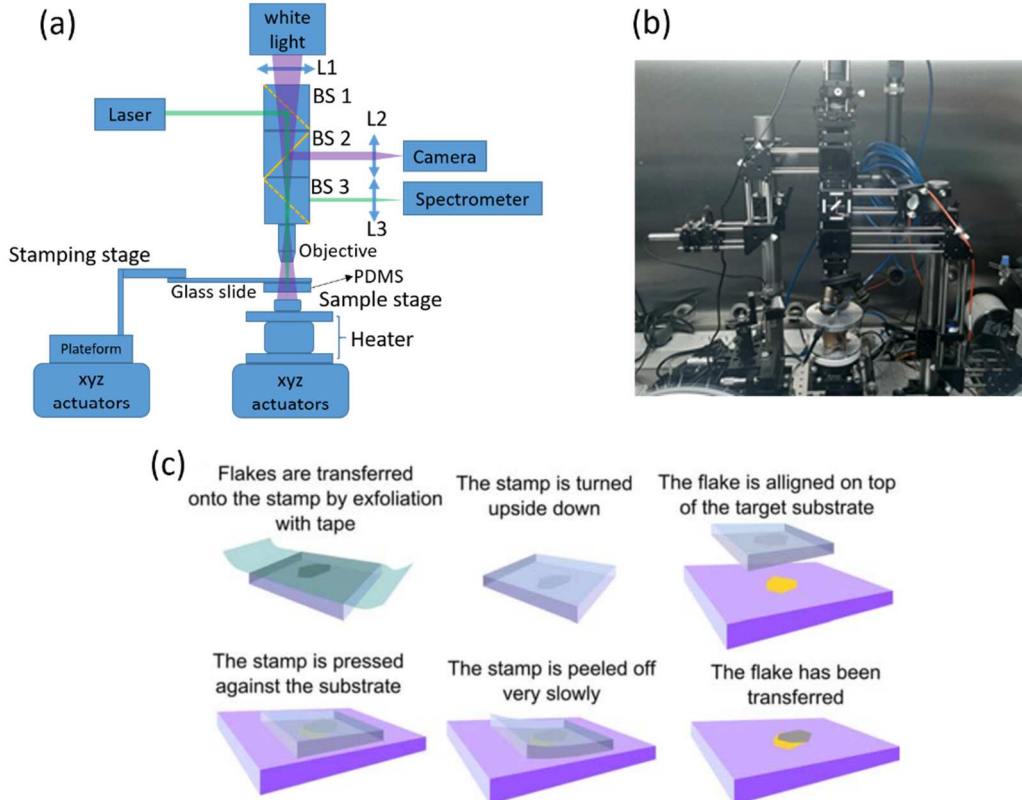


Figure 7.9 Configurations de fabrication et processus de transfert. (a) Croquis des configurations de fabrication maison. BS et L désignent respectivement le séparateur de faisceau et la lentille. Le support de tamponnage contrôle le tampon PDMS sur lequel reposent les couches de TMD exfoliées. La platine échantillon contrôle la position du substrat. L'image de l'ensemble du processus de fabrication peut être surveillée en direct grâce à la caméra. En cas de doute, un laser 532 nm et un spectromètre sont à disposition pour effectuer la mesure PL à température ambiante en insérant les deux séparateurs de faisceau : BS 1 et BS 2. (b) Photo de setup de fabrication maison. L'ensemble des installations est installé à l'intérieur d'une boîte à gants sous atmosphère inerte contrôlée. (c) Schéma des étapes de l'exfoliation des matériaux TMD au transfert déterministe d'une couche unique 2D sur un emplacement sélectionné sur le substrat, extrait de la réf. [109].

Nous pouvons contrôler le dopage dans notre monocouche TMD grâce au dispositif charge-ajustable (illustré à la **Figure 7.10**), qui peut être considéré comme un simple capaciteur. Une monocouche TMD et quelques couches de graphène (FLG) agissent comme les deux plaques opposées et un flocon de hBN avec des centaines de

nanomètres d'épaisseur est utilisée comme environnement diélectrique entre les deux plaques. Afin d'isoler l'ensemble du dispositif, toute la structure du condensateur est noyée dans deux autres flocons de hBN. Au lieu de faire de la lithographie après le transfert des couches, nous transférons précisément les couches exfoliées via la méthode «all-dry-viscoelastic stamping» sur un substrat SiO₂/Si sur lequel les électrodes Ti/Au ont été modelées par lithographie. Les quelques couches de graphène exfoliées à partir d'un cristal de graphite pyrolytique hautement orienté (HOPG) sont utilisées pour la grille arrière et pour contacter la couche TMD. Cette méthode peut produire des échantillons de haute qualité sans hystérésis de la densité de dopage avec le biais appliqué. La largeur de raie PL typique à basse température peut atteindre ~ 2.5 meV (~ 1 meV) pour l'exciton neutre dans la monocouche WSe₂ (MoSe₂), atteignant l'état de l'art [111].

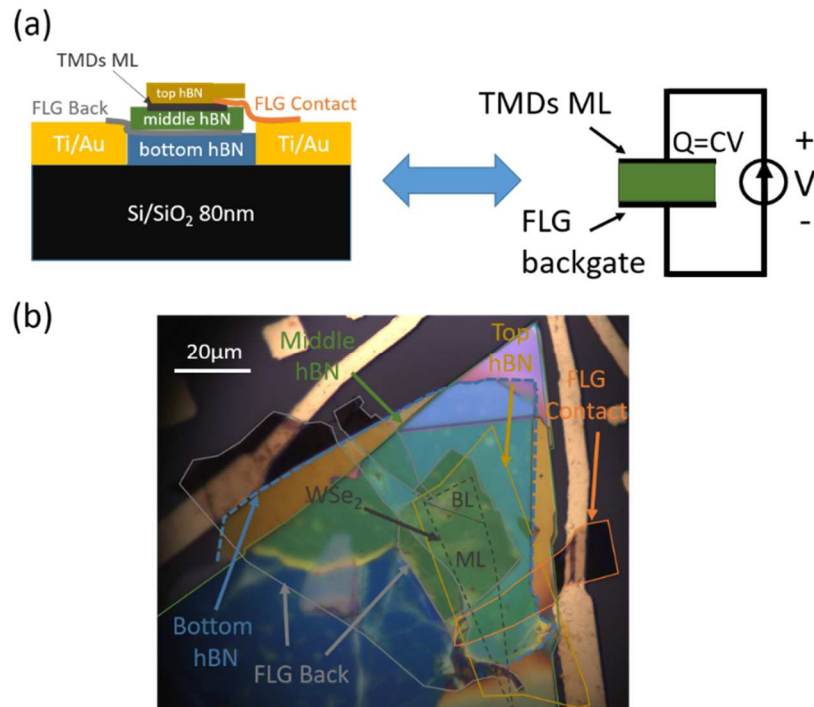


Figure 7.10 Dispositif accordable en charge monocouche TMD. (a) Croquis d'un dispositif accordable en charge monocouche TMD, équivalent à une structure de condensateur, illustré à droite. FLG désigne quelques couches de graphène, qui sert de fil de contact. (b) Une image de microscopie optique d'un dispositif accordable en charge WSe₂.

Configurations de spectroscopie optique

La **Figure 7.11** montre un schéma de nos configurations de spectroscopie optique, qui peuvent être divisées en les parties principales suivantes : source de lumière d'excitation, chemin optique, cryostats, spectromètre et détecteur. Nous pouvons intégrer différents éléments optiques tels que la plaque d'onde et le polariseur pour effectuer diverses mesures de spectroscopie optique, des mesures de photoluminescence et de réflectivité, par exemple. Dans ce qui suit, nous allons détailler toutes les techniques expérimentales utilisées dans cette thèse.

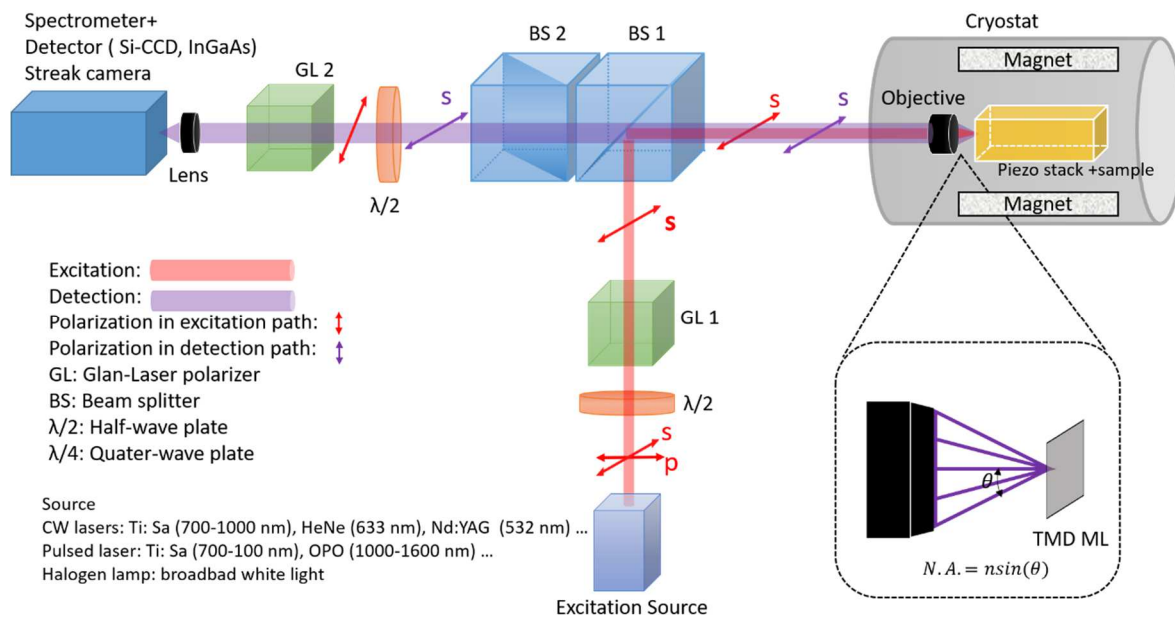


Figure 7.11 Configurations de spectroscopie optique. Nous donnons ici un exemple d'excitation linéaire et de détection linéaire. Selon les cryostats, une bobine supraconductrice peut être intégrée à l'intérieur.

Contrôle de la séparation entre les excitons brillants et noirs à l'aide du décalage de Lamb dans les monocouches WSe₂

Nous avons fabriqué des hétérostructures de van der Waals à base de WSe₂ ML (Top hBN /WSe₂/Bottom hBN) avec la méthode détaillée dans le chapitre 2. L'ensemble de la structure est déposé sur un substrat SiO₂ (83 nm)/Si. L'épaisseur du top hBN ne joue pas un rôle important ici compte tenu de sa petite valeur, typiquement ~ 5-10 nm. Les épaisseurs d de Bottom hBN sont mesurées par AFM. Les quatre échantillons utilisés dans ce chapitre sont caractérisés par différentes épaisseurs de Bottom hBN ; ils sont énumérés ci-dessous dans le **Tableau 7.1**, y compris deux «échantillons rainbows» où le même WSe₂ ML est déposé sur un flocon de hBN présentant différentes terrasses et marches. La **Figure 7.12(a)** montre un schéma d'un «échantillon rainbow» ; La **Figure 7.12(b)** montre une image de microscope optique de l'échantillon IV.

Tableau 7.1 Échantillons caractérisés par différentes épaisseurs de Bottom hBN

Sample	Bottom hBN thickness d (nm)
Sample I	101
	113
Sample II (rainbow)	115
	119
	132
	135
Sample III	186
Sample IV (rainbow)	214
	224
	239
	269

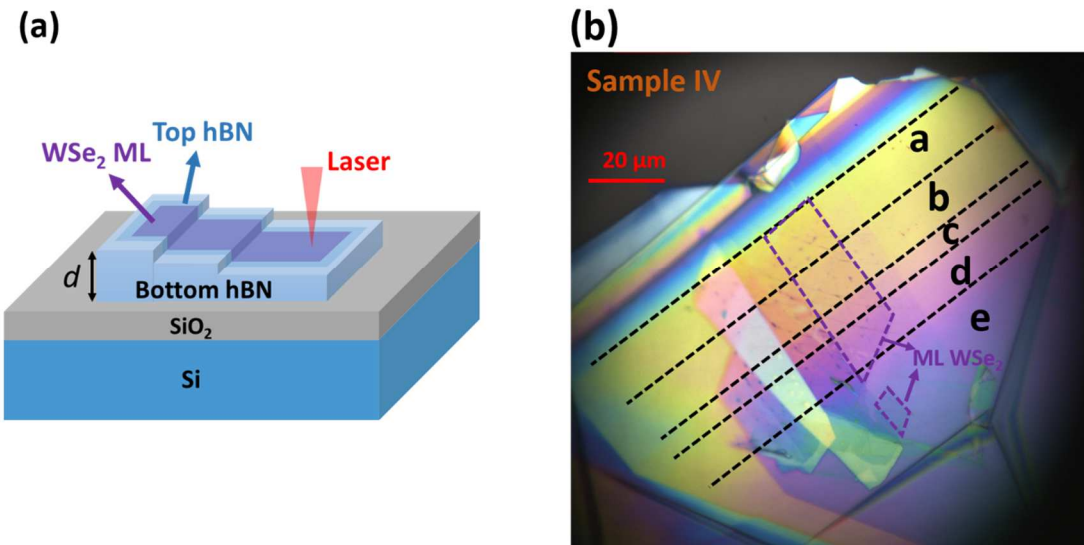


Figure 7.12 (a) Schémas de la monocouche WSe₂ encapsulée dans hBN étudiée, où la même monocouche est intégrée dans une hétérostructure en escalier caractérisée par une épaisseur différente d de bottom hBN. (b) Image de microscope optique de l'échantillon IV montrant différentes épaisseurs de Bottom hBN: a ($d = 210$ nm), b ($d = 214$ nm), c ($d = 224$ nm), d ($d = 239$ nm) et e ($d = 269$ nm). Les lignes pointillées noires séparent différentes terrasses et la monocouche WSe₂ est indiquée par la ligne pointillée violette.

Nous avons réalisé des expériences simples de photoluminescence stationnaire à $T = 5$ K en utilisant un laser He-Ne. La puissance d'excitation typique est de $5 \mu\text{W}$, c'est-à-dire en régime linéaire d'excitation. Des expériences de photoluminescence résolues dans le temps ont été réalisées sur un échantillon de monocouche WSe₂ charge-ajustable, qui est également utilisé au chapitre 6 (voir les détails de l'échantillon à la section 6.2). Dans ce cas, l'échantillon est excité avec un laser à blocage de mode Ti:Sa (695 nm, largeur d'impulsion d'environ 1.5 ps, fréquence de répétition de 80 MHz). La cinétique PL est enregistrée par une caméra à balayage synchronisé Hamamatsu avec une résolution temporelle typique de 2 ps [101]. Nous ne nous

concentrerons pas sur les expériences de photoluminescence résolues en temps dans cette thèse, veuillez consulter les détails sur les montages expérimentaux dans la réf. [83, 101].

Tout d'abord, nous étudions la dépendance de la largeur de raie de luminescence X_0 en fonction de d . La **Figure 7.13(a)** affiche les spectres PL normalisés pour $d = 101$ nm et 186 nm. On observe une nette augmentation de plus d'un facteur 2 (4.3 meV contre 2 meV) de la largeur de raie de luminescence (FWHM). Comme le montre la **Figure 7.13(b)**, $d = 101$ nm et $d = 186$ nm correspondent à la position du ML au nœud et au ventre de l'intensité du champ optique respectivement dans la structure en forme de cavité (calculs basés sur la méthode matrice de transfert, détaillée au chapitre 2). Ainsi, la plus grande largeur de raie PL sur la **Figure 7.13(a)** pour $d = 186$ nm reflète la diminution du temps de recombinaison radiative due à l'effet Purcell déjà observé dans les ML MoSe₂ [101, 160-162]. La **Figure 7.13(b)** présente la variation de X_0 FWHM pour onze valeurs de d , confirmant le contrôle clair de la largeur de raie dû à l'effet de cavité. Afin de réduire les incertitudes, chaque valeur affichée sur la **Figure 7.13(b)** est la moyenne d'une vingtaine de mesures obtenues en différents points de la monocouche pour un d fixé. La nouveauté ici est la démonstration de l'effet en monocouche WSe₂. Contrairement à MoSe₂, l'exciton brillant dans la monocouche WSe₂ se situe au-dessus de l'exciton noir X_D , comme le montre l'encadré de la **Figure 7.14(a)**. La dépendance claire de la largeur de raie de l'exciton brillant mise en évidence sur la **Figure 7.13(a)** démontre qu'elle est dominée par la recombinaison radiative et que le canal de relaxation de l'exciton brillant froid à l'exciton noir situé plus bas joue un rôle mineur.

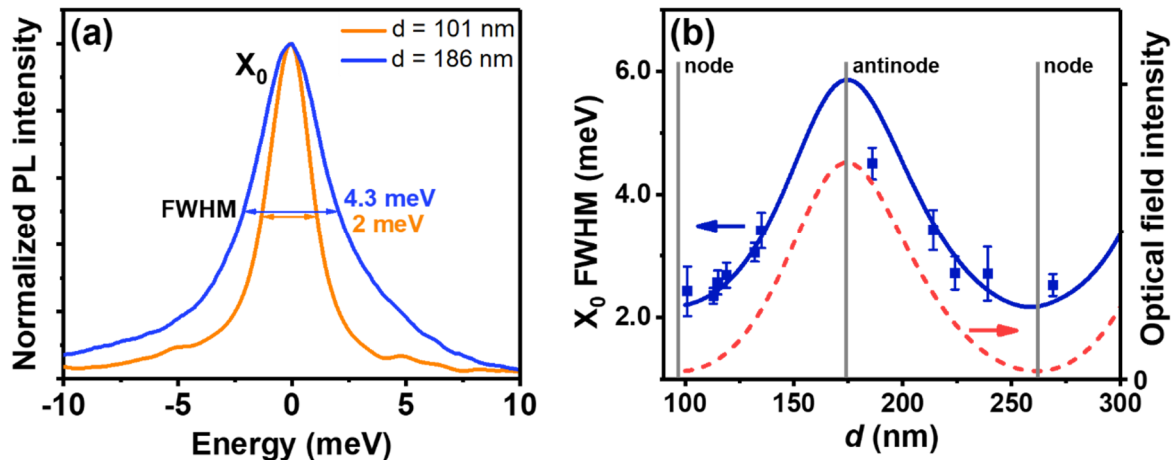


Figure 7.13 (a) Intensité PL normalisée de l'exciton neutre pour $d = 101$ nm et $d = 186$ nm montrant différentes largeurs de raie. Afin de comparer les largeurs de raie, l'origine de l'axe d'énergie est prise au pic PL. Les lignes à double flèche indiquent les largeurs de raie FWHM, qui sont décalées verticalement pour une meilleure visibilité. (b) Largeur de raie d'exciton neutre brillant mesurée (symboles bleus) et calculée (ligne continue bleue) en fonction de l'épaisseur de bottom hBN d . La courbe en pointillés rouges est l'intensité de champ optique calculée au niveau du plan monocouche. L'épaisseur où se trouve le ML aux nœuds et aux ventres est indiquée par les barres grises verticales.

Les **Figure 7.14(a)** et **(b)** présentent le résultat clé de ce chapitre. Nous avons mesuré la séparation de l'énergie des excitons brillants et noirs Δ pour les mêmes échantillons et épaisseurs de hBN d que ceux utilisés pour l'étude de l'effet Purcell. La **Figure 7.14(a)** affiche par exemple les spectres PL pour $d=132$ et $d=214$ nm (l'origine de l'énergie a été choisie à l'énergie X_D de l'exciton noir). On observe très nettement une variation $\delta E = 1.7$ meV du dédoublement. La variation δE de la séparation brillant-noir en fonction de d est représentée sur la **Figure 7.14(b)**. Notez que la séparation entre X_0 and X_D est $\Delta + \delta E$ en choisissant $\delta E = 0$ pour $d=100$ nm, c'est-à-dire lorsque le WSe₂ ML est au nœud du champ électrique dans la structure en forme de cavité. Nous mettons en évidence une modulation significative et oscillatoire de δE en fonction de l'amplitude du champ électromagnétique. Ces résultats démontrent que la différence d'énergie entre les excitons brillants et noirs n'est pas seulement contrôlée par l'interaction d'échange électron-trou et les paramètres de structure de la bande semi-conductrice, mais que le couplage au champ électromagnétique doit également être pris en compte.

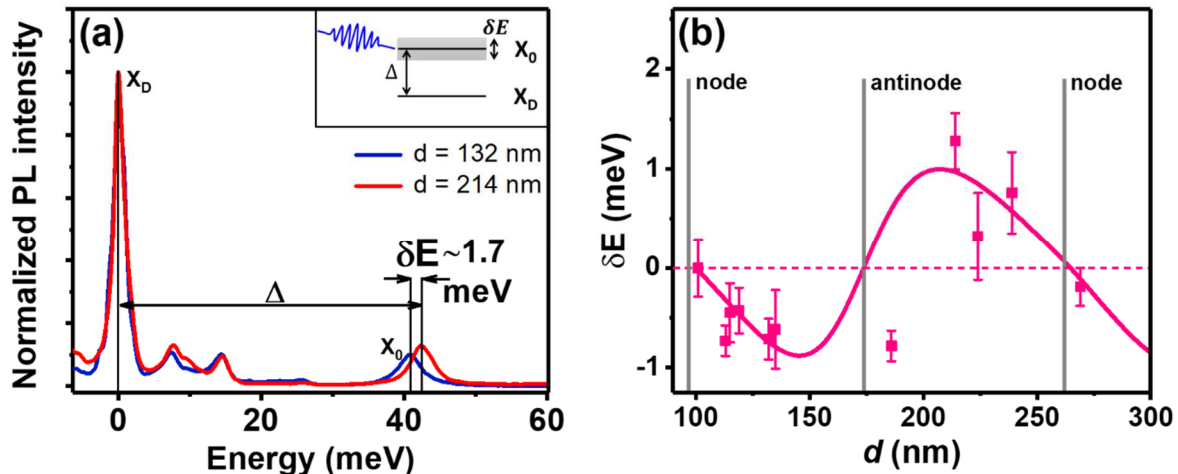


Figure 7.14 Spectres PL normalisés pour $d=132$ nm et $d=214$ nm. L'axe d'énergie est pris au pic X_D PL pour montrer le décalage d'énergie de transition δE de X_0 . Encart : schémas du décalage d'énergie de transition de X_0 (ombre grise) dû au décalage de Lamb. (b) Variation mesurée (symboles roses) et calculée (ligne continue rose) δE de la division de l'exciton brillant-noir en fonction de l'épaisseur du bottom hBN d.

La variation de la largeur de raie de l'exciton et la séparation de l'énergie de l'exciton brillant-noir présentés sur la **Figure 7.13(b)** et la **Figure 7.14(b)** peuvent être bien compris sur un modèle basé sur le formalisme de matrice de transfert et les approches électrodynamiques quantiques (voir l'annexe). Ce modèle a été développé par M. Glazov et M. Semina (Ioffe Institute, St Petersburg). Afin de comparer les expériences et les prédictions théoriques, nous avons calculé les fonctions de réponse linéaires (réflectivité, transmission et absorbance) de notre empilement « top hBN /WSe₂ ML/Bottom hBN/SiO₂/Si » avec top hBN de 10 nm, SiO₂ de 83 nm et bottom hBN variable d. Dans les calculs, nous avons utilisé les indices de réfraction suivants : $n_{\text{hBN}} = 2.2$, $n_{\text{SiO}_2} = 1.46$, $n_{\text{Si}} = 3.5$ [75].

La ligne pleine de la **Figure 7.13(b)** est la dépendance calculée de la largeur de raie d'exciton brillant avec $\Gamma = \Gamma_0 + \Gamma_{nr}$, où Γ_0 and Γ_{nr} sont les contributions radiative et non radiative respectivement extraites du coefficient d'absorption calculé. Nous remarquons un très bon accord entre la dépendance mesurée et calculée en utilisant le taux radiatif de l'exciton dans le vide $\Gamma_0^{\text{vac}} = 2 \text{ meV}$ et $\Gamma_{nr} = 0.6 \text{ meV}$. Notez que le taux de déclin radiative est cohérent avec les estimations expérimentales et théoriques précédentes du taux de recombinaison dans la monocouche WSe₂ où l'effet de cavité n'a pas été pris en compte [80, 83, 163]. Remarquablement, les mêmes paramètres dans le modèle donnent également une très bonne description de la dépendance de la séparation de l'exciton brillant-noir en conséquence du décalage de Lamb, voir la ligne pleine sur la **Figure 7.14(b)**. L'écart observé pour $d = 186 \text{ nm}$ pourrait être dû à une valeur anormalement élevée de la densité de dopage pour ce point attestée par une plus grande intensité trion PL.

En électrodynamique quantique, la variation du taux de déclin radiative et de l'énergie de l'exciton provient de son couplage avec les fluctuations du vide du champ électromagnétique. La modification de l'épaisseur d du bottom hBN modifie la structure locale des modes électromagnétiques dans le système et, par conséquent, Γ_0 et δE . L'analyse en annexe montre que ces grandeurs peuvent également être évaluées de manière semi-classique, en utilisant la méthode de la matrice de transfert et exprimées via la fonction de Green électrodynamique. Des expressions analytiques compactes peuvent être dérivées en négligeant l'effet couche de couverture, dans ce cas (voir annexe et réf. [101]) :

$$\Gamma_0 + i \delta E = \Gamma_0^{\text{vac}} (1 + r_{bg}), \quad (3.1)$$

où r_{bg} est le coefficient de réflexion complexe d'une structure à trois couches "hBN/SiO₂/Si", ainsi le facteur de Purcell et le décalage de Lamb sont proportionnels aux parties réelles et imaginaires du coefficient de réflexion du substrat. Il est instructif de considérer un cas illustratif d'une structure à cavité ouverte simplifiée basée sur un WSe₂ ML situé à une distance d' d'un miroir non absorbant caractérisé par un coefficient de réflexion réel r [164]. Dans ce cas, $r_{bg} = r \exp(2iqd')$, $q = \omega/c$, c est la vitesse de la lumière et $\hbar\omega$ l'énergie de l'exciton, et la largeur de raie radiative de l'exciton et la variation de séparation clair-foncé s'écrivent simplement (voir annexe) :

$$\Gamma_0 = \Gamma_0^{\text{vac}} [1 + r \cos(2qd')], \quad (3.2a)$$

$$\delta E = r \Gamma_0^{\text{vac}} \sin(2qd'). \quad (3.2b)$$

Ces expressions simples montrent directement pourquoi les deux mesures sont en quadrature sur la **Figure 7.13(b)** et la **Figure 7.14(b)**. Contrairement à la largeur de raie qui présente comme prévu des minima et des maxima aux nœuds et ventres respectivement, la variation de séparation brillant-noir δE est strictement nulle pour ces deux positions, en parfait accord avec l'Eq. (3.2b). Un tel comportement est général et découle des relations de dispersion pour la réflectivité dans l'Eq. (3.1), voir l'annexe pour plus de détails.

Pompage spin-vallée des électrons résidents dans les monocouches WSe₂ et WS₂

Nous avons fabriqué un dispositif charge ajustable d'une monocouche WSe₂ avec encapsulation hBN dans une boîte à gants avec l'atmosphère inerte. Le processus de fabrication, le croquis de l'échantillon et l'image de microscope de l'échantillon WSe₂ sont détaillés à la section 2.1. L'échantillon WS₂ ML est fabriqué avec une encapsulation hBN en utilisant la même technique mais sans électrodes. Les expériences sur l'échantillon WS₂ a été réalisée en collaboration avec le groupe de Fabian Cadiz au Laboratoire PMC (Ecole Polytechnique).

En ajustant la tension entre la grille arrière et la monocouche, nous pouvons la doper électrostatiquement. La densité de porteurs dans la monocouche peut être estimée à l'aide d'un simple modèle de capaciteur, connaissant la tension appliquée (V), l'épaisseur hBN t (210 nm dans notre dispositif) et en utilisant une constante diélectrique hBN de $\epsilon_{hBN} \sim 3$ [174, 175]. Le changement de densité d'électrons (trous) Δn (Δp) est lié à un changement de tension ΔV par Δn (Δp) = $\frac{\epsilon_0 \epsilon_{hBN}}{e * t} \Delta V$. Notons que par convention, on choisit qu'un biais positif (négatif) conduit à un dopage de trou (électron).

Alternativement, nous pouvons utiliser les oscillations du spectre de réflectivité de l'exciton brillant en fonction de la tension observée à +9 T dans le régime dopé p (**Figure 7.15(b)**). Comme démontré dans la Réf. [176], ces oscillations sont dues à l'interaction de l'exciton avec les niveaux de Landau quantifiés du trou Mer de Fermi (voir le schéma de la **Figure 7.15(a)**). La période des oscillations ΔV_{LL} est liée au remplissage d'un niveau de Landau $P_{LL} = \frac{eB}{2\pi\hbar} = 2.18 \times 10^{11} \text{ cm}^{-2}$. On peut ainsi calculer la densité de trous en fonction de la tension de grille par: $\Delta p = \Delta V \frac{P_{LL}}{\Delta V_{LL}}$. On obtient ainsi la même estimation de la densité de porteurs que celle déduite du modèle de capaciteur. L'avantage de cette méthode est qu'elle ne nécessite pas la connaissance des paramètres du matériau (épaisseur hBN et constante diélectrique).

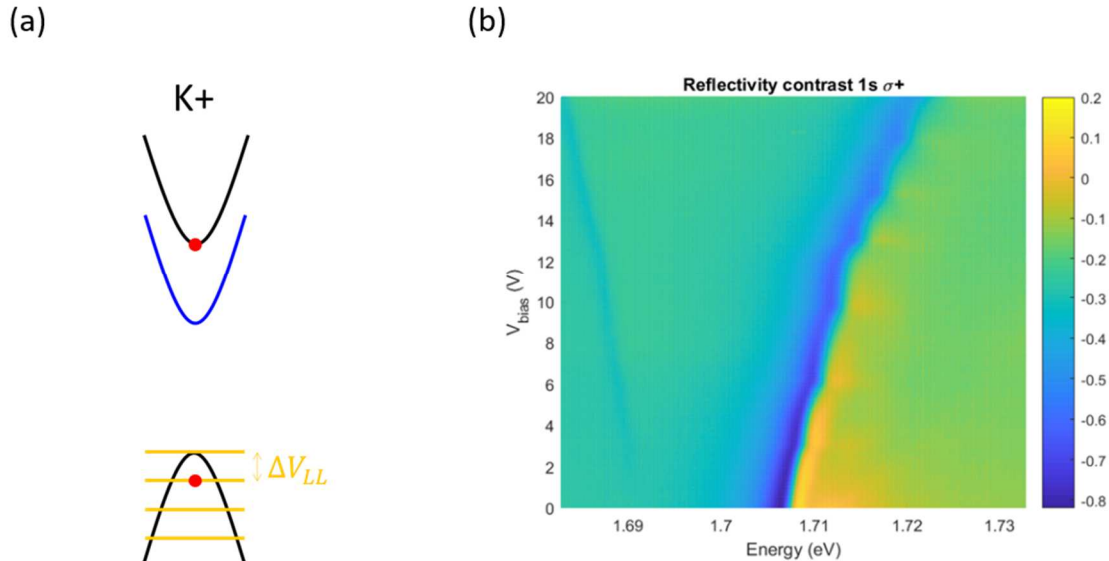


Figure 7.15 (a) Schéma de la structure de bande de la vallée K^+ (en régime dopé p) à champ magnétique positif montrant les niveaux de Landau. (b) Première dérivée du contraste de réflectivité avec σ^+ détection en fonction de la tension de grille à +9 T.

Les mesures de polarisation sont effectuées dans les montages de spectroscopie optique présentés dans la section 2.3.4. Pour WSe₂, nous utilisons un laser He-Ne de 632.8 nm à T = 4 K. Sauf indication contraire, la puissance d'excitation est de 5 µW. Comme déjà expliqué au chapitre 1, nous limitons notre étude à des densités d'électrons modérées de quelques 10¹¹ cm² dans le WSe₂ ML afin que l'image simple à trois particules (c'est-à-dire les trions) soit équivalente à l'image à plusieurs corps (c'est-à-dire les polarons de Fermi). Pour le WS₂ ML naturellement dopé n sans réglage de charge, un laser à colorant continu à une longueur d'onde de 570 nm avec une puissance d'excitation de 18 µW à T = 20 K a été utilisé. Les mesures de polarisation sont effectuées dans les montages de spectroscopie optique présentés dans la section 2.3.4. Les mesures de photoluminescence résolue en temps (TRPL) présentées ci-après sont réalisées dans des conditions similaires : nous avons utilisé un laser ps-pulsé (Ti:Sa) à une longueur d'onde de 695 nm pour WSe₂, et un OPO à 570 nm pour WS₂. Le signal est détecté par une caméra à balayage Hamamatsu avec une résolution temporelle d'environ 2-3 ps.

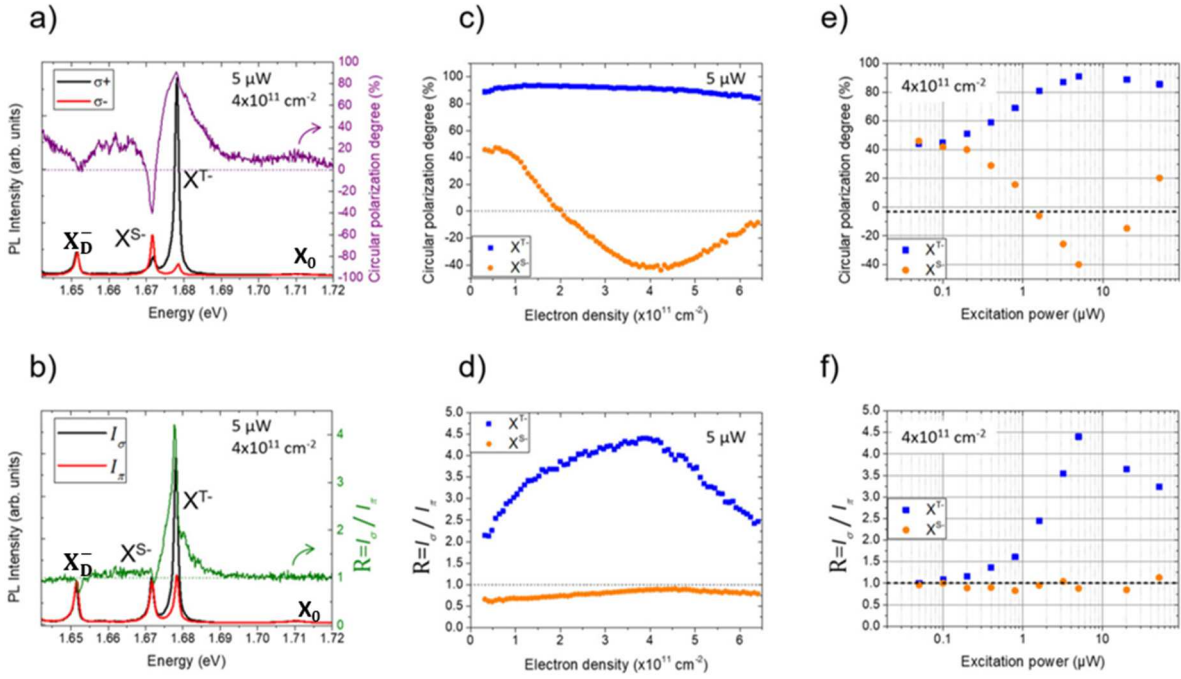


Figure 7.16 Observations expérimentales dans WSe_2 dopé n . (a) Spectres de photoluminescence et de polarisation circulaire pour les détections σ^+ et σ^- avec σ^+ excitation. (b) Spectres de photoluminescence totale avec excitation circulaire et excitation linéaire. (c) Degré de polarisation circulaire au pic des trions négatifs triplet et singulett en fonction de la densité électronique. (d) Rapport des intensités PL entre les excitations circulaires et linéaires au pic pour le triplet et le singulett en fonction de la densité d'électron. (e) Degré de polarisation circulaire au sommet du triplet et du singulett en fonction de la puissance d'excitation. (f) Rapport des intensités PL entre les excitations circulaires et linéaires au pic pour le triplet et le singulett en fonction de la puissance d'excitation.

Excitation circulaire et détection. La Figure 7.16 présente les principaux résultats de ce chapitre. Dans la Figure 7.16(a), nous montrons les spectres de photoluminescence pour les détections σ^+ et σ^- suite à une excitation σ^+ . Alors que l'exciton brillant X_0 présente une polarisation circulaire positive inférieure à +20 % en raison de l'interaction d'échange efficace à longue distance, les lignes du doublet trion brillant présentent une forte polarisation circulaire de signe opposé: +91 % pour X^{T-} et -40 % pour X^{S-} au pic. Notez que cette polarisation négative sur le singulett a été observée ailleurs récemment dans des échantillons de l'état de l'art [178]. Le trion noir X_D^- ne montre aucune polarisation circulaire en accord avec sa polarisation hors plan [86,177,180].

Excitation circulaire et linéaire. Ensuite, nous passons à l'excitation linéaire π_X et mesurons à la fois les intensités colinéaires I_X et transversales I_Y . Nous définissons l'intensité PL totale suite à une excitation linéaire comme $I_\pi = I_X + I_Y$ et l'intensité totale suite à une excitation circulaire comme $I_\sigma = I_{\sigma^+} + I_{\sigma^-}$. Nous montrons sur la Figure 7.16(b) à la fois I_π et I_σ et le rapport $R = \frac{I_\sigma}{I_\pi}$. Il n'y a pas de différence d'intensité pour X_0 entre l'excitation linéaire et circulaire (c'est-à-dire $R=1$). En revanche, R atteint une valeur très élevée de 4.4 au sommet de X^{T-} et légèrement inférieure à 1 pour X^{S-} .

et X_D^- . En d'autres termes et de manière surprenante, l'intensité PL de X^{T-} est plus de 4 fois plus grande lorsque nous excitons avec une lumière polarisée circulairement.

Dépendances de la densité d'électron et de la puissance d'excitation. Sur la **Figure 7.16(c) et (d)**, nous montrons P_c et R mesurés aux pics d'émission du doublet trion brillant en fonction de la densité électronique pour une puissance d'excitation fixe de $5 \mu\text{W}$. La très grande polarisation positive de X^{T-} est presque constante tandis que pour X^{S-} elle varie de positive à faible dopage à négative pour des densités supérieures à $2 \times 10^{11} \text{ cm}^2$ et atteint la valeur minimale de -40% pour $4 \times 10^{11} \text{ cm}^2$. Concernant le rapport des intensités PL entre les excitations circulaires et linéaires (voir **Figure 7.16(d)**), il reste supérieur à $R=2$ dans toute la gamme de densité électronique étudiée pour X^{T-} et légèrement inférieur à 1 pour X^{S-} . Enfin, nous présentons sur la **Figure 7.16(e) et (f)** la dépendance de la puissance d'excitation à une densité de dopage électronique de $4 \times 10^{11} \text{ cm}^{-2}$. On voit clairement que lorsqu'on diminue la puissance d'excitation, P_c converge vers une valeur autour de 50 % pour X^{T-} et X^{S-} et que R diminue et se rapproche de 1 pour X^{T-} , alors qu'il reste constant et proche de 1 pour X^{S-} .

Nous montrons sur la **Figure 7.17(a)** les configurations à trois particules des trions triplet et singulet σ^+ et σ^- . Comme déjà expliqué précédemment, un trion triplet est constitué d'une paire électron-trou photo-générée (exciton constitué d'un électron dans la bande de conduction la plus haute et d'un trou dans la même vallée) liée à un électron résident dans la bande de conduction inférieure située dans l'autre vallée. D'autre part, un trion singulet est composé d'une paire électron-trou photo-générée liée à un électron résident dans la même vallée. Expérimentalement, nous observons que lors de l'excitation avec un laser polarisé σ^+ , les deux pics PL les plus forts sont le trion triplet σ^+ et le trion singulet σ^- (voir **Figure 7.16(a)**). Ces deux configurations sont surlignées en rouge sur la **Figure 7.17(a)**. Dans les deux cas, l'électron résident dans le complexe à trois particules se trouve dans la vallée K^- . Ainsi, si nous supposons que les mécanismes de formation des trions triplet et singulet sont les mêmes, le signe opposé de la polarisation des trions triplet et singulet ne peut s'expliquer que par une plus grande population d'électrons résidents dans la vallée K^- par rapport à la K^+ vallée.

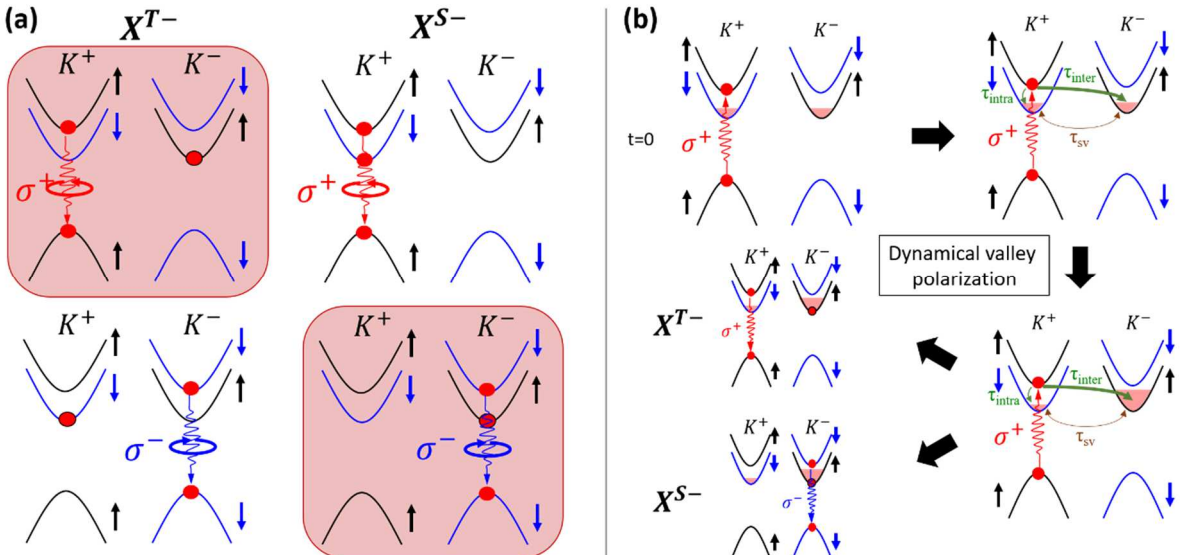


Figure 7.17 Mécanisme de pompage spin-vallée. (a) Croquis des images de trois particules du triplet brillant X^{T-} et du singulet X^{S-} trions négatifs avec σ^+ et σ^- émission. Les deux trions majoritaires suite à une excitation σ^+ cw sont surlignés en rouge. (b) Esquisse de la polarisation dynamique des électrons résidents avec σ^+ excitation. τ_{inter} (τ_{intra}) représente les temps de relaxation de l'intervallée conservant le spin (intravallée spin-flip) des électrons les plus hauts tandis que τ_{sv} correspond au temps de relaxation spin-vallée des électrons résidents.

Nous proposons sur la **Figure 7.17(b)** un mécanisme qui polarise dynamiquement les électrons résidents, d'une manière analogue à la polarisation de spin dynamique dans les semi-conducteurs conventionnels [183–185].

Sans excitation optique ni champ magnétique, les densités d'électrons résidents sont similaires dans les vallées K^+ et K^- . En excitant continuellement avec de la lumière polarisée σ^+ , les électrons sont photo-générés dans la vallée supérieure de la bande de conduction de K^+ . Ces électrons sont libres ou liés à des trous photo-générés et peuvent se détendre vers les bandes de conduction inférieures à la fois dans les vallées K^+ et K^- par différents mécanismes. La relaxation intra-vallée (constante de temps τ_{intra} sur la **Figure 7.17(b)**) nécessite un retournement de spin électronique alors que la relaxation intervallée (constante de temps τ_{inter} sur la **Figure 7.17(b)**) conserve le spin de l'électron. Lorsque la relaxation d'énergie est régie par des interactions électron-phonon, la relaxation conservatrice de spin est associée au gradient de la composante indépendante du spin du potentiel cristallin, tandis que les interactions spin-flip sont associées à la composante d'interaction spin-orbite. Tant que les états électroniques ne sont pas fortement mélangés en spin, les processus de conservation du spin sont généralement plus forts, ce qui entraîne une relaxation de l'impulsion plus rapide par rapport à la relaxation du spin (c'est-à-dire $\tau_{inter} < \tau_{intra}$). Récemment, He et al. ont analysé la polarisation des trions noirs dans un ML WSe₂ et ont montré que la relaxation par intervalles conservant le spin, médiée par les phonons de bord de zone, est en effet plus forte que la relaxation intravallée de spin-flip qui est médiée par les phonons de centre de zone [178]. Par conséquent, la population d'électrons dans la bande de conduction K^- la plus basse devient plus grande que la

population d'électrons dans la bande de conduction K^+ la plus basse lors de l'excitation par une lumière polarisée circulairement σ^+ (c'est-à-dire la polarisation de la vallée).

Sous excitation cw, le mécanisme de la **Figure 7.17(b)** est répété plusieurs fois, ce qui entraîne une accumulation dynamique de la polarisation de la vallée. Cette polarisation de vallée dynamique est durable si le taux de génération de paires électron-trou photo-excitées est plus rapide que le taux auquel les électrons rétablissent l'équilibre thermique entre les vallées de bande de conduction les plus basses de K^+ et K^- par relaxation de spin intermittente (le temps de relaxation de vallée de spin τ_{sv} sur la **Figure 7.17(b)**). Ce dernier est un processus relativement lent à basse température, mesuré pour être aussi long que 100 ns à plusieurs μ s dans un WSe₂ ML [105–108] car il est médié par des transitions spin-flip intervallée, qui sont interdits à l'ordre de tête par symétrie d'inversion du temps [186, 187]. Ainsi, même si l'accumulation de la polarisation dynamique de la vallée est lente parce que la relaxation conservant le spin de l'intervalle (τ_{inter}) n'est pas beaucoup plus rapide que celle du spin-flip intravalley (τ_{intra}), la polarisation de la vallée atteignable peut encore être très grande (nous donnerons une estimation de ~80% dans ce qui suit). Nous mentionnons que d'autres mécanismes de transfert de polarisation des porteurs photo-générés aux électrons résidents ont été proposés par Ersfeld et al. [188] et Fu et al. [189] considérant les différences dans les taux de recombinaison des excitons indirects et des excitons noirs à spin interdit ou les différences dans les taux de relaxation du singule et du triplet aux trions noirs. Dans chaque scénario, les deux ingrédients sont les mêmes : création d'une asymétrie dans la population d'électrons résidents et longs temps de relaxation spin-flip intervallée.

Une fois que l'on considère que les électrons résidents peuplent principalement la vallée K^- , on peut expliquer la très grande polarisation du trion triplet et la polarisation négative du trion singule. Avant une discussion détaillée sur la polarisation des deux trions, nous supposons d'abord que les trions brillants sont formés par la liaison d'excitons brillants photo-générés avec un électron résident (c'est-à-dire une formation bimoléculaire [190]).

Avant d'entrer dans le détail de ce modèle, nous faisons deux hypothèses qui sont justifiées dans le chapitre 4:

(1) La densité électronique est beaucoup plus grande que la densité d'excitons photo-générés. Cette hypothèse peut exclure que le trion puisse affecter de manière importante la population d'électrons résidents, justifiant que la polarisation circulaire des deux trions soit une « sonde » de la polarisation des électrons résidents.

(2) La relaxation de spin des trions est beaucoup plus lente que leur durée de vie de recombinaison (c'est-à-dire que la polarisation observée dans les expériences cw correspond à la polarisation à la formation du trion).

Maintenant, nous pouvons estimer la polarisation circulaire des deux trions sur la base du modèle de formation bimoléculaire simple par (voir le modèle en détail dans le chapitre 4):

$$P_c(X^{T-}) = \frac{P_0 - P_e}{1 - P_0 P_e}$$

$$P_c(X^{S-}) = \frac{P_0 + P_e}{1 + P_0 P_e}$$

où P_0 est le degré de polarisation de l'exciton lumineux photo-généré (excitons chauds photo-générés ; ou paires électron-trou non liées qui finissent par se lier aux électrons résidents pour former des trions) et P_e est le degré de polarisation de électrons résidents.

Ainsi le rapport des intensités entre excitation circulaire et linéaire s'écrit simplement:

$$R(X^{T-}) = \frac{I_{circ}(X^{T-})}{I_{lin}(X^{T-})} = 1 - P_0 P_e$$

$$R(X^{S-}) = \frac{I_{circ}(X^{S-})}{I_{lin}(X^{S-})} = 1 + P_0 P_e$$

Les résultats de la **Figure 7.16(a)** ($P_c(X^{T-})=91\%$ et $P_c(X^{S-})=-40\%$) correspondent bien avec $P_0=51\%$ et $P_e=-76\%$; c'est-à-dire que les électrons résidents sont fortement polarisés dans la vallée K^- . Voir les défauts de ce model et les résultats similaires sur la monocouche WS₂ dans le chapitre 4.

Détection optique de longues longueurs de transport de spin d'électrons dans les monocouches WSe₂

Nous utilisons le même dispositif charge ajustable WSe₂ ML mentionné au chapitre 4 pour effectuer une expérience pompe-sonde à résolution spatiale. La **Figure 7.18** présente un schéma de l'expérience PL pompe-sonde réalisée sur le dispositif. Nous limitons toujours notre étude à des densités d'électron modérées de quelques 10^{11} cm^2 dans WSe₂ ML comme dans le dernier chapitre. Des faisceaux laser He-Ne à onde continue ($\lambda=632.8 \text{ nm}$) sont utilisés à la fois pour la pompe et la sonde. En utilisant le même objectif à grande ouverture numérique, les deux faisceaux sont focalisés sur l'échantillon à deux positions différentes séparées par une distance d . Le faisceau pompe est polarisé circulairement droit (σ^+) tandis que le faisceau sonde est polarisé linéairement (σ_x). Nous détectons à la fois la luminescence polarisée circulairement droite (σ^+) et gauche (σ^-) déclenchée par le faisceau sonde, en fonction de la séparation pompe-sonde d . La lumière polarisée circulairement σ^+ peut créer localement des électrons résidents polarisés en spin sous le point de pompe comme détaillé au chapitre 4. La lumière polarisée linéairement σ_x (puissance d'excitation beaucoup plus faible par rapport à la pompe) sert de sonde pour détecter la polarisation circulaire de la deux trions sous la tache de la sonde, qui est un indicateur de la polarisation de spin de l'électron résident. Au final, on peut cartographier la polarisation de spin de l'électron résident en faisant varier la distance pompe-sonde d .

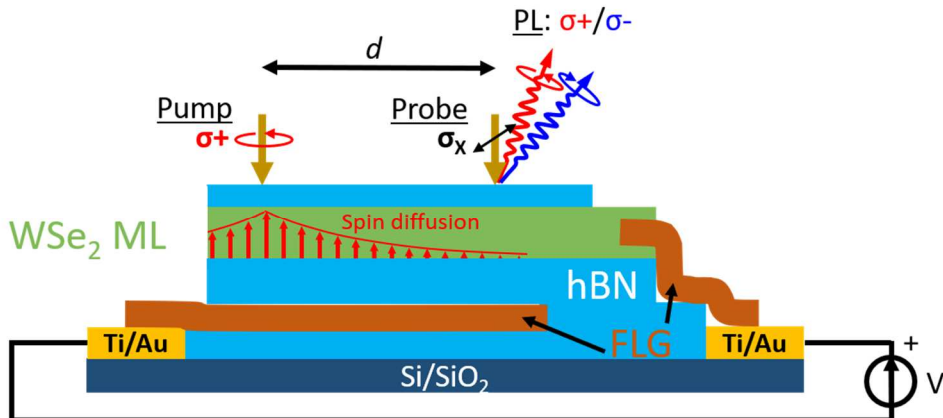


Figure 7.18 Croquis du WSe₂ ML réglable en charge. Deux spots laser (pompe et sonde) séparés d'une distance d , sont focalisés sur l'échantillon. La pompe est polarisée circulairement (σ^+) et polarise dynamiquement les électrons résidents dans la vallée K^- avec spin up. Cette polarisation spin/vallée diffuse sur de longues distances (schématisées par les flèches rouges verticales représentant le spin électronique moyen selon la direction perpendiculaire au ML) et est détectée par une sonde polarisée linéairement (σ_x). La polarisation circulaire des X^{S-} et X^{T-} PL induits par la sonde fournit une mesure quantitative de la polarisation de la mer d'électrons 2D à l'emplacement de la tache de la sonde.

Il est important de noter que le degré de polarisation circulaire du trion X^{T-} et X^{S-} PL peut servir de sonde quantitative de la polarisation de la vallée de spin des électrons résidents, comme démontré dans le chapitre précédent et résumé ci-dessous. En supposant que les trions sont formés par la liaison d'excitons lumineux photo-générés avec un électron résident (c'est-à-dire un processus de formation bimoléculaire [190]), la polarisation circulaire du triplet $P_c(X^{T-})$ et du singulette $P_c(X^{S-})$ sont simplement liés à la polarisation de spin des électrons résidents $P_e = \frac{n_e^{\uparrow K^-} - n_e^{\downarrow K^+}}{n_e^{\uparrow K^-} + n_e^{\downarrow K^+}}$ (où $n_e^{\uparrow K^-}$ et $n_e^{\downarrow K^+}$ sont les populations d'électrons résidents avec spin up (K^- vallée) et spin down (K^+ vallée) et la polarisation des excitons photogénérés $P_0 = \frac{N_0^{K^+} - N_0^{K^-}}{N_0^{K^+} + N_0^{K^-}}$ (où $N_0^{K^+}$ et $N_0^{K^-}$ sont les populations d'excitons lumineux photo-générés avec des porteurs dans les vallées K^+ et K^-). Notez que dans le chapitre précédent nous avons défini $P_e = \frac{n_e^{K^+} - n_e^{K^-}}{n_e^{K^+} + n_e^{K^-}}$ et ici nous redéfinissons P_e en évitant le degré de polarisation de spin négatif. Suivant cette nouvelle convention, le degré de polarisation de spin est maintenant positif car il y a plus d'électrons résidents dans la vallée K^- que dans la vallée K^+ suite à une excitation σ^+ .) ; On obtient:

$$\text{Triplet} \quad P_c(X^{T-}) = \frac{P_0 + P_e}{1 + P_0 P_e} \quad (5.1)$$

$$\text{Singulette} \quad P_c(X^{S-}) = \frac{P_0 - P_e}{1 - P_0 P_e} \quad (5.2)$$

En mesurant à la fois $P_c(X^{T-})$ et $P_c(X^{S-})$ nous pouvons donc facilement quantifier la polarisation des électrons résidents P_e .

Nous caractérisons d'abord sur la **Figure 7.19(a)** les spectres PL émis suite à une excitation laser polarisée circulairement (σ^+) (puissance=5 μ W et densité de dopage électronique= 4×10^{11} cm $^{-2}$). La polarisation circulaire du trion triplet X^{T-} PL atteint de très grandes valeurs positives, alors qu'elle est négative pour le trion singulet X^{S-} PL. Comme détaillé dans le chapitre précédent, C'est une conséquence directe d'un mécanisme de pompage de la vallée de spin qui polarise dynamiquement les électrons résidents dans la vallée K^- avec spin up. Notez que l'efficacité du mécanisme de pompage de la vallée de spin dépend à la fois de la puissance d'excitation et de la densité de dopage. La densité électronique choisie ici maximise la polarisation en spin des électrons tout en gardant un trion PL suffisamment intense. En utilisant les valeurs de $P_c(X^{T-})$ et $P_c(X^{S-})$, on trouve que la polarisation des électrons résidents induite par le laser atteint des valeurs aussi grandes que $P_e=76\%$ (i.e. les électrons résidents peuplent principalement la bande de conduction de spin-up inférieure dans la vallée K^-) tandis que la polarisation des excitons photogénérés P_0 est de 51 %.

Nous montrons ensuite, sur la **Figure 7.9(b)** les spectres PL émis suite à une excitation laser faiblement polarisée linéairement (σ_X) (puissance=200 nW). Comme prévu, il n'y a pas de polarisation circulaire de X^{T-} ou X^{S-} PL car $P_0 = 0$ (excitation linéaire) et $P_e = 0$ (pas de mécanisme de pompage spin/vallée pour l'excitation linéaire).

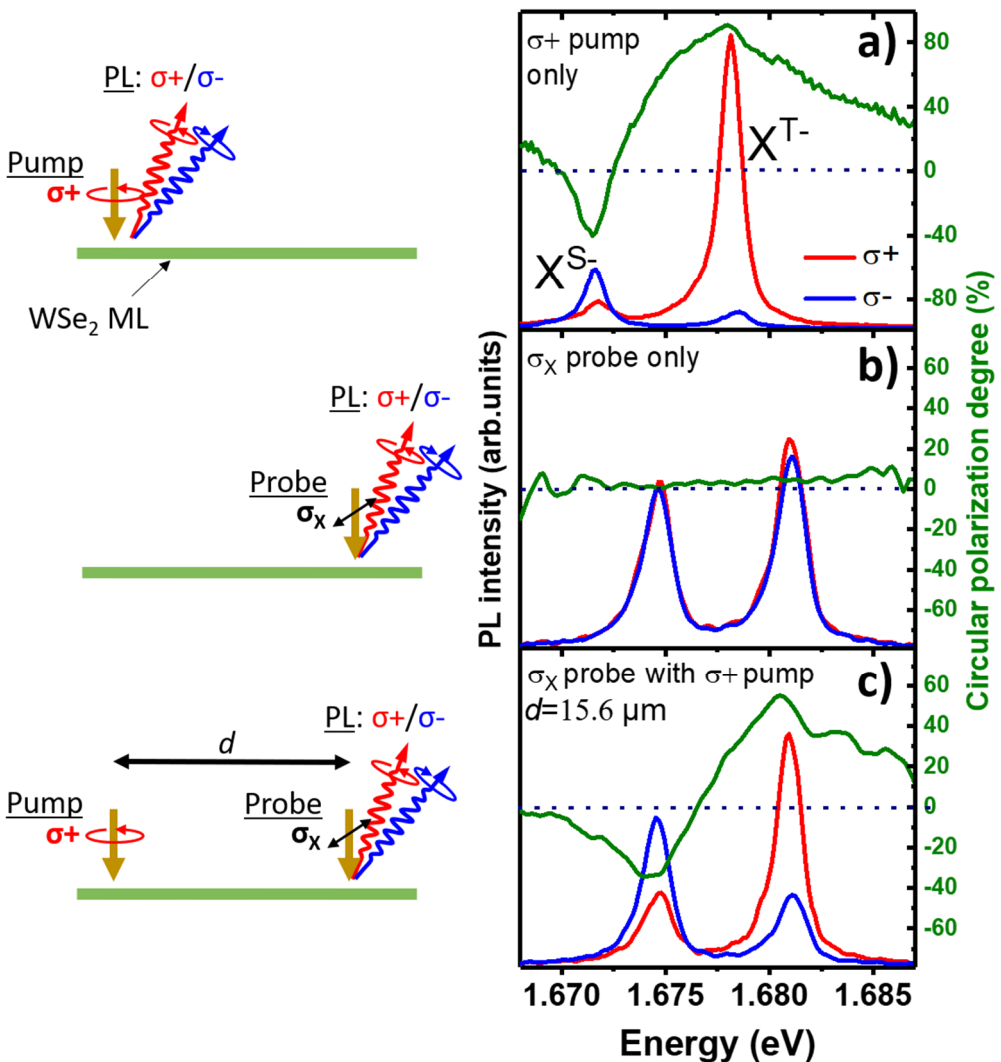


Figure 7.19 Spectres PL à polarisation circulaire droite (σ^+) et gauche (σ^-) et degré de polarisation circulaire correspondant, en réponse à (a) la pompe σ^+ uniquement, (b) la sonde linéaire σ_x uniquement et (c) la Sonde σ_x en présence d'une pompe σ^+ séparée par une distance $d=15.6 \mu\text{m}$. La forte polarisation circulaire du trion PL démontre que les électrons résidents sont fortement polarisés en vallée de spin à la position du laser sonde. $T=5\text{K}$.

La **Figure 7.19(c)** montre le premier résultat clé de ce chapitre. Il présente le spectre PL induit par le laser σ_x faible (sonde), mais maintenant en présence du laser σ^+ (pompe) qui est séparé par une distance $d=15.6 \mu\text{m}$ (représenté schématiquement sur la **Figure 7.18**) Remarquablement, maintenant nous observons une très grande polarisation circulaire pour les deux trions (~+50% pour X^{T-} et ~-40% pour X^{S-}). Comme $P_0 = 0$ pour la sonde (excitation linéaire), ce résultat révèle directement la polarisation des électrons résidents à l'emplacement de la sonde (i.e. $P_c(X^{T-}) = P_e$ et $P_c(X^{S-}) = -P_e$; voir les équations (6.1) et (6.2)). Parce que la sonde à polarisation linéaire elle-même ne polarise pas les électrons résidents (comme indiqué ci-dessus),

cela démontre que la polarisation de spin des électrons résidents induite par la pompe se propage dans le plan de couche 2D et peut être détectée en mesurant la polarisation circulaire du trion PL sous la sonde. Un avantage clé de cette expérience pompe-sonde basée sur PL par rapport aux méthodes d'imagerie de rotation de spin Kerr/Faraday bien connues et puissantes [224,225] est qu'elle permet de quantifier, en termes absolus, la polarisation de spin de la mer de Fermi d'électrons.

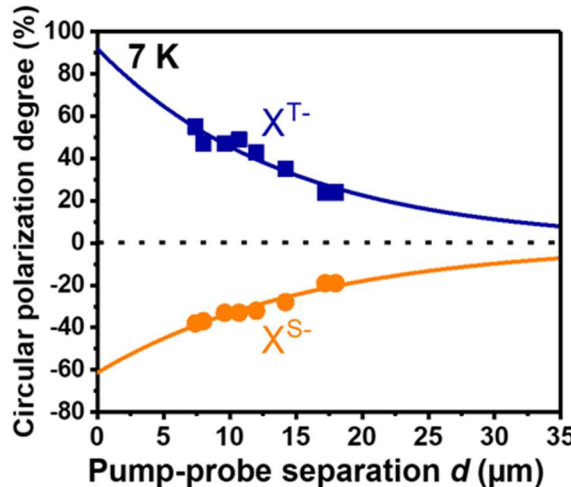


Figure 7.20 Degré de polarisation circulaire du trion X^{T-} et X^{S-} PL, en fonction de la séparation pompe-sonde d . Les lignes pleines sont des ajustements exponentiels.

La **Figure 7.20** présente le résultat principal de ce travail. Il affiche la dépendance de la sonde PL polarisation circulaire des deux trions en fonction de la séparation pompe-sonde d . Une décroissance spatiale de la polarisation de spin des électrons résidents est clairement mise en évidence, mais la polarisation des électrons résidents induite par la pompe peut se propager sur des échelles de longueur supérieures à 20 μm . Nous constatons que la polarisation de spin décroît approximativement de façon exponentielle avec une longueur de diffusion de spin de $L_s=18 \pm 3 \mu\text{m}$. C'est l'une des plus longues longueurs de diffusion de spin rapportées dans les semi-conducteurs, malgré une mobilité des porteurs modeste [226-228]. Elle est dix fois plus grande que L_s mesurée dans le silicium ou le GaAs de type p à basse température, et est similaire à la longueur de diffusion de spin mesurée dans la masse de GaAs dopé n [225, 229-231] ou les puits quantiques [232-234]. Remarquablement, la longueur de diffusion de spin que nous mesurons ici pour un WSe₂ ML est très similaire à celle déterminée dans les monocouches de graphène, qui sont généralement caractérisées par une mobilité électronique beaucoup plus grande et un couplage spin-orbite plus faible. En utilisant des géométries de valve de spin «non locales» dans le graphène, des longueurs de diffusion de spin de 2 μm ont été mesurées et des valeurs record de $L_s = 30 \mu\text{m}$ ont été rapportées plus récemment [235, 236]. Cela souligne le rôle clé joué par l'effet de verrouillage de la vallée de spin dans les TMD ML sur la propagation du spin des porteurs.

Measurement of Conduction and Valence Bands g-factors in WSe₂ Monolayers

Dans ce travail, nous utilisons un échantillon charge ajustable similaire à celui utilisé dans les chapitres 4 et 5. La seule différence est que les contacts métalliques ont été réalisés par lithographie par faisceau d'électrons après la fabrication de l'hétérostructure. Les mêmes résultats ont été obtenus dans l'échantillon utilisé au chapitre 4.

Des expériences magnéto-PL à T = 5 K et dans des champs magnétiques jusqu'à 9 T ont été réalisées dans la configuration du microscope confocal mentionnée dans la section 2.3.5. L'échantillon est excité par un laser He-Ne (1,96 eV) à polarisation linéaire et les signaux PL polarisés σ^+ et σ^- sont détectés à l'aide d'un retardateur à cristaux liquides et d'un analyseur dans le chemin de détection. La puissance moyenne du laser est d'environ 10 μW , ce qui est toujours dans le régime d'absorption linéaire.

La méthode présentée ci-dessous pour déterminer les facteurs-g de CB et VB sera appliquée d'abord dans le régime de très faible densité de dopage, typiquement $p \sim 10^{11} \text{ cm}^{-2}$, afin d'éviter les effets de renormalisation de la bande interdite [271]. Notez que cette densité de dopage est de deux ordres de grandeur plus faible que la densité de Mott critique dans ML WSe₂ [272, 273].

La **Figure 7.21(b)** présente schématiquement la structure de bande à une seule particule de ML WSe₂ au voisinage de ses bords CB et VB, ainsi que les règles de sélection optique associées à la recombinaison radiative du trion noir X_D^+ et de ses répliques de phonons $X_{D,K3}^+$ dans un champ magnétique positif hors plan ($B > 0$). Elle nous permettra de présenter la méthode qui permet de déterminer les facteurs-g CB et VB.

Comme expliqué au chapitre 1, l'absorption/émission de la lumière polarisée circulairement droite et gauche se produit dans les vallées inéquivalentes K^+ et K^- de la zone de Brillouin hexagonale 2D [58, 274–277]. Ici, nous nous concentrerons sur les transitions d'énergie les plus basses impliquant uniquement le sommet VB, caractérisées par un facteur-*g* g_v . Les facteurs-g CB inférieur et supérieur sont respectivement étiquetés g_{c1} et g_{c2} . Le facteur-*g* d'une transition donnée avec un dipôle dans le plan (X_0 , $X_{D,K3}^+$) s'écrit simplement : $E_{\sigma^+} - E_{\sigma^-} = g\mu_B B$. Pour les transitions avec une sortie -dipôle plan (X_D , X_D^+), la polarisation de la lumière est perpendiculaire au plan ML et on définit le facteur-*g* par $E_{K^+} - E_{K^-} = g\mu_B B$ (voir **Figure 7.21(b)** et **(c)**). La **Figure 7.21(a)** montre le changement de structure de bande de ML WSe₂ sous l'application d'un champ magnétique ($B > 0$). Pour une transition d'exciton neutre brillante dans la vallée de K^+ ($X_0(\sigma^+)$), l'énergie de transition est $E_{X_0(\sigma^+),B>0} = E_{X_0(\sigma^\pm),B=0} + (g_{c2}\mu_B B - g_v\mu_B B)$ et de même, on a $E_{X_0(\sigma^-),B>0} = E_{X_0(\sigma^\pm),B=0} + (-g_{c2}\mu_B B + g_v\mu_B B)$ pour $X_0(\sigma^-)$, où $E_{X_0(\sigma^\pm),B=0}$ est l'énergie de transition sans champ magnétique. Alors on peut facilement obtenir $g_{X_0}\mu_B B = E_{X_0(\sigma^+),B>0} - E_{X_0(\sigma^-),B>0} = -2(g_v - g_{c2})\mu_B B$. En conséquence, nous pouvons déterminer le facteur *g* de la transition d'exciton neutre brillant (X_0) :

$$g_{X_0} = -2(g_v - g_{c2}). \quad (6.1a)$$

De même, nous pouvons obtenir le facteur g de la transition de l'exciton neutre sombre (X_D) :

$$g_{X_D} = -2(g_v - g_{c1}). \quad (6.1b)$$

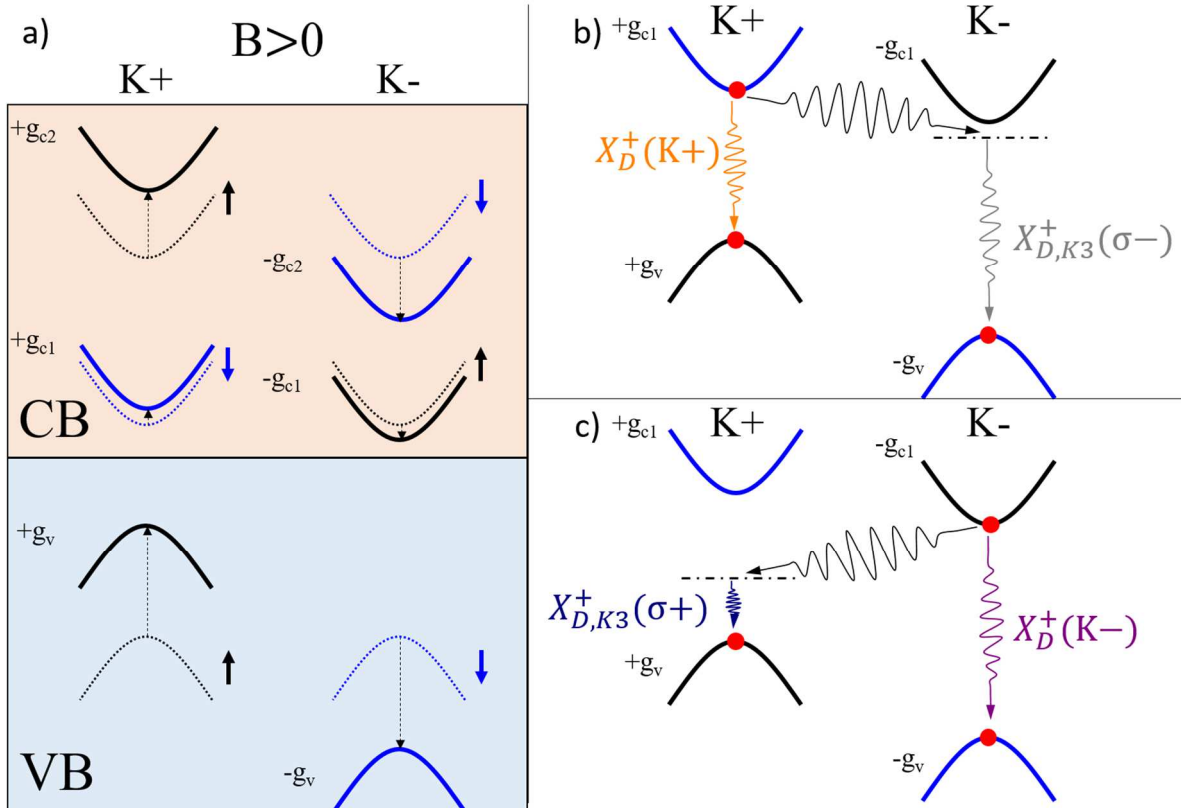


Figure 7.21 (a) Schéma de la structure des bandes dans les vallées K^+ et K^- de ML WSe₂ au point de neutralité ; les lignes pointillées et pleines correspondent respectivement aux bandes avec $B=0$ et $B>0$. Les lignes pointillées verticales indiquent le décalage induit par le champ magnétique des bandes. Seule la bande de valence supérieure est considérée ici (transitions optiques de type A). Schémas de la structure de bande pour $B>0$ et dopage des trous affichant la transition optique correspondant à la réplique du phonon K_3 du trion noir positif, $X_{D,K3}^+$, dans (b) vallée K^- et (c) vallée K^+ . La transition optique de X_D^+ est également indiquée. Les meilleures CB ne sont pas affichées.

En accord avec les rapports précédents [178,241], nous trouvons $g_{X_0} = -4,5 \pm 0,1$ et $g_{X_D} = -10,2 \pm 0,1$. Comme ces deux transitions impliquent deux CB différents, ces mesures ne permettent pas de déterminer les facteurs g CB et VB (voir équation (6.1)). Par contre, les règles de sélection associées aux transitions optiques positives du trion noir X_D^+ et $X_{D,K3}^+$ permettent de résoudre ce problème. La différence d'énergie entre les transitions optiques X_D^+ et $X_{D,K3}^+$ ne dépendra que des facteurs- g à bande unique g_{c1} et g_v et de l'énergie du phonon E_{K_3} :

$$\begin{aligned}\Delta E_1 &= E(X_D^+(K+)) - E(X_{D,K3}^+(\sigma^-)) = E_{K_3} - 2g_v\mu_B B, \\ \Delta E_2 &= E(X_D^+(K-)) - E(X_{D,K3}^+(\sigma^+)) = E_{K_3} + 2g_v\mu_B B,\end{aligned}$$

$$\begin{aligned}\Delta E_3 &= E(X_D^+(K-)) - E(X_{D,K3}^+(\sigma^-)) = E_{K3} - 2g_{c1}\mu_B B, \\ \Delta E_4 &= E(X_D^+(K+)) - E(X_{D,K3}^+(\sigma^+)) = E_{K3} + 2g_{c1}\mu_B B.\end{aligned}\quad (6.2)$$

La **Figure 7.22(b)** présente la variation de $\Delta E_2 - \Delta E_1$ en fonction du champ magnétique appliqué. La pente de la courbe ($4g_v\mu_B B$) de la **Figure 7.22(b)** donne une détermination directe du facteur g de la bande de valence. On trouve $g_v = 6.1 \pm 0.1$. La **Figure 7.22(c)** présente la variation du champ magnétique de la différence $\Delta E_4 - \Delta E_3$ en suivant la même procédure. La pente donne une détermination directe du facteur g CB inférieur; on mesure $g_{c1} = 0.86 \pm 0.1$. Ensuite, en utilisant le facteur g mesuré de la transition de l'exciton neutre (**Figure 7.22(a)**. et Eq. (6.1)), nous pouvons déduire le facteur g CB supérieur: $g_{c2} = 3.84 \pm 0.1$. Enfin, nous extrayons le facteur g VB inférieur, g_{v2} , en utilisant la relation $g_{X_0,B} = -2(g_{v2} - g_{c1})$, où $g_{X_0,B}$ correspond à l'exciton neutre de type B (transition optique avec in-dipôle plan entre le bas VB et CB). À partir de la valeur précédemment mesurée de $g_{X_0,B} = -3.9 \pm 0.5$ [247], et de notre résultat pour $g_{c1} = 0.86 \pm 0.1$, nous obtenons que $g_{v2} = 2.81 \pm 0.5$.

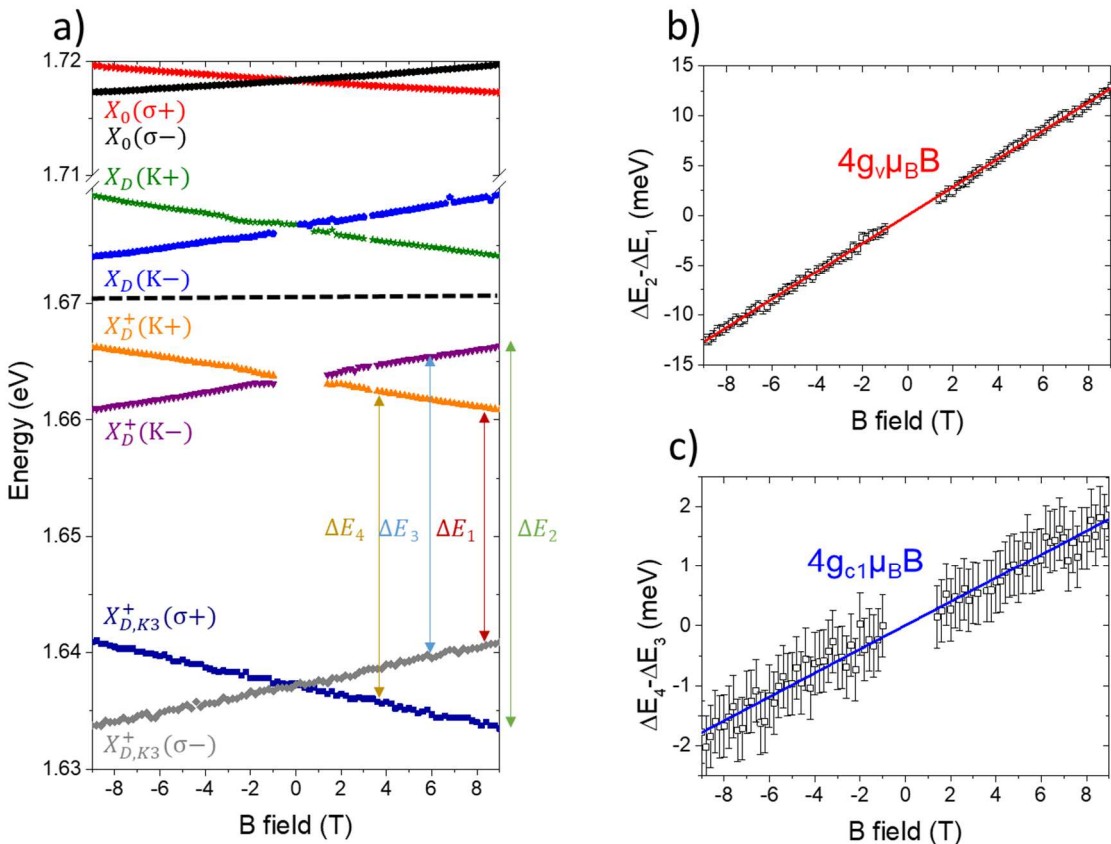


Figure 7.22 (a) Dépendance au champ magnétique des excitons clairs et sombres au point de neutralité de l'appareil et du trion noir positif, X_D^+ , et sa réplique de phonons impliquant le phonon inter-vallées K3, $X_{D,K3}^+$, mesuré pour $p=1.4\times10^{11} \text{ cm}^{-2}$. Dépendance au champ magnétique de la différence d'énergie des transitions optiques (b) $\Delta E_2 - \Delta E_1$ et (c) $\Delta E_3 - \Delta E_4$ donnant la détermination de g_v et g_{c1} (voir flèches en (a)).

Conclusion and Perspective

We have fabricated van der Waals heterostructures based on WSe₂ monolayers and high-quality hBN crystals. Encapsulation of the WSe₂ MLs by hBN enables to reach spectral linewidths almost limited by the radiative rate of excitons. This simple van der Waals heterostructure is thus a good platform to study the intrinsic properties of WSe₂ MLs. We have performed various optical spectroscopy measurements to make some progress on the understanding of the exciton and spin-valley properties in WSe₂ monolayers.

First, we have conducted photoluminescence spectroscopy experiments to measure accurately the energy splitting between the bright and dark neutral exciton. We have demonstrated in Chapter 3 that this splitting can be tuned by a few meV by changing the hBN encapsulation layer thickness, as a result of a significant Lamb shift of the optically active exciton. This effect arises from virtual photons emission and absorption triggered by the vacuum fluctuations of the electromagnetic field. We also demonstrate that the variations of few meV in the bright exciton radiative linewidth is the result of the Purcell effect. All these experimental results, illustrating the strong sensitivity of the excitons to local vacuum, are in very good agreement with a model based either on electrodynamical Green's function approach (transfer matrix formalism) or quantum-electrodynamical approaches (model developed by M. Glazov and M. Semina from Ioffe Institute). The next step could be to control the exciton fine structure in MoSe₂ monolayer. The energy splitting between the bright and dark exciton is around -1.4 meV in MoSe₂ monolayer [88], *i.e.* the bright state is below the dark one. Then, it may be possible to tune the transition energy of the bright exciton through Lamb shift so that the bright state can jump above the dark one. The difficulty is that we have to apply an in-plane magnetic field to brighten the dark exciton otherwise it is not visible in optical spectra. Instead of applying an in-plane magnetic field, we can set the trion transition as a reference (thanks to its relatively weak oscillator strength, we expect rather negligible Lamb shift) and measure the energy splitting between bright neutral exciton and trion to quantify the transition energy shift of the bright neutral exciton. If the bright neutral exciton shifts above the dark one we might also observe some effects on the luminescence yield of the bright neutral exciton as well as on its circular polarization.

In Chapter 4, we demonstrated very efficient spin-valley pumping of resident electrons in both WSe₂ and WS₂ monolayers using circularly polarized light. Spin-valley polarization of the resident electrons up to 80% can be obtained in WSe₂ monolayer. This process manifests as a large positive circular polarization of the triplet trion, a negative polarization of the singlet trion and a large increase of the triplet trion PL intensity with circular excitation as compared to linear excitation. Interestingly, these results demonstrate that circularly polarized excitation photo-generates electron-hole pairs in one valley and dynamically polarizes resident electrons in the opposite

valley. This work could thus be an important step towards the development of valleytronic devices based on TMD MLs.

In Chapter 5, we have investigated the spin-valley diffusion transport of free electrons in a WSe₂ ML via a spatially-resolved pump-probe technique we have developed. By locally pumping the Fermi sea of 2D electrons to a high degree of spin-valley polarization (up to 80%) using circularly-polarized light, the lateral diffusion of the electron polarization can be mapped out via the photoluminescence induced by a spatially-separated and linearly-polarized probe laser. The efficient spin-valley pumping of resident electrons allow us to evidence transport of spin-valley information over very long distances, with a typical diffusion length of 18 μm. This is a consequence of the long spin-valley relaxation time induced by the unique spin-valley locking effect in this atomically-thin crystal. To separate the effects of diffusion and relaxation, spin grating experiments could be performed in the future to measure accurately the spin diffusion coefficient independently from the charge diffusion coefficient [232,233]. We also anticipate that improvements in the charge mobility of carriers in higher quality material [294] may result in longer spin diffusion length. Spatially-extended hole spin diffusion is also expected in these TMD monolayers, given similarly long spin-valley lifetimes and even stronger spin-valley locking due to the huge spin-orbit splitting in the valence bands. The control of the spin transport properties with an in-plane electric field could be the next challenge for future possible applications in spin(valley)tronics.

In Chapter 6, we have performed magneto-photoluminescence spectroscopy in gated ML-WSe₂ device. Based on the knowledge of the optical selection rules of different exciton complexes and their phonon replica, we have proposed a new method to measure the single particle *g*-factor. Our method works at low densities (few 10¹¹ cm⁻²), which can avoid the strong renormalization effects usually occurring in transport measurements. Our method yields a direct determination of single band *g*-factors. We measure $g_{c1} = 0.86 \pm 0.1$, $g_{c2} = 3.84 \pm 0.1$ for the bottom (top) conduction bands and $g_v = 6.1 \pm 0.1$ for the valence band of monolayer WSe₂. These measurements are helpful for quantitative interpretation of optical and transport measurements performed in magnetic fields. In addition, the measured *g*-factors are valuable input parameters for optimizing band structure calculations of these 2D materials. The next challenge is to measure the *g*-factors of the conduction and valence bands for MoSe₂ and MoS₂ monolayers. However, there is no equivalent phonon replicas in those two Mo-based monolayers due to their different conduction band structure. This means that we have to find another method to measure the single particle *g*-factors of these two Mo-based monolayers.

Appendix

Calculation of the Exciton Lamb shift and Purcell effect

This model has been developed by M. Glazov and M. Semina from Ioffe Institute. Let us consider a TMD ML in van der Waals heterostructures (top hBN layer/WSe₂ ML/bottom hBN layer/SiO₂/Si) described in Chapter 3 [101]. Below we calculate the excitonic Lamb shift and radiative decay rate with two approaches: the classical electrodynamical Green's function approach (transfer matrix method) and quantum electrodynamical (QED) approach. We demonstrate that these approaches are equivalent for our problem.

In the classical electrodynamical Green's function approach we calculate the eigenmodes of electromagnetic field in the presence of a monolayer (exciton-polaritons in terms of bulk crystals) and extract the polariton energy and its damping from the elementary response functions, e.g., from the absorption [101,138,295]. In the QED approach we quantize the electromagnetic modes in the structure and calculate exciton energy renormalization due to coupling with the quantized modes using the second-order perturbation theory.

To illustrate that electrodynamical Green's function approach and quantum-electrodynamical approaches give the same results we consider a simplified setting of the problem with the monolayer being at a distance d' from a mirror (barrier) characterized by the reflection coefficient r and transmission coefficient t (inset of **Figure 3.6** in Chapter 3). We assume that the mirror is non-absorbing.

I.1 Green's function for 1D electromagnetic waves

Our system is translationally invariant in a 2D monolayer plane (xy) and inhomogeneous along the z axis. Let us consider the 1D Maxwell equation for the in-plane electric field component $E = E_x$ or E_y [138]

$$\frac{d^2E}{dz^2} + q^2\epsilon(z)E = -4\pi q^2P_{exc}(z) \quad (1)$$

Here $q = \omega/c$, ϵ is the dielectric constant of the system and $P_{exc}(z)$ is the polarization induced by the exciton. We introduce the electrodynamical Green's function $G_\omega(z, z')$ as a solution of Eq. (1) with the δ -function source:

$$\left[\frac{d^2}{dz^2} + q^2\epsilon(z) \right] G_\omega(z, z') = \delta(z - z') \quad (2)$$

In a vacuum where $\epsilon(z) = 1$ the Green's function reads

$$G_\omega(z, z') = \frac{\exp(iq|z - z'|)}{2iq} \quad (3)$$

In the presence of a barrier the Green's function can be also readily found by matching the solutions. To that end we assume that the barrier is at $z = 0$ and the monolayer is at $z \equiv z_{ML} = -d'$. For the calculations of the Purcell factor and Lamb shift presented in the following we need the Green's function at the monolayer only ($z = z' = z_{ML}$) but we present more general solution with $z' = z_{ML}$ and arbitrary $z < 0$:

$$G_\omega(z, -d') = \frac{1}{2iq} \begin{cases} e^{iq(z+d')} + re^{2iqd' - iq(z+d')}, & -d' < z < 0, \\ e^{-iq(z+d')}(1 + re^{2iqd'}), & z < -d' \end{cases} \quad (4)$$

It can be checked by substitution that the function (4) satisfies the Maxwell's equation (2), it is continuous at $z = z_{ML}$ and its derivative has a jump by 1 at $z = z' = z_{ML}$. Moreover, it satisfies the boundary condition at the barrier.

It is instructive to derive Eqs. (3) and (4) using the normal mode decomposition. In the free space the normal modes are the plane waves

$$E_{k_z}(z) = e^{ik_z z}, \quad (5)$$

where we assume the normalization length to be unity and

$$G_\omega(z, z') = \sum_{k_z} \frac{E_{k_z}(z)E_{k_z}^*(z')}{q^2 - k_z^2 + i0}, \sum_{k_z} \dots = \int_{-\infty}^{\infty} \frac{dk_z}{2\pi} \dots \quad (6)$$

The summation can be efficiently carried out using the residue theorem and taking into account that

$$q^2 - k_z^2 + i0 = (q - k_z + i0)(q + k_z + i0)$$

The pole with $k_z = q + i0$ should be used for $z - z' > 0$ and the pole with $k_z = -q - i0$ for $z - z' < 0$ as a result we have Eq. (3).

The calculation in the presence of the barrier is performed in the following way. Making use of the expressions presented in the supplement to Ref. [101] (see also Ref. [296]) we obtain for the fields

$$E_{k_z}^{(1)}(z) = \begin{cases} e^{ik_z z} + re^{-ik_z z}, & z < 0, \\ te^{ik_z z}, & z > 0, \end{cases} \quad (7a)$$

$$E_{k_z}^{(2)}(z) = \begin{cases} t'e^{-ik_z z}, & z < 0, \\ e^{-ik_z z} + r'e^{ik_z z}, & z > 0. \end{cases} \quad (7b)$$

In both cases we assume that $k_z > 0$, the wave (1) corresponds the field incident from the $z = -\infty$ and the wave (2) corresponds to the field incident at $z = +\infty$. The

time-reversal symmetry dictates the following requirement for the relation between t , t' , r and r' :²

$$t' = t, \quad r' = -r^* \frac{t}{t^*}, \quad \text{or } t^*r' + r^*t = 0 \quad (8)$$

Hence, $|r| = |r'|$ and, in the absence of losses, $|t|^2 + |r|^2 = 1$. As a result the modes are properly normalized and orthogonal, see Ref. [101,296] for details. Let us find the Green's function at $z = z' = -d'$ explicitly using the normal mode decomposition [cf. Eq. (6)]

$$G_\omega(z, z') = \sum_{i=1,2} \int_0^\infty \frac{dk_z}{2\pi} \frac{E_{k_z}^{(i)}(z) E_{k_z}^{(i)*}(z')}{q^2 - k_z^2 + i0}, \quad (9)$$

namely

$$G_\omega(z_{ML}, z_{ML}) = \int_0^\infty \frac{dk_z}{2\pi} \frac{|e^{-ik_z d} + r e^{ik_z d}|^2}{q^2 - k_z^2 + i0} + \int_0^\infty \frac{|t'|^2}{q^2 - k_z^2 + i0} \frac{dk_z}{2\pi}, \quad (10)$$

where the first term comes from the solution (1) and the second term comes from the solution (2) in Eq. (7).

We now show that Eq. (10) equivalent to Eq. (4). Note that the following relations are fulfilled for any non-absorbing barrier:

$$t'(k_z) = t(k_z), \quad r(k_z) = r^*(-k_z). \quad (11)$$

Both these relations are a consequence of the time-reversal symmetry. As a result, Eq. (10) can be recast as

$$G_\omega(z_{ML}, z_{ML}) = \frac{1}{2} \int_{-\infty}^\infty \frac{dk_z}{2\pi} \frac{2 + r e^{2ik_z d} + r^* e^{-2ik_z d}}{q^2 - k_z^2 + i0}, \quad (12)$$

where we made use of the fact that $|t|^2 + |r|^2 = 1$ and that the subintegral expression is an even function of k_z . Integration in Eq. (12) can be performed via the residue theorem. To that end we note that all poles of $r(k_z)$ in the complex plane have negative imaginary parts. It is a result of the causality.³ Hence, while integrating the term $r \exp(2ik_z d')$ we close the contour in the upper half-plane, $\text{Im}k_z > 0$. In this way, the Jordan's lemma is fulfilled, and we need to take into account the only pole of the denominator with $k_z = q + i0$ and disregards the poles of $r(k_z)$. While integrating the term with $r^* \exp(-2ik_z d')$ we close the contour in the lower half-plane, $\text{Im}k_z < 0$. Again, the Jordan's lemma is fulfilled, and we need to take into account the only pole

² We recall that the transfer matrix through a barrier takes the form $\hat{T} = \begin{bmatrix} 1/t^* & -r^*/t^* \\ -r/t & 1/t \end{bmatrix}$

³ This fact can be illustrated by a simple example of a barriers considered in Ref. [101], Eqs. (S36), (S37): Their denominators as functions of k_z read $D(k_z) = 1 - \rho \exp(ik_z l)$ where ρ is the product of corresponding reflection coefficients and l is the effective length. The zeros of $D(k_z)$ take the form $k_z^{(n)} = il^{-1} \ln \rho + 2\pi n/l$ with $n \in \mathbb{Z}$ and, since $|\rho| < 1$ and $l > 0$, $\text{Im}\{k_z^{(n)}\} < 0$.

of the denominator with $k_z = -q - i0$. Making use again of Eq. (11) we arrive at

$$G_\omega(z_{ML}, z_{ML}) = \frac{1 + r \exp(2iqd')}{2iq}, \quad (13)$$

in full agreement with Eq. (4). The derived Green's function allows us to evaluate the Purcell effect and the Lamb shift semiclassically, see SII.3. Before doing so, let us present the results of the quantum-mechanical calculation.

I.2 Quantum-mechanical calculation

We use standard QED approach to calculate the shift of the exciton energy within the second-order perturbation theory in the light-matter coupling. The renormalization of the energy results from the process of the virtual emission of a photon (exciton virtually recombines) and re-absorption of the same photon. Corresponding expression for the energy shift reads [297,298]

$$\delta E_{\text{exc}} = \sum_j \frac{|V_j|^2}{E_{\text{exc}} - \hbar\omega_j + i0}. \quad (14)$$

Here j enumerates the photon states ($j = k_z$ in the case of a free space, or $j = (k_z, i)$ with $k_z > 0$ and $i = (1,2)$ in the presence of a barrier), V_j is the matrix element of the light-matter interaction, E_{exc} is the bare exciton energy, ω_j is the photon dispersion. We have added $i0$ in the denominator in accordance with the general prescriptions of the scattering theory to ensure causality, imaginary part of δE_{exc} gives the exciton radiative broadening (with the negative sign):

$$\Gamma_0 = -\text{Im}\delta E_{\text{exc}}. \quad (15)$$

In the case of a resonant structure, e.g., if a ML semiconductor is placed in a microcavity with highly reflective mirrors [299] it is sufficient to keep only one, resonant, term in Eq. (14). In this way we recover standard expressions for the energy shift of an exciton resonance due to the polariton effect (in the weak coupling regime):

$$\delta E = \frac{|V_0|^2}{E_{\text{exc}} - \hbar\omega_0},$$

where ω_0 is the frequency of the photon mode in the cavity.

Our system consists of a monolayer semiconductor sandwiched between hBN layers and deposited on the SiO₂/Si substrate. Such a structure "hBN/SiO₂/Si" is highly non-resonant, and we need to take into account all modes of electromagnetic field propagating in the structure. Thus, in the case of interest, V_j can be written as

$$V_j = -\sqrt{2\pi\hbar\omega_j} D_{\text{exc}} E_{k_z}^{(i)}(z_{ML}), \quad (16)$$

where D_{exc} is the exciton microscopic dipole moment, $E_{k_z}^{(i)}(z_{ML})$ are the eigenmodes of the field at the position of the monolayer, Eq. (7), and the factor $\sqrt{2\pi\hbar\omega_j}$ results from

the field normalization per photon. Equation (14) provides the shift of the excited state of the crystal, namely, of the exciton. However, the process of the photon emission and corresponding re-absorption also affects the energy of the ground state of the crystal as

$$\delta E_0 = \sum_j \frac{|V_j|^2}{-E_{\text{exc}} - \hbar\omega_j + i0}. \quad (17)$$

The observed energy shift of the bright exciton line is given by

$$\delta E = \delta E_{\text{exc}} - \delta E_0 = 2E_{\text{exc}} \sum_j \frac{|V_j|^2}{E_{\text{exc}}^2 - |\hbar\omega_j|^2 + i0} = 4\pi\hbar E_{\text{exc}} |D_{\text{exc}}|^2 \sum_{\substack{k_z > 0 \\ i=1,2}} \frac{c|k_z| |E_{k_z}^{(i)}(z_{ML})|^2}{E_{\text{exc}}^2 - (\hbar ck_z)^2 + i0}. \quad (18)$$

The real part of Eq. (18) diverges. This divergence is known from the quantum electrodynamics and related to the renormalization of the free electron mass. The simplest way to remove the divergence is, following Refs. [152,297], to remove the contribution $\delta m_{QED} v^2/2$ from the energy.⁴ As a result we have

$$\delta E = 4\pi \left| \frac{E_{\text{exc}} D_{\text{exc}}}{\hbar c} \right|^2 G_{\frac{E_{\text{exc}}}{\hbar}}(z_{ML}, z_{ML}), \quad (19)$$

where in the last equality we introduced the Green's function of electrodynamic problem, Eqs. (9) and (12).

I.3 Comparison of the results

Let us now explicitly check that both approaches give the same result. In the classical electrodynamic treatment we need to solve Eq. (1) together with the material equation for the exciton polarization P_{exc} [84,101,138]

$$(E_{\text{exc}} - \hbar\omega)P_{\text{exc}}(z) = |D_{\text{exc}}|^2 E(z_{ML})\delta(z - z_{ML}). \quad (20)$$

substituting Eq. (20) into Eq. (1) and solving it using the Green's function as

$$E(z) = -4\pi \left(\frac{\omega}{c} \right)^2 \frac{|D_{\text{exc}}|^2}{E_{\text{exc}} - \hbar\omega} E(z_{ML}) G_{\frac{E_{\text{exc}}}{\hbar}}(z, z_{ML}),$$

we arrive, setting $z = z_{ML}$, at the following self-consistency equation

$$\hbar\omega - E_{\text{exc}} = 4\pi \left| \frac{E_{\text{exc}} D_{\text{exc}}}{\hbar c} \right|^2 G_{\frac{E_{\text{exc}}}{\hbar}}(z_{ML}, z_{ML}), \quad (21)$$

⁴ The renormalization can be performed as follows. We consider a shift of a given electronic level s as a result of its coupling with all the levels, cf. Eq. (14), and subtract the contribution related to the diagonal matrix element of the velocity in this state [152,297]:

$$\delta E_s = 2\pi \sum_{j,s'} \frac{\hbar\omega_j |D_{s's}|^2 |E_j|^2}{E_s - E_{s'} - \hbar\omega + i0} \rightarrow 2\pi \sum_{j,s'} \left\{ \frac{\hbar\omega_j |D_{s's}|^2 |E_j|^2}{E_s - E_{s'} - \hbar\omega + i0} - \frac{\hbar\omega_j |D_{s's}|^2 |E_j|^2}{-\hbar\omega + i0} \right\} = 2\pi \sum_{j,s'} \frac{(E_s - E_{s'}) |D_{s's}|^2 |E_j|^2}{E_s - E_{s'} - \hbar\omega + i0}$$

where we replaced ω by E_{exc}/\hbar in the right-hand side taking into account that the energy shifts are small [121,295] (we operate in a weak coupling regime). This calculation is fully equivalent to the transfer matrix calculation. It is seen that that Eq. (21) fully agrees with Eq. (19) derived above from the QED.

In free space for the renormalization of the energy and radiative damping we have:

$$\delta E^{\text{vac}} = 0, \quad (22a)$$

$$\Gamma_0^{\text{vac}} = 2\pi \frac{E_{\text{exc}} |D_{\text{exc}}|^2}{\hbar c}. \quad (22b)$$

The fact that $\delta E^{\text{vac}} = 0$ corresponds to the regularization procedure we used where all “remaining” quantum electrodynamical contributions are already included in the transition energy. In the presence of the barrier the results change as

$$\delta E = \Gamma_0^{\text{vac}} r \sin(2qd'), \quad (23a)$$

$$\Gamma_0 = \Gamma_0^{\text{vac}}(1 + r \cos(2qd')). \quad (23b)$$

The fact that δE vanishes at the nodes and antinodes of the electromagnetic field, where $2k_z d' = n\pi$ with $n \in \mathbb{N}$, can be understood from simple qualitative arguments: According to Eq. (14) the energy shift of the exciton due to the coupling with the photon with the frequency ω_j is an odd function of the detuning $E_{\text{exc}} - \hbar\omega_j$, $\delta E \propto (E_{\text{exc}} - \hbar\omega_j)^{-1}$. For the case of the antinode or node of electromagnetic field at the monolayer, $k_z d' = n\pi/2$, the photon density of states is approximately symmetric with respect to E_{exc} and the total shift vanishes. If the condition $k_z d' = n\pi/2$ is not fulfilled the photon density of states is no longer symmetric with respect to E_{exc} and the Lamb shift appears as illustrated in **Figure 1**.

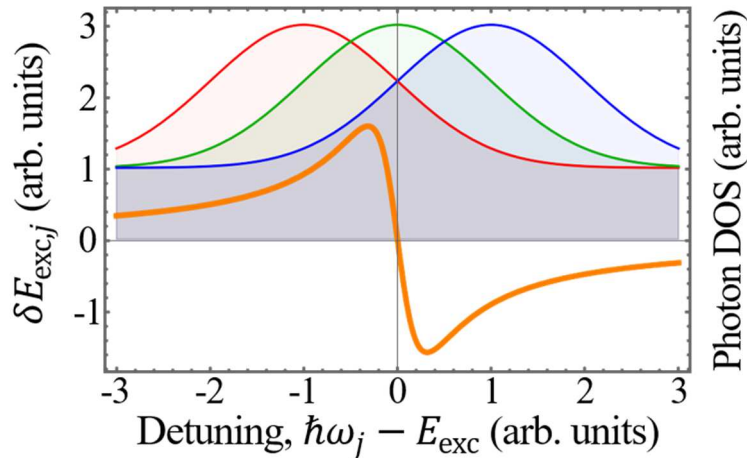


Figure 1 Illustration of the cancellation of the Lamb shift at the “resonant” case of the antinode of the field. Orange dispersive curve shows the contribution of the photon mode with the frequency ω_j to the Lamb shift, Eq. (14). Red, green, and blue peaked functions illustrate the photon density of states for the detuned cases (red and blue) and resonant, $k_z d' = n\pi/2$ (green) case.

I.4 Kramers-Kronig-like relation between the Lamb shift and Purcell effect

Generally, in the structure with an arbitrary barrier the electrodynamical treatment shows that

$$\delta E = \Gamma_0 \text{Im}\{r\}, \quad (24a)$$

$$\Gamma_0 = \Gamma_0^{\text{vac}}(1 + \text{Re}\{r\}), \quad (24b)$$

where $r \equiv r(\frac{E_{\text{exc}}}{\hbar})$ is the reflection coefficient of the barrier taken at the exciton resonance frequency. There is a deep connection between δE and Γ_0 based on the causality principle. It follows that the real and imaginary parts of the reflection coefficient are interrelated by the Kramers-Kronig type relation [300,301]

$$\text{Im}\{r(\omega)\} = -\frac{2\omega}{\pi} v.p. \int_0^\infty \frac{\text{Re}\{r(\omega')\}}{\omega'^2 - \omega^2} d\omega', \quad \text{Re}\{r(\omega)\} = -\frac{2\omega}{\pi} v.p. \int_0^\infty \frac{\text{Im}\{r(\omega')\}}{\omega'^2 - \omega^2} d\omega'. \quad (25)$$

Note that the real and imaginary parts of the electrodynamical Green's function $G_\omega(z, z')$ obeys the same relations, see Ref. [302] for details. To demonstrate this relations we plotted in **Figure 2** the reflection coefficient of a typical hBN/SiO₂/Si substrate calculated by the transfer matrix method [75,101] and, for the imaginary part, using the relation (25). A very good agreement (within the numerical accuracy) is seen. It also shows a phase-shift of a $\pi/2$ between the Purcell enhancement and the Lamb shift as a function of the hBN thickness.

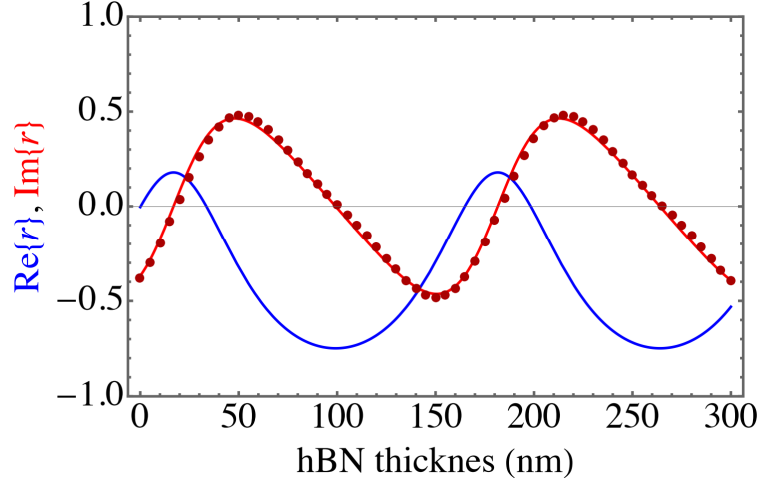


Figure 2 Background reflectivity of the hBN/SiO₂/Si van der Waals heterostructure as a function of the hBN thickness at the WSe₂ exciton energy $E_{\text{exc}} = 1.71$ eV. SiO₂ thickness is 83 nm. Blue and red curves show the real part of the reflection coefficient found using the transfer matrix method, Refs. [75,101] dark red dots show $\text{Im}\{r\}$, calculated after Eq. (25) via $\text{Re}\{r\}$.

List of Publications and Conferences

Publications

- (1) **L. Ren***, L. Lombez*, C. Robert*, D. Beret, D. Lagarde, B. Urbaszek, P. Renucci et al. "Optical detection of long electron spin transport lengths in a monolayer semiconductor." *Physical Review Letters* 129, no.2 (2022): 027402. (*co-first author)
- (2) **L. Ren**, C. Robert, B. Urbaszek, X. Marie, M. Semina, and M. M. Glazov. "Tuning absorption and emission in monolayer semiconductors: a brief survey." *Comptes Rendus. Physique* 22, no. S4 (2021): 1-10.
- (3) M. Yang*, **L. Ren***, C. Robert*, D. V. Tuan, L. Lombez, B. Urbaszek, X. Marie, and H. Dery. "Relaxation and darkening of excitonic complexes in electrostatically doped monolayer WSe₂: Roles of exciton-electron and trion-electron interactions." *Physical Review B* 105, no. 8 (2022): 085302. (* co-first author)
- (4) A. Rousseau, **L. Ren**, A. Durand, P. Valvin, B. Gil, K. Watanabe, T. Taniguchi et al. "Monolayer boron nitride: hyperspectral imaging in the deep ultraviolet." *Nano Letters* 21, no. 23 (2021): 10133-10138.
- (5) A. I. Prazdnichnykh, M. M. Glazov, **L. Ren**, C. Robert, B. Urbaszek, and X. Marie. "Control of the exciton valley dynamics in atomically thin semiconductors by tailoring the environment." *Physical Review B* 103, no. 8 (2021): 085302.
- (6) C. Robert, H. Dery, **L. Ren**, D. V. Tuan, E. Courtade, M. Yang, B. Urbaszek et al. "Measurement of conduction and valence bands g-factors in a transition metal dichalcogenide monolayer." *Physical Review Letters* 126, no. 6 (2021): 067403.
- (7) C. Robert, S. Park, F. Cadiz, L. Lombez, **L. Ren**, H. Tornatzky, A. Rowe et al. "Spin/valley pumping of resident electrons in WSe₂ and WS₂ monolayers." *Nature communications* 12, no. 1 (2021): 1-7.
- (8) C. Maestre, Y. Li, V. Garnier, P. Steyer, S. Roux, A. Plaud, A. Loiseau, **L. Ren** et al. "From the synthesis of hBN crystals to their use as nanosheets in van der Waals heterostructures." *2D Materials* 9, no. 3 (2022): 035008.
- (9) P. Li, C. Robert, D. V. Tuan, **L. Ren**, M. Yang, X. Marie, and H. Dery. "Intervalley electron-hole exchange interaction and impurity-assisted recombination of indirect excitons in WS₂ and WSe₂ monolayers." *Physical Review B*, no. 106 (2022): 085414.
- (10) Z. Zhou, P. Marcon, X. Devaux, P. Pigeat, A. Bouché, S. Migot, A. Jaafar, **L. Ren** et al. "Large perpendicular magnetic anisotropy in Ta/CoFeB/MgO on full-coverage monolayer MoS₂ and first-principles study of its electronic structure." *ACS Applied Materials & Interfaces* 13, no. 27 (2021): 32579-32589.

Poster presentations

1. **L. Ren**, L. Lombez, C. Robert, P. Renucci, D. Bere, D. Lagarde, B. Urbaszek, T. Taniguchi, K. Watanabe, S.A. Crooker, X. Marie. Optical detection of long electron spin transport lengths in a monolayer semiconductor", ***NanoX-FERMI Days 2022***, Toulouse, France.
2. **L. Ren**, L. Lombez, C. Robert, P. Renucci, D. Bere, D. Lagarde, B. Urbaszek, T. Taniguchi, K. Watanabe, S.A. Crooker, X. Marie. " Optical detection of long electron spin transport lengths in a monolayer semiconductor", ***ICFO International School on the Frontiers of Light 2022***, Castelldefels, Spain.

Conference Participation

1. **L. Ren**, M. Yang, C. Robert, D. V. Tuan, L. Lombez, B. Urbaszek, X. Marie, and H. Dery "Relaxation and darkening of excitonic complexes in electrostatically doped monolayer WSe₂: Roles of exciton-electron and trion-electron interactions." ***Journées de la Matière Condensée 2022***, Lyon, France. (Oral)
2. **L. Ren**, L. Lombez, C. Robert, D. Beret, D. Lagarde, B. Urbaszek, P. Renucci, T. Taniguchi, K. Watanabe, S. A. Crooker, and X. Marie "Optical detection of long electron spin transport lengths in monolayer WSe₂." ***Howdi Annual Meeting 2022***, Paris, France. (Oral)
3. **L. Ren**, C. Robert, S. Park, F. Cadiz, L. Lombez, H. Tornatzky, A. Rowe, D. Paget, F. Sirotti, M. Yang, D. V. Tuan, T. Taniguchi, B. Urbaszek, K. Watanabe, T. Amand, H. Dery, S. A. Crooker, X. Marie "Dynamic polarization of resident electrons in WSe₂ and WS₂ monolayers." ***March Meeting of the American Physical Society 2022***. (Online oral)
4. **L. Ren**, C. Robert, S. Park, F. Cadiz, L. Lombez, H. Tornatzky, A. Rowe, D. Paget, F. Sirotti, M. Yang, D. V. Tuan, T. Taniguchi, B. Urbaszek, K. Watanabe, T. Amand, H. Dery, X. Marie "Spin/valley pumping of resident electrons in WSe₂ and WS₂ monolayers." ***Graphene Conference 2021***, Grenoble, France. (Oral)
5. **L. Ren**, C. Robert, H. Dery, D. Van Tuan, E. Courtade, M. Yang, B. Urbaszek, D. Lagarde, K. Watanabe, T. Taniguchi, T. Amand, and X. Marie "Measurement of conduction and valence bands g-factors in a transition metal dichalcogenide monolayer." ***Optics of Excitons in Confined Systems (OECS17) 2021***. (Online oral)
6. **L. Ren**, C. Robert, H. Dery, D. Van Tuan, E. Courtade, M. Yang, B. Urbaszek, D. Lagarde, K. Watanabe, T. Taniguchi, T. Amand, and X. Marie "Measurement of conduction and valence bands g-factors in a transition metal dichalcogenide monolayer." ***March Meeting of the American Physical Society 2021***. (Online oral)

Bibliography

- [1] J. Yin et al., *Entanglement-Based Secure Quantum Cryptography over 1,120 Kilometres*, Nature **582**, 7813 (2020).
- [2] J. Kang, W. Cao, X. Xie, D. Sarkar, W. Liu, and K. Banerjee, *Graphene and Beyond-Graphene 2D Crystals for next-Generation Green Electronics*, in edited by T. George, M. S. Islam, and A. K. Dutta (Baltimore, Maryland, USA, 2014), p. 908305.
- [3] K. S. Novoselov, A. K. Geim, S. V. Morozov, D. Jiang, Y. Zhang, S. V. Dubonos, I. V. Grigorieva, and A. A. Firsov, *Electric Field Effect in Atomically Thin Carbon Films*, Science **306**, 666 (2004).
- [4] D. C. Elias et al., *Dirac Cones Reshaped by Interaction Effects in Suspended Graphene*, Nature Phys **7**, 701 (2011).
- [5] A. S. Mayorov et al., *Micrometer-Scale Ballistic Transport in Encapsulated Graphene at Room Temperature*, Nano Lett. **11**, 2396 (2011).
- [6] A. A. Balandin, S. Ghosh, W. Bao, I. Calizo, D. Teweldebrhan, F. Miao, and C. N. Lau, *Superior Thermal Conductivity of Single-Layer Graphene*, Nano Lett. **8**, 902 (2008).
- [7] C. Lee, X. Wei, J. W. Kysar, and J. Hone, *Measurement of the Elastic Properties and Intrinsic Strength of Monolayer Graphene*, Science **321**, 385 (2008).
- [8] Q. H. Wang, K. Kalantar-Zadeh, A. Kis, J. N. Coleman, and M. S. Strano, *Electronics and Optoelectronics of Two-Dimensional Transition Metal Dichalcogenides*, Nature Nanotech **7**, 699 (2012).
- [9] J. A. Wilson and A. D. Yoffe, *The Transition Metal Dichalcogenides Discussion and Interpretation of the Observed Optical, Electrical and Structural Properties*, Advances in Physics **18**, 193 (1969).
- [10] A. D. Yoffe, *Layer Compounds*, Annu. Rev. Mater. Sci. **3**, 147 (1973).
- [11] Y. Li, A. Chernikov, X. Zhang, A. Rigosi, H. M. Hill, A. M. van der Zande, D. A. Chenet, E.-M. Shih, J. Hone, and T. F. Heinz, *Measurement of the Optical Dielectric Function of Monolayer Transition-Metal Dichalcogenides: MoS₂, MoSe₂, WS₂, and WSe₂*, Phys. Rev. B **90**, 205422 (2014).
- [12] T. Cheiwchanchamnangij and W. R. L. Lambrecht, *Quasiparticle Band Structure Calculation of Monolayer, Bilayer, and Bulk MoS₂*, Phys. Rev. B **85**, 205302 (2012).
- [13] D. Y. Qiu, F. H. da Jornada, and S. G. Louie, *Optical Spectrum of MoS₂: Many-Body Effects and Diversity of Exciton States*, Phys. Rev. Lett. **111**, 216805 (2013).
- [14] A. Chernikov, T. C. Berkelbach, H. M. Hill, A. Rigosi, Y. Li, O. B. Aslan, D. R. Reichman, M. S. Hybertsen, and T. F. Heinz, *Exciton Binding Energy and Nonhydrogenic Rydberg Series in Monolayer WS₂*, Phys. Rev. Lett. **113**, 076802 (2014).
- [15] K. He, N. Kumar, L. Zhao, Z. Wang, K. F. Mak, H. Zhao, and J. Shan, *Tightly Bound Excitons in Monolayer WSe₂*, Phys. Rev. Lett. **113**, 026803 (2014).
- [16] G. Wang, X. Marie, I. Gerber, T. Amand, D. Lagarde, L. Bouet, M. Vidal, A. Balocchi, and B. Urbaszek, *Giant Enhancement of the Optical Second-Harmonic*

Emission of WSe₂ Monolayers by Laser Excitation at Exciton Resonances, Phys. Rev. Lett. **114**, 097403 (2015).

- [17] B. Radisavljevic, A. Radenovic, J. Brivio, V. Giacometti, and A. Kis, *Single-Layer MoS₂ Transistors*, Nature Nanotech **6**, 147 (2011).
- [18] A. Daus, S. Vaziri, V. Chen, Ç. Körögülu, R. W. Grady, C. S. Bailey, H. R. Lee, K. Schable, K. Brenner, and E. Pop, *High-Performance Flexible Nanoscale Transistors Based on Transition Metal Dichalcogenides*, Nat Electron **4**, 7 (2021).
- [19] J. Choukroun, M. Pala, S. Fang, E. Kaxiras, and P. Dollfus, *High Performance Tunnel Field Effect Transistors Based on In-Plane Transition Metal Dichalcogenide Heterojunctions*, Nanotechnology **30**, 025201 (2018).
- [20] H. Ilatikhameneh, Y. Tan, B. Novakovic, G. Klimeck, R. Rahman, and J. Appenzeller, *Tunnel Field-Effect Transistors in 2-D Transition Metal Dichalcogenide Materials*, IEEE Journal on Exploratory Solid-State Computational Devices and Circuits **1**, 12 (2015).
- [21] Z.-Q. Fan, X.-W. Jiang, J. Chen, and J.-W. Luo, *Improving Performances of In-Plane Transition-Metal Dichalcogenide Schottky Barrier Field-Effect Transistors*, ACS Appl. Mater. Interfaces **10**, 19271 (2018).
- [22] H. Park, D. S. Oh, K. J. Lee, D. Y. Jung, S. Lee, S. Yoo, and S.-Y. Choi, *Flexible and Transparent Thin-Film Transistors Based on Two-Dimensional Materials for Active-Matrix Display*, ACS Appl. Mater. Interfaces **12**, 4749 (2020).
- [23] D. Jiang, Z. Liu, Z. Xiao, Z. Qian, Y. Sun, Z. Zeng, and R. Wang, *Flexible Electronics Based on 2D Transition Metal Dichalcogenides*, Journal of Materials Chemistry A **10**, 89 (2022).
- [24] J. Pu, K. Funahashi, C.-H. Chen, M.-Y. Li, L.-J. Li, and T. Takenobu, *Highly Flexible and High-Performance Complementary Inverters of Large-Area Transition Metal Dichalcogenide Monolayers*, Advanced Materials **28**, 4111 (2016).
- [25] J. Kim et al., *Wafer-Scale Production of Transition Metal Dichalcogenides and Alloy Monolayers by Nanocrystal Conversion for Large-Scale Ultrathin Flexible Electronics*, Nano Lett. **21**, 9153 (2021).
- [26] A. Pospischil, M. M. Furchi, and T. Mueller, *Solar-Energy Conversion and Light Emission in an Atomic Monolayer p-n Diode*, Nature Nanotech **9**, 257 (2014).
- [27] J. Pu and T. Takenobu, *Monolayer Transition Metal Dichalcogenides as Light Sources*, Advanced Materials **30**, 1707627 (2018).
- [28] J. Wang, I. Verzhbitskiy, and G. Eda, *Electroluminescent Devices Based on 2D Semiconducting Transition Metal Dichalcogenides*, Advanced Materials **30**, 1802687 (2018).
- [29] S. Hwangbo, L. Hu, A. T. Hoang, J. Y. Choi, and J.-H. Ahn, *Wafer-Scale Monolithic Integration of Full-Colour Micro-LED Display Using MoS₂ Transistor*, Nat. Nanotechnol. **17**, 5 (2022).
- [30] H. Li, Z. Yin, Q. He, H. Li, X. Huang, G. Lu, D. W. H. Fam, A. I. Y. Tok, Q. Zhang, and H. Zhang, *Fabrication of Single- and Multilayer MoS₂ Film-Based Field-Effect Transistors for Sensing NO at Room Temperature*, Small **8**, 63 (2012).
- [31] D. J. Late et al., *Sensing Behavior of Atomically Thin-Layered MoS₂ Transistors*, ACS Nano **7**, 4879 (2013).
- [32] F. K. Perkins, A. L. Friedman, E. Cobas, P. M. Campbell, G. G. Jernigan, and B. T. Jonker, *Chemical Vapor Sensing with Monolayer MoS₂*, Nano Lett. **13**, 668 (2013).
- [33] A. Koma, *Van Der Waals Epitaxy—a New Epitaxial Growth Method for a Highly Lattice-Mismatched System*, Thin Solid Films **216**, 72 (1992).

- [34] T. Norden, C. Zhao, P. Zhang, R. Sabirianov, A. Petrou, and H. Zeng, *Giant Valley Splitting in Monolayer WS₂ by Magnetic Proximity Effect*, Nat Commun **10**, 4163 (2019).
- [35] D. Zhong et al., *Layer-Resolved Magnetic Proximity Effect in van Der Waals Heterostructures*, Nat. Nanotechnol. **15**, 187 (2020).
- [36] A. Ciarrocchi, F. Tagarelli, A. Avsar, and A. Kis, *Excitonic Devices with van Der Waals Heterostructures: Valleytronics Meets Twistronics*, Nat Rev Mater **7**, 449 (2022).
- [37] A. K. Geim and I. V. Grigorieva, *Van Der Waals Heterostructures*, Nature **499**, 419 (2013).
- [38] Y. Cao, V. Fatemi, S. Fang, K. Watanabe, T. Taniguchi, E. Kaxiras, and P. Jarillo-Herrero, *Unconventional Superconductivity in Magic-Angle Graphene Superlattices*, Nature **556**, 43 (2018).
- [39] M. Liao et al., *Precise Control of the Interlayer Twist Angle in Large Scale MoS₂ Homostructures*, Nat Commun **11**, 2153 (2020).
- [40] E. Y. Andrei, D. K. Efetov, P. Jarillo-Herrero, A. H. MacDonald, K. F. Mak, T. Senthil, E. Tutuc, A. Yazdani, and A. F. Young, *The Marvels of Moiré Materials*, Nat Rev Mater **6**, 201 (2021).
- [41] C. Ataca, H. Şahin, and S. Ciraci, *Stable, Single-Layer MX₂ Transition-Metal Oxides and Dichalcogenides in a Honeycomb-Like Structure*, J. Phys. Chem. C **116**, 8983 (2012).
- [42] A. Kuc, N. Zibouche, and T. Heine, *Influence of Quantum Confinement on the Electronic Structure of the Transition Metal Sulfide TS₂*, Phys. Rev. B **83**, 245213 (2011).
- [43] K. Kobayashi and J. Yamauchi, *Electronic Structure and Scanning-Tunneling-Microscopy Image of Molybdenum Dichalcogenide Surfaces*, Phys. Rev. B **51**, 17085 (1995).
- [44] T. Li and G. Galli, *Electronic Properties of MoS₂ Nanoparticles*, J. Phys. Chem. C **111**, 16192 (2007).
- [45] S. Lebègue and O. Eriksson, *Electronic Structure of Two-Dimensional Crystals from ab Initio Theory*, Phys. Rev. B **79**, 115409 (2009).
- [46] A. Splendiani, L. Sun, Y. Zhang, T. Li, J. Kim, C.-Y. Chim, G. Galli, and F. Wang, *Emerging Photoluminescence in Monolayer MoS₂*, Nano Lett. **10**, 1271 (2010).
- [47] A. Kormányos, G. Burkard, M. Gmitra, J. Fabian, V. Zólyomi, N. D. Drummond, and V. Fal'ko, *K-p Theory for Two-Dimensional Transition Metal Dichalcogenide Semiconductors*, 2D Mater. **2**, 022001 (2015).
- [48] Y. Zhang et al., *Direct Observation of the Transition from Indirect to Direct Bandgap in Atomically Thin Epitaxial MoSe₂*, Nature Nanotech **9**, 111 (2014).
- [49] S.-K. Mo, *Angle-Resolved Photoemission Spectroscopy for the Study of Two-Dimensional Materials*, Nano Convergence **4**, 6 (2017).
- [50] N. Alidoust et al., *Observation of Monolayer Valence Band Spin-Orbit Effect and Induced Quantum Well States in MoX₂*, Nat Commun **5**, 4673 (2014).
- [51] P.-C. Yeh et al., *Layer-Dependent Electronic Structure of an Atomically Heavy Two-Dimensional Dichalcogenide*, Phys. Rev. B **91**, 041407 (2015).
- [52] W. Jin et al., *Direct Measurement of the Thickness-Dependent Electronic Band Structure of MoS₂ Using Angle-Resolved Photoemission Spectroscopy*, Phys. Rev. Lett. **111**, 106801 (2013).
- [53] M. M. Ugeda et al., *Giant Bandgap Renormalization and Excitonic Effects in a Monolayer Transition Metal Dichalcogenide Semiconductor*, Nature Mater **13**, 1091 (2014).

- [54] S. Tongay, J. Zhou, C. Ataca, K. Lo, T. S. Matthews, J. Li, J. C. Grossman, and J. Wu, *Thermally Driven Crossover from Indirect toward Direct Bandgap in 2D Semiconductors: MoSe₂ versus MoS₂*, *Nano Lett.* **12**, 5576 (2012).
- [55] H. Henck et al., *Electronic Band Structure of Two-Dimensional WS₂/Graphene van Der Waals Heterostructures*, *Phys. Rev. B* **97**, 155421 (2018).
- [56] A. Kormányos, G. Burkard, M. Gmitra, J. Fabian, V. Zólyomi, N. D. Drummond, and V. Fal'ko, *Corrigendum: K.p Theory for Two-Dimensional Transition Metal Dichalcogenide Semiconductors*, *2D Mater.* **2**, 049501 (2015).
- [57] A. Molina-Sánchez, D. Sangalli, K. Hummer, A. Marini, and L. Wirtz, *Effect of Spin-Orbit Interaction on the Optical Spectra of Single-Layer, Double-Layer, and Bulk MoS₂*, *Phys. Rev. B* **88**, 045412 (2013).
- [58] D. Xiao, G.-B. Liu, W. Feng, X. Xu, and W. Yao, *Coupled Spin and Valley Physics in Monolayers of MoS₂ and Other Group-VI Dichalcogenides*, *Phys. Rev. Lett.* **108**, 196802 (2012).
- [59] G.-B. Liu, W.-Y. Shan, Y. Yao, W. Yao, and D. Xiao, *Three-Band Tight-Binding Model for Monolayers of Group-VIB Transition Metal Dichalcogenides*, *Phys. Rev. B* **88**, 085433 (2013).
- [60] A. Kormányos, V. Zólyomi, N. D. Drummond, and G. Burkard, *Spin-Orbit Coupling, Quantum Dots, and Qubits in Monolayer Transition Metal Dichalcogenides*, *Phys. Rev. X* **4**, 011034 (2014).
- [61] Z. Y. Zhu, Y. C. Cheng, and U. Schwingenschlögl, *Giant Spin-Orbit-Induced Spin Splitting in Two-Dimensional Transition-Metal Dichalcogenide Semiconductors*, *Phys. Rev. B* **84**, 153402 (2011).
- [62] J. A. Miwa, S. Ulstrup, S. G. Sørensen, M. Dendzik, A. G. Čabo, M. Bianchi, J. V. Lauritsen, and P. Hofmann, *Electronic Structure of Epitaxial Single-Layer MoS₂*, *Phys. Rev. Lett.* **114**, 046802 (2015).
- [63] G. Wang, A. Chernikov, M. M. Glazov, T. F. Heinz, X. Marie, T. Amand, and B. Urbaszek, *Colloquium : Excitons in Atomically Thin Transition Metal Dichalcogenides*, *Rev. Mod. Phys.* **90**, 021001 (2018).
- [64] Mark Fox, *Optical Properties of Solids*, Second Edition (Oxford University Press, 2010).
- [65] Bir, G. L., and G. E. Pikus, *Symmetry and Strain-Induced Effects in Semiconductors* (Wiley/Halsted Press, New York/ Toronto, 1974).
- [66] M. M. Glazov, E. L. Ivchenko, G. Wang, T. Amand, X. Marie, B. Urbaszek, and B. L. Liu, *Spin and Valley Dynamics of Excitons in Transition Metal Dichalcogenide Monolayers: Spin and Valley Dynamics of Excitons in Transition Metal Dichalcogenide Monolayers*, *Phys. Status Solidi B* **252**, 2349 (2015).
- [67] G. Wang, I. C. Gerber, L. Bouet, D. Lagarde, A. Balocchi, M. Vidal, T. Amand, X. Marie, and B. Urbaszek, *Exciton States in Monolayer MoSe₂: Impact on Interband Transitions*, *2D Mater.* **2**, 045005 (2015).
- [68] G. G. Macfarlane, T. P. McLean, J. E. Quarrington, and V. Roberts, *Exciton and Phonon Effects in the Absorption Spectra of Germanium and Silicon*, *Journal of Physics and Chemistry of Solids* **8**, 388 (1959).
- [69] M. A. Green, *Improved Value for the Silicon Free Exciton Binding Energy*, *AIP Advances* **3**, 112104 (2013).
- [70] S. Chichibu, T. Azuhata, T. Sota, and S. Nakamura, *Spontaneous Emission of Localized Excitons in InGaN Single and Multiquantum Well Structures*, *Appl. Phys. Lett.* **69**, 4188 (1996).
- [71] J. Singh, *Excitation Energy Transfer Processes in Condensed Matter* (Springer US, Boston, MA, 1994).

- [72] Claus F Klingshirn, *Semiconductor Optics* (Springer Science & Business Media, 2012).
- [73] N.S. Rytova, *The Screened Potential of a Point Charge in a Thin Film*, Moscow University Physics Bulletin **22**, 18 (1967).
- [74] L.V. Keldysh, *Coulomb Interaction in Thin Semiconductor and Semimetal Films*, JETP Letter **29**, 658 (1979).
- [75] C. Robert et al., *Optical Spectroscopy of Excited Exciton States in MoS₂ Monolayers in van Der Waals Heterostructures*, Phys. Rev. Materials **2**, 011001 (2018).
- [76] B. Han et al., *Exciton States in Monolayer MoSe₂ and MoTe₂ Probed by Upconversion Spectroscopy*, Phys. Rev. X **8**, 031073 (2018).
- [77] A. V. Stier, N. P. Wilson, K. A. Velizhanin, J. Kono, X. Xu, and S. A. Crooker, *Magneto optics of Exciton Rydberg States in a Monolayer Semiconductor*, Phys. Rev. Lett. **120**, 057405 (2018).
- [78] M. Goryca et al., *Revealing Exciton Masses and Dielectric Properties of Monolayer Semiconductors with High Magnetic Fields*, Nat Commun **10**, 1 (2019).
- [79] G. Moody et al., *Intrinsic Homogeneous Linewidth and Broadening Mechanisms of Excitons in Monolayer Transition Metal Dichalcogenides*, Nat Commun **6**, 1 (2015).
- [80] M. Palummo, M. Bernardi, and J. C. Grossman, *Exciton Radiative Lifetimes in Two-Dimensional Transition Metal Dichalcogenides*, Nano Lett. **15**, 2794 (2015).
- [81] C. Poellmann, P. Steinleitner, U. Leierseder, P. Nagler, G. Plechinger, M. Porer, R. Bratschitsch, C. Schüller, T. Korn, and R. Huber, *Resonant Internal Quantum Transitions and Femtosecond Radiative Decay of Excitons in Monolayer WSe₂*, Nature Mater **14**, 9 (2015).
- [82] T. Jakubczyk, V. Delmonte, M. Koperski, K. Nogajewski, C. Faugeras, W. Langbein, M. Potemski, and J. Kasprzak, *Radiatively Limited Dephasing and Exciton Dynamics in MoSe₂ Monolayers Revealed with Four-Wave Mixing Microscopy*, Nano Lett. **16**, 5333 (2016).
- [83] C. Robert et al., *Exciton Radiative Lifetime in Transition Metal Dichalcogenide Monolayers*, Phys. Rev. B **93**, 205423 (2016).
- [84] M. M. Glazov, T. Amand, X. Marie, D. Lagarde, L. Bouet, and B. Urbaszek, *Exciton Fine Structure and Spin Decoherence in Monolayers of Transition Metal Dichalcogenides*, Phys. Rev. B **89**, 201302 (2014).
- [85] A. O. Slobodeniuk and D. M. Basko, *Spin–Flip Processes and Radiative Decay of Dark Intravalley Excitons in Transition Metal Dichalcogenide Monolayers*, 2D Mater. **3**, 035009 (2016).
- [86] G. Wang et al., *In-Plane Propagation of Light in Transition Metal Dichalcogenide Monolayers: Optical Selection Rules*, Phys. Rev. Lett. **119**, 047401 (2017).
- [87] Y. Zhou et al., *Probing Dark Excitons in Atomically Thin Semiconductors via Near-Field Coupling to Surface Plasmon Polaritons*, Nature Nanotech **12**, 856 (2017).
- [88] C. Robert et al., *Measurement of the Spin-Forbidden Dark Excitons in MoS₂ and MoSe₂ Monolayers*, Nat Commun **11**, 4037 (2020).
- [89] M. Zinkiewicz et al., *Neutral and Charged Dark Excitons in Monolayer WS₂*, Nanoscale **12**, 18153 (2020).
- [90] M. Zinkiewicz et al., *Excitonic Complexes in N-Doped WS₂ Monolayer*, Nano Lett. **21**, 2519 (2021).

- [91] X.-X. Zhang et al., *Magnetic Brightening and Control of Dark Excitons in Monolayer WSe₂*, *Nature Nanotech* **12**, 883 (2017).
- [92] D. Y. Qiu, T. Cao, and S. G. Louie, *Nonanalyticity, Valley Quantum Phases, and Lightlike Exciton Dispersion in Monolayer Transition Metal Dichalcogenides: Theory and First-Principles Calculations*, *Phys. Rev. Lett.* **115**, 176801 (2015).
- [93] C. Robert, T. Amand, F. Cadiz, D. Lagarde, E. Courtade, M. Manca, T. Taniguchi, K. Watanabe, B. Urbaszek, and X. Marie, *Fine Structure and Lifetime of Dark Excitons in Transition Metal Dichalcogenide Monolayers*, *Phys. Rev. B* **96**, 155423 (2017).
- [94] D. K. Efimkin and A. H. MacDonald, *Many-Body Theory of Trion Absorption Features in Two-Dimensional Semiconductors*, *Phys. Rev. B* **95**, 035417 (2017).
- [95] M. Sidler, P. Back, O. Cotlet, A. Srivastava, T. Fink, M. Kroner, E. Demler, and A. Imamoglu, *Fermi Polaron-Polaritons in Charge-Tunable Atomically Thin Semiconductors*, *Nature Phys* **13**, 3 (2017).
- [96] M. M. Glazov, *Optical Properties of Charged Excitons in Two-Dimensional Semiconductors*, *J. Chem. Phys.* **153**, 034703 (2020).
- [97] J. Ribeiro-Soares, R. M. Almeida, E. B. Barros, P. T. Araujo, M. S. Dresselhaus, L. G. Cançado, and A. Jorio, *Group Theory Analysis of Phonons in Two-Dimensional Transition Metal Dichalcogenides*, *Phys. Rev. B* **90**, 115438 (2014).
- [98] D. Xiao, G.-B. Liu, W. Feng, X. Xu, and W. Yao, *Coupled Spin and Valley Physics in Monolayers of MoS₂ and Other Group-VI Dichalcogenides*, *Phys. Rev. Lett.* **108**, 196802 (2012).
- [99] T. Cao et al., *Valley-Selective Circular Dichroism of Monolayer Molybdenum Disulphide*, *Nat Commun* **3**, 887 (2012).
- [100] D. Lagarde, L. Bouet, X. Marie, C. R. Zhu, B. L. Liu, T. Amand, P. H. Tan, and B. Urbaszek, *Carrier and Polarization Dynamics in Monolayer MoS₂*, *Phys. Rev. Lett.* **112**, 047401 (2014).
- [101] H. H. Fang et al., *Control of the Exciton Radiative Lifetime in Van Der Waals Heterostructures*, *Phys. Rev. Lett.* **123**, 067401 (2019).
- [102] T. Korn, S. Heydrich, M. Hirmer, J. Schmutzler, and C. Schüller, *Low-Temperature Photocarrier Dynamics in Monolayer MoS₂*, *Appl. Phys. Lett.* **99**, 102109 (2011).
- [103] C. R. Zhu, K. Zhang, M. Glazov, B. Urbaszek, T. Amand, Z. W. Ji, B. L. Liu, and X. Marie, *Exciton Valley Dynamics Probed by Kerr Rotation in WSe₂ Monolayers*, *Phys. Rev. B* **90**, 161302 (2014).
- [104] G. Wang, L. Bouet, D. Lagarde, M. Vidal, A. Balocchi, T. Amand, X. Marie, and B. Urbaszek, *Valley Dynamics Probed through Charged and Neutral Exciton Emission in Monolayer WSe₂*, *Phys. Rev. B* **90**, 075413 (2014).
- [105] J. Li, M. Goryca, K. Yumigeta, H. Li, S. Tongay, and S. A. Crooker, *Valley Relaxation of Resident Electrons and Holes in a Monolayer Semiconductor: Dependence on Carrier Density and the Role of Substrate-Induced Disorder*, *Phys. Rev. Materials* **5**, 044001 (2021).
- [106] P. Dey, L. Yang, C. Robert, G. Wang, B. Urbaszek, X. Marie, and S. A. Crooker, *Gate-Controlled Spin-Valley Locking of Resident Carriers in WSe₂ Monolayers*, *Phys. Rev. Lett.* **119**, 137401 (2017).
- [107] M. Goryca, N. P. Wilson, P. Dey, X. Xu, and S. A. Crooker, *Detection of Thermodynamic “Valley Noise” in Monolayer Semiconductors: Access to Intrinsic Valley Relaxation Time Scales* / *Science Advances* **5**, eaau4899 (2019).

- [108] T. Yan, S. Yang, D. Li, and X. Cui, *Long Valley Relaxation Time of Free Carriers in Monolayer WSe₂*, Phys. Rev. B **95**, 241406 (2017).
- [109] A. Castellanos-Gomez, M. Buscema, R. Molenaar, V. Singh, L. Janssen, H. S. J. van der Zant, and G. A. Steele, *Deterministic Transfer of Two-Dimensional Materials by All-Dry Viscoelastic Stamping*, 2D Mater. **1**, 011002 (2014).
- [110] M. A. Meitl, Z.-T. Zhu, V. Kumar, K. J. Lee, X. Feng, Y. Y. Huang, I. Adesida, R. G. Nuzzo, and J. A. Rogers, *Transfer Printing by Kinetic Control of Adhesion to an Elastomeric Stamp*, Nature Mater **5**, 33 (2006).
- [111] C. Robert et al., *Spin/Valley Pumping of Resident Electrons in WSe₂ and WS₂ Monolayers*, Nat Commun **12**, 5455 (2021).
- [112] A. Jain, P. Bharadwaj, S. Heeg, M. Parzefall, T. Taniguchi, K. Watanabe, and L. Novotny, *Minimizing Residues and Strain in 2D Materials Transferred from PDMS*, Nanotechnology **29**, 265203 (2018).
- [113] E. Khestanova, F. Guinea, L. Fumagalli, A. K. Geim, and I. V. Grigorieva, *Universal Shape and Pressure inside Bubbles Appearing in van Der Waals Heterostructures*, Nat Commun **7**, 12587 (2016).
- [114] F. Cadiz et al., *Excitonic Linewidth Approaching the Homogeneous Limit in MoS₂-Based van Der Waals Heterostructures*, Phys. Rev. X **7**, 021026 (2017).
- [115] M. Ouyang, C. Yuan, R. J. Muisener, A. Boulares, and J. T. Koberstein, *Conversion of Some Siloxane Polymers to Silicon Oxide by UV/Ozone Photochemical Processes*, Chem. Mater. **12**, 1591 (2000).
- [116] Emmanuel Courtade, High Quality van Der Waals Heterostructures for Optoelectronics and Spintronics, Thesis, University of Toulouse, 2019.
- [117] T. Taniguchi and K. Watanabe, *Synthesis of High-Purity Boron Nitride Single Crystals under High Pressure by Using Ba-BN Solvent*, Journal of Crystal Growth **303**, 525 (2007).
- [118] Y. Li, V. Garnier, P. Steyer, C. Journet, and B. Toury, *Millimeter-Scale Hexagonal Boron Nitride Single Crystals for Nanosheet Generation*, ACS Appl. Nano Mater. **3**, 1508 (2020).
- [119] C. Maestre et al., *From the Synthesis of HBN Crystals to Their Use as Nanosheets for Optoelectronic Devices*, 2D Mater. **9**, 035008 (2022).
- [120] K. F. Mak, C. Lee, J. Hone, J. Shan, and T. F. Heinz, *Atomically Thin MoS₂: A New Direct-Gap Semiconductor*, Phys. Rev. Lett. **105**, 136805 (2010).
- [121] A. I. Prazdnichnykh, M. M. Glazov, L. Ren, C. Robert, B. Urbaszek, and X. Marie, *Control of the Exciton Valley Dynamics in Atomically Thin Semiconductors by Tailoring the Environment*, Phys. Rev. B **103**, 085302 (2021).
- [122] A. Raja et al., *Dielectric Disorder in Two-Dimensional Materials*, Nat. Nanotechnol. **14**, 832 (2019).
- [123] A. V. Stier, N. P. Wilson, G. Clark, X. Xu, and S. A. Crooker, *Probing the Influence of Dielectric Environment on Excitons in Monolayer WSe₂: Insight from High Magnetic Fields*, Nano Lett. **16**, 7054 (2016).
- [124] M. Rösner, C. Steinke, M. Lorke, C. Gies, F. Jahnke, and T. O. Wehling, *Two-Dimensional Heterojunctions from Nonlocal Manipulations of the Interactions*, Nano Lett. **16**, 2322 (2016).
- [125] A. Raja et al., *Coulomb Engineering of the Bandgap and Excitons in Two-Dimensional Materials*, Nat Commun **8**, 1 (2017).
- [126] Y. Cho and T. C. Berkelbach, *Environmentally Sensitive Theory of Electronic and Optical Transitions in Atomically Thin Semiconductors*, Phys. Rev. B **97**, 041409 (2018).

- [127] K. T. Winther and K. S. Thygesen, *Band Structure Engineering in van Der Waals Heterostructures via Dielectric Screening: The GAW Method*, 2D Mater. **4**, 025059 (2017).
- [128] H. Zeng, J. Dai, W. Yao, D. Xiao, and X. Cui, *Valley Polarization in MoS₂ Monolayers by Optical Pumping*, Nature Nanotech **7**, 490 (2012).
- [129] A. Neumann, J. Lindlau, L. Colombier, M. Nutz, S. Najmaei, J. Lou, A. D. Mohite, H. Yamaguchi, and A. Högele, *Opto-Valleytronic Imaging of Atomically Thin Semiconductors*, Nature Nanotech **12**, 329 (2017).
- [130] G. Kioseoglou, A. T. Hanbicki, M. Currie, A. L. Friedman, D. Gunlycke, and B. T. Jonker, *Valley Polarization and Intervalley Scattering in Monolayer MoS₂*, Appl. Phys. Lett. **101**, 221907 (2012).
- [131] F. Cadiz et al., *Ultra-Low Power Threshold for Laser Induced Changes in Optical Properties of 2D Molybdenum Dichalcogenides*, 2D Mater. **3**, 045008 (2016).
- [132] M. Currie, A. T. Hanbicki, G. Kioseoglou, and B. T. Jonker, *Optical Control of Charged Exciton States in Tungsten Disulfide*, Appl. Phys. Lett. **106**, 201907 (2015).
- [133] Z. He, X. Wang, W. Xu, Y. Zhou, Y. Sheng, Y. Rong, J. M. Smith, and J. H. Warner, *Revealing Defect-State Photoluminescence in Monolayer WS₂ by Cryogenic Laser Processing*, ACS Nano **10**, 5847 (2016).
- [134] Y. Liu, P. Stradins, and S.-H. Wei, *Van Der Waals Metal-Semiconductor Junction: Weak Fermi Level Pinning Enables Effective Tuning of Schottky Barrier*, Sci. Adv. **2**, e1600069 (2016).
- [135] S. Shree, I. Paradisanos, X. Marie, C. Robert, and B. Urbaszek, *Guide to Optical Spectroscopy of Layered Semiconductors*, Nat Rev Phys **3**, 39 (2021).
- [136] G. Wang, X. Marie, B. L. Liu, T. Amand, C. Robert, F. Cadiz, P. Renucci, and B. Urbaszek, *Control of Exciton Valley Coherence in Transition Metal Dichalcogenide Monolayers*, Phys. Rev. Lett. **117**, 187401 (2016).
- [137] A. M. Jones et al., *Optical Generation of Excitonic Valley Coherence in Monolayer WSe₂*, Nature Nanotech **8**, 634 (2013).
- [138] E. L. Ivchenko, *Optical Spectroscopy of Semiconductor Nanostructures* (Alpha Science Int'l Ltd., 2005).
- [139] G. E. PIKUS and G. L. BIR, *Exchange Interaction in Excitons in Semiconductors*, Sov. Phys. JETP **33**, 108 (1971).
- [140] M. M. Denisov and V. P. Makarov, *Longitudinal and Transverse Excitons in Semiconductors*, Physica Status Solidi (b) **56**, 9 (1973).
- [141] L. C. Andreani and F. Bassani, *Exchange Interaction and Polariton Effects in Quantum-Well Excitons*, Phys. Rev. B **41**, 7536 (1990).
- [142] E. Blackwood, M. J. Snelling, R. T. Harley, S. R. Andrews, and C. T. B. Foxon, *Exchange Interaction of Excitons in GaAs Heterostructures*, Phys. Rev. B **50**, 14246 (1994).
- [143] T. Amand, X. Marie, P. Le Jeune, M. Brousseau, D. Robart, J. Barrau, and R. Planel, *Spin Quantum Beats of 2D Excitons*, Phys. Rev. Lett. **78**, 1355 (1997).
- [144] M. Bayer et al., *Fine Structure of Neutral and Charged Excitons in Self-Assembled In(Ga)As/(Al)GaAs Quantum Dots*, Phys. Rev. B **65**, 195315 (2002).
- [145] E. Poem, Y. Kodriano, C. Tradonsky, N. H. Lindner, B. D. Gerardot, P. M. Petroff, and D. Gershoni, *Accessing the Dark Exciton with Light*, Nature Phys **6**, 12 (2010).
- [146] M. Dyksik, H. Duim, D. K. Maude, M. Baranowski, M. A. Loi, and P. Plochocka, *Brightening of Dark Excitons in 2D Perovskites*, Science Advances **7**, eabk0904 (2021).

- [147] M. Gramlich, M. W. Swift, C. Lampe, J. L. Lyons, M. Döbling, A. L. Efros, P. C. Sercel, and A. S. Urban, *Dark and Bright Excitons in Halide Perovskite Nanoplatelets*, Advanced Science **9**, 2103013 (2022).
- [148] X.-X. Zhang, Y. You, S. Y. F. Zhao, and T. F. Heinz, *Experimental Evidence for Dark Excitons in Monolayer WSe₂*, Phys. Rev. Lett. **115**, 257403 (2015).
- [149] G. Wang et al., *Spin-Orbit Engineering in Transition Metal Dichalcogenide Alloy Monolayers*, Nat Commun **6**, 10110 (2015).
- [150] A. Arora, M. Koperski, K. Nogajewski, J. Marcus, C. Faugeras, and M. Potemski, *Excitonic Resonances in Thin Films of WSe₂: From Monolayer to Bulk Material*, Nanoscale **7**, 10421 (2015).
- [151] W. E. Lamb and R. C. Rutherford, *Fine Structure of the Hydrogen Atom by a Microwave Method*, Phys. Rev. **72**, 241 (1947).
- [152] H. A. Bethe, *The Electromagnetic Shift of Energy Levels*, Phys. Rev. **72**, 339 (1947).
- [153] R. Friedberg, S. R. Hartmann, and J. T. Manassah, *Frequency Shifts in Emission and Absorption by Resonant Systems Of Two-Level Atoms*, Physics Reports **7**, 101 (1973).
- [154] R. Röhlsberger, K. Schlage, B. Sahoo, S. Couet, and R. Rüffer, *Collective Lamb Shift in Single-Photon Superradiance*, Science **328**, 1248 (2010).
- [155] J. Keaveney, A. Sargsyan, U. Krohn, I. G. Hughes, D. Sarkisyan, and C. S. Adams, *Cooperative Lamb Shift in an Atomic Vapor Layer of Nanometer Thickness*, Phys. Rev. Lett. **108**, 173601 (2012).
- [156] A. M. Jones, H. Yu, J. R. Schaibley, J. Yan, D. G. Mandrus, T. Taniguchi, K. Watanabe, H. Dery, W. Yao, and X. Xu, *Excitonic Luminescence Upconversion in a Two-Dimensional Semiconductor*, Nature Phys **12**, 323 (2016).
- [157] E. Courtade et al., *Charged Excitons in Monolayer WSe₂: Experiment and Theory*, Phys. Rev. B **96**, 085302 (2017).
- [158] M. He et al., *Valley Phonons and Exciton Complexes in a Monolayer Semiconductor*, Nat Commun **11**, 618 (2020).
- [159] J. P. Echeverry, B. Urbaszek, T. Amand, X. Marie, and I. C. Gerber, *Splitting between Bright and Dark Excitons in Transition Metal Dichalcogenide Monolayers*, Phys. Rev. B **93**, 121107 (2016).
- [160] Y. Zhou et al., *Controlling Excitons in an Atomically Thin Membrane with a Mirror*, Phys. Rev. Lett. **124**, 027401 (2020).
- [161] C. Rogers, D. Gray, N. Bogdanowicz, T. Taniguchi, K. Watanabe, and H. Mabuchi, *Coherent Feedback Control of Two-Dimensional Excitons*, Phys. Rev. Research **2**, 012029 (2020).
- [162] M. Först, L. Colombier, R. K. Patel, J. Lindlau, A. D. Mohite, H. Yamaguchi, M. M. Glazov, D. Hunger, and A. Högele, *Cavity-Control of Interlayer Excitons in van Der Waals Heterostructures*, Nat Commun **10**, 1 (2019).
- [163] C. Boule, D. Vaclavkova, M. Bartos, K. Nogajewski, L. Zdražil, T. Taniguchi, K. Watanabe, M. Potemski, and J. Kasprzak, *Coherent Dynamics and Mapping of Excitons in Single-Layer MoSe₂ and WSe₂ at the Homogeneous Limit*, Phys. Rev. Mater. **4**, 034001 (2020).
- [164] J. Horng, Y.-H. Chou, T.-C. Chang, C.-Y. Hsu, T.-C. Lu, and H. Deng, *Engineering Radiative Coupling of Excitons in 2D Semiconductors*, Optica, OPTICA **6**, 1443 (2019).
- [165] Q. Sun, M. Al-Amri, A. Kamli, and M. S. Zubairy, *Lamb Shift Due to Surface Plasmon Polariton Modes*, Phys. Rev. A **77**, 062501 (2008).

- [166] P. Li, C. Robert, D. Van Tuan, L. Ren, M. Yang, X. Marie, and H. Dery, *Intervalley Electron-Hole Exchange Interaction and Impurity-Assisted Recombination of Indirect Excitons in WS₂ and WSe₂ Monolayers*, Phys. Rev. B **106**, 085414 (2022).
- [167] Z. Lu et al., *Magnetic Field Mixing and Splitting of Bright and Dark Excitons in Monolayer MoSe₂*, 2D Mater. **7**, 015017 (2019).
- [168] H. Shan et al., *Brightening of a Dark Monolayer Semiconductor via Strong Light-Matter Coupling in a Cavity*, Nat Commun **13**, 3001 (2022).
- [169] M. Combescot, F. Dubin, and S.-Y. Shieh, *Signature of Electromagnetic Quantum Fluctuations in Exciton Physics*, EPL **138**, 3 (2022).
- [170] G. Moody, J. Schaibley, and X. Xu, *Exciton Dynamics in Monolayer Transition Metal Dichalcogenides*, JOSA B, **33**, C39-C49 (2016).
- [171] C. Jiang, W. Xu, A. Rasmita, Z. Huang, K. Li, Q. Xiong, and W. Gao, *Microsecond Dark-Exciton Valley Polarization Memory in Two-Dimensional Heterostructures*, Nat Commun, **9**, 753 (2018).
- [172] P. Rivera, K. L. Seyler, H. Yu, J. R. Schaibley, J. Yan, D. G. Mandrus, W. Yao, and X. Xu, *Valley-Polarized Exciton Dynamics in a 2D Semiconductor Heterostructure*, Science **351**, 688 (2016).
- [173] F. Qu, H. Bragança, R. Vasconcelos, F. Liu, S.-J. Xie, and H. Zeng, *Controlling Valley Splitting and Polarization of Dark- and Bi-Excitons in Monolayer WS₂ by a Tilted Magnetic Field*, 2D Mater. **6**, 045014 (2019).
- [174] P. Back, M. Sidler, O. Cotlet, A. Srivastava, N. Takemura, M. Kroner, and A. İmamoğlu, *Giant Paramagnetism-Induced Valley Polarization of Electrons in Charge-Tunable Monolayer MoSe₂*, Phys. Rev. Lett. **118**, 237404 (2017).
- [175] Z. Wang, J. Shan, and K. F. Mak, *Valley- and Spin-Polarized Landau Levels in Monolayer WSe₂*, Nature Nanotechnology **12**, 144 (2017).
- [176] E. Liu, J. van Baren, T. Taniguchi, K. Watanabe, Y.-C. Chang, and C. H. Lui, *Landau-Quantized Excitonic Absorption and Luminescence in a Monolayer Valley Semiconductor*, Phys. Rev. Lett. **124**, 097401 (2020).
- [177] Z. Li et al., *Direct Observation of Gate-Tunable Dark Trions in Monolayer WSe₂*, Nano Lett. **19**, 6886 (2019).
- [178] M. He et al., *Valley Phonons and Exciton Complexes in a Monolayer Semiconductor*, Nat Commun **11**, 618 (2020).
- [179] Z. Li, T. Wang, S. Miao, Z. Lian, and S.-F. Shi, *Fine Structures of Valley-Polarized Excitonic States in Monolayer Transitional Metal Dichalcogenides*, Nanophotonics **9**, 1811 (2020).
- [180] E. Liu, J. van Baren, Z. Lu, M. M. Altaiary, T. Taniguchi, K. Watanabe, D. Smirnov, and C. H. Lui, *Gate Tunable Dark Trions in Monolayer WSe₂*, Phys. Rev. Lett. **123**, 027401 (2019).
- [181] H. Yu, G.-B. Liu, P. Gong, X. Xu, and W. Yao, *Dirac Cones and Dirac Saddle Points of Bright Excitons in Monolayer Transition Metal Dichalcogenides*, Nat Commun **5**, 3876 (2014).
- [182] E. Liu, J. van Baren, C.-T. Liang, T. Taniguchi, K. Watanabe, N. M. Gabor, Y.-C. Chang, and C. H. Lui, *Multipath Optical Recombination of Intervalley Dark Excitons and Trions in Monolayer WSe₂*, Phys. Rev. Lett. **124**, 196802 (2020).
- [183] F. Meier and B. P. Zakharchenia, editors, *Optical Orientation* (North-Holland ; Sole distributors for the U.S.A. and Canada, Elsevier Science Pub. Co, Amsterdam ; New York, 1984).
- [184] J. M. Kikkawa and D. D. Awschalom, *Resonant Spin Amplification in n-Type GaAs*, Phys. Rev. Lett. **80**, 4313 (1998).

- [185] L. Childress, M. V. Gurudev Dutt, J. M. Taylor, A. S. Zibrov, F. Jelezko, J. Wrachtrup, P. R. Hemmer, and M. D. Lukin, *Coherent Dynamics of Coupled Electron and Nuclear Spin Qubits in Diamond*, *Science* **314**, 281 (2006).
- [186] H. Dery and Y. Song, *Polarization Analysis of Excitons in Monolayer and Bilayer Transition-Metal Dichalcogenides*, *Phys. Rev. B* **92**, 125431 (2015).
- [187] Y. Song and H. Dery, *Transport Theory of Monolayer Transition-Metal Dichalcogenides through Symmetry*, *Phys. Rev. Lett.* **111**, 026601 (2013).
- [188] M. Ersfeld et al., *Unveiling Valley Lifetimes of Free Charge Carriers in Monolayer WSe₂*, *Nano Lett.* **20**, 3147 (2020).
- [189] J. Fu, J. M. R. Cruz, and F. Qu, *Valley Dynamics of Different Trion Species in Monolayer WSe₂*, *Appl. Phys. Lett.* **115**, 082101 (2019).
- [190] M. T. Portella-Oberli, J. Berney, L. Kappei, F. Morier-Genoud, J. Szczytko, and B. Deveaud-Plédran, *Dynamics of Trion Formation in In_xGa_{1-x}As Quantum Wells*, *Phys. Rev. Lett.* **102**, 096402 (2009).
- [191] C. Weisbuch and G. Lampel, *Spin-Dependent Recombination and Optical Spin Orientation in Semiconductors*, *Solid State Communications* **14**, 141 (1974).
- [192] D. Paget, *Optical-Pumping Study of Spin-Dependent Recombination in GaAs*, *Phys. Rev. B* **30**, 931 (1984).
- [193] D. Lagarde, L. Lombez, X. Marie, A. Balocchi, T. Amand, V. K. Kalevich, A. Shiryaev, E. Ivchenko, and A. Egorov, *Electron Spin Dynamics in GaAsN and InGaAsN Structures*, *Physica Status Solidi (a)* **204**, 208 (2007).
- [194] A. Singh et al., *Trion Formation Dynamics in Monolayer Transition Metal Dichalcogenides*, *Phys. Rev. B* **93**, 041401 (2016).
- [195] G. Plechinger, P. Nagler, A. Arora, R. Schmidt, A. Chernikov, A. G. del Águila, P. C. M. Christianen, R. Bratschitsch, C. Schüller, and T. Korn, *Trion Fine Structure and Coupled Spin–Valley Dynamics in Monolayer Tungsten Disulfide*, *Nat Commun* **7**, 12715 (2016).
- [196] D. Vaclavkova, J. Wyzula, K. Nogajewski, M. Bartos, A. O. Slobodeniuk, C. Faugeras, M. Potemski, and M. R. Molas, *Singlet and Triplet Trions in WS₂ Monolayer Encapsulated in Hexagonal Boron Nitride*, *Nanotechnology* **29**, 325705 (2018).
- [197] M. Paur, A. J. Molina-Mendoza, R. Bratschitsch, K. Watanabe, T. Taniguchi, and T. Mueller, *Electroluminescence from Multi-Particle Exciton Complexes in Transition Metal Dichalcogenide Semiconductors*, *Nat Commun* **10**, 1 (2019).
- [198] D. Xiao, G.-B. Liu, W. Feng, X. Xu, and W. Yao, *Coupled Spin and Valley Physics in Monolayers of MoS₂ and Other Group-VI Dichalcogenides*, *Phys. Rev. Lett.* **108**, 196802 (2012).
- [199] G. Sallen et al., *Robust Optical Emission Polarization in MoS₂ Monolayers through Selective Valley Excitation*, *Phys. Rev. B* **86**, 081301 (2012).
- [200] K. F. Mak, K. He, J. Shan, and T. F. Heinz, *Control of Valley Polarization in Monolayer MoS₂ by Optical Helicity*, *Nature Nanotech* **7**, 494 (2012).
- [201] T. Cao et al., *Valley-Selective Circular Dichroism of Monolayer Molybdenum Disulphide*, *Nat Commun* **3**, 887 (2012).
- [202] J. Kim et al., *Observation of Ultralong Valley Lifetime in WSe₂/MoS₂ Heterostructures*, *Science Advances* **3**, e1700518 (2017).
- [203] L. Wang and M. W. Wu, *Electron Spin Diffusion in Monolayer MoS₂*, *Phys. Rev. B* **89**, 205401 (2014).
- [204] X. Lin, W. Yang, K. L. Wang, and W. Zhao, *Two-Dimensional Spintronics for Low-Power Electronics*, **2**, 10 (2019).

- [205] P. Back, M. Sidler, O. Cotlet, A. Srivastava, N. Takemura, M. Kroner, and A. İmamoğlu, *Giant Paramagnetism-Induced Valley Polarization of Electrons in Charge-Tunable Monolayer MoSe₂*, Phys. Rev. Lett. **118**, 237404 (2017).
- [206] M. E. Flatté and J. M. Byers, *Spin Diffusion in Semiconductors*, Phys. Rev. Lett. **84**, 4220 (2000).
- [207] J. E. H. Braz, B. Amorim, and E. V. Castro, *Valley-Polarized Magnetic State in Hole-Doped Monolayers of Transition-Metal Dichalcogenides*, Phys. Rev. B **98**, 161406 (2018).
- [208] D. K. Mukherjee, A. Kundu, and H. A. Fertig, *Spin Response and Collective Modes in Simple Metal Dichalcogenides*, Phys. Rev. B **98**, 184413 (2018).
- [209] J. G. Roch, Dmitry Miserev, G. Froehlicher, N. Leisgang, L. Sponfeldner, K. Watanabe, T. Taniguchi, J. Klinovaja, D. Loss, and R. J. Warburton, *First-Order Magnetic Phase Transition of Mobile Electrons in Monolayer MoS₂*, Phys. Rev. Lett. **124**, 187602 (2020).
- [210] T. S. Ghiasi, J. Inglá-Aynés, A. A. Kaverzin, and B. J. van Wees, *Large Proximity-Induced Spin Lifetime Anisotropy in Transition-Metal Dichalcogenide/Graphene Heterostructures*, Nano Lett. **17**, 7528 (2017).
- [211] Y. K. Luo, J. Xu, T. Zhu, G. Wu, E. J. McCormick, W. Zhan, M. R. Neupane, and R. K. Kawakami, *Opto-Valleytronic Spin Injection in Monolayer MoS₂/Few-Layer Graphene Hybrid Spin Valves*, Nano Lett. **17**, 3877 (2017).
- [212] M. Schwemmer, P. Nagler, A. Hanninger, C. Schüller, and T. Korn, *Long-Lived Spin Polarization in n-Doped MoSe₂ Monolayers*, Appl. Phys. Lett. **111**, 082404 (2017).
- [213] E. J. McCormick, M. J. Newburger, Y. K. Luo, K. M. McCreary, S. Singh, I. B. Martin, E. J. Cichewicz, B. T. Jonker, and R. K. Kawakami, *Imaging Spin Dynamics in Monolayer WS₂ by Time-Resolved Kerr Rotation Microscopy*, 2D Mater. **5**, 011010 (2017).
- [214] M. Kulig, J. Zipfel, P. Nagler, S. Blanter, C. Schüller, T. Korn, N. Paradiso, M. M. Glazov, and A. Chernikov, *Exciton Diffusion and Halo Effects in Monolayer Semiconductors*, Phys. Rev. Lett. **120**, 207401 (2018).
- [215] G. Wang, A. Chernikov, M. M. Glazov, T. F. Heinz, X. Marie, T. Amand, and B. Urbaszek, *Colloquium: Excitons in Atomically Thin Transition Metal Dichalcogenides*, Rev. Mod. Phys. **90**, 021001 (2018).
- [216] F. Cadiz et al., *Exciton Diffusion in WSe₂ Monolayers Embedded in a van Der Waals Heterostructure*, Appl. Phys. Lett. **112**, 152106 (2018).
- [217] D. Unuchek, A. Ciarrocchi, A. Avsar, K. Watanabe, T. Taniguchi, and A. Kis, *Room-Temperature Electrical Control of Exciton Flux in a van Der Waals Heterostructure*, Nature **560**, 340 (2018).
- [218] R. Pereira-Causín, S. Brem, R. Rosati, R. Jago, M. Kulig, J. D. Ziegler, J. Zipfel, A. Chernikov, and E. Malic, *Exciton Propagation and Halo Formation in Two-Dimensional Materials*, Nano Lett. **19**, 7317 (2019).
- [219] T. Hotta, S. Higuchi, A. Ueda, K. Shinokita, Y. Miyauchi, K. Matsuda, K. Ueno, T. Taniguchi, K. Watanabe, and R. Kitaura, *Exciton Diffusion in hBN-Encapsulated Monolayer MoSe₂*, Phys. Rev. B **102**, 115424 (2020).
- [220] S. Batalden and V. Sih, *Spatially-Resolved Measurements of Spin Valley Polarization in MOCVD-Grown Monolayer WSe₂*, Opt. Express, OE **29**, 17269 (2021).
- [221] E. Barré, J. A. C. Incorvia, S. H. Kim, C. J. McClellan, E. Pop, H.-S. P. Wong, and T. F. Heinz, *Spatial Separation of Carrier Spin by the Valley Hall Effect in Monolayer WSe₂ Transistors*, Nano Lett. **19**, 770 (2019).

- [222] S. Liang et al., *Electrical Spin Injection and Detection in Molybdenum Disulfide Multilayer Channel*, Nat Commun **8**, 14947 (2017).
- [223] C. Jin et al., *Imaging of Pure Spin-Valley Diffusion Current in WS₂ -WSe₂ Heterostructures*, Science **360**, 893 (2018).
- [224] J. M. Kikkawa and D. D. Awschalom, *Lateral Drag of Spin Coherence in Gallium Arsenide*, Nature **397**, 139 (1999).
- [225] S. A. Crooker and D. L. Smith, *Imaging Spin Flows in Semiconductors Subject to Electric, Magnetic, and Strain Fields*, Phys. Rev. Lett. **94**, 236601 (2005).
- [226] R. Pisoni et al., *Interactions and Magnetotransport through Spin-Valley Coupled Landau Levels in Monolayer MoS₂*, Phys. Rev. Lett. **121**, 247701 (2018).
- [227] S. Larentis, H. C. P. Movva, B. Fallahazad, K. Kim, A. Behroozi, T. Taniguchi, K. Watanabe, S. K. Banerjee, and E. Tutuc, *Large Effective Mass and Interaction-Enhanced Zeeman Splitting of K-Valley Electrons in MoSe₂*, Phys. Rev. B **97**, 201407 (2018).
- [228] Y. Wang, T. Sohier, K. Watanabe, T. Taniguchi, M. J. Verstraete, and E. Tutuc, *Electron Mobility in Monolayer WS₂ Encapsulated in Hexagonal Boron-Nitride*, Appl. Phys. Lett. **118**, 102105 (2021).
- [229] T. Sasaki, T. Oikawa, T. Suzuki, M. Shiraishi, Y. Suzuki, and K. Noguchi, *Temperature Dependence of Spin Diffusion Length in Silicon by Hanle-Type Spin Precession*, Appl. Phys. Lett. **96**, 122101 (2010).
- [230] N. P. Stern, D. W. Steuerman, S. Mack, A. C. Gossard, and D. D. Awschalom, *Drift and Diffusion of Spins Generated by the Spin Hall Effect*, Appl. Phys. Lett. **91**, 062109 (2007).
- [231] M. Furis, D. L. Smith, S. Kos, E. S. Garlid, K. S. M. Reddy, C. J. Palmstrøm, P. A. Crowell, and S. A. Crooker, *Local Hanle-Effect Studies of Spin Drift and Diffusion in n:GaAs Epilayers and Spin-Transport Devices*, New J. Phys. **9**, 347 (2007).
- [232] S. G. Carter, Z. Chen, and S. T. Cundiff, *Optical Measurement and Control of Spin Diffusion in n-Doped GaAs Quantum Wells*, Phys. Rev. Lett. **97**, 136602 (2006).
- [233] C. Hu, H. Ye, G. Wang, H. Tian, W. Wang, W. Wang, B. Liu, and X. Marie, *Room Temperature Spin Diffusion in (110) GaAs/AlGaAs Quantum Wells*, Nanoscale Research Letters **6**, 149 (2011).
- [234] G. Wang, B. L. Liu, A. Balocchi, P. Renucci, C. R. Zhu, T. Amand, C. Fontaine, and X. Marie, *Gate Control of the Electron Spin-Diffusion Length in Semiconductor Quantum Wells*, Nat Commun **4**, 2372 (2013).
- [235] N. Tombros, C. Jozsa, M. Popinciuc, H. T. Jonkman, and B. J. van Wees, *Electronic Spin Transport and Spin Precession in Single Graphene Layers at Room Temperature*, Nature **448**, 571 (2007).
- [236] M. Drögeler, C. Franzen, F. Volmer, T. Pohlmann, L. Banszerus, M. Wolter, K. Watanabe, T. Taniguchi, C. Stampfer, and B. Beschoten, *Spin Lifetimes Exceeding 12 Ns in Graphene Nonlocal Spin Valve Devices*, Nano Lett. **16**, 3533 (2016).
- [237] C. Robert et al., *Spin/Valley Pumping of Resident Electrons in WSe₂ and WS₂ Monolayers*, Nat Commun **12**, 5455 (2021).
- [238] K. Hao, R. Shreiner, A. Kindseth, and A. A. High, *Optically Controllable Magnetism in Atomically Thin Semiconductors*, Science Advances **8**, eabq7650 (2022).
- [239] Y. Li et al., *Valley Splitting and Polarization by the Zeeman Effect in Monolayer MoSe₂*, Phys. Rev. Lett. **113**, 266804 (2014).

- [240] A. Srivastava, M. Sidler, A. V. Allain, D. S. Lembke, A. Kis, and A. İmamoğlu, *Valley Zeeman Effect in Elementary Optical Excitations of Monolayer WSe₂*, *Nature Phys* **11**, 141 (2015).
- [241] G. Wang, L. Bouet, M. M. Glazov, T. Amand, E. L. Ivchenko, E. Palleau, X. Marie, and B. Urbaszek, *Magneto-Optics in Transition Metal Diselenide Monolayers*, *2D Mater.* **2**, 034002 (2015).
- [242] G. Aivazian, Z. Gong, A. M. Jones, R.-L. Chu, J. Yan, D. G. Mandrus, C. Zhang, D. Cobden, W. Yao, and X. Xu, *Magnetic Control of Valley Pseudospin in Monolayer WSe₂*, *Nature Phys* **11**, 148 (2015).
- [243] D. MacNeill, C. Heikes, K. F. Mak, Z. Anderson, A. Kormányos, V. Zólyomi, J. Park, and D. C. Ralph, *Breaking of Valley Degeneracy by Magnetic Field in Monolayer MoSe₂*, *Phys. Rev. Lett.* **114**, 037401 (2015).
- [244] A. A. Mitioglu, P. Plochocka, Á. Granados del Aguila, P. C. M. Christianen, G. Deligeorgis, S. Anghel, L. Kulyuk, and D. K. Maude, *Optical Investigation of Monolayer and Bulk Tungsten Diselenide (WSe₂) in High Magnetic Fields*, *Nano Lett.* **15**, 4387 (2015).
- [245] A. Arora, R. Schmidt, R. Schneider, M. R. Molas, I. Breslavetz, M. Potemski, and R. Bratschitsch, *Valley Zeeman Splitting and Valley Polarization of Neutral and Charged Excitons in Monolayer MoTe₂ at High Magnetic Fields*, *Nano Lett.* **16**, 3624 (2016).
- [246] A. V. Stier, K. M. McCreary, B. T. Jonker, J. Kono, and S. A. Crooker, *Exciton Diamagnetic Shifts and Valley Zeeman Effects in Monolayer WS₂ and MoS₂ to 65 Tesla*, *Nat Commun* **7**, 10643 (2016).
- [247] M. Koperski, M. R. Molas, A. Arora, K. Nogajewski, M. Bartos, J. Wyzula, D. Vaclavkova, P. Kossacki, and M. Potemski, *Orbital, Spin and Valley Contributions to Zeeman Splitting of Excitonic Resonances in MoSe₂, WSe₂ and WS₂ Monolayers*, *2D Mater.* **6**, 015001 (2018).
- [248] H. C. P. Movva, B. Fallahazad, K. Kim, S. Larentis, T. Taniguchi, K. Watanabe, S. K. Banerjee, and E. Tutuc, *Density-Dependent Quantum Hall States and Zeeman Splitting in Monolayer and Bilayer WSe₂*, *Phys. Rev. Lett.* **118**, 247701 (2017).
- [249] E. L. Ivchenko, *Optical Spectroscopy of Semiconductor Nanostructures*, Alpha Science International Ltd (2005).
- [250] D. D. Awschalom, D. Loss, and N. Samarth, *Semiconductor Spintronics and Quantum Computation*, in (Springer, 2010).
- [251] M. I. Dyakonov, editor , *Spin Physics in Semiconductors*, Vol. 157 (Springer International Publishing, Cham, 2017).
- [252] G. R. Johnson, A. Kana-ah, B. C. Cavenett, M. S. Skolnick, and S. J. Bass, *Magnetic Resonance of 2D Electrons in a Single Quantum Well of InP/GaInAs*, *Semicond. Sci. Technol.* **2**, 182 (1987).
- [253] M. Dobers, K. v. Klitzing, and G. Weimann, *Electron-Spin Resonance in the Two-Dimensional Electron Gas of GaAs-Al_xGa_{1-x}As Heterostructures*, *Phys. Rev. B* **38**, 5453 (1988).
- [254] M. J. Snelling, G. P. Flinn, A. S. Plaut, R. T. Harley, A. C. Tropper, R. Eccleston, and C. C. Phillips, *Magnetic g Factor of Electrons in GaAs/Al_xGa_{1-x}As Quantum Wells*, *Phys. Rev. B* **44**, 11345 (1991).
- [255] A. P. Heberle, W. W. Röhle, and K. Ploog, *Quantum Beats of Electron Larmor Precession in GaAs Wells*, *Phys. Rev. Lett.* **72**, 3887 (1994).
- [256] T. Amand, X. Marie, P. Le Jeune, M. Brousseau, D. Robart, J. Barrau, and R. Planell, *Spin Quantum Beats of 2D Excitons*, *Phys. Rev. Lett.* **78**, 1355 (1997).

- [257] V. F. Sapega, T. Ruf, M. Cardona, K. Ploog, E. L. Ivchenko, and D. N. Mirlin, *Resonant Raman Scattering Due to Bound-Carrier Spin Flip in GaAs/Al_xGa_{1-x} As Quantum Wells*, Phys. Rev. B **50**, 2510 (1994).
- [258] L. M. Roth, B. Lax, and S. Zwerdling, *Theory of Optical Magneto-Absorption Effects in Semiconductors*, Phys. Rev. **114**, 90 (1959).
- [259] D. Xiao, W. Yao, and Q. Niu, *Valley-Contrasting Physics in Graphene: Magnetic Moment and Topological Transport*, Phys. Rev. Lett. **99**, 236809 (2007).
- [260] M. Oestreich, S. Hallstein, A. P. Heberle, K. Eberl, E. Bauser, and W. W. Rühle, *Temperature and Density Dependence of the Electron Landé g Factor in Semiconductors*, Phys. Rev. B **53**, 7911 (1996).
- [261] W. Zawadzki, P. Pfeffer, R. Bratschitsch, Z. Chen, S. T. Cundiff, B. N. Murdin, and C. R. Pidgeon, *Temperature Dependence of the Electron Spin g Factor in GaAs*, Phys. Rev. B **78**, 245203 (2008).
- [262] S. Larentis, H. C. P. Movva, B. Fallahazad, K. Kim, A. Behroozi, T. Taniguchi, K. Watanabe, S. K. Banerjee, and E. Tutuc, *Large Effective Mass and Interaction-Enhanced Zeeman Splitting of K -Valley Electrons in MoSe₂*, Phys. Rev. B **97**, 201407 (2018).
- [263] R. Pisoni et al., *Interactions and Magnetotransport through Spin-Valley Coupled Landau Levels in Monolayer MoS₂*, Phys. Rev. Lett. **121**, 247701 (2018).
- [264] A. Kormányos, G. Burkard, M. Gmitra, J. Fabian, V. Zólyomi, N. D. Drummond, and V. Fal'ko, *K.p Theory for Two-Dimensional Transition Metal Dichalcogenide Semiconductors*, 2D Mater. **2**, 022001 (2015).
- [265] M. M. Glazov, M. A. Semina, C. Robert, B. Urbaszek, T. Amand, and X. Marie, *Intervalley Polaron in Atomically Thin Transition Metal Dichalcogenides*, Phys. Rev. B **100**, 041301 (2019).
- [266] Z. Wang, J. Shan, and K. F. Mak, *Valley- and Spin-Polarized Landau Levels in Monolayer WSe₂*, Nature Nanotech **12**, 144 (2017).
- [267] S. Borghardt, B. E. Kardynał, J.-S. Tu, T. Taniguchi, and K. Watanabe, *Interplay of Excitonic Complexes in p -Doped WSe₂ Monolayers*, Phys. Rev. B **101**, 161402 (2020).
- [268] Z. Ye et al., *Efficient Generation of Neutral and Charged Biexcitons in Encapsulated WSe₂ Monolayers*, Nat Commun **9**, 3718 (2018).
- [269] M. Barbone et al., *Charge-Tunable Biexciton Complexes in Monolayer WSe₂*, Nat Commun **9**, 3721 (2018).
- [270] G. F. Koster, J. O. Dimmock, G. Wheeler, and R. G. Satz, *Properties of Thirty-Two Point Groups* (M.I.T. Press, Cambridge, 1963).
- [271] B. Scharf, D. Van Tuan, I. Žutić, and H. Dery, *Dynamical Screening in Monolayer Transition-Metal Dichalcogenides and Its Manifestations in the Exciton Spectrum*, J. Phys.: Condens. Matter **31**, 203001 (2019).
- [272] A. Chernikov, A. M. van der Zande, H. M. Hill, A. F. Rigos, A. Velauthapillai, J. Hone, and T. F. Heinz, *Electrical Tuning of Exciton Binding Energies in Monolayer WS₂*, Phys. Rev. Lett. **115**, 126802 (2015).
- [273] F. Liu, M. E. Ziffer, K. R. Hansen, J. Wang, and X. Zhu, *Direct Determination of Band-Gap Renormalization in the Photoexcited Monolayer MoS₂*, Phys. Rev. Lett. **122**, 246803 (2019).
- [274] G. Sallen et al., *Robust Optical Emission Polarization in MoS₂ Monolayers through Selective Valley Excitation*, Phys. Rev. B **86**, 081301 (2012).
- [275] K. F. Mak, K. He, J. Shan, and T. F. Heinz, *Control of Valley Polarization in Monolayer MoS₂ by Optical Helicity*, Nature Nanotech **7**, 494 (2012).

- [276] T. Cao et al., *Valley-Selective Circular Dichroism of Monolayer Molybdenum Disulphide*, Nat Commun **3**, 887 (2012).
- [277] G. Kioseoglou, A. T. Hanbicki, M. Currie, A. L. Friedman, D. Gunlycke, and B. T. Jonker, *Valley Polarization and Intervalley Scattering in Monolayer MoS₂*, Appl. Phys. Lett. **101**, 221907 (2012).
- [278] E. Liu, J. van Baren, T. Taniguchi, K. Watanabe, Y.-C. Chang, and C. H. Lui, *Valley-Selective Chiral Phonon Replicas of Dark Excitons and Trions in Monolayer WSe₂*, Phys. Rev. Research **1**, 032007 (2019).
- [279] For simplicity, the same label, K3, is used for the phonon connecting the valleys K+ to K- and K- to K+ (a straightforward application of group theory should lead to the notations K3 and K2 respectively)., *For Simplicity, the Same Label, K3, Is Used for the Phonon Connecting the Valleys K+ to K- and K- to K+ (a Straightforward Application of Group Theory Should Lead to the Notations K3 and K2 Respectively)*.
- [280] T. Deilmann, P. Krüger, and M. Rohlfing, *Ab Initio Studies of Exciton g Factors: Monolayer Transition Metal Dichalcogenides in Magnetic Fields*, Phys. Rev. Lett. **124**, 226402 (2020).
- [281] J. Förste, N. V. Tepliakov, S. Y. Kruchinin, J. Lindlau, V. Funk, M. Förg, K. Watanabe, T. Taniguchi, A. S. Baimuratov, and A. Högele, *Exciton G-Factors in Monolayer and Bilayer WS₂ from Experiment and Theory*, Nature Commun, **11**, 4539 (2020).
- [282] T. Woźniak, P. E. F. Junior, G. Seifert, A. Chaves, and J. Kunstmann, *Exciton G-Factors of van Der Waals Heterostructures from First Principles Calculations*, Phys. Rev. B **101**, 235408 (2020).
- [283] F. Xuan and S. Y. Quek, *Valley Zeeman Effect and Landau Levels in Two-Dimensional Transition Metal Dichalcogenides*, Phys. Rev. Research, **2**, 033256 (2020).
- [284] D. V. Rybkovskiy, I. C. Gerber, and M. V. Durnev, *Atomically Inspired k · p Approach and Valley Zeeman Effect in Transition Metal Dichalcogenide Monolayers*, Phys. Rev. B **95**, 155406 (2017).
- [285] J. R. Schaibley, H. Yu, G. Clark, P. Rivera, J. S. Ross, K. L. Seyler, W. Yao, and X. Xu, *Valleytronics in 2D Materials*, Nat Rev Mater **1**, 16055 (2016).
- [286] C. Weisbuch and C. Hermann, *Optical Detection of Conduction-Electron Spin Resonance in GaAs, Ga_{1-x}In_xAs, and Ga_{1-x}Al_xAs*, Phys. Rev. B **15**, 816 (1977).
- [287] J. Hübner, S. Döhrmann, D. Hägele, and M. Oestreich, *Temperature-Dependent Electron Landé g Factor and the Interband Matrix Element of GaAs*, Phys. Rev. B **79**, 193307 (2009).
- [288] A. V. Stier, N. P. Wilson, K. A. Velizhanin, J. Kono, X. Xu, and S. A. Crooker, *Magnetooptics of Exciton Rydberg States in a Monolayer Semiconductor*, Phys. Rev. Lett. **120**, 057405 (2018).
- [289] J. Zhu, H. L. Stormer, L. N. Pfeiffer, K. W. Baldwin, and K. W. West, *Spin Susceptibility of an Ultra-Low-Density Two-Dimensional Electron System*, Phys. Rev. Lett. **90**, 056805 (2003).
- [290] R. Pisoni et al., *Interactions and Magnetotransport through Spin-Valley Coupled Landau Levels in Monolayer MoS₂*, Phys. Rev. Lett. **121**, 247701 (2018).
- [291] M. V. Gustafsson, M. Yankowitz, C. Forsythe, D. Rhodes, K. Watanabe, T. Taniguchi, J. Hone, X. Zhu, and C. R. Dean, *Ambipolar Landau Levels and Strong Band-Selective Carrier Interactions in Monolayer WSe₂*, Nature Mater **17**, 411 (2018).

- [292] E. Liu, J. van Baren, T. Taniguchi, K. Watanabe, Y.-C. Chang, and C. H. Lui, *Landau-Quantized Excitonic Absorption and Luminescence in a Monolayer Valley Semiconductor*, Phys. Rev. Lett. **124**, 097401 (2020).
- [293] T. Smoleński et al., *Interaction-Induced Shubnikov–de Haas Oscillations in Optical Conductivity of Monolayer MoSe₂*, Phys. Rev. Lett. **123**, 097403 (2019).
- [294] D. Edelberg et al., *Approaching the Intrinsic Limit in Transition Metal Diselenides via Point Defect Control*, Nano Lett. **19**, 4371 (2019).
- [295] M. M. Glazov, E. L. Ivchenko, A. N. Poddubny, and G. Khitrova, *Purcell Factor in Small Metallic Cavities*, Phys. Solid State **53**, 1753 (2011).
- [296] F. De Martini, M. Marrocco, P. Mataloni, L. Crescentini, and R. Loudon, *Spontaneous Emission in the Optical Microscopic Cavity*, Phys. Rev. A **43**, 2480 (1991).
- [297] A.I. Akhiezer and V.B. Berestetskii, *Quantum Electrodynamics* (Interscience publishers, 1965).
- [298] V. B. Berestetskii, E. M. Lifshitz, and L. P. Pitaevskii, *Quantum Electrodynamics, Second Edition*, Vol. 4 (Butterworth-Heinemann, Oxford, 1999).
- [299] H. Shan et al., *Brightening of a Dark Monolayer Semiconductor via Strong Light-Matter Coupling in a Cavity*, Nat Commun **13**, 1 (2022).
- [300] V. Lucarini, F. Bassani, K. E. Peiponen, and J. J. Saarinen, *Dispersion Theory and Sum Rules in Linear and Nonlinear Optics*, Riv. Nuovo Cim. **26**, 1 (2003).
- [301] K.-E. Peiponen, E. Gornov, Y. Svirko, Y. Ino, M. Kuwata-Gonokami, and V. Lucarini, *Testing the Validity of Terahertz Reflection Spectra by Dispersion Relations*, Phys. Rev. B **72**, 245109 (2005).
- [302] B. Gralak, *Analytic Properties of the Electromagnetic Green's Function*, J. Math. Phys. **58**, 071501 (2017).